Thèse de doctorat

Université de Limoges

Université de Limoges

École Doctorale Sciences et Ingénierie pour l'Information, Mathématiques (ED 521)

Institut de Recherche Xlim, Limoges

Thèse pour obtenir le grade de

Docteur de l'Université de Limoges

Electronique des Hautes Fréquences, Photoniques et Systèmes

Présentée et soutenue par

Muhammad Adnan

Le 18/12/2017

Experimental platform towards in-fibre atom optics and laser cooling

Thèse dirigée par Fetah BENABID et codirigée par Frédéric GEROME

JURY :

Président du jury :
Mme Valérie Madrangeas, Professeur, XLIM-Axe RF Elite, Université de Limoges.

Rapporteurs :
M. Jean-Claude Garreau, Directeur de recherche, Laboratoire PhLAM, Université de Lille.
M. Shau-Yu Lan, Professeur, Nanyang Technological University, Singapore.

Examinateurs :
M. Ouali Acef, Ingénieur de recherche, Observatoire de Paris, SYRTE, Paris.
Mme Isabelle Zaquine, Professeur, Telecom Paris Tech, Paris-Saclay.
M. Fetah BENABID, Directeur de Recherche, XLIM-GPPMM, Université de Limoges.
Mr. Frédéric GEROME, Chargé de Recherche, XLIM-GPPMM, Université de Limoges.

Acknowledgment

First of all, I would like to to pay special thankfulness, warmth and appreciations to my supervisor and mentor Dr. Fetah Benabid for his constant guidance and support throughout my thesis work and also for his patience, motivation and sharing his valuable knowledge. This would not have been possible without his timely support, guidance despite of his very busy schedule. I also thank to my co-supervisor Dr. Frederic Gerome for his guidance, valuable comments and encouragement. Dr. Foued Amrani helped me a lot for experimental data acquisition, simulations and thesis writing. I would also thank jury members Mr. Jean-Claude Garreau, Mr. Shau-Yu Lan, Mr Ouali Acef, Mme Isabelle Zaquine and Mme Valérie Madrangeas, My sincere thanks also go to Dr. Benoit Debort, Dr. Benoit. Beaudou and Dr. Jean-Marc Blondy for their knowledge sharing and their precious support which taught me sufficient experimental skills in the laboratory to conduct this research.

I would also pay thanks to Prof. Dr. Patrick Windpassinger, Institute for Physics, University of Mainz, Germany for giving me an opportunity to spend two weeks in his laboratory for secondment and whole team of QTea (Quantum sensor Technologies and applications).

Also, I thank my colleagues in GPPMM, Dr. Aurelien Benoit, Dr. Jonas H. Osorio, Jerome Alibert, Martin Maurel, Mathieu Chafer, David Kergoustin, Ximeng Zheng, Frédéric Delahaye, Alexandre Gorse, Maxime Delgrange, Thomas Billotte and Karim Frigui, all the GLO photonics team members for being in support at my experiment especially whenever we unsealed our vacuum system to do modifications inside. I will pay warm thanks to Frugier Patrick, Martin Pierre-Olivier (POM), Caperan Jean-Francois, Rainaud Ludovic, Quentin Lekiefs, Alexandre Lavigne for machining of vaccum components for my experimental set up. My special thanks go to my dearest friend Dr. Abhilash Amsanpally for his brotherly support during my stay in Limoges and to compensate my critical times with spicy and tasty curries.

Finally I would like to thank my sister, brothers (Muhammad Imran & Atta Ullah), my nephews (Tabish, Tashfeen, Zulkifl, Zulbakht and Usairum) for their moral support during my thesis and to my friends (in Limoges) Oussama, Faten, Ines, Shaima, Oualid, Yassine, Saleh, Hamid, Jamilah, Nadia, Kausar. Very special thanks go to my late parents and late brother.

Abstract

To cool atoms by means of laser has achieved the attraction because of their applications in quantum optics. It boosted up the technological and scientific field. It also revolutionized the functionalities frequency reference, atomic clocks, interferometer, gyroscope by their applications from laboratory environment to community users through the development of compact, stable, user-friendly and stand-alone atom-optic devices. To bring atoms from free space to nano- or micro geometries is flourishing field. This was started in the early of 90s from their confinement in capillary and now this field is matured in expertise.

The aim of this thesis is to build a versatile experimental platform for in-fiber laser cooling of Rb atoms and compact photonic device, photonic microcell (PMC) containing Rb atoms, later is not the part of this work. These photonic devices would be able to cool atoms by exciting the proper mode. These modes would be contained on far-off red detuned fundamental mode to confine and cool the atoms in longitudinal direction and blue detuned donut mode to trap them in transverse direction. We have put IC Kagome fibers with different geometries. As a whole our system has IC Kagome with different geometries with inner surface coated with materials and uncoated. Here we will focus only the nano- or micro geometries as host for cold or thermal atoms. HC-PCFs give long interactions length between gas and laser light and small modal area. After having cold or thermal atoms inside the hollow-core fibers, it is challenging to keep them inside the micro-geometries by reducing their interaction with inner glass surface. These geometries, because of their small core size, provide large surface-to-volume ratio to the atoms confined in it and needs to address the questions like the coherence relaxation dynamics and the nature and effect of the atom-surface interaction. In addition to these questions, there are challenging technological needs to be met properly such as the identification of the proper HC-PCF design so to support the appropriate spatial modes to keep these atoms confined in small core PCF, the identification of the most

performant coating materials for the HC-PCF core inner-surface. Towards the main aim, we have successfully achieved MOT of both isotopes of Rb atoms and we characterized the temperature and number of atoms. Also we loaded thermal atoms inside hollow-core of fibers to see the difference between coated, uncoated fibers and background rubidium. Our group has vast expertise in this direction and demonstrated handful results.

Table of Contents

List of Figures

List of Tables

Abbreviations

HC-PCF	**Hollow-Core Photonic crystal fiber**
PMC	**Photonic MicroCell**
BEC	**Bose-Einstein Condensate**
MEMS	**Micro Electro Mechanical Systems**
SQUID	**Superconducting QUantum Interference Device**
OFC	**Optical Fiber Capillary**
EIT	**Electromagnetically Induced Transparency**
IC	**Inhibited Coupling**
UHV	**Ultra-High Vacuum**
TBM	**Tight Binding Model**
DOPS	**Density Of Photonic States**
MFD	**Mode Field Diameter**

Definition of symbols

$\boldsymbol{\beta}$	Axial component of wavevector k
$\boldsymbol{c}$	Speed of light in a vacuum
$\boldsymbol{h}$	Planck's constant
$\boldsymbol{\hbar}$	Reduced Planck's constant $(h/2\pi)$
$\boldsymbol{k}$	Wavevector, $1/\lambda$
$\boldsymbol{k_B}$	Boltzmann constant
$\boldsymbol{k\Lambda}$	Normalised frequency
$\boldsymbol{\Lambda}$	Fibre cladding pitch
$\boldsymbol{\lambda}$	Wavelength mean-free-path
μ	Transitional dipole moment kinematic viscosity
$\boldsymbol{n}$	Refractive index
$\boldsymbol{n_{eff}}$	Effective refractive index

Chapter 1

Cold-atom optics overview

This chapter presents a historical review of laser cooling and trapping of atoms and the current trends in this field with an emphasis on atom-optics in hollow-core photonic crystal fibre (HC-PCF). After listing the key fundamental and technological developments that led to the emergence of the field, we highlight the basic physical principals behind the atom motion control with lasers, which then led to atom cooling and trapping. We then survey the current trends in cold atom. We will emphasize on the different platforms that are currently explored for making thermal and cold atoms in miniaturized devices, with a particular focus on HC-PCF and its functionalized form photonic microcell (PMC). We will then finish this chapter by describing the motivations and the work undertaken in this thesis to address the challenges towards the long-term goal of "in-fibre laser cooling".

1.1 Introduction

Atomic cooling by laser means has been one of the most successful endeavours in atomic physics in the last thirty years, illustrated by the large number of Nobel prizes in this field [1]. Indeed, since the first theoretical proposals in the 70s [2], the field has gone from successfully demonstrating the principle of laser-induced cooling neutral atom to decreasing the temperature to the Doppler limit (*i.e.* the lowest temperature possible by virtue of the effect of Doppler [3]). Then to below this limit with the advent of new concepts such as Sisyphus cooling [4], and later to generate a new phase of matter, namely, Bose-Einstein Condensates (BEC) with temperature-level as low as nano-Kelvin range using evaporative cooling effect in late 80s early 90s [5]. Today, cooling atoms with laser has reached a level of maturity that BEC can be formed at below 500 picoKelvin temperature [6].

Such a progress in laser-cooling atoms was both a technological and scientific adventure and its impact is still timely. It revolutionized the optical metrology in direction of distances and dimensions, temperature, frequency and time. The potential of atomic optics revealed by the atomic interferometers [7], such as Sagnac gyroscope [8] and Mach-Zehnder interferometers [9] boost its performance compares to its optical counterparts. Physical quantities like gravity [10] and electric polarizability [11] could be measured accurately with atomic interferometers than an optical interferometer.

Today, laser-cooled atoms are used both as a technological tool in several research area and a subject of fundamental physics such as atomic clocks [12], interferometry [9] and Rydberg atoms [13] for ultra-precision sensing and quantum information. On the other hand, they are a platform to observe novel physical phenomena at very low energy scale such as phase transition to new form of matter. Laser cooling techniques are also a major tool to cool molecules or to synthesize them via photo-association.

Another route that is of more interest towards industrial applications use by the broader academic communities is to miniaturize the laser cooling set-up and/or to be available commercially in the form of compact atomic device. This work aligns itself with this broad and ambitious aim by exploring the feasibility of laser cooling atoms that are inside a hollow-core photonic crystal fibre (HC-PCF). Furthermore, the present work stems from both the field of cold atoms and that of photonics. This platform will be based on HC-PCF for its ability to host both gas phase media and photon within micro-meter scaled effective area and to make them interact over lengths which can be easily well over 10 orders of magnitude longer than the typical Rayleigh length. When the HC-PCF is filled with a gas-phase medium and then spliced in a hermetic and low optical loss manner to a solid optical fibre, it takes the form of what is called photonic microcell (PMC) [14]. Thus a PMC is a seemingly a standalone optical fibre that also act as a vapor cell, and has now proved to be an excellent photonic component for several fields including spectroscopy [15-16]. This work is developed with the aim to first create an experimental platform for studying and controlling cold as well as thermal atoms inside HC-PCF, and then to be used to explore the feasibility of "in-fibre laser cooling" whereby thermal atoms confined in a PMC can be cooled at any time by an appropriate modal excitation of the PMC.

In this chapter, we will give a historical review on how laser cooling has been developed. Then we will provide a survey on current state-of-the-art applications in this field and list the major research trends, with an emphasis on the works related to laser cooling in compact devices or in confined geometries. In a following section, we will focus on the prior works related to the attempts of manipulation of thermal and cold atoms in hollow-core waveguides.

1.2 Laser cooling and trapping of neutral atoms

1.2.1 Historical overview

Manipulating atoms, molecules or particles with light has been a subject of research since Johannes Kepler in the 17th century [17] whereby the momentum carried by a photon has already been identified as a possible means to apply a mechanical force on atoms, molecules or particles [3]. The first prediction that light exerts pressure upon any surface exposed to it was proposed in 1871 by James Clerk Maxwell. Later, in 1901, J. N. Lebedev [18] measured the movement induced by light on a suspended metallic mirror in a high vacuum. According to these early work, a planar electromagnetic wave with an average Poynting vector $\langle S \rangle$ exerts a pressure P on a fully absorbing surface given by $P = \langle S \rangle / c$, with c being the speed of light. Nicholas and Hull [19] confirmed the first quantitative proof of Maxwell's electromagnetic theory in the same year. With the invention of the laser, such proposals of mechanically controlling matter with light witnessed a renewed interest and experienced a radically new outcome with atom control. The possibility of interaction between atoms and a laser standing-wave was first introduced by Letokhov in 1968 [20]. Further insights were sought by A. Ashkin [2] who developed the concept of cooling and trapping atoms using light radiation pressure in 1970. Particularly, Ashkin introduced the impact of resonant absorption and spontaneous emission (see Figure. 1.1) on the atomic translational motion, he assumed that because of random direction of spontaneous emission, the momentum of the exciting photon during absorption is communicated to the atom momentum. Later, T.W. Hansch and A.L. Schawlow [21] extended on Ashkin work to point out that atoms can be cooled (that's the atom translational kinetic energy can be reduced by virtue of the relation between the r.m.s. thermal velocity v_t and the temperature T: $v_t = \sqrt{3k_B T/m}$. Here, k_B is the Boltzmann

constant and m the mass of the atom) by a laser with a frequency that is red-detuned by around half the Doppler width from the atom resonance. This cooling concept is illustrated in Figure. 1.2, and is now part of the standard techniques in laser-cooling of atoms, and is coined as Doppler cooling.

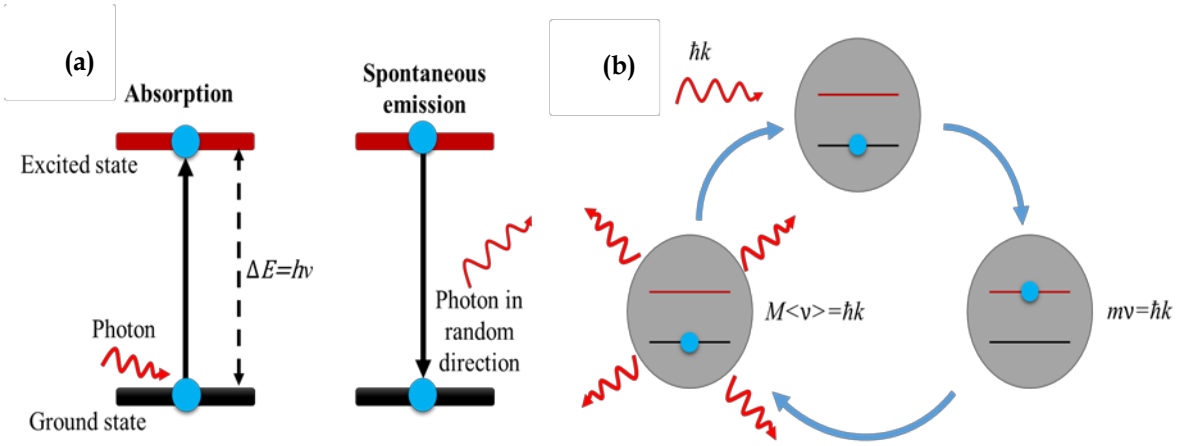

Figure 1.1: (a) Mechanism of the interaction between an atom and a photon. A photon with an energy $h\nu$ equal to the difference between the two atomic energy levels and with a well-defined momentum $\hbar k$ is absorbed to excite the atom in a higher energy level. The excited atom returns to its ground state by spontaneously emitting a photon in a random direction. (b) The net momentum exchange during a cycle of absorption and spontaneous emission. As photons are reemitted in random directions, an average of many scattering events gives an atom a net scattering force along the direction of light.

The cycle of Doppler cooling is the following: an atom moving away from the red-detuned laser, absorbs a photon of momentum $\hbar k$ and gets excited. The frequency of the light will appear lowered out of resonance with the scattering transition, and the atoms can only lose energy and momentum by scattering of the laser light, and never gain. If the light comes from all directions, atoms will lose energy by scattering the oncoming light, while the Doppler-shift will detune any light wave traveling in the same direction as the atoms. In this way the translational temperature of the atoms can be reduced until ultimately the Doppler line width is as small as the natural line width [21].

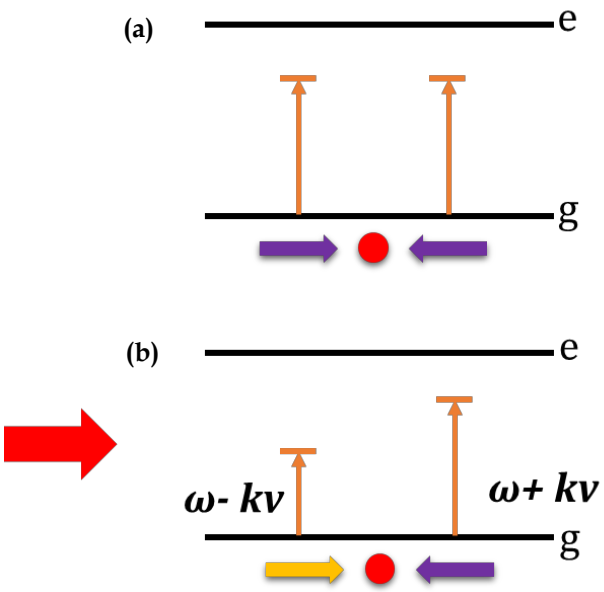

Figure 1.2: Principle of Doppler cooling. (a) When the laser frequency is slightly red-detuned from the atomic resonance (b) moving atom subject to damping force mechanism of the interaction between an atom and a photon. A photon with an energy $h\nu$ equal to the difference between the two atomic energy levels and with a well-defined momentum $\hbar k$ is absorbed to excite the atom in a higher state.

The first experimental demonstration of the above principles was achieved in 1985 by Steven Chu et *al.* [3] who reported cooling and viscous confinement of neutral sodium atoms in three dimensions by using three orthogonal pairs of counter propagating red-detuned laser beams intersecting each other at the centre which formed the trap. In this trap, a cloud of slow atoms (optical molasses) exhibiting a density of ~10^6/cm^3 were confined in 0.2 cm^3 volume for 0.1 sec. The lowest measured temperature was then about ~240 µK (which is the limit set by Doppler cooling with Na). Here, atoms were not confined spatially (optical molasses), and can thus slowly drift out the cooling volume. In this seminal work of S. Chu et *al.* [3], the optical molasses' atoms are confined only in velocity space but not in position space. To ensure atom's confinement in both velocity-space and coordinate-space, the magneto optical trap (MOT) is developed and reported in 1987 by E. L. Raab and colleagues. The principle of a MOT is illustrated in Figure. 1.3 where a magnetic trapping is added to the optical trap described above by adding a spatially varying magnetic quadrupole field using a pair of anti-Helmholtz

coils. This causes a Zeeman shift in atom energy levels that increases with the radial distance from the centre of the trap. In turn, by virtue of Lorentz force an atom moves away from the centre of the trap feels a force that pushes it back to the centre of the trap. This confers the ability of MOT both to cool and confine atoms in velocity-space and coordinate-space. The MOT is, nowadays, the most common tool to create cold neutral atoms. In its first demonstration, Raab et *al*. confined and cooled down to ~0.4 K optically dense cloud of 10^7 neutral sodium within a volume of ~ 0.5 mm in diameter and with a density $10^{11}/cm^3$ for two minutes. They trapped and cooled atoms with temperature less than milliKelvin with trapping and ~0.4 K deep [22].

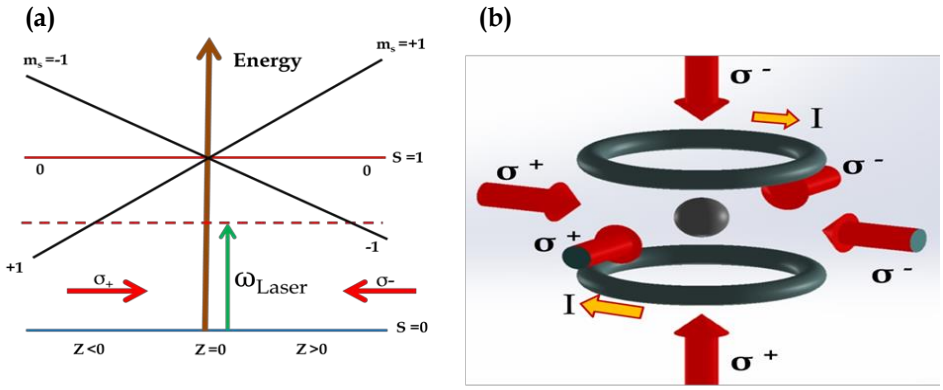

Figure 1.3: (a) Arrangement for 1D MOT. The horizontal dashed line represents the laser frequency seen by an atom at rest in the centre of trap. The linearly magnetic field (from anti-Helmholtz coils) produces the Zeeman shits in the atomic transition frequencies. So atoms at z>0 are closer to resonance with σ^- laser beam than with σ^+ beam and are therefore towards the centre of trap and same effect happens for z<0. The current in set of anti-Helmholtz coils is in opposite directions which produce the effect z=0 at middle of both coils and the laser beams intersect each other at same point. (b) When this effect is expanded for all six beams.

Another major milestone in the history of cold atoms is the achievement of cooling atoms to a temperature below the limit set by the Doppler cooling model. Indeed, in 1988 William D. Phillips and co-workers achieved a cold sodium cloud with temperature 10 times below their Doppler limited temperature, which is 240 μK [23]. It turns out that the two-level atom of the Doppler cooling model was too simple to capture all the dynamics of such laser-atom interaction. In 1989, J. Dalibard and C. Cohen-Tannoudji [4] provided the theoretical explanation of such sub-Doppler limited temperature, and whereby they demonstrated that the polarization gradient of the counter-propagating laser cooling beams alter

significantly the internal state of the atomic ground-state Zeeman levels (see the section below); a phenomena that was coined "Sisyphus Cooling". The latter results concluded the exciting history of the advent of cold atoms by the award of the 1997 Nobel Prize to S. Chu, W. Philips and C. Cohen-Tannoudji [1]. Furthermore, Sisyphus cooling opened a new chapter of cold atoms by allowing the achievement of temperature ranges below the critical temperature, $T_c = 0.089\ (h^2/mk_B)n^{2/3}$ [5], for a phase transition to BEC. Here, n is the density of the cold atoms. The first demonstration of BEC was reported in 1995 by M. H. Anderson et *al.* and was achieved with vapor of Rb^{87} atoms (see Figure. 1.4) having temperature as low as 170 nK and density of $2.5X10^{12}$. The advent of BEC was also being recognized through the Nobel Prize to Eric Cornell, Carl Wieman and Wolfgang Ketterle in 2001.

In the above section, we have described how the field of cold atom evolved historically. Here, we give the basic physical effects that are behind optical cooling.

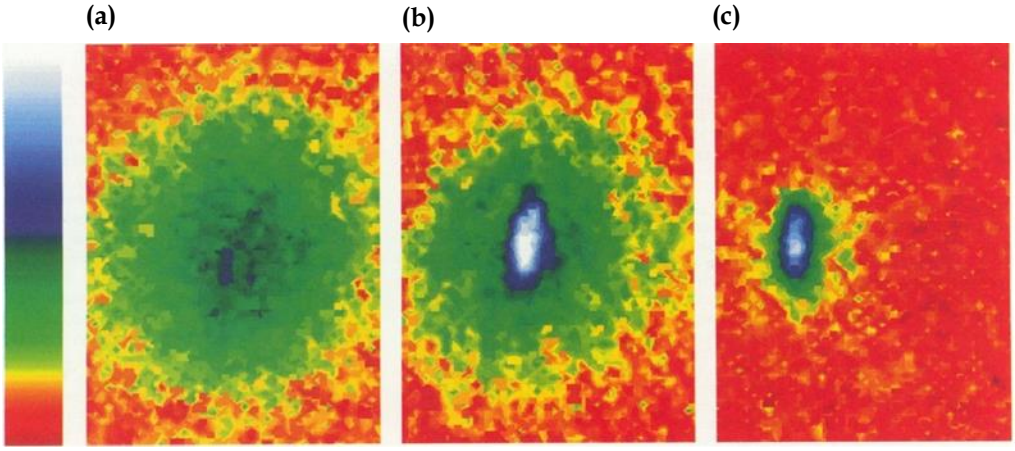

Figure 1.4: A sequence of appearance of BEC (a) Just before (b) after and (c) pure condensate [5].

1.2.2 Basic principles

1.2.2.1 Radiation pressure

During the cycle of a near-resonant photon absorption-spontaneous emission, a two-level atom with a transition frequency ω_0 and a natural linewidth of Γ sees its velocit change by:

$$\Delta \vec{v} = \frac{\eta \vec{k}}{m} \tag{1.1}$$

This means that the radiation pressure force, also called the scattering force, exerted by a plane electromagnetic wave on the atom during this cycle is:

$$\overrightarrow{F_{RP}} = m\frac{\Delta \vec{v}}{\Delta t} = \hbar \vec{k} \Gamma \rho_{22} \tag{1.2}$$

Here, ρ_{22} is the population of the excited and $\Gamma(\rho_{22} - \rho_{11})$ represents the scattering rate. The above force expression can be further developed by using Bloch equation to take the following form [13]:

$$\overrightarrow{F_{RP}} = \hbar \vec{k} \frac{\Gamma}{2} \frac{I/I_s}{1+I/I_s+(2\delta/\Gamma)^2} \tag{1.3}$$

Here, I and I_s are the total intensity of laser beam and saturation intensity respectively. The quantity δ is the frequency detuning of the laser frequency from the atom transition frequency. This radiation pressure force reaches a maximum of $\hbar k\Gamma/2$ when the laser frequency is resonant with the atomic transition ($\delta = 0$) and its intensity well above the saturation limit. It is noteworthy, that the magnitude of such a force can be 6 orders of magnitude larger than the gravitational force for atoms such as Rb, Na or Cs.

1.2.2.2 Viscous force and Doppler cooling

The detuning δ term in the pressure radiation force (equation. 1.3) depends on the atom velocity and can be replaced by $\delta \pm \vec{k}\vec{v}$. Furthermore, if one considers a counter-propagating laser beams (here a planar wave approximation is assumed), the net force of the two radiation pressure forces $\overrightarrow{F_{RP+}}$ and $\overrightarrow{F_{RP-}}$ from the two beams takes the form below for the case of $\vec{k}\vec{v} \ll \Gamma$ (*i.e.* we take into account only the velocity class that are within the FWHM of the absorption line):

$$\overrightarrow{F_{Dop}} = \overrightarrow{F_{RP+}} + \overrightarrow{F_{RP-}} = \left(8\frac{\hbar k^2 \delta}{\Gamma}\frac{I/I_s}{1+I/I_s+(2\delta/\Gamma)^2}\right)\vec{v} = -\beta\vec{v} \tag{1.4}$$

As predicted by Hansch and Schawlow [21], this force is a viscous force that tends to decelerate the atom (*i.e.* to cool them) with a damping coefficient which depends on both laser detuning and intensity. Figure 1.5 below shows velocity dependence of optical damping force for four de-tunings (-Γ/8, -Γ/2, -Γ and -2Γ) in one

dimension [24]. The lowest velocity or temperature achieved using this model is set by the equilibrium between the cooling rate and the heating rate. The heating rate is set by the diffusion and the atom random walk. Indeed, while the atom's velocity can reduce to zero, the mean squared velocity remains non-nil. During the absorption-emission cycle the atom acquires momentum by the effect of recoil and energy $E_{cycle} = 2\hbar\omega_r$. Here, ω_r is the recoil frequency given by $\omega_r = \hbar k^2/2m$. These rates are then given by:

$$\begin{cases} \left(\frac{dE}{dt}\right)_{cool} = -\overrightarrow{F_{Dop}}\vec{v} = \beta v^2 \\ \left(\frac{dE}{dt}\right)_{heat} = -\Gamma\rho_{22}E_{cycle} \end{cases} \tag{1.5}$$

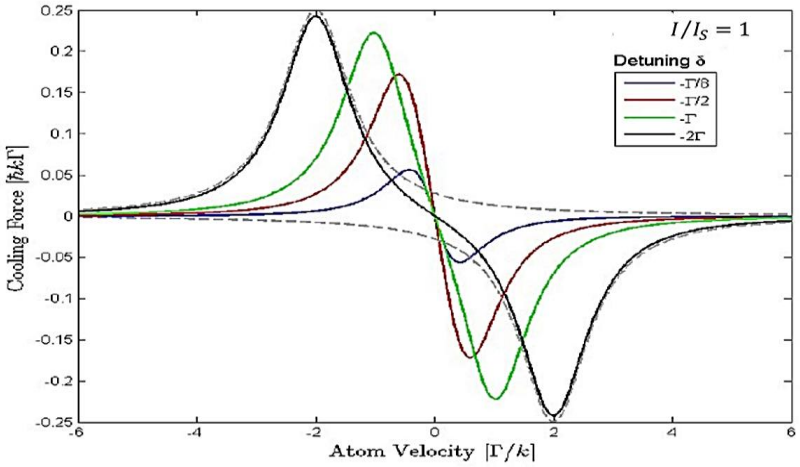

Figure 1.5: One-dimensional velocity dependence of optical damping force for 4 different de-tunings [24].

At equilibrium, we have $mv^2 = (\hbar\Gamma/4)[(2\delta/\Gamma) + (\Gamma/2\delta)]$, and the minimum kinetic energy is reached at a detuning $\delta = \Gamma/2$. Consequently the lowest temperature achieved by Doppler cooling is:

$$T_{min}^{D} = \frac{\hbar\Gamma}{2k_B} \tag{1.6}$$

For the case of Rubidium cooled at D2 transition, which is part of our experimental conditions, we have T_{min}^{D}~146 μK.

1.2.2.3 Magnetic and optical trapping

The above model doesn't completely represent the experimental conditions of a typical laser cooling, and as mentioned before, it failed to explain the sub-Doppler temperature achieved experimentally. The latter will be addressed in the following section. In the present section, we complete the Doppler model by describing the additional forces that are at play in a typical MOT. In most of the commonly used MOTs there are at least two additional trapping forces that were not mentioned in the previous section. The first one is a magnetic force that results from the magnetic gradient generated by the pair of anti-Helmholtz coils. The second one is an optical dipole force which is caused by the intensity transverse gradient. The magnetic force caused by the Zeeman shift of the ground state levels can be deduced in a similar manner as the radiation pressure force, meaning by expressing the change in the detuning that is induced by the magnetic gradient; *i.e.* δ is replaced by $\pm\omega_{Zeeman}$. Here, ω_{Zeeman} is the shift between two Zeeman levels in the ground state. The expression of the net magnetic force is:

$$\overrightarrow{F_{mag}} = \left(8\frac{\hbar k^2 \delta_m (\partial B/\partial z)}{\Gamma}\frac{I/I_s}{1+I/I_s+(2\delta/\Gamma)^2}\right) z = -\kappa\vec{z} \tag{1.7}$$

Here, $\vec{z}$ is the quantization axis, δ_m is the Zeeman level frequency shift and $(\partial B/\partial z)$ is the magnetic field gradient.

In conclusion, the atoms near the canter of the MOT experience a force in the form:

$$\overrightarrow{F_{MOT}} = -\beta\vec{v} - \kappa\vec{z} \tag{1.8}$$

If we have to include the transverse profile of the laser beams, the force induced by a laser beam is now comprised with the radiation pressure force and a dipole force:

$$\overrightarrow{F_{op}} = \langle\vec{d}\rangle \cdot \nabla\vec{E} = \overrightarrow{F_{RP}} + \overrightarrow{F_{dip}} = \hbar\vec{k}\Gamma\rho_{22} + \frac{d}{2(\rho_{12}+\rho^*_{12})}\nabla E(\vec{r}) \tag{1.9}$$

Here, $\langle\vec{d}\rangle$ is the average dipole of the atomic transition, and the dipole force is responsible for the atom radial trapping. For a laser beam with intensity profile $I(r)$, the dipole force takes the following form:

$$\overrightarrow{F_{dip}} = -2\,\hbar\delta\frac{1}{1+I/I_s+(2\delta/\Gamma)^2}\nabla_r I(r) \tag{1.10}$$

If we consider a collimated beam (*i.e.* its beam size, w, is uniform the its propagation axis) with a Gaussian profile, the intensity profile is $I(r) = (P/2\,w)e^{-2(r/w)^2}$, and the dipole force takes the following form:

$$\overrightarrow{F_{dip}} = -8\,\frac{\hbar\delta}{\pi\,w^2}\,\frac{I(r)}{1+I/I_s+(2\delta/\Gamma)^2}\,r\overrightarrow{e_r} \tag{1.11}$$

The above expression shows a restoring force along the transverse plane of the laser propagation axis. Furthermore, combining this force with the one in eq. (1.8), we have a system that have a restoring force over all the spatial coordinates for trapping and one force in the velocity space for cooling.

1.2.2.4 Sisyphus cooling

In the above Doppler cooling model, the atom has been pictured as a two level system, which is not the case of real atoms. For example, the ground state of the atoms (especially alkali ones) in a MOT exhibits a Zeeman manifold levels and are magnetically sensitive (Zeeman effect). This internal state structure turned out to have a significant impact in the atom cooling that led to sub-Doppler temperature. The theoretical model to explain this sub-Doppler cooling, reported by J. Dalibard and C. Cohen-Tannoudji [4], relies on the polarization gradient of the counter-propagating laser fields. The resulting overlapping counter-propagating, polarization orthogonal field exhibits polarization spatial modulation dependance. In turn, because of the difference in the Clebsch-Gordan coefficients of the transitions between the different Zeeman levels, the spatial polarization gradient and modulation will spatially modulate the energy Zeeman levels with a period of half the laser wavelength. This phenomenon, called Sisyphus cooling is illustrated in Figure 1.6. Considering the two common polarization configuration of the counter-propagating lasers, namely $lin \perp lin$ for two orthogonal linearly polarized beams and $\sigma_+ \perp \sigma_-$ for two orthogonal circularly polarized beams, the cooling force expression in equation. (1.4), is replaced by the following [4]:

$$\overrightarrow{F_{lin\perp lin}} = -\left(3\,\frac{\hbar k^2|\delta|}{\Gamma}\frac{1}{1+\left(\frac{v}{v_c}\right)^2}\right)\vec{v} \tag{1.12}$$

for a $lin \perp lin$ polarization configuration, and

$$\overrightarrow{F_{\sigma_+ \perp \sigma_-}} = -\left(\frac{120}{85}\,\frac{\hbar k^2}{\delta}\frac{\Gamma}{0.8+\left(\frac{\Gamma}{\delta}\right)^2}\right)\vec{v} \tag{1.13}$$

for $\sigma_+ \perp \sigma_-$ polarization configuration.

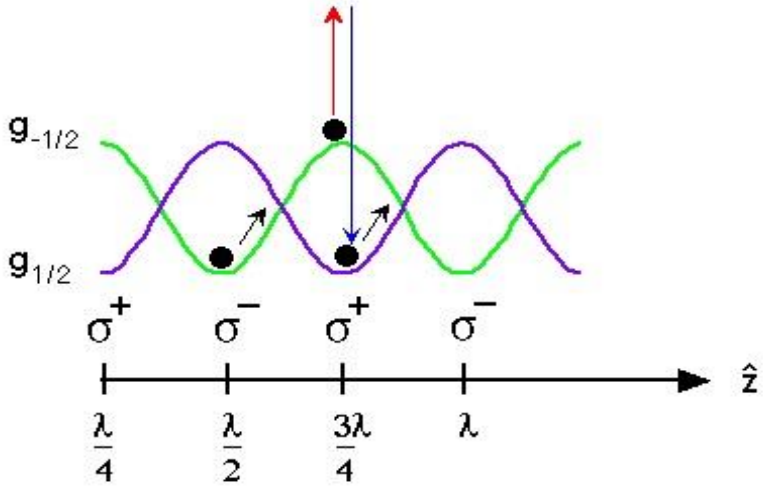

Figure 1.6: The laser cooling mechanism (known as Sisyphus cooling) in a standing wave with a spatially varying polarization. The light perturbs the energy levels of atom in periodic way because of this effect atoms travel up and down in hills and valleys (maxima and minima) in the potential energy. Atom loses kinetic energy when absorbs laser light at the top of a hill and emits a spontaneous photon of higher frequency, so that it ends up in a valley. This process provides stronger laser cooling. Thus atoms in a standing wave are cooled below the Doppler cooling limit (the lowest temperature achievable with scattering force alone) [13].

Here, v_c is the critical velocity given by $v_c = \gamma/2k$, with γ being a transition rate between two Zeeman levels of the ground state.

Using the balance between the cooling and the heating rate as above, and considering that the atom will always acquire a recoil kick in a spontaneous emission, the lowest temperature in Sisyphus cooling can only a few times the recoil-limit temperature, which is set by:

$$T_{min}^{recoil} = \frac{\hbar^2 k^2}{k_B m} \tag{1.14}$$

For rubidium atoms excited at its D2 transition, the recoil-limit temperature is as low as 362 nanoKelvin, which is more than 400 times cooler than the Doppler limit. In practice however, the temperature achieved with MOT remains considerably above the recoil limit. Getting closer to the recoil limit is achieved by yet another cooling technique coined "evaporative cooling".

1.2.2.5 Evaporative cooling

The principle of evaporative cooling, first proposed by H.F. Hess for hydrogen atoms [25], stems from the fact that the hottest confined atoms in a potential well lie in the highest energy level of the well whilst the coolest occupy the lowest energy level of the trapping well.

By reducing the well potential-depth (as illustrated in Figure 1.7) let hotter atoms to escape, leaving cooler atoms in deep potential well to form BEC. At this BEC regime the cold atom temperature is below the critical temperature given by $\boldsymbol{T_c \sim 0.94\, \hbar \omega_0 k_B^{-1} N^{1/3}}$.

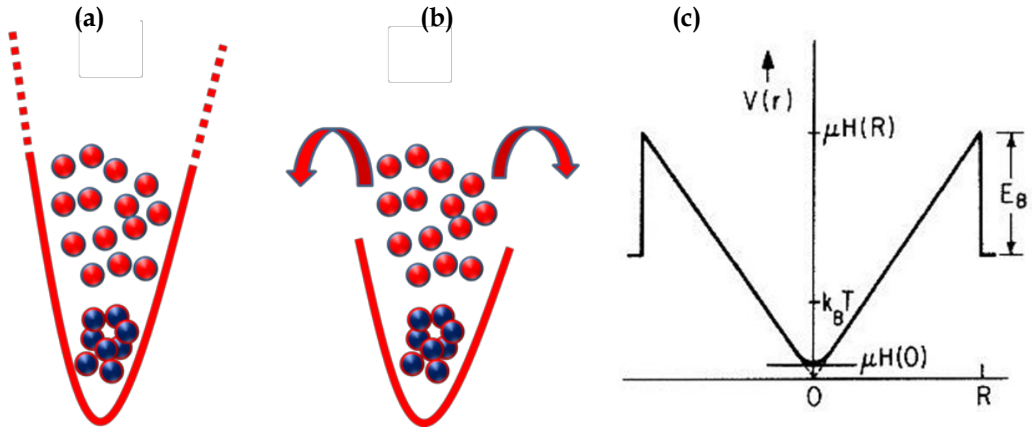

Figure 1.7 (a) Schematic representation of harmonic potential in which atoms are confined (b) The atoms with above-energy escape as the height of potential is reduced. It is noteworthy that there are other schemes in cooling and manipulating atoms such as sideband and Raman cooling [26]. However, the above physical principles and techniques are the most commonly used and represent the founding physical principles of the whole field of cold atom physics. (c): Potential energy of atoms as a function of radial distance from the axis.

1.3 Current trends in cold atom optics

Cold atom physics has now matured to a level where it is used as a tool in a number of applications such as atomic clocks and quantum sensors [27]. It also remains a timely and exciting field for fundamental research. Nowadays we can describe the current research involving cold atoms into three main trends: (1) tool for fundamental quantum physics; (2) high precision quantum sensors, and (3) miniaturized atom optics platforms and devices.

In fundamental physics, cold atom physics branched into four main routes: (a) quantum computation with ultracold polar molecules [28], (b) fundamental physics test such as the "constancy" of the physical constants [29-30], (c) simulation of condensed matter systems (quantum simulator [31]) whereby optical lattice become an interesting test bed to explore phenomena that was impossible or highly difficult to do with solid state materials [31], and (d) quantum chemistry at ultracold temperatures [32]. In applied physics and technology, cold atoms are now a well-established material for highly sophisticated set-ups such as primary atomic clocks [33], magnetometers [29], quantum inertial sensors such gravimeters [30], gradiometers or rotation sensors [34]. Today complex quantum systems based on ensembles of ultracold atoms can be controlled to an extent that has led to the emergence of quantum technology in a number of areas of physics. The overarching possibilities of this technology, its growth and success have been identified as one of the grand challenges in science around the world, most notably by the United States National Science Foundation and EU. Atomic physics, with a focus on ultracold gases, quantum optics, condensed matter and semiconductor physics, nanotechnology and surface science as well as laser physics, photonics and fibre optics are fields would play a major role in this development. In parallel with the above-mentioned expanding applications of cold atoms, there is an on-going effort to provide the performance of these cold-atom based set-ups in a highly miniaturized physical packages. Indeed, while the laboratory based cold atom enabled performances such as the ultra-stability of the atomic clock frequency has

gone through a continuous and a dramatic progress, the large size and the complexity of these set-ups limited their impact on a number of scientific and technological applications (*e.g.* geophysical explorations, navigation and physical constants measurement). For example, the need for compact atomic clock is exemplified by the high investment of NIST which led to the micro-chip atomic clock (see a section below). In our group GPPMM in XLIM, we are exploring another route to develop miniatured atomic clock based on HC-PCF, and which hold the potential of achieving a much lower relative frequency fluctuations. The work of this thesis is related with our group endeavour to develop atom-optics based photonic components using atom-filled HC-PCF [14].

1.3.1 Cold atom based sensors

Atomic clocks and frequency references: The importance of cold atom in science and technology is exemplified by the history of atomic clocks, where atoms absorption lines exhibiting extremely narrow line-widths are used as stable and accurate frequency references to which radio, microwave or optical signals are locked into so to form "pure-signal oscillators". For more than 40 years, thermal and cold neutral atom-based clocks have played a critical role in basic science, precision measurements, and technical applications. In fact a high precision clock systematically dictates the performance of not only any set-up in sensing, telecommunication, navigation and instrumentation, but also fundamental research, which requires ultra-high resolution spectroscopy [35]. Furthermore, the ever increasing need for more precise timing and synchronization, for a range of applications including navigation systems [36], telecommunications, VLBI telescopes [37], and tests of fundamental physics [35] has been one of the driving force in the development of cold atom physics. This is illustrated with very rapid use of cold atoms by metrology research groups and the subsequent development of atomic fountain microwave clocks in the 1990s, which first demonstration represented almost a two orders of magnitude improvement in frequency-stability when compared to the best thermal atomic clocks [35]. Figure 1.8 shows the timeline

evolution of the atomic clock frequency-stability since its invention by Essen in 1960 [38]. The first cold atomic clock exhibits a frequency-stability $\delta f/f$ of only a few 10^{-15}, which is almost 100 times more stable than the thermal atomic clock, and it keeps improving by a factor of 10 every decade (dashed blue line of Figure.1.8).

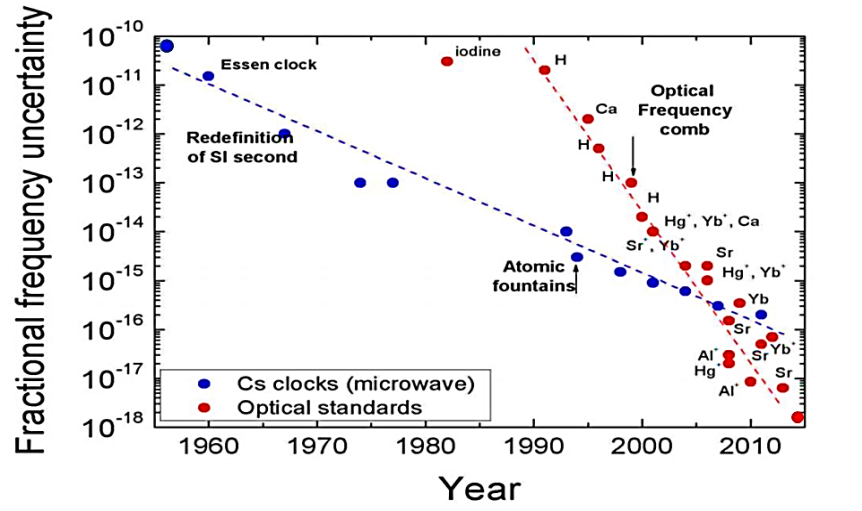

Figure 1.8 : Evolution of fractional frequency uncertainties of atomic frequency standards based on microwave (Cs clocks) and optical transitions.

In parallel, with the progress on microwave clocks where a hyperfine transition of Cs and Rb is used as a reference for microwave spectral range, cold atoms were also very quickly identified as excellent candidates for optical atomic clock, where the frequency reference is provided from a dipole transition with a frequency range within the optical domain. This development was also enabled with the stability of laser sources, which is now starting to surpass the best microwave sources, and broadly tuneable, optical-frequency synthesizers with a frequency resolution of better than one part in 10^{14} are now commercially available. As shown in Figure. 1.8, the use of optical reference represents a revolutionary step forward in the evolution of atomic frequency and time standards [39-40-41]. A fractional frequency uncertainty in the 10^{-18} region have been reported with a number of atoms such as with ^{87}Sr optical lattice clock at JILA [42-43], or Yb lattice clock, which demonstrated a fractional instability (not uncertainty) of 1.8×10^{-18} for 25,000 s of averaging time [44]. In order to illustrate this achievement in frequency stability, we recall that two clocks with 10^{-18} fractional frequency uncertainty placed at height difference of only

1 cm can detect the gravitational red-shift. Now, optical clocks are very exciting and active research in institutions world-wide. Furthermore, atomic clocks based on cold-atom are also considered for gravitational wave detectors [45].

Inertial quantum sensors: The advent of cold atoms and the subsequent BEC led to the advent of matter-wave interferometers, which are based on coherent manipulation of matter with light pulses. These interferometers proved to be very sensitive sensors to inertial forces, in particular gravitational and rotational acceleration. The unprecedented sensitivity and practically drift-free operation make cold-atomic sensors very appealing, which is reflected in numerous projects across the world (QUANTUS, ICE, FINAQS and other projects) [46]. Current state-of-the-art in sensitivities are 4.2X10^{-9} $ms^{-2}/\sqrt{Hz}$ (over a 70 cm baseline) for gravitational acceleration [47], 100 $nrad/s/\sqrt{Hz}$ rotational sensitivity and 1 nrad/s rotational stability for 10^4 second of integration time rotational sensor based on cold atom gyroscope of 11cm^3 Sagnac area [48] while 0.6 $nrad/s$ for 1 s integration using thermal beam [49], *i.e.* already beating classical devices in proof-of-principle experiments. Among the current trends in this field is to export the technology by developing robust, integrated, portable devices to develop mobile integrated gravity and rotation sensors for applications as varied as archaeology, underground mapping, natural resource exploration, environmental and climate studies.

Field magnetic sensors: In recent years, cold atom and quantum optics based probes have become the highest performance magnetometers in a range of relevant parameter regimes [50]. Cold atoms have been demonstrated to provide high-resolution, high-sensitivity maps of current and magnetic field distributions in surfaces, and enabled cold magnetometry with 10^{-11} T/√Hz sensitivities at the micron scale, and $5.4 \times 10^{-16}\ T/\sqrt{Hz}$ with a measurement volume of 0.3 cm^3 [51]. This magnetometry takes advantage of unique properties of atomic Bose-Einstein condensates with internal spin degrees of freedom, and offers an alternative to SQUID magnetometers [52] because it doesn't not require cryogenic instruments, and thus small low-cost implementation may be possible. Furthermore BECs offer an ideal testing ground to experimentally study the fundamental performance of

optical magnetometers [53]. Currently effort is made to improve the sensitivity by two orders of magnitude by utilizing Feshbach resonance [50].

1.3.2 Miniaturized atomic optical devices

Miniaturizing atomic, being hot or cold, optical set-ups mentioned above represents among one of the most important emerging trends. Indeed, though the performance of the atomic based devices is unquestioned and is adequately celebrated (J. Hall [39] and T. Hänsch [40]), their size and complexity, and hence their accessibility are still an issue. For example, the atomic beam and fountain clocks for primary standards are run like a large facility requiring high degree of maintenance and man-power [54]. On the other hand, the widespread and the ubiquity of clocks in virtually every human activity call for high performance clocks to be delivered in a small and compact package. For example a high precision clock would, *e.g.*, substantially reduce the complexity of time-frequency transfer, synchronisation and dissemination protocols such as Global Positioning System (GPS) [55-56]. Furthermore, as mentioned earlier, the functionalities of atomic clocks extend beyond their timekeeping capabilities as their quantum resonances and coherences are at the heart of ultra-stable laser sources, high precisions magnetometers, gravimeters or gyroscopes play a fundamental role in quantum information. As a matter of fact, in today's world, the craving for these high performance functionalities to be brought in a miniature and portable devices is as pervasive as pressing. This is illustrated in the recent high profile accorded to compact atomic clocks at the major international metrology institutions [54-55], which led to the development of today's state-of-the-art miniatured atomic clock, called Chip-Scale Atomic Clock (CSAC). In parallel, the ability of gas-filled HC-PCF [14-58] to confine together gases and light over mode areas of micrometer scale whilst keeping them in interaction over length scales a million times longer than the Rayleigh range created a new paradigm in gas-laser interaction, which could have lasting impact on atom photonics.

MEMS enabled chip-scale atomic devices. Previously, atomic devices have their atomic vapour confined in macroscopic gas cells fabricated by means of traditional glass-blowing techniques and requiring 1 W power to operate. This kind of physics packages are no longer compatible with a number of applications such as navigation, and which necessitate high performance to be delivered in a small package and consuming very little power. The micro-fabrication approach developed by NIST addressed these issues by developing MEMS based alkali vapour cells (see Figure 1.9). In this technique, cells are made by sandwiching a wafer of silicon, with a hole drilled between two glass wafers. They used low powered vertical-cavity surface-emitting laser (VCSEL) with high modulation efficiency, and availability of single-mode devices at the 852 nm optical transitions in Cs and the 795 nm optical transition in Rb. Among the demonstrated atomic devices, we count a chip-scale atomic clocks (CSAC) with volume near 100 cm^3, consumes 50 mW of power with very low cost, giving fractional frequency instability of ~10^{-10} at one second, reported by J. Kitching [554], see Figure 1.9. The best foreseeable long-term fractional frequency instability is 10^{-12}, which is due to the limits set on the signal-to-noise ratio (SNR) and on the resonance linewidth by the short interaction length available and the high laser-power required [59]. Finally, while this scheme of atomic clock miniaturization implements the advantages of integration, it still relies on bulk optics and collimated beams; raising thus concerns over their robustness.

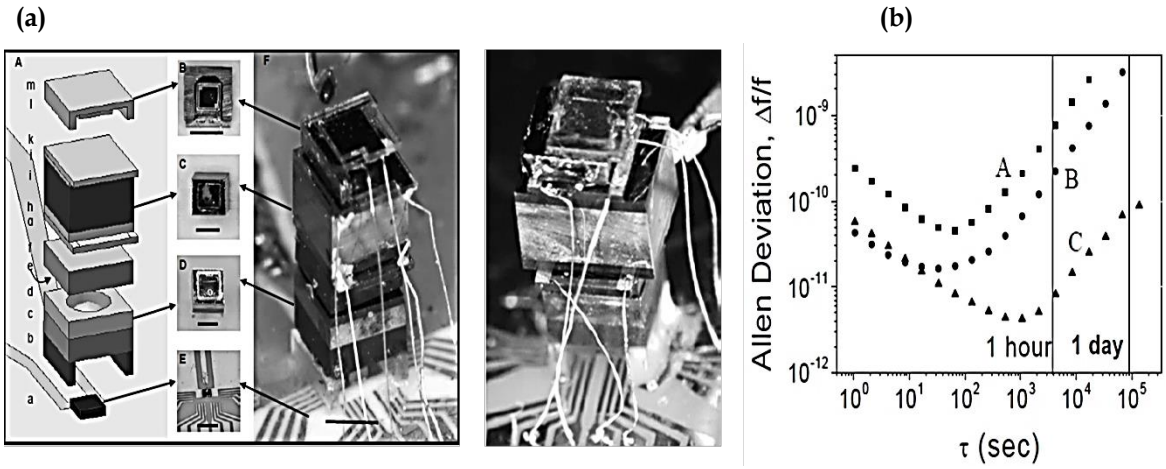

Figure 1.9: (a) The micro-fabricated atomic clock physics package based on Cs atoms (Upper right) A CSAC physics package based on a cell containing Rb^{87} (b) Fractional frequency instability of the micro-fabricated devices as a function of integration time. Squares indicate stability of Cs physics package, circles indicate stability of Rb^{87} physics package, and triangles indicate stability of Rb^{87} cell fabricated with the beam filling technique [54].

These MEMS based atomic devices have also been used as atomic magnetometers [59] with a sensitivity of as low as $1\ fT\ Hz^{-1/2}$ [61], and nuclear magnetic resonance gyroscopes [61]. Further improvements in size, power dissipation, and magnetic field sensitivity are immediately foreseeable, and such a device could provide a hand-held battery-operated magnetometer with an atom shot-noise limited sensitivity of $0.05\ pT\ Hz^{-1/2}$ [63]. We can divide the inertial and physical sensors in two classes based on interferometry and atomic spectroscopy: one is room temperature vapour cell based and second is laser cooled atoms confined by optical and magnetic field (cold atoms). Neutral atoms or ions based sensors like atomic clocks, atomic magnetometers, NMR gyroscopes, atom interferometers achieved higher stability. Best performing gravimeters, gyroscopes and clocks are based on laser cooled atoms. Atomic vapours, typically by using Rydberg atoms, can also be used to measure the electric field with high sensitivity. Rydberg atoms have large electric dipole moment which leads to large frequency shift of atomic level with electric field [60].

Waveguides based atomic optics: An alternative to MEMS based atomic devices emerged with the advent of HC-PCF and the first demonstration of gas-filled HC-PCF reported in 2002 and the subsequent invention of PMC (see Figure. 1.10). This

unique technology of fabricating and gas loading HC-PCF produces photonic microcells that can host any given gas at virtually any pressure. This gas can be confined in meters of HC-PCF with both ends spliced to a conventional optical fibre forming seemingly one single piece of optical fibre which can be coiled up to a tiny volume with a minimum optical transmission loss (see Figure.1.10). In addition to this compactness, the use of HC-PCF confers the PMC with an efficiency in gas-laser interaction that cannot be matched by other techniques such as MEMS cells, and which illustrated by the early results in demonstrating extremely low-light level nonlinear optics (14-15-16) laser induced particle guidance [64], quantum optics [65] and laser frequency metrology (14).

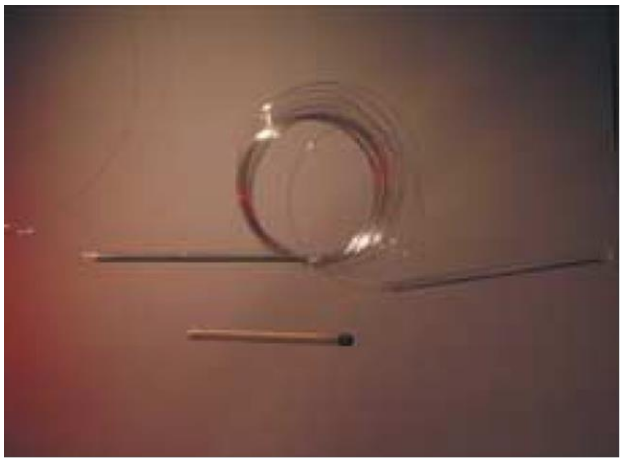

Figure 1. 10: A photonic microcell [14]

Indeed, because in HC-PCF [66] gas-phase materials and light are micro-confined together over several meters without the constraints of light diffraction nor that of optical loss, weak nonlinear effects and resonances saw their strengths improved by a factor that could reach more than a million even when low-light levels were applied (see section below). This was shown in a number of demonstrations led by our group such as ultra-low threshold stimulated Raman scattering [15-67-68] and, the development of an all-fibre laser-frequency stabilisation unit where ultra-enhanced acetylene absorption line contrast (nearly unity) in a 5 meters of acetylene MPC is achieved despite the low laser-powers and the tiny ~100 nl of gas-volume

involved. In atom optics, the first demonstrations of using atom confined HC-PCF were achieved in our group GPPMM, then based at the University of Bath, and in Cornel University. Here rubidium-filled HC-PCFs were used to demonstrate electromagnetically induced transparency (EIT) [69]. Since these seminal works, several results based atom or molecular vapour filled HC-PCF were reported, and which we detail below some representative ones. With regard to the future trend of HC-PCF based atomic devices, current work is underway to extend PMC to atom vapors, which will provide a truly integrated solution compared to the MEMS approach. In the following section, we give a more detailed account on the devices.

1.4 Hollow-core photonic crystal fibre enabled atom optics

Using optical waveguide in atom optics has been identified as a key element for many cold atoms related phenomena since the early days of cold atoms. For example, optical waveguides are proposed as a means for guiding atoms by coupling them coherently in a single mode fibre to enhance the capabilities of atomic lithography by allowing the direct etching (without a mask), selective doping of specific or writing-in structures almost atom-by-atom [70]. A fibre-guided source of atoms could provide a highly coherent beam that would allow such large area atomic interferometers and therefore improving gravimeter precision. The principle of atom guidance using optical waveguide was proposed for the case of hollow-core capillary in 1983 by Balykin and Letokhov [71]. They proposed to create a red-detuned potential well by using laser beam guided in the Gaussian-like HE_{11} mode of the hollow fibre. Such a laser beam enables the "high field-seeking" atoms to be trapped in the centre of the beam via dipole force and to push them along the laser beam propagation via radiation pressure. A year later, Marksteiner et *al.* [72] used a blue-detuned laser scheme by guiding the light in the cladding of the capillary. This mode, which is guided by total internal reflection, has the advantage of lower light propagation loss than the core HE_{11} mode [65]. The "donut-shaped" profile of this mode, along with its blue-detuned frequency from the atomic

resonance, results in "low field-seeking" atoms which are pushed by a centripetal force to the centre of the fibre hollow-core. The advent of HC-PCF, renewed the interest for optical waveguides for atom optics [73] because, unlike optical capillary fibres, HC-PCF supports truly guided modes exhibiting propagation loss in 10 dB/km range and modal field diameters as small as only a few μm, and can be excited in a single-mode regime. Furthermore, this new type of fibres represents an original platform that can be used for example to accurately probe van der Waals and Casimir-Polder forces. Despite its recent development, HC-PCF have already proven to be extremely interesting for cold-atom field as illustrated with the cold Sr guidance and spectroscopy in Kagome HC-PCF [16]. Currently, several research groups are investigating the use of HC-PCFs for several atom-optics related applications from Rydberg state spectroscopy for quantum information to sub-Doppler spectral-line generation for microwave and/or optical clocks [74-75]. The present work is aligned with this strand of research and technology trend, and whose aim is to investigate further these HC-PCFs for thermal and cold atom optics (see below). Within this framework, in the following subsections we will review the early work on atom guidance in optical capillary fibres (OCF) and then list the seminal and most representative works on HC-PCF based atom optics.

1.4.1 Guidance of thermal and cold atoms through optical capillary fibres

The first demonstration of thermal atom guidance through optical capillary fibre OFC) was reported by Renn et *al.* in 1995 using the red-detune laser scheme [76], and in 1996 using the blue-detuned laser scheme to guide Rb inside an OFC. Here, the atoms are both guided along the OFC axis and transversely confined via the scattering or radiation force (eqution. (1.3)) and the dipole force (see equation. (1.11)) respectively, hence forming an atom waveguide. The dipole force controls the atom's transverse motion by both engineering guided modes with a particular transverse profile and by setting the laser frequency relative to the atom resonance. In order to understand how the laser mode intensity profile and its frequency affect

the atom's motion, we recall the associated potential of the dipole force by simply deducing it from the expression in equation 1.11:

$$U = \frac{\hbar\delta}{2} ln\left(1 + \frac{\Omega^2/2}{\delta^2+\Gamma^2/4}\right). \quad 1.15)$$

Here, $\Omega = \Gamma\sqrt{I(r,z)/2I_s}$ is the Rabi frequency. For the case of a low loss waveguide, the intensity is uniform with z (axis of propagation), and thus only the transverse profile has an impact of the potential exerted on the atom. For large frequency detuning (*i.e.* $\delta \gg \Omega, \Gamma$), the potential expression shortens to $U = \frac{\hbar\Gamma^2}{2\delta} I(r)/I_s$, and shows that for red-detuned configuration (*i.e.* $\delta < 0$), the potential is attractive, and the atoms are attracted to the centre (*i.e.* $r = 0$) where the intensity is maximum. Here, we say that the atoms are "high-field seeking". When the detuning is positive, the atoms tend to go where the intensity is minimum, and are called "low-field seeking". In the case of OFC, one can excite modes whose profile is amenable for red-detuned as well as blue-detuned atom guiding.

An OFC consists of an annular high-index glass core around an air hole and guides light via Fresnel's reflection [77]. The light is guided in the hollow region of the OFC via Fresnel reflection, and the modes are not properly guided modes and exhibit large attenuation values (typically 10dB/m for 125µm core diameter and 18.5µm thickness). For the HE_{11} mode, which the lowest attenuation loss mode and for OFC core diameter larger than the optical wavelength, the intensity profile is $I_{HE11}(r) = I_0 J_0^2\left(2.405\, r/R_f\right)$. Consequently, its associated potential $U_{HE11} = \frac{\hbar\Gamma^2}{2\delta}\left(I_0/I_s\right) J_0^2\left(2.405\, r/R_f\right)$ for the red-detuned case shows a well centred at the centre of the hollow-core of the OFC.

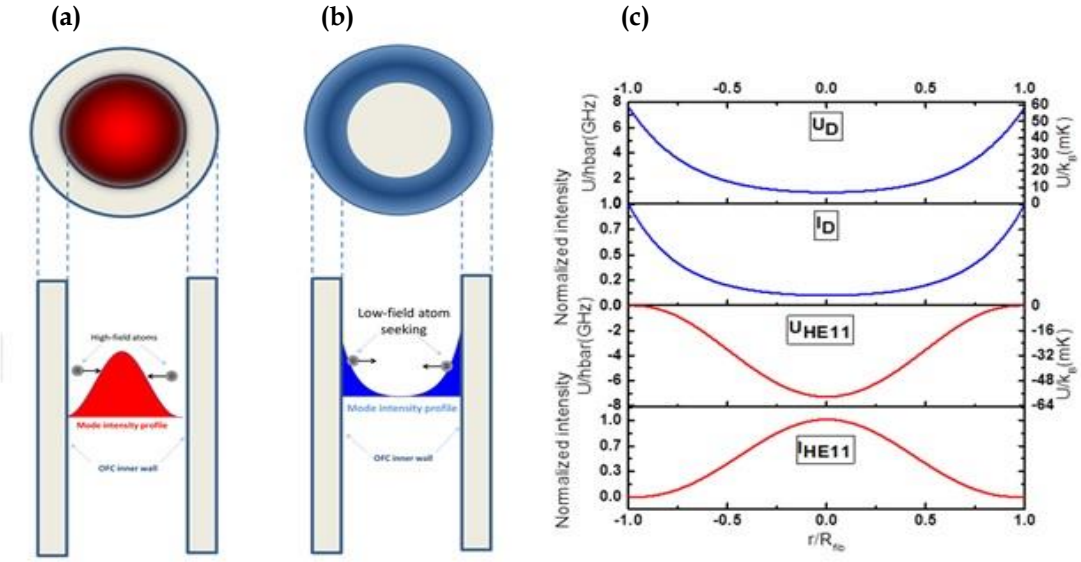

Figure 1.11: (a) Mode profile intensity for red-detuned (b) blue-detuned inside the hollow-core region of an OFC (c) plots of normalised intensity and their associated potential for an OFC at 780nm.

Also, light can be guided in the glass ring through via total internal reflection, with an evanescent field into the hollow region. The intensity profile of such a mode over the hollow region has a donut profile and can be written as $I_D(r) = I_0 I_0\left(2.405\, r/R_f\right)$. Figures. 1.11(a) and 1.11(b) show schematically the profile of the mode intensity inside the hollow-core region for the red detuned and blue-detuned configurations respectively. Figure. 1.11(c) plots the two mode normalised intensity profiles and their associated potential in function of the OFC for the case of Rb D2 line, a maximum intensity I_0 equal to ~200 W/cm² (*i.e.* ~10^6 time the saturation intensity) and for a detuning of 6 GHz (*i.e.* $\delta \approx \mp 10^3\Gamma$) for the red-detuning HE_{11} and the blue-detuned donut-shaped mode respectively. Both potential show a depth, ΔU, of a few tens of milliKelvin, corresponding to transverse velocity capture, $v_c \sim \sqrt{2\Delta U/m}$, of a few m/s. In turn, and in this case of the red-detuned scheme, this velocity figure set the atom flux, $\approx \left(\frac{1}{2}\sqrt{m/2\pi k_B T}\; n_0 A_{eff}\right) v_c^2$, the OFC can achieve. Here, n_0 *and* A_{eff} are the thermal atomic density and the mode effective area. Renn et *al.* exploited both configurations which experimental set-ups are shown in Figure. 1.12(a) and 1.12(c) respectively. In the case of a red-detuned laser configuration, they

used a 3.1 cm long OFC, with a hollow-core radius R_f=40 µm (see Figure. 1.12(a)). The evolution of the flux of Rb with frequency detuning and intensities (from 0.75 to 60mW) [78] is presented in Figure. 1.12(b). They obtained a maximum flux of ~800 atom/s at low intensity (< 500W/cm^2), for small negative detuning. The flux figure increases with intensity up to more than 3000 atom/s. However, other effects induced from light scattering (*e.g.* viscous Dipole heating [4]) along with the propagation loss of the OFC mode limited the atomic guidance distance to well below 20 cm. Using blue-detuned evanescent wave guidance lift such light scattering [76], and was demonstrated for the first time in 1996 [79]. Figures. 1.12 (c) and (d) show the experimental set up and the resulting Rb flux for a 6 cm long OFC. Here, the OCF has core hollow diameter of 10 µm and a cladding outer diameter of 77 µm, the blue-detuned laser light was coupled into the capillary solid glass region, whilst a low intensity red-detuned laser was coupled into the hollow-core region. Guidance was greatly improved with a flux of up to 30000 atoms/s. In 2000, the first cold atoms of Rb were guidance in OFC was reported by D. Muller *et al.* [80]. In their experimental cold Rb from a MOT were blue-detuned evanescent guided in a ~24 cm long and 100 µm core diameter OFC. They achieved a flux of 590 000 Rb atoms/s using a 55mW power, and 6 GHz blue-detuned laser, and identified two major loss mechanisms were: collisions with background atoms because the vacuum in the core was not perfect and collision losses due to the interference generated speckle pattern in the evanescent fields of the multi-modes coupled in the capillary.

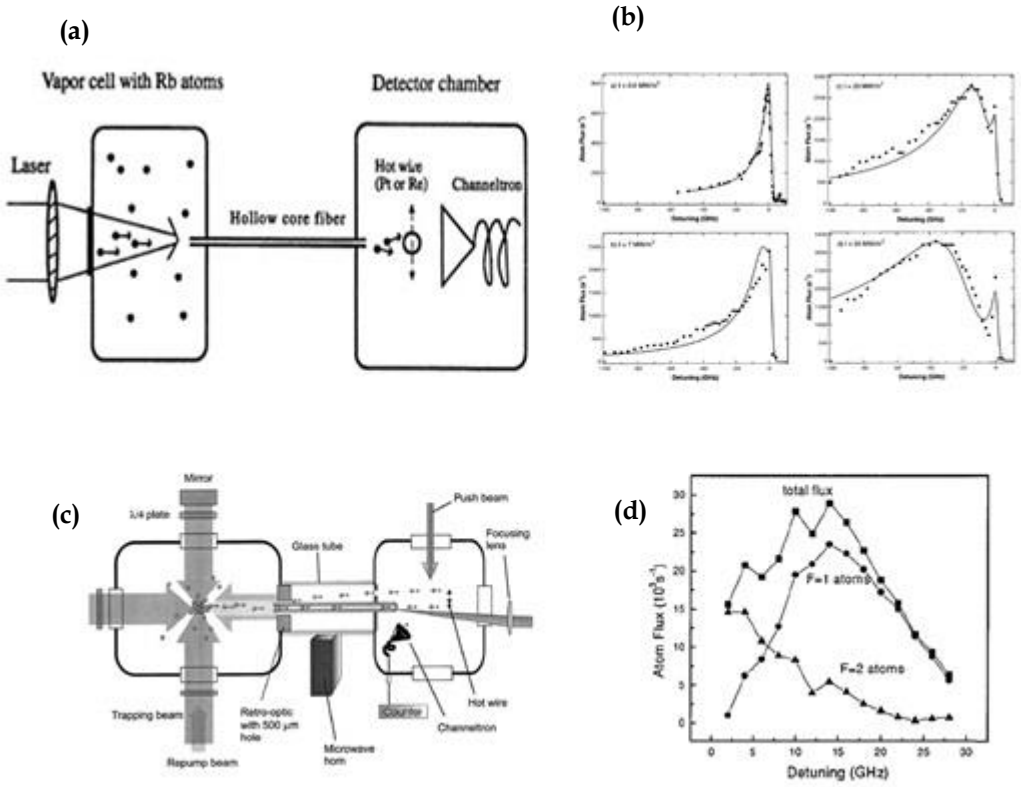

Figure 1.12 (a) Experimental set-up: laser beam is coupled into the grazing incidence mode of a hollow-core fibre. Rb atoms are guided from source chamber, where these are extracted from Rb source, to detection chamber through hollow-core fiber [76]. (b) Guided atomic flux VS laser detuning from resonance at several laser intensities [78]. (c) Experimental set-up: Cold atoms are generated using MOT in source chamber are guided in to detection chamber via hollow-core fibres of length about 24 cm which is connected in between these two chambers. (d) Detuning dependence guided atoms. At small detunings the atoms are optically pumped into the F=2 ground state (triangles). At large detunings the total flux (squares) consists to 90% of atoms in the F=1 ground state (circles) which indicates suppression of spontaneous emission during the guiding process [80].

1.4.2 Hot (thermal) atoms filled HC-PCF

As previously mentioned, in the early years of 2000s, a new type of optical fibre emerged, coined HC-PCF [67] which consists of a hollow-core surrounded by a micro-structured cladding. Unlike OFC, HC-PCF guides light in micro-meter scale hollow-core with extremely low transmission loss and no sensitivity to bend, and can operate in a single mode regime. These properties have the potential of lifting the observed drawbacks in OFC such as the rapid attenuation of the trap beam or the formation of the speckle patterns, which result from the multimode propagation

of light inside the OFC, thus creating attractive spots on the capillary walls and cause significant atom loss.

Today, we count two independent families of hollow-core fibres: one guide via photonic bandgap (PBG) mechanism [81] and the second via Inhibited Coupling (IC) mechanism [82]. In chapter two, we detail the principles and properties of these guidance mechanisms. The development of HC-PCF has created a new paradigm gas-laser interaction, thanks to its enhanced interaction length and small effective area. In fact, the first demonstration of gas-filled HC-PCF and the demonstration of low-threshold nonlinear effect reported by Benabid et *al.* [15] led the emergence of a new field coined "Gas-Photonics" whereby gas-filled HC-PCF is now used in a number of applications and across several scientific communities [83]. Furthermore, loading HC-PCF with atomic and molecular vapours is also a growing practice in varied fields including those related to cold atoms. Below we limit a review to the seminal demonstrations.

Seminal works on atoms inside HC-PCF: The first work related to thermal atom filled HC-PCF was reported by Gaeta group et *al.* [84] in Cornell University and Benabid group in the University of Bath [69]. Both works reported on the generation of electromagnetically-induced transparency (EIT) in Rb-filled HC-PCF. In 2006, S. Ghosh et *al.* [84] reported on a V-type EIT of 60MHz linewidth at very low powers (see Figure. 1.13). Here, they used a PBG guiding HC-PCF with 6 μm core diameter and 25 cm length. The fibre guides over 750-810 nm wavelength range and its inner wall surface was coated with octadecyldimethylmethoxysilane (ODMS) to reduce physico-chemical reaction with the wall. Similarly, in Light et *al.* [69] generation of EIT (see Figure 1.14) in inner core coated HC-PCF was reported. However, there are several differences with the work of Gosh *et al.* [84]. First, in [69], they used scheme so to discriminate unambiguously the generated transparency from those generated via optical pumping.

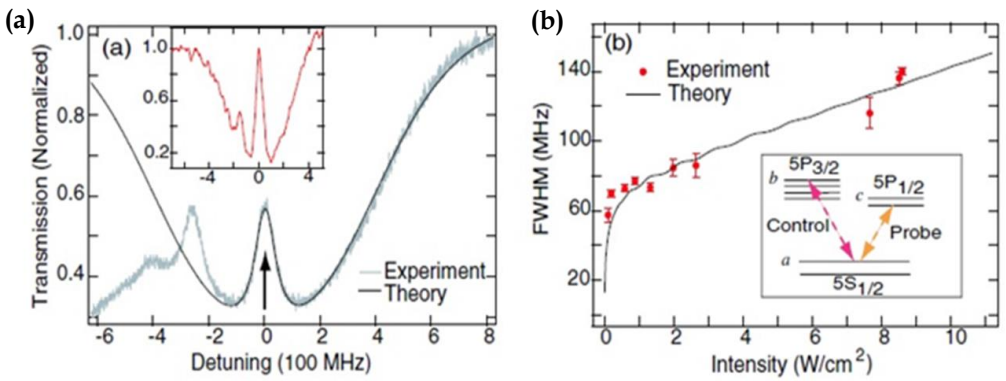

Figure 1.13: (a) Transparency window due to EIT in the presence of 361nW control field. (inset) They achieved transparency larger than 90% when a probe scanned over $5S_{1/2}$, F = 1 to $5P_{1/2}$, F′= 1 with a 2.65 μW control field tuned to $5S_{1/2}$, F =1 to $5P_{3/2}$, F′= 1 transition. (b) Study on the variation of the linewidth of EIT as a function of control intensity (figures taken from [84]).

Second, they used an IC guiding Kagome-lattice HC-PCF, 11 μm coated with polydimethylsiloxane (PDMS).

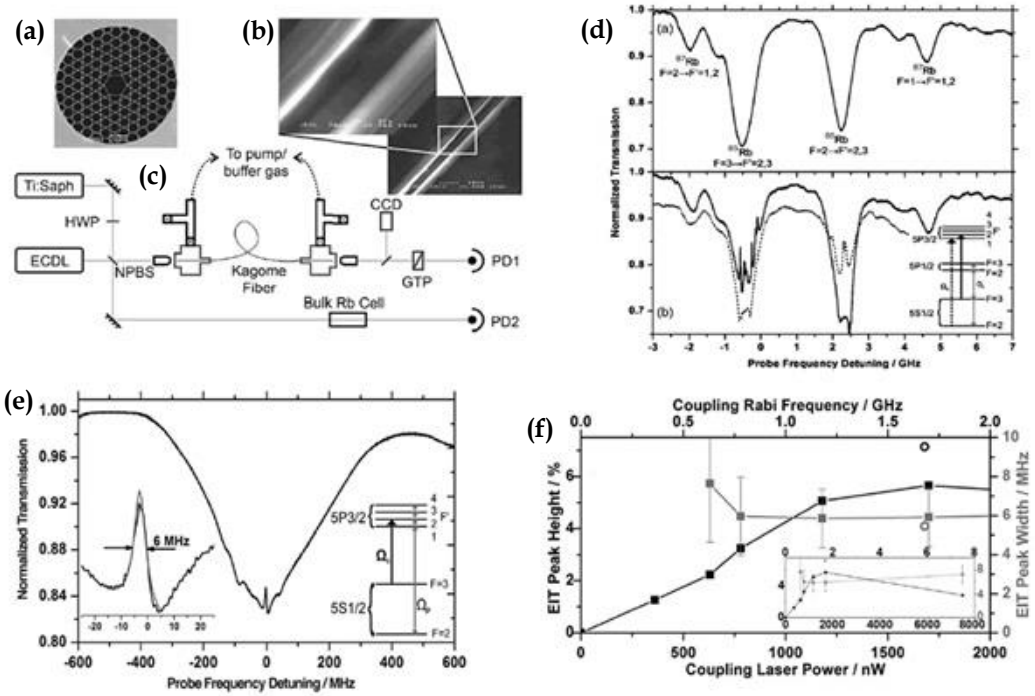

Figure 1.14 (a) SEM image of kagome HC-PCF (b) SEM image of the core after coated with PDMS (c) Experimental set up with two lasers used one is (ECDL) probe and Ti:Saph (coupling) (d) Absorption spectra in the presence of probe only to prove that Rb is inside the hollow-core of fibre. (e) EIT is observed when probe beam of power 5nW interact with 1.6μW coupling beam in core of 30 cm long kagome HC-PCF filled with Rb. Inset (left) Zoomed peak showing the linewidth. Inset (right) Lambda energy level scheme of Rb^{85} (f) Coupling power of laser VS EIT height and width [69

These differences led to ten-folder narrower linewidth of 6 MHz. Furthermore, the Kagome HC-PCF provides broadband guidance [15], and exhibited low loss transmission in 780 nm which is working wavelength for this experiment. The large core has two advantages: Rb atoms are filled rapidly in the core and it offers reduced collisional rate of atoms with the silica core wall as this effect depends on the size of core wall.

In addition to the use of Rb filled HC-PCF for coherent optics, atom guidance inside a PBG HC-PCF was reported in 2007 for the first time by Takekoshi et *al.* [85-86]. Rubidium atoms injected from a thermal oven were guided over 6 cm of fibre by a red-detuned beam far from resonance of the D2 line of Rb, and an impressive guiding efficiency of over 70%, was achieved, thus demonstrating well

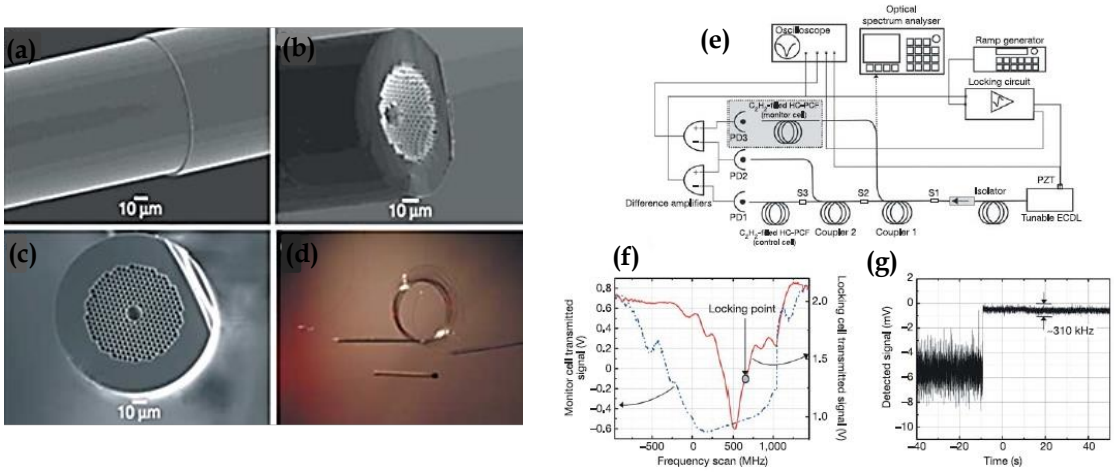

Figure 1.15: (a) Side view of splice: An HC-PCF spliced with single mode fibre (SMF) (b) End view of an HC-PCF when cleaved at the junction of the splice. (c) Shows clearly the preservation of structure when cleaved few mm from splice. Fibre is same as in (a) and (b). (d) Photograph of a 5-m-long hydrogen-filled HC-PCF gas cell. Its size is comparable with matchstick (e) frequency stabilization set up (f) small circle on red curve shows the locking point of P9 absorption line of acetylene (g) left-hand side part of trace: is frequency fluctuation when laser is free running- right-hand side part of trace: when laser is locked, exhibits maximum r.m.s frequency deviation of 310 KHz (figures taken from [14]).

the lead of HC-PCF over simple capillaries.

HC-PCF based stand-alone gas cell: Another important advance in gas-filled HC-PCF is the development of a stand-alone HC-PCF based gas cell, later coined Photonic MicroCell (PMC) [14], as was mentioned earlier. A PMC (see figure 1.15) is photonic device consisting of a length of HC-PCF filled with a given gas and

spliced, hermetically with single mode optical fibres, at both ends as shown in Figure 1.15(d). Such a result would open the prospects of reproducing the above mentioned work, which were all achieved in a UHV system harbouring the HC-PCF, to be undertaken in a stand-alone optical fibre. This prospect has been obtained using molecular gas [14] by demonstrating enhanced stimulated Raman scattering in Hydrogen PMC, and laser frequency stabilisation with acetylene PMC. These first PMCs exhibit HC-PCF to SMF splicing loss of a typical of 1–2 dB, and down to 0.6–0.8 dB by using improved splicing procedure. However, so far achieving alkali vapour PMC is yet to be achieved if we exclude the iodine vapour PMC, which was made at the expense of bad HC-PCF termination [69].

1.4.3 Cold atom filled HC-PCF

With respect to cold atoms manipulation inside HC-PCF, a rapid progress was made in the last few years despite the experimental difficulties that loading cold atoms inside a micro-meter scaled hollow-core entails. The first work on loading cold atoms inside a HC-PCF was reported in 2009 by Bajcsy et *al.* where they demonstrated an optical switch [87-88]. Figure 1.16 summarises the experimental

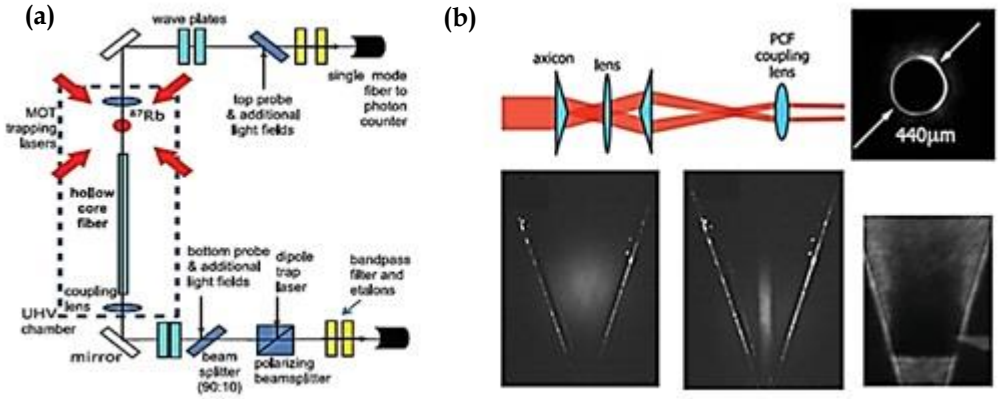

Figure 1.16: (a) Experimental set up. (b) Atomic waveguide based on hollow beam (figures taken from [87-88]).

set-up. Here, atoms from ^{87}Rb MOT with temperature of 40 µK were loaded by simultaneously using a red-detuned dipole trap formed by a single beam coupled into the fibre from the bottom side, and a magnetic quadruple funnel shaped with four electrical wires. Atoms from the MOT are then released and gravity pulls them

down toward the bi-force funnel. Red-detuned dipole trap formed by a single beam coupled into the fibre from the bottom side. The laser induced dipole potential well exhibited a depth of ~10 mK. The fibre is a PBG guiding HC-PCF with a 7 µm diameter hollow-core, and a transmission window between 780 and 900 nm. The authors reported on loading of ~30,000 rubidium atoms, corresponding to an optical depth of ~180 and atom lifetime inside the fibre ranging from 100 ms down to 10 ms.

A second demonstration of cold atom loading in HC-PCF was reported by Vorrath et *al.* [89]. Here, they used a very far red-detuned beam (100 THz below resonance) with a power of 2.3 W to demonstrate guidance of cold atoms in 8.8 cm long, 12 µm

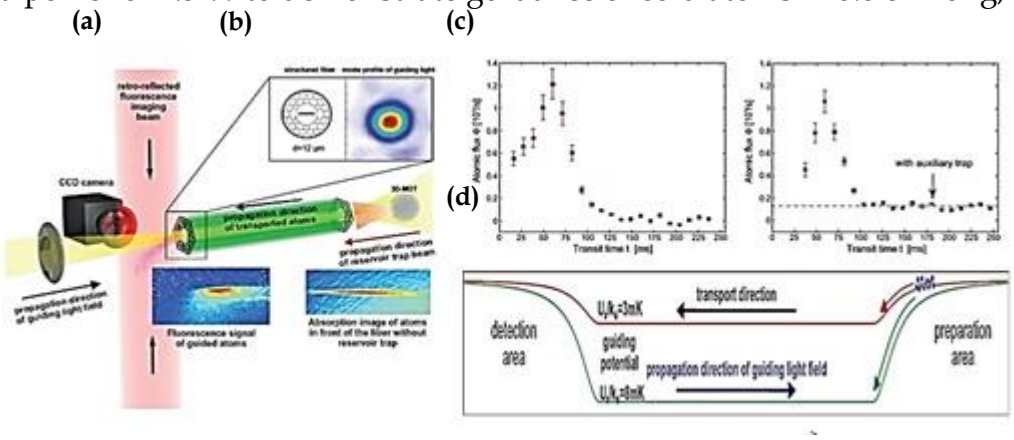

Figure 1.17: (a) Experimental set up showing the position of 3D- MOT, which is created at the one face of PBG HC-PCF. The position of trapped atoms is changed by changing the position of additional magnetic field. The atoms are detected by fluorescence imaging with a retro-reflected laser beams and photons are collected, with an intensified CCD camera, after guiding therough the fibre. Observed atomic flux, after loading into the fibre as a function of time (b) A peak flux of (1.2±0.1) X10^5 atoms s^{-1} can be seen when atoms are loaded directly from optical molasses and this flux is extended over 50 ms. (c) The peak flux remains unchanged but a constant flux of 1.5X10^4 atoms is maintained for more than 150 ms by creating an auxiliary reservoir dipole trap at the fibre input. (d) Schematic of potential to guide the cold atoms: from their preparation (right side) and exit on other side. [89]).

diameter HC-PCF. Here the fibre was also a PBG HC-PCF, however its transmission window was centred at 1067 nm. First they prepared cooled ensembles of Rb^{85} atoms to 10 µK in an optical molasses phase and brought closer to the fibre end by moving the zero-point of the magnetic field. Figure 1.17 shows the experimental set-up and the main results. The maximum atomic flux through achieved was over 10^5 atoms/s. It was reported that the long distance transportation of atoms is feasible

which would be easy route to guided matter wave interferometry, large-area Sagnac-type interferometers.

The above demonstrations were motivated by applications in quantum information, hence the choice of PBG HC-PCF which have much smaller core diameter than the IC HC-PCF such as Kagome fibre. Another seminal demonstration of cold atom's loading HC-PCF was motivated to explore them for quantum metrology and optical atomic clocks, and was reported by collaboration between our group and the University of Tokyo [16]. Here, by designing an IC Kagome HC-PCF with a sufficiently large core diameter (34 μm) and low residual birefringence, they successfully loaded cold ^{88}Sr atoms from MOT (see Figure. 1.18) in to fibre by using optical lattice whose potential depth was 30μK, whilst keeping the atoms trapped within the wells of an optical lattice. The major result of this work is the demonstration of an absorption line whose linewidth is set by the lifetime of the excited state instead of atom-wall collisional dephasing as one would expect given the micro-confinement of the atoms. Consequently, this would open prospects in quantum metrology [31], such as atomic clocks [54], atom interferometer [11], magnetometers [51] and quantum simulators [31], and where long coherence times of atoms and photons to perform measurements at the quantum limits are paramount. Here, the suppression or at least the sufficient reduction of de-coherence due to the atom-atom and atom-wall interactions was achieved by singly trapping atoms in a magic lattice and loading them almost adiabatically into an IC kagome-lattice HC-PCF.

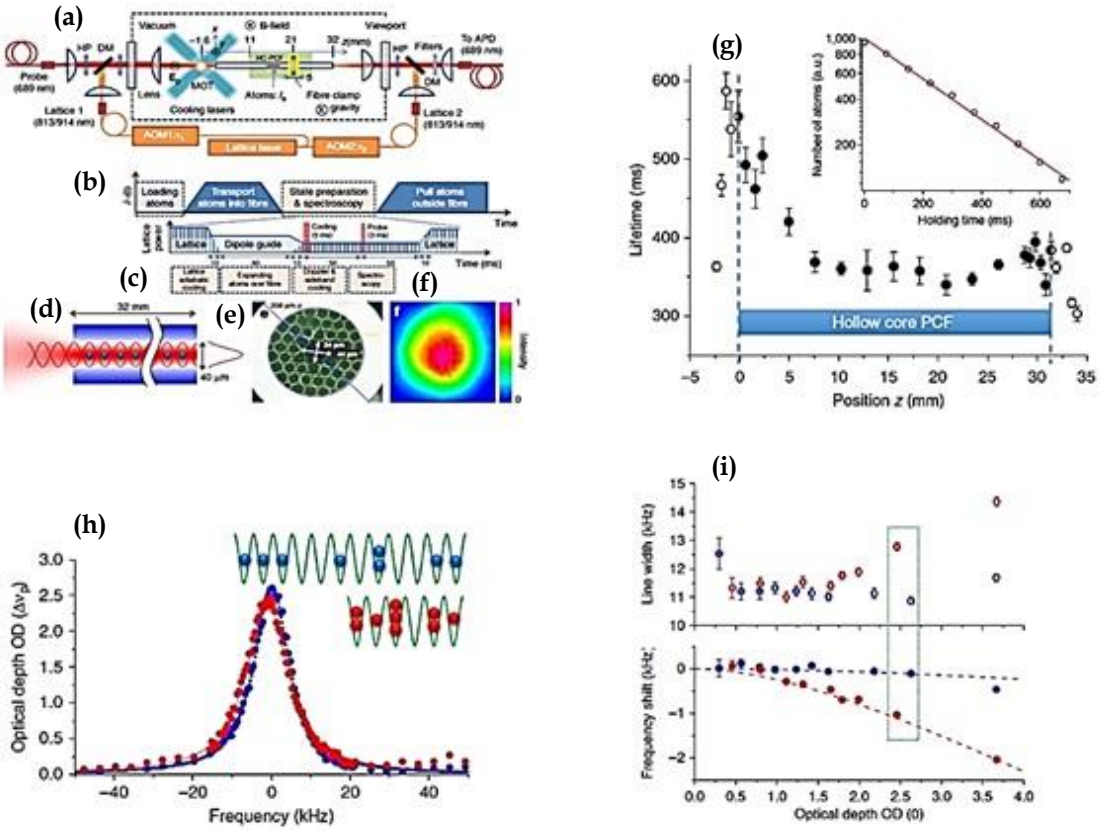

Figure 1.18: (a) MOT atoms are -1.6 mm away from the face of fibre. (b) The atoms are transported in to HC-PCF by tuning the frequency of the lattice laser (c) Protocol for atomic expansion. (d) Atoms in HC-PCF are confined axially and radially by the optical lattice preventing the atoms to interact with fibre-core wall (e) SEM image of kagome fibre (f) Far-field mode profile. (upper right) The blue region indicates the fibre. After cooling atoms are loaded at z=0 in 32mm long fibre. (g) Due to increase in the collision with residual gases the lifetime inside the fibre (filled circles) decreases towards the middle of the fibre. The lifetime determined by them is about ~ 347 ms. (h) Absorption spectra with and without atomic expansion over lattice sites (inset) are displayed by red and blue symbols respectively. Distribution of atoms over lattice site corresponding to mean atom occupation of m′ = 0.45 and m′ = 1.7. (i) Spectral width: The shift of spectrum and atomic number-dependent broadening are suppressed by applying a lattice-expansion protocol [16].

The cold ^{88} Sr are loaded into 32 mm long IC HC-PCF, whose guidance windows cover the experimental wavelength (689-914 nm) and exhibits a single HE_{11} mode operation. The optical lattice is formed by two counter-propagating beams from a laser at λ = 813nm with potential depth about 30 μK at MOT position and 300 μK inside the fibre core. 10^4 atoms are adiabatically accelerated up to v_m = 53 mm/s by sweeping the frequency difference of two lattice laser beams. The authors observed a lifetime τ =500 ms near the entrance of fibre which decreases to τ = 350 ms in the middle of fibre due to atoms' acceleration during the transport, thus no extra heating loss from the fact that the atoms are confined within the fibre. They

successfully reduce this heating loss of atoms by applying laser cooling during transport them into the fibre. To make the high optical depth compatible with reduced atomic-atomic interactions, the atomic cloud is expanded over the lattice site in the fibre for short time of ~60 ms, while maintaining the dipole trap in the radial directions. This procedure reduces the mean atom occupation with the optical lattice wells from m ~1.7 down to m ~ 0.45 (see Figure 1.18), while preserving the optical depth. The collisional and broadening shifts are successfully suppressed by this procedure and achieved linewidth of 11 KHz, which later reduced to ~7 kHz, which corresponds to the probed transition lifetime.

1.5 Laying the foundations for in-fibre laser cooling

The results of the work described in the above sections clearly show the enabling power of HC-PCF for atom optics in general and for cold atom in particular. The scope and motivations of the present thesis are part of a long term goal which can be entitled as "in-fibre laser cooling of Rb". This consists of exploring the feasibility of laser cooling of thermal atoms (here rubidium) that are loaded in a Photonic MicroCell [14].

The approach can be described broadly as follows: a rubidium PMC, which is seemingly a length of optical fibre is designed and assembled in such a way that its HC-PCF supports purposely engineered spatial modes that one could excite selectively, and at will, Gaussian and/or donut like modes. Furthermore, this HC-PCF will be core inner-wall coated with judicious materials to address issues such as atom-surface interaction or physicochemical reactions. The above processes are already or currently developed in our group, and are beyond the scope of this thesis. Furthermore, the approach for "in-fibre laser cooling" will entail exciting the Rb filled optical fibre in a sequential manner by the following lasers: a bi-chromatic lasers to provide high velocity capture cooling, then far-off red detuned counter-propagating laser beam coupled to the HE_{11} mode of the PMC for longitudinal Doppler atom cooling, along with a blue detuned laser coupled to PMC with higher

order mode(s) with donut-shaped profile for transverse trapping of the atoms. The net result is a photonic crystal fibre whose core is made of cold atoms. If successful, such a compact and portable photonic component will be used as portable Rb based cold atomic clock and quantum sensors based on guided matter wave interferometry [89]. Furthermore, cooling atoms inside HC-PCF has also fundamental interest as the laser-atom interaction and the light modal structure is completely different from the existing free-space.

Whilst this aim is supported by several previous results, several preliminary experiments are required and several questions must be addressed before concluding on the feasibility of in-fibre laser cooling and the cold-atom PMC. Our current knowledge on surface science and atomic physics is limited to fully and reasonably quickly simulate some of these questions such as the nature and dynamic of atom-surface interaction for both thermal and cold atom with a spatial resolution comparable to the surface roughness, and how this would impact cold atom guidance in fibre, in-fibre atom trapping and cooling. Another raised question relates to the effect of the surface material on the collision rate and Casimir-Polder forces, but also on the evolution of the surface with time as atoms such as rubidium tend to stick to surfaces. In addition to these fundamental questions, challenging technological points must be lifted such as the identification of the proper HC-PCF design so to support the appropriate spatial modes for cooling and trapping, the identification of the most performant coating material for the HC-PCF core inner-surface. In order to ensure a successful outcome to this highly challenging objective, this thesis is set to put the emphasis in building an experimental set-up that is sufficiently versatile to address the above points.

The thesis objective is the design and the development of an experimental set up that is amenable to accommodate different fibre configurations and atom phases, to explore several techniques in loading thermal and cold atoms inside different HC-PCF, to collect the necessary information for assessing the performance of the system, to host several spectroscopic measurements and to investigate atom-surface

interaction by exploring different coating materials. This platform will then be exploited as a foundation for the assembly of Rb PMC and in-fibre laser cooling in the future. Figure 1.19 describes schematically the experimental platform for in-fibre laser cooling. The experimental platform consists of UHV system that can accommodate several HC-PCF to evaluate, several techniques of atom guidance including pre-cooled atoms, and of course be able to explore the laser cooling of atom inside HC-PCF. Towards achieving this platform, the thesis has been broken down into four programs: (1) HC-PCF design and fabrication; (2) Design and construction of UHV, (3) Laser systems and frequency stabilization; and (4) Laser atom cooling and guidance. Each program calls for specific and multidisciplinary fields involving fibre photonics, atom optics, laser science, frequency metrology and vacuum engineering.

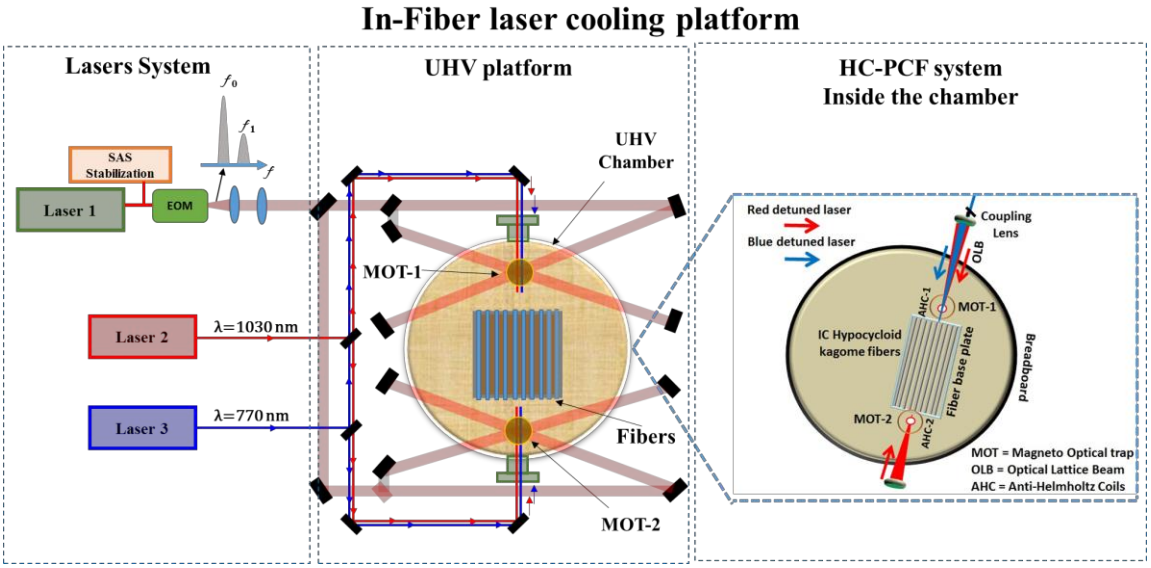

Figure 1.19: Schematic of the experimental platform for in-fibre laser cooling. Laser 1 is a frequency-stabilized laser for cooling and re-pumping for both isotopes (Rb^{85}-Rb^{87}), laser 2 is tunable Red-detuned laser for dipole res-detuned trapping and guidance of atoms and laser 3 is tuneable Blue-detuned laser for dipole blue-detuned trapping and guidance.

The UHV chamber will comprise a HC-PCF set holder that can accommodate up to 10 HC-PCF with 10 cm length. The system will comprise two MOTs located at each end of a HC-PCF from one of the fibre set. The system can load both thermal as well as cold atoms. Loading thermal atoms will be based on molecular diffusion or far-red detuned lasers. The UHV chamber stands out relative to the common MOT

UHV by its large volume and an optical table-like layout so to be able to explore different laser excitation and detection schemes. In particular, the UHV system will harbour an optical system that can achieve the following: (1) Rb loading in different HC-PCF; (2) Two MOTs; and (3) Metrological measurements like optical depth, interaction of Rb with the fibre's core wall; (4) Cold atom transport in HC-PCF; (5) In-fibre cold atom optical lattice.

In addition to conventional and established techniques for generating MOT and loading thermal atoms inside HC-PCF, the platform can be used to explore various methods to transport cold/thermal atoms from MOT/background to HC-PCF, such as (1) Hollow-beam blue-detuned dipole traps [68] and adiabatic transport using optical lattice [73] [70].

1.6 Structure and content of the thesis

The thesis comprises four additional chapters and covers the description and results in building from scratch an experimental platform that comprises most of the component for cold and thermal atom control in HC-PCF. The thesis chapters are organised as follow:

Chapter 2 reviews the optical guidance mechanisms in HC-PCF and the main properties of these fibres which has a strong impact on in-fibre atom optics such as the interaction length enhancement, the atom-wall collision and the content and profile of the different modes supported by HC-PCF. The chapter also presents the different HC-PCF fabricated for the project.

Chapter 3 presents the design, fabrication and assembly of the ultra-high vacuum system. A rationale and the motivation of the UHV system design will be given. The construction and/or the implementation of the UVH system components, such as the anti-Helmholtz coils, the fibre coating and the Rb dispensers, are described. The chapter shows the results in characterizing the vacuum pumping capability of the

system and in assessing the HC-PCF transmission signal upon releasing the Rb inside the system.

Chapter 4 details the laser system of the platform. In particular, it presents the cooling - repumping laser architecture and its frequency stabilisation.

Chapter 5 describes the MOT, the laser cooling process and the characterization of the generated MOT. The chapter also presents the preliminary work for cold-atom guidance inside HC-PCF using both blue-detuned and red-detuned schemes.

Finally, Chapter 6 concludes the manuscript by summarizing the experimental achievements and their significance for future atom optics experiments that the platform can support in the immediate and intermediate term.

References

1- https://www.nobelprize.org/nobel_prizes/physics/laureates/

2- *Atomic-beam deflection by resonance-radiation pressure",* **A. Ashkin.** Phys. Rev. Lett. 25 (1970) 1321.

3- *"Three dimensional viscous confinement and cooling of atoms by resonance radiation pressure",* **Steven Chu, L. Hollberg, J . E. Bjorkholm, Alex Cable, and A. Ashkin,** Phys. Rev. Lett., vol. 53: p. 48-51 (1985).

4- *"Laser cooling below the Doppler limit by polarization gradients: simple theoretical models",* **Dalibard J. and Cohen-Tannoudji, C**. J. Optical Soc. Amer. B, 6, 2023 (1989).

5- *"Observation of Bose-Einstein Condensation in a Dilute Atomic Vapor",* **M. H. Anderson, J. R. Ensher, M. R. Matthews, C. E. Wieman and E. A. Cornell.** Science, vol. 269, Issue 5221, pp. 198-201, (1995).

6- *"Cooling Bose-Einstein condensates below 500 picokelvin.",* **A. E. Leanhardt, T. A. Pasquini, M. Saba, A. Schirotzek, Y. Shin, D. Kielpinski, D. E. Pritchard and W. Ketterle,** Science, vol. 301, p. 1513-5 (2003).

7- *"Lasers Revolutionized Optical Metrology*", **M. Takeda and M. Kujawinska,** SPIE Professional, October, 2010.

8- "*Long-term stability of an area-reversible atom-interferometer sagnac gyroscope*", **Durfee D. S., Shaham Y. K. and Kasevich M. A.,** Phys. Rev. Lett. 97(24): 240801, (2006).

9- "*Fringe contrast in three grating Mach-Zehnder atomic interferometers*", **C. Champenois, M. Buchner and J. Vigue,** Eur. Phys. J. D 5, 363-374 (1999).

10- "*High-precision gravity measurements using atom interferometry*", **A. Peters, K. Y. Chung and S. Chu,** Metrologia, vol. 38, p. 25-61, (2001).

11- "*Measurement of the electric polarizability of sodium with an atom interferometer*", **C. Ekstrom, J. Schmiedmayer, M. Chapman, T. Hammond and D. Pritchard,** Phys. Rev. A, vol. 51, p. 3883-3888 (1995).

12- "*An atomic clock with 10^{-18} instability*", **N. H. Hinkley** et al, Science vol. 341, Issue 6151, pp. 1215-1218, (2013).

13- "*Atomic physics*", **C. J. Foot,** Oxford (2005).

14- "*Compact, stable and efficient all-fiber gas cells using hollow-core photonic crystal fibers*"**, F. Benabid, F. Couny, J. C. Knight, T. A. Birks and P. St J. Russell**, Nature vol. 434, pages 488–491 (2005).

15- "*Stimulated Raman Scattering in Hydrogen-Filled Hollow-Core Photonic Crystal Fiber*", **F. Benabid, J. C. Knight, G. Antonopoulos** *et al.*, Science, vol.**298** 399-402 (2002).

16- "*Lamb-Dicke spectroscopy of atoms in a hollow-core photonic crystal fiber*", **S. Okaba, T. Takano, F. Benabid, T. Bradley, L. Vincetti, Z. Maizelis, V. Yampol'skii, F. Nori and H. Katori**, Nature Comm., vol. 5, p. 4096 (2014).

17- "*Optical dipole traps and atomic waveguides based on Bessel light beams*", **J. Arlt, K. Dholakia, J. Soneson and E. M. Wright,** Phys. Rev. A, vol. 63, 063602, (2001)

18- "*Untersuchunen uber die druckkrafte des lichtes*", **P. N. Lebedev**, Annalen physik, vol. 6, p. 443, (1901).

19- "*A preliminary communication on the pressure of heat and light radiation*", **E. F. Nichols and G. F. Hulls**, Phys. Rev. (series-I), vol. 13, p. 307-320 , (1901).

20- "*Translational atomic motion in a single frequency standing light wave*", **V. S. Lethokov,** JETP Lett., vol. 7, p. 272 (1968).

21- "*Cooling of gases by laser radiation*", **T.W. Hansch and A.L. Schawlow.** Optics Comm., vol. 13, p 68-69, (1975).

22- "*Trapping of neutral sodium atoms with radiation pressure*", **E. L. Raab, M. Prentiss, A. Cable, S. Chu and D. Pritchard,** Phys. Rev. Lett. vol. 59, 2631 (1987)

23- "*Observation of atoms laser cooled below the Doppler limit*" , **P. Lett, R. Watts, C. Westbrook, W. Phillips, and H. Metcalf**, Phys. Rev. Lett., vol. 61, p. 169-172 (1988).

24- "T*owards cold atom guidance in hollow-core photonic crystal fiber using a blue de-tuned hollow laser beam*", **J. Poulin**, PhD thesis, 2015, University of Montreal.

25- *"Evaporative cooling of magnetically trapped and compressed spin-polarized hydrogen"*, **Harald F. Hess**, Phys. Rev. B, vol. 34, (1986).

26- *"Coherence and Raman Sideband Cooling of a Single Atom in an Optical Tweezer"*, **J. D. Thompson, T. G. Tiecke, A. S. Zibrov, V. Vuletic´ and M. D. Lukin**, Phys. Rev. Lett. vol. 110, 133001 (2013).

27- *"Atomic clocks and inertial sensors"*, **C. J. Borde,** *Metrologia* vol. 39 435, (2002).

28- *"Schemes for robust quantum computation with polar molecules"*, **S. F. Yelin, K. Kirby, and Robin Côté,** Phys. Rev. A, vol. 74, 050301(R), (2006).

29- "*Optical magnetometry*", **Budker D. & Romalis M.**, Nat. Phys. vol. 3, 227–234 (2007).

30- *"A mobile high-precision absolute gravimeter based on atom Interferometry"*, **M. Schmidt, A. Senger, M. Hauth, C. Freier, V. Schkolnik, and A. Peters,** ISSN 2075_1087, Gyroscopy and Navigation, vol. 2, pp. 170–177, (2011).

31- *"Quantum simulations with ultracold atoms in optical lattices"*, **C. Gross and I. Bloch,** Science vol. 357, 995–1001 (2017).

32- *"Quantum-State controlled chemical reactions of ultracold potassium-rubidium molecules"*, **S. Ospelkaus, K.K. Ni, D. Wang, M. H. G. de Miranda, B. Neyenhuis, G. Quéméner, P. S. Julienne, J. L. Bohn, D. S. Jin, J. Ye,** Science vol. 327, 853-857, (2010)

33- *"Long-term comparison of caesium fountain primary frequency standards"*, **T. E Parker** ,Metrologia vol. 47, 1–10, (2010).

34- *"Compact atom-interferometer gyroscope based on an expanding ball of atoms"*, **S. Riedl, G. W. Hoth, B. Pelle, J. Kitching and E. A. Donley,** Journal of Physics: Conference Series 723, 012058, (2016).

35- *"Optical atomic clocks"*, **Andrew D. Ludlow, Martin M. Boyd, and Jun Ye,** Rev. of Mod. Phys., vol. 87, (2015).

36- *"The International GNSS Service in a changing land scape of Global Navigation Satellite Systems"*, **John M. Dow, R. E. Neilan, C. Rizos,** J. Geod. vol. 83:191–198 (2009).

37- "*First global telescope opens an eye on the cold universe*",**D. Normile and D. Clery**, Science, vol. 333, pp 1820-1823 (2011).

38- "*The caesium resonator as astandard of frequency and time*", **Essen L., D. Sc, and Parry J. V. L.** , *Phil. Trans. R. Soc.* A vol. 250, 45, (1957).

39- "*Nobel Lecture: Defining and measuring optical frequencies*", **Hall J. L.,** Rev. Mod. Phys., vol. 78, 1279 (2006).

40- "*Nobel Lecture: Passion for precision*", **Hansch T. W.,** Rev. Mod. Phys., vol. 78, 1297 (2006).

41- "*Nobel Lecture: Superposition, entanglement, and raising Schrodinger's cat*", **Wineland D. J.,** Rev. Mod. Phys., vol. 85, 1103, (2013).

42- "*An optical lattice clock with accuracy and stability at the 10^{-18} level*", **Bloom B. J., Nicholson T. L., Williams J. R., Campbell S. L., Bishof M., Zhang X., Zhang W., Bromley S. L. and Ye J**., Nature 506, pp. 71-75, (2014).

43- "*Sr Lattice Clock at 1×10^{-16} Fractional uncertainty by remote optical evaluation with a Ca Clock*", *A. D. Ludlow et al,* Science, vol. 319, 1805 (2008)

44- "*An atomic clock with 10^{-18} instability*", **N. H. Hinkley** et al, Science vol. 341, pp. 1215-1218, (2013).

45- "*Gravitational wave detection with optical lattice clocks*", **S. Kolkomwitz, I. Pikovski, N. Langellier, M. D. Lukin, R. L. Walsworth and J. Ye**, Phys. Rev. D 94, 124043 (2016).

46- "*QUANTUS:Applications of Bose-Einstein Condensate in microgravity*", **T. V. Zoest**, et al, 38th COSPAR Scientific Assembly 2010,

47- "*Testing gravity with cold atom-interferometers*", **G. W. Biedermann** *et al*, Phys. Rev. A, vol. 91, 033629 (2015).

48- "*Continuous Cold-Atom Inertial Sensor with 1 nrad/sec Rotation Stability*", **I. Dutta** *et al*, Phys. Rev. Lett. vol. 116, 183003 (2016).

49- "*Versatile compact atomic source for high-resolution dual atom interferometry*" Phys. Rev. A, vol. 76, 063611 (2007).

50- "*Principles and Methods of Quantum Information Technologies*", **Eto Y., Sadrove M., Hirano T.** Lecture Notes in Physics, vol. 911.

51- *"A subfemtotesla multichannel atomic magnetometer"*, **I. K. Kominis, T. W. Kornack, J. C. Allred & M. V. Romalis**, Nature, vol. 422, pp. 596-599, (2003).

52- *"Superconducting Quantum Interference Device Magnetometry, in Methods in Physical Chemistry"*, **Lueken, H.** (2012)

53- "*Optical magnetometry*", **Budker, D. & Romalis, M.**, Nat. Phys. vol. 3, pp. 227–234, (2007).

54- "*Chip-scale atomic clocks at NIST*" **J. Kitching, S. Knappe, L. Liew, J. Moreland, H. G. Robinson, P. Schwindt, V. Shah, V. Gerginov and L. Hollberg,** NCSL International Workshop and Symposium (2005).

55- *"Absolute frequency measurement of the $^{88}Sr^{+}$ clock transition using a GPS link to the SI second"*, **Pierre Dubé, John E Bernard and Marina Gertsvolf,** Metrologia, vol. 54, pp.290–298, (2017)

56- *"Long-Distance Frequency Dissemination with a Resolution of 10^{-17}"*, **C. Daussy, O. Lopez, A. Amy-Klein, A. Goncharov, M. Guinet, and C. Chardonnet,** Phys. Rev. Lett. vol. 94, 203904, (2005)

57- *"A microfabricated atomic clock"*, **S. Knappe, V. Shah, Peter D. D. Schwindt, L. Hollberg, and J. Kitching,** Appl. Phys. Lett. vol. 85, 1460 (2004)

58- "*Stimulated Raman Scattering in Hydrogen-Filled Hollow-Core Photonic Crystal Fiber*", **F. Benabid, J. C. Knight & G. Antonopoulos** *et al.*, Science, vol. 298, 399-402, (2002).

59- *"Atomic vapor cells for chip-scale atomic clocks with improved long-term frequency stability"*, **S. Knappe, V. Gerginov, P. D. D. Schwindt, V. Shah, H. G. Robinson, L. Hollberg, and J. Kitching,** Opt. Lett. vol. 30, pp. 2351-2353, (2005).

60- *"Atomic Sensors – A Review"*, **J. Kitching, S. Knappe, and Elizabeth A. Donley,** IEEE sensors journal, vol. 11, (2011)

61- *"A subfemtotesla multichannel atomic magnetometer"*, **K. Kominis, T. W. Kornack, J. C. Allred, and M. V. Romalis,** Nature, vol. 422, pp. 596–599, (2003).

62- *"Nuclear Magnetic Resonance Gyroscopes"*, **E. A. Donley**, IEEE sensors 2010 Conference

63- *"Chip-scale atomic magnetometer"*, **Peter D. D. Schwindt, S. Knappe, V. Shah, L. Hollberg, J. Kitching, Li-A. Liew and J. Moreland**, App. Phys. Lett., vol. 85, no. 26, (2004).

64- *"Trapping of ultracold atoms in a hollow-core photonic crystal fiber"*, **Caleb A. Christensen, Sebastian Will, Michele Saba, Gyu-Boong Jo, Yong-Il Shin,** Phys. Rev. A vol. **78**, 033429 (2008).

65- *"Resonator-Aided Single-Atom Detection on a Microfabricated Chip"*, **Igor Teper, Yu-Ju Lin, and V. Vuletic,** Phys. Rev. Lett. vol. **97,** 023002 (2006)

66- "*Low loss Inhibited coupling Hollow-core photonic crystal fiber with ultrabroad Fundamental Band*", **B. Debord, A. Amsanpally, J. Blondy, F. Gérôme, and F. Benabid**, Conference on Lasers and Electro-Optics, OSA Technical Digest (2016) (Optical Society of America, 2016), paper STu4P.2.

67- *"Subwatt threshold cw Raman fiber-gas laser based on H2-filled hollow-core photonic crystal fiber"*, **F. Couny, F. Benabid, and P. S. Light ,** Phys. Rev. Lett. vol. 99**,** 143903 (2007).

68- *"Enhanced SRS in H2 filled hollow-core photonic crystal fiber by use of fiber Bragg grating"*, **F. Couny, F. Benabid and O. Carraz,** J. Opt. A: Pure Appl. Opt. vol. 9, pp. 156–159, (2007).

69- *"Electromagnetically induced transparency in Rb-filled coated hollow-core photonic crystal fiber"*, **P. S. Light, F. Benabid, F. Couny, M. Maric and A. N. Luiten,** Optics Lett**.**, vol. 32, No. 10, (2007).

70- *"Atom trap and waveguide using a two-color evanescent light field around a subwavelength-diameter optical fiber"*, **F. Le Kien, V. I. Balykin, and K. Hakuta,** Phys. Rev. A vol. 70, 063403 (2004).

71- *"Laser guiding of atoms in a hollow optical fiber*", **M. A. OlShanii, Y. B. Ovchinnikov and V. S. Letokhov**, Opt. Comm., vol. 98, p. 77-79, (1993).

72- *"Coherent atomic waveguides from hollow optical fibers: quantized atomic motion*", **S. Marksteiner, C. M. Savage, P. Zoller and S. L. Rolston**, Phys. Rev. A, vol. 50, no. 3, pp. 2680-2690, (1994).

73- *"Hollow-core photonic bandgap fiber: new light guidance for new science and technology"*, **F. Benabid,** Phil. Trans. R. Soc. A, vol. 364, pp. 3439–3462, (2006).

74- *"Rydberg atoms in hollow-core photonic crystal fibers"*, **G. Epple, K.S. Kleinbach, T.G. Euser, N.Y. Joly, T. Pfau, P. St. J. Russell & R. Low,** Nature Communications, vol. 5, (2014).

75- *"Saturation spectroscopy of iodine in hollow-core optical fiber"*, **Anna Lurie, Philip S. Light, James Anstie, Thomas M. Stace, Paul C. Abbott, Fetah Benabid, and Andre N. Luiten,** , Opt. Exp., vol. 20, No. 11, 11906, (2012).

76- *"Laser-guided atoms in hollow-core optical fibers"*, **M. J. Renn, D. Montgomery, O. Vdovin, D. Anderson, C. Wieman and E. Cornell,** Phys. Rev. Lett., vol. 75, p. 3253-3256, (1995).

77- *"Capillary optical fibers : design and applications for attaining a large effective mode area"*, **A. Dutt, S. Mahapatra and S. K. Varshney**, J. Opt. Soc. of America B, vol. 28, p. 1431-1438, (2011).

78- *"Optical dipole-force-fiber guiding and heating of atoms"*, **M. J. Renn, A. A. Zozulya, E. A. Donley, E. A. Cornell and D. Z. Anderson,** Phys. Rev. A, vol. 55, no. 5 ,pp. 3684-3696, (1997).

79- *"Evanescent-wave guiding of atoms in hollow optical fibers"*, **M. J. Renn, E. A. Donley, E. A. Cornell, C. E. Wieman and D. Z. Anderson**, Phys. Rev. A, vol. 53, no. 2, p. 648-651, (1996).

80- *"Guiding laser-cooled atoms in hollow-core fibers"*, **D. Muller, E. A. Cornell, D. Z. Anderson and E. R. I. Abraham,** Phys. Rev. A, vol. 61, p. 033411.1-6, (2000).

81- *"Full 2-D photonic bandgaps in silica/air structures"*, **T.A. Birks, P.J. Roberts, P. St. J. Russell, D.M. Atkin and T.J. Shepherd,** *Eec. Lett. 26th,* vol. 31 *No. 22, (1995)*

82- *"Generation and photonic guidance of multi-octave optical-frequency combs"*, **F. Couny, F. Benabid, P. J. Roberts, P. S. Light, and M. G. Raymer**, Science, vol. 318, no. 2007, pp. 1118–1121, (2007).

83- *"Generation and photonic guidance of multi-octave optical-frequency combs"*, **F. Couny, F. Benabid, P. J. Roberts, P. S. Light, M. G. Raymer,** Science, vol. 318, pp. 1118-1121, (2007).

84- "*Low-Light-Level Optical Interactions with Rubidium Vapor in a Photonic Band-Gap Fiber*", **S. Ghosh, A. Bhagwat, C. Renshaw, S. Goh, A. L. Gaeta and B. Kirby,** Phys. Rev. Lett., vol. 97, p. 023603, (2006).

85- *"Optical Guiding of Atoms through a Hollow-Core Photonic Band-Gap Fiber*", **T. Takekoshi and R. J. Knize,** Phys. Rev. Lett., vol. 98, p. 210404.1-4, (2007).

86- *"Optical Guiding of Atoms through a Hollow-Core Photonic Band-Gap Fiber*", **R. J. Knize and T. Takekoshi,** in Quantum Electronics and Laser Science Conference (QELS), vol. 1, (San Jose), p. 2, 2008.

87- "Efficient All-Optical Switching Using Slow Light within a Hollow Fiber", **M. Bajcsy, S. Hofferberth, V. Balic, T. Peyronel, M. Hafezi, A. S. Zibrov, V. Vuletic, and M. D. Lukin,** Phys. Rev. Lett. vol. 102, 203902 (2009).

88- *"Laser-cooled atoms inside a hollow-core photonic-crystal fiber"*, **M. Bajcsy, S. Hofferberth, T. Peyronel, V. Balic, Q. Liang, A. S. Zibrov, V. Vuletic, and M. D. Lukin,** Phys. Rev. A vol. 83, 063830 (2011).

89- *"Efficient guiding of cold atoms through a photonic band gap fiber",* **S Vorrath, S A Moller, P Windpassinger, K Bongs and K Sengstock,** New Journal of Physics, vol. 12, 123015, (2010).

Chapter 2

Hollow-core photonic crystal fibres for atom-optic experiments

This chapter covers three main themes. First, we will introduce hollow-core photonic crystal (HC-PCF) whereby two guidance mechanisms, namely Photonic Band Gap (PBG) and Inhibited Coupling (IC) are presented. We will then draw the main physical and optical properties of each these two types of HC-PCF. Second, we will describe how these fibres can impact the field of atom optics in general and that of cold atom in particular. We will list the main advantages and challenges of introducing HC-PCF and atom and cold atom optics. Finally, we will present the fibres designs fabricated for the purpose of the present thesis, which is in-fibre cold and thermal atom spectroscopy inside the fibers, which is the necessary condition to address the feasibility of in-fibre laser cooling mentioned in Chapter 1.

2.1 Introduction

Optical fibers are used for a variety of applications including telecommunications and interferometry. The most conventional are silica glass, first developed in the 1960s, in which light was confined into the core by total internal reflection due to the higher refractive index of the material than the one of the surrounding cladding. The refractive index contrast is usually created through dopant addition to the core and/or the cladding region. The extremely low attenuation of these fibres (0.1484 dB/km at 1550 nm [1], combined with their relatively low cost explained why they are now used extensively in the telecommunications industry.

More recently, a new paradigm in fibre optics has emerged with the ability of optical guidance in an air or vacuum by other guidance mechanisms, and which hold potential of overcoming several shortcomings in conventional solid core optical fibres. Indeed, conventional all-silica optical fibres have reached their minimum attenuation level which is set by the fundamental limit named Rayleigh scattering ($\alpha\lambda^{-4}$) which is due to small refractive index variations of the glass. Consequently, having guidance within an air core provides the potential to overcome this issue. Furthermore, conventional fibre cores are formed from silica glass which is optically transparent between approximately 0.4 and 3 µm [2], limiting their range of operation. Again, air-guidance will increase this low loss window and then enable transmission to the UV and at the opposite in the mid- to far-IR. Crucially, air-guidance will also push the threshold intensity for the onset of heating and nonlinear effects which can occur at high energy in silica core fibres and therefore degrade the optical performances. Finally, a further motivation, which directly related to the scope of this thesis, is linked with the possibility of loading the hollow core with gases or liquids in order to provide a novel regime to both confined light and fluids over distances of many meters or even kilometers. Such approach creates strong enhancement in gas-laser interactions and finds applications ranging from quantum optics to gas sensing as it will be developed in the following of my thesis.

In this context, the first hollow core photonic crystal fibre (HC-PCF) was fabricated in 1999 [3], however, the first relatively low loss HC-PCF has been reported in 2002 [4] which resulted from new fabrication processes and better understanding on how the guidance mechanisms. The year of 2002 was then the triggering time for the development of two types of HC-PCF that are currently used. The first one is based on the mechanism of photonic band gap (PBG) and the second HC-PCF guides via a mechanism related to Bound-state-in a continuum and coined Inhibited Coupling (IC).

As mentioned above, this form of optical fibre does not follow the conventional guidance on total internal reflection (TIR). Instead, the fibre cladding, typically a periodic transverse arrangement of air holes in a silica matrix, is designed to exhibit a PBG. A PBG is a region in the β-ω space where light cannot propagate in the cladding structure. Here, β is the propagation constant of the propagating mode, and is related to the wavevector magnitude k and effective index of the mode n_{eff} by $\beta \equiv n_{eff}k$. The quantity ω is the angular frequency and is related to the wavelength or the wavevector by $\omega = kc = 2\pi/\lambda$.. Similarly to solid-state physics, If a core defect is introduced it breaks the cladding structure symmetry. Furthermore, if the core index and geometry are set so to support modes with the PBG of the cladding, theses modes are trapped in the core and guided with no leakeage. Using this principle, PBG guiding HC-PCF with an attenuation loss as low as 1.2 dB/km in the telecom wavelength range was developed in 2005 [5]. In parallel to the development of such PBG HC-PCF, a second type of HC-PCF like Kagome lattice HC-PCF, enables both low loss attenuation and broadband guidance as indicated in Figure 2.1 and guides via IC. This type of fibre was first reported in 2002 [4], but its guidance mechanism was elucidated later on in 2007 [6]. IC guiding HC-PCFs have been first referred as “large pitch” HC-PCF because the photonic structure has a pitch that is much larger than the wavelength at which the HC-PCF operates. The most notable example is Kagome lattice HC-PCF [6-7]. The IC guidance is a mechanism akin to Von-Neumann Wigner bounds states within a continuum as the β-ω of the core defect guided mode is embedded within a

continuum of the modal spectrum of the cladding without significant coupling between these two types of modes [6]. Currently, and especially with the seminal introduction of negative curvature in this fibres in 2010 by our group, engineering such fibres is attracting a lot of efforts. Today, IC HC-PCF exhibit loss figures of only a few tens of dB/km loss level with a record of 7.7 dB/km in the near-infrared region demonstrated in 2017 by our group [8].

The chapter is then divided as follow: the first section will give further details about the two optical guidance mechanisms (PBG and IC) with updated state-of-the-art performances. Then, we will describe how these HC-PCFs can impact the field of atom optics in general and in particular for cold atom. For that we will introduce the figure of merit, the dephasing effect, the surface induced potential and the impact of the specific modal properties of those fibres.

Finally, the last section will be devoted to describe the different fibres used for the thesis in term of design and transmission/loss spectra.

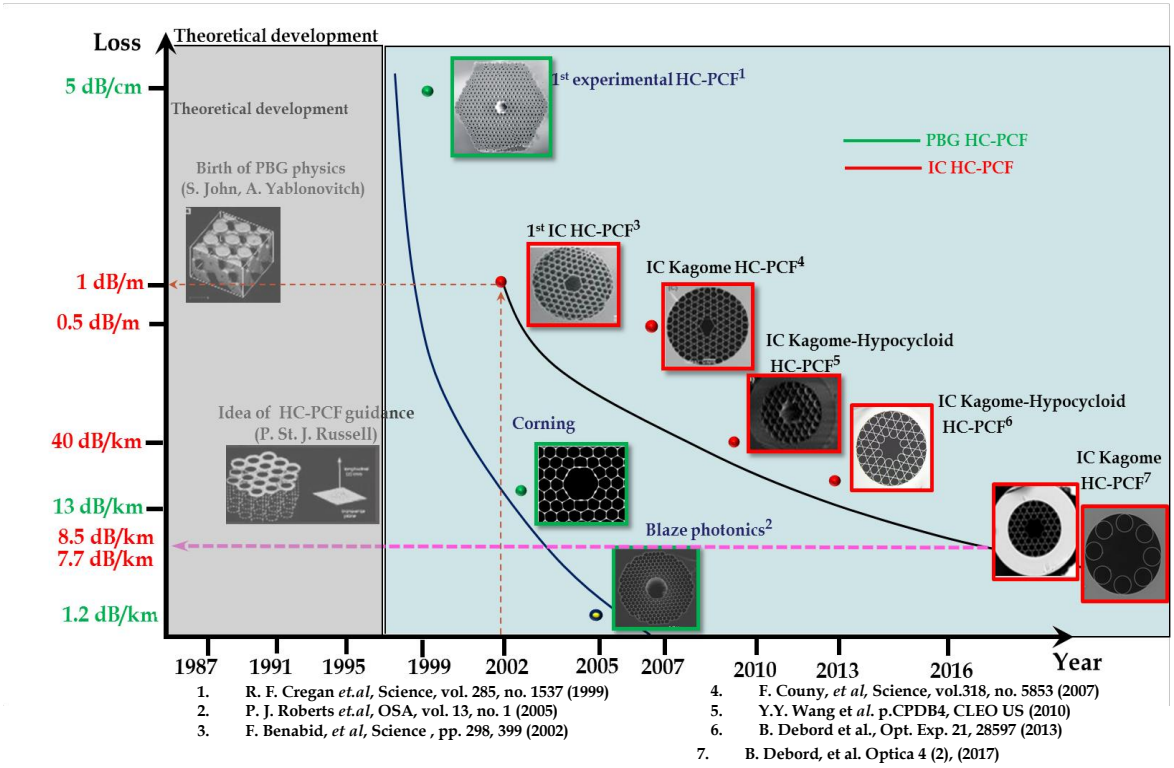

Figure 2.1: Summary of historical development of HC-PCF technology based on PBG and IC guidance. The area in gray color in the graph represents the years of theoretical developments from PBG guidance to first HC-PCF invention. The blue area represents development of HC-PCF based on PBG (in solid line borders) and IC (dashed boarders) [9].

2.2 Guidance mechanism

2.2.1 Guidance mechanism of Photonic BandGap HC-PCF

To confine light in an air core, the first family of HC-PCFs was based on the formation of an out-of-plane bandgap of the micro-structured cladding [10-11]. Owing to the structural features, these fibres ensure light confinement within the core formed by proper defect choice provided its effective index lies within the PBG of the cladding β-ω space [12-14]. Hence, the trapped light inside the hollow-core defect would have no coupling channel to couple out through the cladding.

Benabid and co-workers (reported in Couny *et al.* [15]) proposed a model analogous to the tight binding model (TBM) that is used in solid state physics to explain the existence of allowed and forbidden electronic band. This model photonic TBM (PTBM) gives a simple method on how PBG in fibres are formed and in identifying the modal spectrum of heterogeneous dielectric structures, and is currently used to design HC-PCF. Recalling that in solid-state physics, the TBM shows that solid or crystal material energy structure is formed from its constitutive individual atoms. When individual atoms are brought together sufficiently close to each other, the degeneracies in their energy levels is lifted and the energy levels split to form bands. Each band is formed by electronic wave functions, *i.e.* Bloch modes, with energy lower than those of the individual atoms (binding states) and Bloch states with energy higher than those of the individual atoms (anti-binding states). This results in the formation of allowed electronic bands and conversely, the existence of forbidden bands of the crystal structure.

The first demonstration of PTBM [15] was undertaken using a PBG guiding HC-PCF. The Figure 2.2(I) summarizes the modal spectrum of this HC-PCF. The fibre has a cladding of triangular arrangement of air holes and silica web of hexagonal shape (see the insets at the top and the bottom of the density of state diagram). For this fibre, the PTBM shows three key guiding features in the HC-PCF cladding structure which defines the bandgap characteristics *i.e.* 'strut', 'apex' and 'air' modes (see Figure 2.2(I) b-c-d). Each of these guiding features can be viewed as photonic

analogues of the individual constitutive atoms to form the crystal molecule.

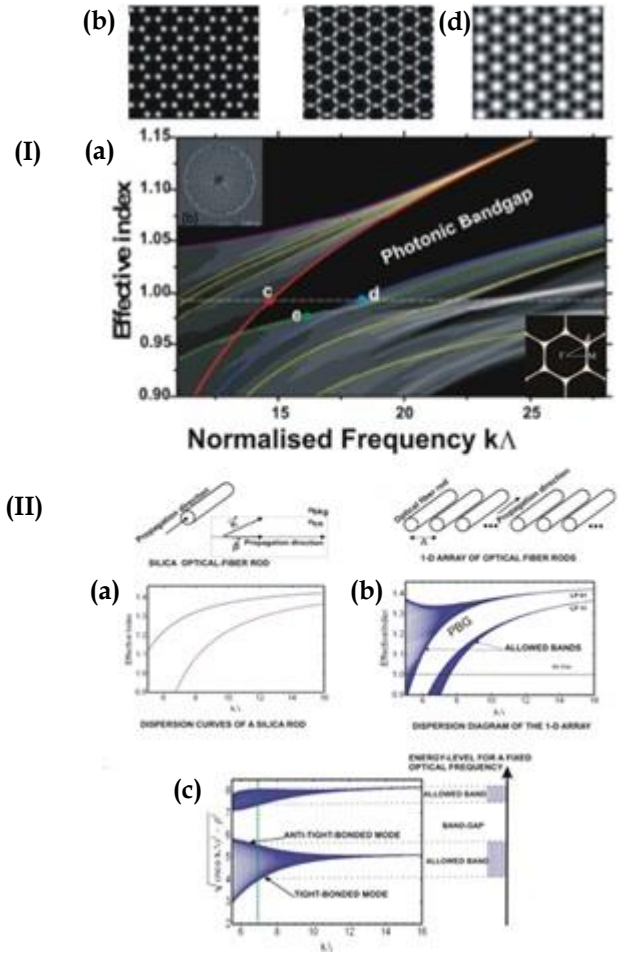

Figure 2.2: (I): (a) Density of photonic states calculated for a cladding structure with a 91.9% air-filling fraction (shown inset). (b) Apex, (c) strut and (d) airy modes which define the bandgap are highlighted by red, blue and green dash lines respectively [15]. (II): Photonic Tight-Binding model, (a) Dispersion curve of fundamental and second higher-order modes of a silica rod. Here the modes below the air-line are ignored (b) Dispersion diagram of an array of silica rods. (c) Dispersion diagram of an array of silica rods after an appropriately transformation [15].

In the case of the fibre the "molecule" is represented by the unit cell (bottom inset in the density of photonic state as shown in Figure 2.2 (I)). This model is illustrated in a more simple manner with a 1D photonic structure made by silica rods with a radius ρ and spaced by a pitch Λ. Each rod has a distinct set of modes in which light can be propagated through TIR as illustrated in Figure 2.2 (II). Figure 2.2 (II-a) shows the dispersion curves for the fundamental mode and the degenerate second order modes. Figure 2.2 (II-b) shows the dispersion of these modes for the case of an array of 1000 glass rods. The plot clearly shows the formation of the allowed photonic

bands whose spread in effective index increases as the normalized frequency becomes smaller. The plot also illustrates the existence of a PBG which extends to effective indices lower than 1, indicating the possibility of trapping light in a hollow defect. In order to draw a clear parallel with the TBM used in atomic physics, Figure 2.2 (II-c) shows the same dispersion information as Figure 2.2 (II-b) but the index is replaced by $\sqrt{(n_{co}.k)^2 - \beta^2}$. This figure shows the splitting of the fundamental mode and its transformation into an allowed band as kΛ decreases, which can be realized either by moving the rods closer to each other or reducing the frequency. Furthermore, by direct analogy with the TBM, the mode of the lowest energy corresponds to the most strongly confined mode (tight-bonded mode). This mode is also named the fundamental space-filling mode in the community of PCF [16]. Finally, one notices that the PBG becomes weakly dependent on the pitch as kΛ increases and that asymptotically the band-edges are solely determined by dispersion curve for the mode of a single rod. This behavior is the central premise behind the ARROW model [17]. Consequently, the PTBM offers a simple and powerful framework for the study of the formation of PBG in photonic structures.

For the case of a real triangular-lattice PBG HC-PCF, the location of PBG is usually given by the plot of the density of optical photonic states (DOPS) as shown in Figure 2.2 (I-a). The greyscale indicates the density of cladding modes. So, the PBG corresponds to the regions where zero density of states, *i.e.* black in the figure. This diagram is essentially equivalent to the ones shown in the previous section and gives precise details of the continuum modes about the band gaps formed. The upper edge of the bandgap shown in red color represents localized modes in the interstitial apex of the cladding (Figure 2.2 (I-c)), whilst the lower edge is formed by two modes of different symmetry, one being guided predominantly in the air holes (Figure 2.2 (I-d)) and the mode guides within and close to the silica struts which join the neighboring apices (Figure 2.2 (I-e)). Notice that the overlap between those modes can be increased by decreasing the cladding pitch of the structure, resulting in an increase of the allowed cladding bandwidth, thus decreasing the PBG width and shifting it to shorter wavelengths with less spatial extent.

Consequently, the width and depth of the PBG is defined by the dispersion of these modes and their understanding has permitted more recently the fabrication of HC-PCF with higher order bandgaps [18]. Furthermore, for any PBG HC-PCF based on air and silica, the fundamental PBG is the largest in bandwidth and lies in a frequency range of $k\Lambda \sim$ 15-20. This means that a fibre that operates near 780 nm, the pitch is less than 2.4 μm and core diameter less than 7.5 μm. Consequently, such a core diameter is too small for a number of applications where the coherence is important. PBG HC-PCFs also exhibit other guided modes called interface or surface modes. These are highly localized in the core silica surround and can strongly hybridized with the core modes. This effect disadvantaged the use of this fibre in coherent optics. Consequently, in this thesis, we are not going to use PBG HC-PCF, instead we only use IC guiding HC-PCF. The guidance mechanism of such fibres is described in the following section.

2.2.2 Guidance mechanism of Kagome lattice HC-PCF

As it has been described in the previous paragraph, the transmission bandwidth is limited to 70 THz in the case of the PBG fibres. To increase this bandwidth, which can be view as a drawback for several applications, Kagome lattice HC-PCF was first proposed by Benabid *et al.* in 2002 [4]. The word "Kagome" comes from Japanese "bamboo basket", which is similar to structure formed by a tessellated "star of David". For those large pitch Kagome lattice HC-PCFs, the ratio between the central guiding wavelength λ and cladding pitch Λ can be ~ 8 even ~30. Notice that this ratio for PBG HC-PCF is much smaller ~ 2. In this context, Couny *et al.* [6] in 2007 reported for the first time the physics of guidance mechanism of such HC-PCF. It relies on what is called "inhibited coupling (IC)" which can be explained by the analogy to the Von Neumann Wigner electronic state in quantum physics. This class of fibre does not show any photonic bandgap on its modal spectrum of the cladding but a continuum of modes as shown in Figure 2.3. Notice that high density of states regions appeared which correspond to the resonance with cladding

structure and cause increase of the transmission losses. The spectral positions of the low-loss windows are then predicted at cut-off wavelengths λ_m as:

$$\lambda_{m=}\frac{2t}{m}\sqrt{n_g^2-n_{air}^2} \tag{2.1}$$

where m is the mode order, t is the thickness of strut, n_g is the silica glass refractive index, n_{air} is the refractive index in air.

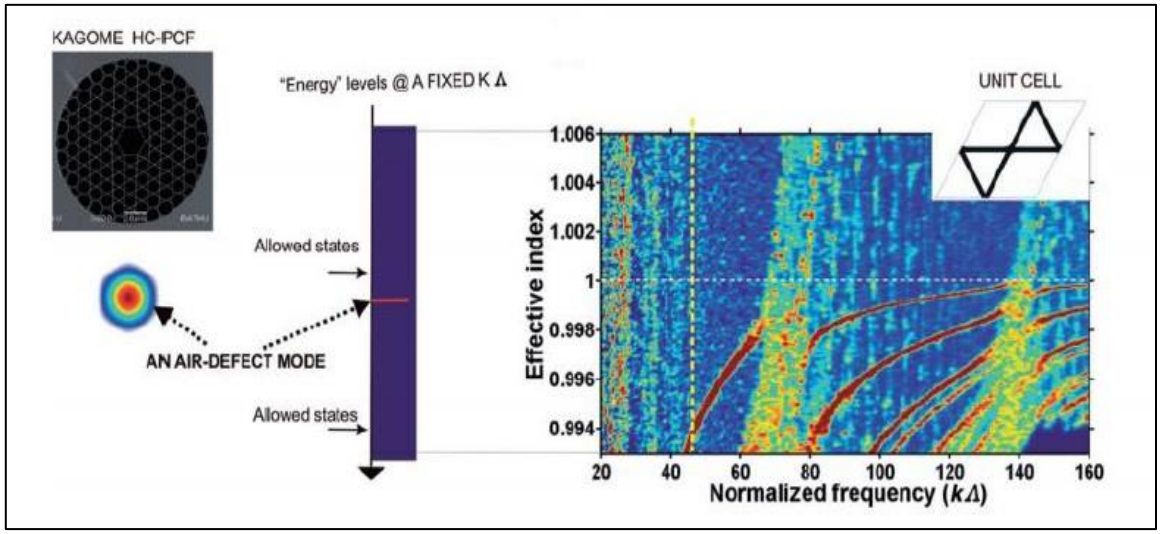

Figure 2.3: Density of optical photonic states calculated for a kagome lattice HC-PCF.

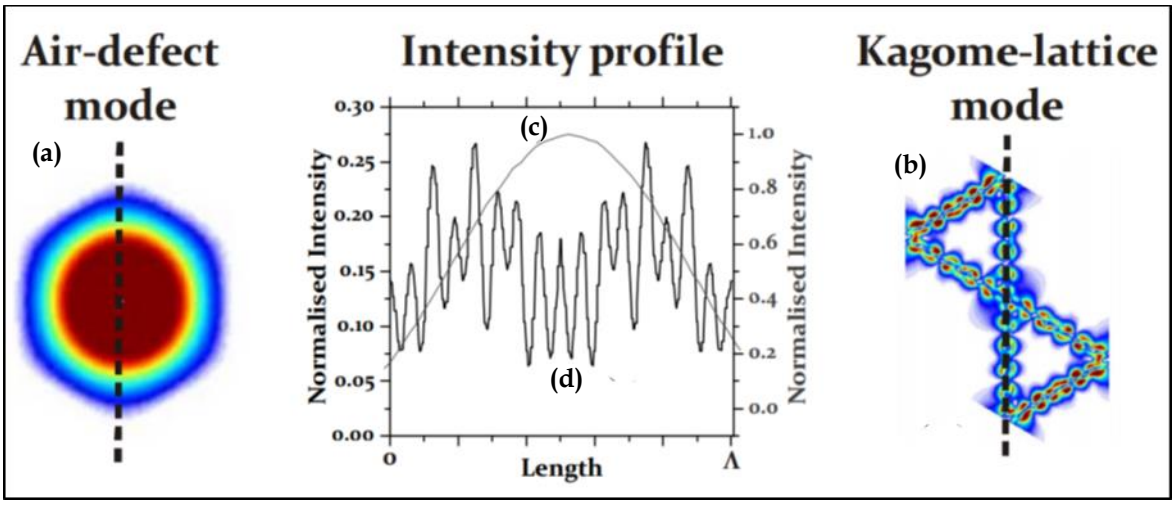

Figure 2.4: (a) Core guiding mode of Kagome lattice HC-PCF, (b) Fast oscillating cladding mode of Kagome HC-PCF. Middle image is the intensity plot of (c) core mode (d) cladding modes along length Λ identified by dashed line [8].

In this region and according to this guidance mechanism, the core guided-modes and cladding modes can have the same effective index but propagate without strongly interactions between them. This can be summarized by considering the dot product between core mode $|\varphi_{core}\rangle$ and cladding mode $|\varphi_{clad}\rangle$ that is reduced strongly (*i.e.*, $\langle\varphi_{clad}|\,\Delta n^2|\varphi_{core}\rangle \longrightarrow 0$, with Δn being the photonic structure transverse index profile) by a small field spatial intersection or by a strong mismatch in their transverse phase.

The reason for this unconventional coupling inhibition is due to small spatial optical overlap of the field and large transverse phase mismatch between slowly varying core modes and fast oscillating cladding modes presenting high azimuthal number (m) as illustrated in Figure 2.4. Therefore, the condition $\Delta\beta=0$ is not sufficient for the coupling of core and cladding modes in case of IC guidance. The high azimuthal number modes could have very close propagation constant with a core guided mode (*i.e.* $\Delta\beta \sim 0$) without strongly interacting. The figure of merit of coupled waveguides are usually represented by $X = \Delta\beta/\kappa$. Here, $\Delta\boldsymbol{\beta}$ is the longitudinal wavevector mismatch; $\boldsymbol{\kappa}$ is the coupling coefficient between the two waveguides. The maximum coupling between the waveguides takes place for $X = 0$, and the coupling becomes weaker as $|X|$ increases. This quantity is proportional to the scalar product between the electric field of the two modes (*i.e.* overlap integral over the transverse dimension of the electric field distribution of the two modes). Applying this coupling figure of merit to IC HC-PCF, we notice that because of the extremely small $\boldsymbol{\kappa}$ (*i.e.* close to zero) between the highly localized and fast oscillating silica cladding modes and the air-core mode, they can co-exist with little interaction even when their $\boldsymbol{n_{eff}}$ are very close (*i.e.* $\Delta\boldsymbol{n_{eff}} \approx \mathbf{0}$) [6]. Within this context, we note that the normal modes of each wave guiding features are not necessarily orthogonal, but their anti-crossing gap, which is indicative of the hybridization between modes, can be extremely small if $\boldsymbol{\kappa} \approx \mathbf{0}$. Therefore, in order to increase IC one requires decreasing the spatial overlap of core mode with silica cladding modes. This in turn demands for a cladding structure with very thin and elongated glass web with no sharp bend or connecting nodes. Based on these guiding rules, optimal physical and

geometrical parameters to achieve strong coupling inhibition for low loss and broader transmission IC HC-PCF have been recently discussed.

Indeed, to reduce the loss figure of dB/m to dB/km loss level, a first attempt was reported by Wang *et al.* [19-20] in 2010. The idea consisted of making a core shaping at the interface between the core and cladding. The result was to shift from the conventional circular shape to an exotic hypocycloid shape (or core contour with negative curvature) [21]. Mode field nature and distribution in such enhanced hypocycloid core and circular core shapes of kagome HC-PCF can be seen in Figure 2.5. The red dots localized in the silica core contour indicate the fast oscillating modes and the core fundamental mode field profile is zero order Bessel function.

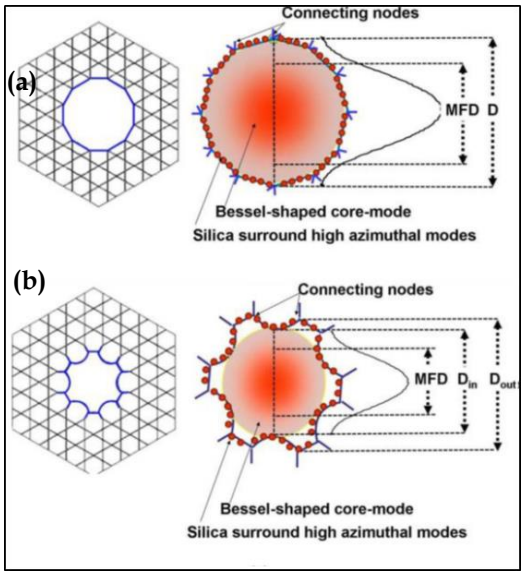

Figure 2.5: Illustration of the enhanced IC guidance by using hypocycloid core contour. (a) Idealized traditional kagome HC-PCF, core mode overlap with low azimuthal number cladding modes, and 2D profile distribution of core mode field which diameter is related to core boundary. (b) The same for a hypocycloidal kagome HC-PCF [22].

This design presents two main advantages:

1- Elongated core contour path increases the azimuthal like number of the silica core contour mode and consequently implies the reduction of the core mode coupling to cladding.

2- Linked silica nodes of the core contour confining low azimuthal number modes are pushed away from the confined core mode.

In circular core shape, the mode field diameter is related to the fibre core diameter D which is written as $MFD = (\pi/4)*D$. But for hypocycloid core shape, the Bessel shape core mode is strict to the inward cups diameter D_{in} and this value has to be used.

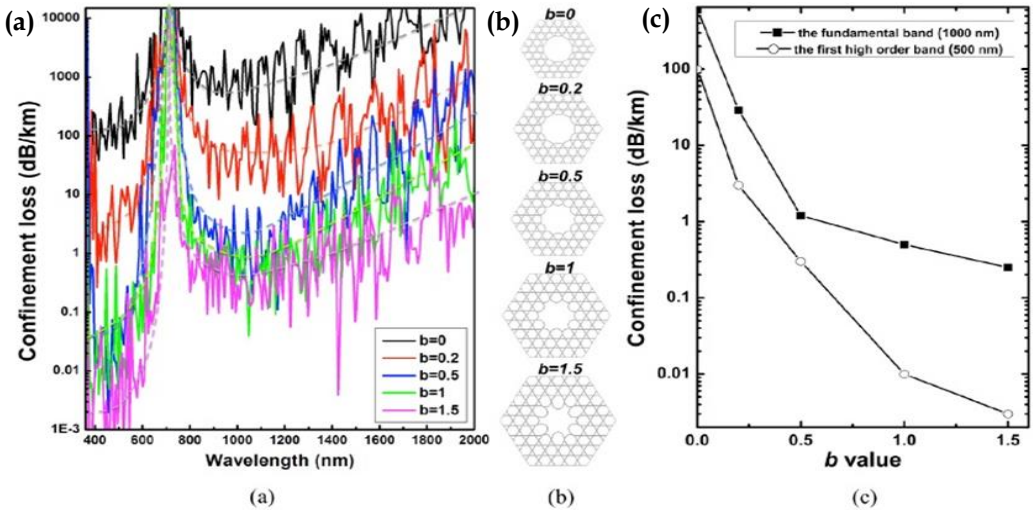

Figure 2.6: (a) Computed confinement loss evolution of kagome-lattice HC-PCF with the varying arc curvatures (b = 0, 0.2, 0.5, 1 and 1.5). The dashed lines are added for eye-guidance. (b) The fibre structure transverse profile for the different b values. (c) Evolution with b of the transmission loss figures for 1000 nm (joined solid squares) and for 500 nm (joined open circles) wavelengths [21].

Notice that the parameter $b = (d/r)$ quantifies the curvature of the hypocycloid-like core, where d is the distance between the top of the arcs and the chord joining the nodes connecting the inward arc to its two neighboring ones and r is half the chord-length. By definition the conventional core contour designs are approximated as "quasi" circular core with b=0, whilst b =1 corresponds to circular shaped arcs core contour. Below are some theoretical results showing the reduction of losses depending on different arc curvatures. Indeed, losses drops from 1000 dB/km to below 0.1 dB/km as by simply increasing the b parameters from 0 to 1.5 for hypocycloid core in the IR region and with similar trend in the visible part. Notice that a high loss transmission region appears at 700 nm due to resonances with the glass struts as expected by equation 2.1.

These results have then been experimentally confirmed to reach record loss values below 10 dB/km at 1 µm for the first time with an optimum *b* closed to 1 in a Kagome lattice design.

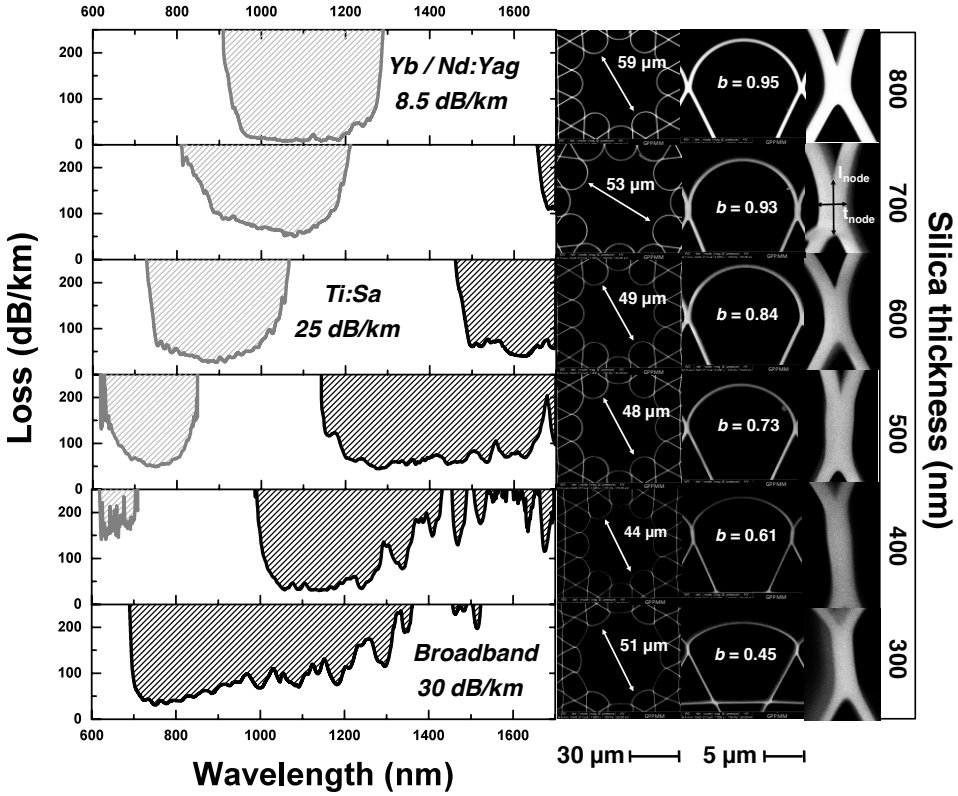

Figure 2.7: Loss spectra evolution versus the wavelength for several fabricated IC kagome lattice HC-PCFs with different silica strut thickness. The SEM images of the cross section of the fibres and the geometrical parameters are added.

From this fabrication, by making thinner the strut while keeping the curvature as pronounced as possible, 25 dB/km was demonstrated at 800 nm. Moreover, the bandwidth of the low-loss window can be managed with the silica thickness and a realization with loss figure of 30 dB/km associated to more than one octave bandwidth has been obtained. These different realizations are summarized in the Figure 2.7 [23].

Finally, in the last two years, the limits observed in the kagome lattice structure have pushed our group to optimize the fibre design with respect to the cladding. This design was based on tubular lattice (TL) cladding which consists of an arrangement

of isolated thin glass. By using such TL design, we can have in the same time elongated, optimum curved and non-touching silica cups. These features will permit better IC especially at high frequency ranges. A first experimental fabrication was reported by Pryamikov *et al.* [24] and then F. Yu *et al.* [25] where transmission in the spectral regions greater than 3 µm was achieved. In 2016, by thinning the lattice tubes down to 830 nm [26] and then 360 nm [27], transmissions loss of few tens of dB/km around 1 µm were obtained. Finally this year, our group demonstrated state-of-art performance in terms of loss with an impressive 7.7 dB/km at 750 nm and in term of broadband guidance with more than one octave guidance with losses between 10-20 dB/km [8].

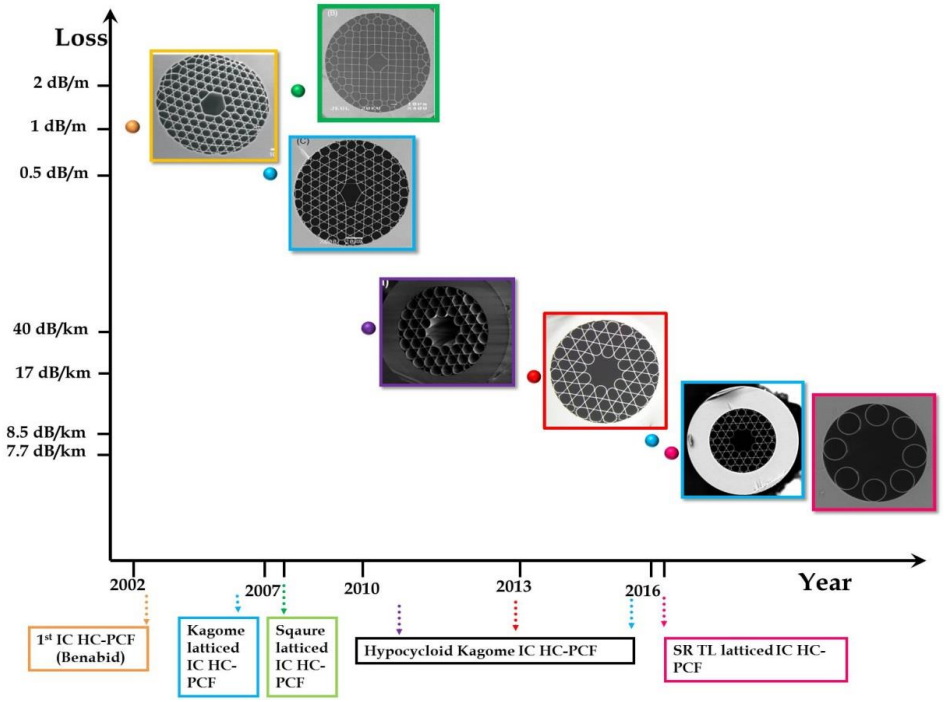

Figure 2.8: Summary of the historical development of IC Kagome HC-PCFs and their respective loss figures with SEM images.

This new step in optical performances is illustrated by the Figure 2.8. It is important to note that these new realizations reach now the level of confinement loss (CL) and became limited by the surface roughness which appears during the fibre fabrication resulting in surface capillary waves and associated extra losses [5,28-29]. This point is currently under investigation in our group. In the next section we will present the

physical and modal properties of such HC-PCFs which play role in atom optics, in particular to investigate the dephasing effect and the optical forces that are induced.

2.3 HC-PCF for cold atom and properties

In this section, we will consider some specific properties of HC-PCF which make them as a suitable candidate for atom-optics.

In addition to its compactness, the main attractive feature of HC-PCF for any gas-laser interaction is its extremely low transmission loss and small modal area. The low transmission loss means a very large interaction length is now available for gas-laser phenomena. The small core diameter in atom optics, however, has also a drawback. As a matter of fact, the success of in-fibre laser cooling will be chiefly determined by three major characteristics in the HC-PCF. First and most importantly dephasing and decoherence effects [30-32] which arises due to atom-wall collision must be kept to a minimum. This is one of the reasons that we only use IC HC-PCF (see following section on the fabricated fibres). Indeed, such fibres can exhibit a large core diameter, which reduces the dephasing due to atom-wall collisions. The second one is the nature of the core inner surface. Here the latter is engineered by coating the fibre-core inner wall with different materials depending on the aim. For example, PDMS or OTS coating are well known to have anti-relaxation properties and can preserve atomic polarization state upon several collisions without dephasing. Another example is Aluminosilicate ceramic coating, which has proved by our group to strong reduce the effect of atom to sticking to the wall. Finally, coating material that can be electrically conducting or exhibiting plasmonic resonance could be used to avoid charge accumulation on the surface or to engineer the potential well of the surface. All these examples call for a means to engineer the fibre core inner surface.

Finally, the third important feature that our HC-PCF must fulfill is a modal content which can comprise low-loss modes with both Gaussian-like intensity profiles and donut-like profiles and to be able to excite them selectively so we can create optical induced wells for both cooling and trapping in the three spatial coordinates. For

example a blue detuned donut mode would keep the atoms away from the wall, and a red-detuned counter propagating Gaussian-like modes will provide the Doppler cooling conditions in the longitudinal direction. Physical properties of fibre matter a lot for selection of fibre for atom optics. Below we detail the aforementioned features and will present route that how to prepare the fibres for our experimental platform.

2.3.1 Figure of merit

For conventional experiments of laser-matter interaction, a laser beam is focused to increase the intensity over a limited short interaction distance named Rayleigh length and expressed as $\left(z_R = \frac{w_0^2}{\lambda} \right)$ where w_0 is the beam waist of the laser. The effective interaction volume is then given by the equation $V = \pi w_0^2 z_R$. Consequently, the comparison between the intensity and interaction length gives a trade-off to increase the interaction efficiency which is expressed by a figure of merit (FOM) [4]:

$$f_{OM} = \frac{L_{INT}\lambda}{A_{Eff}} \qquad (2.2)$$

where L_{INT} is the effective interaction length, λ is the wavelength and A_{Eff} is the effective cross-section area. The FOM for different waveguides are plotted in the figure below highlighting our recent state-of-the-art HC-PCF developments:

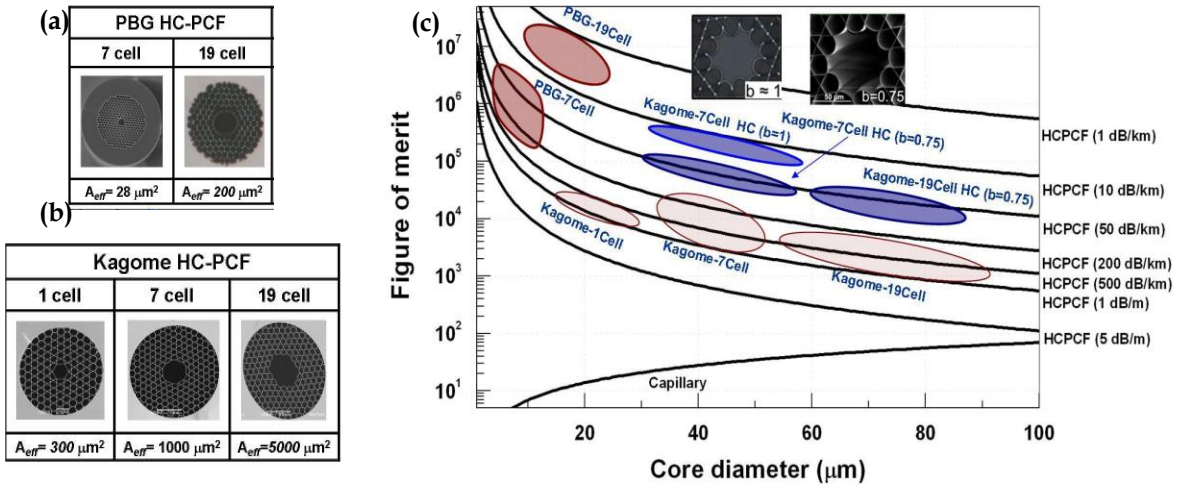

Figure 2.9: (a) SEM of PBG (b) SEM of Kagome (c) comparison of FOM for capillary and different transmission loss HC-PCF [22].

As an example, for an HC-PCF with core radius of 10 µm and attenuation 50 dB/km, FOM is ~ 10^5 times higher than the capillary waveguide. These performances allow a strong reduction of the operated power required for quantum sensor applications resulting in minimizing stark shift and power broadening effects.

2.3.2 The dephasing effect

Generally, in atom optics it is vital to avoid any dephasing or decoherence effect. For HC-PCF, because of its micro-scaled core atom-wall collisions are a major source of dephasing or decoherence. It reduces or even completely extinguishes coherence by perturbing the phase of the oscillations of individual atoms relative to the phase of the atomic ensemble. This is because of free path of thermal atoms or molecules can be much larger than core diameter of host fibre, which is usually in micrometers. Generally, the time of fly for atom between two-wall collisions is shorter than 100 ns for a core diameter of 50 µm. This dephasing effect of atom-wall collision is a significant limiting factor in the linewidth broadening. The transit time broadening and atom wall broadening are given by the following [30] [31]:

$$\gamma_{TT} = \frac{0.58}{\pi R_{MFD}} \sqrt{\frac{2k_B T}{m}} \tag{2.3}$$

and

$$\gamma_{wall} = \frac{2.405^2 D}{R_{core}^2}\left(\frac{1}{1+cK_n}\right) \quad (2.4)$$

where $k_{B\ is}$ Boltzmann constant, T is ambient temperature, m is the mass of atom, c is 6.8 in the limit of hard-sphere model, K_n is the Knudsen number and D is self-diffusion co-efficient given by

$$D = \frac{1.86\times10^{-22}T^{3/2}}{P\sigma^2\sqrt{m}} \quad (2.5)$$

where P is the atom or molecular gas pressure and σ is the atomic collisional cross section [28] which equals $2.9 \times 10^{-9}cm^2$ for Rb^{85}.

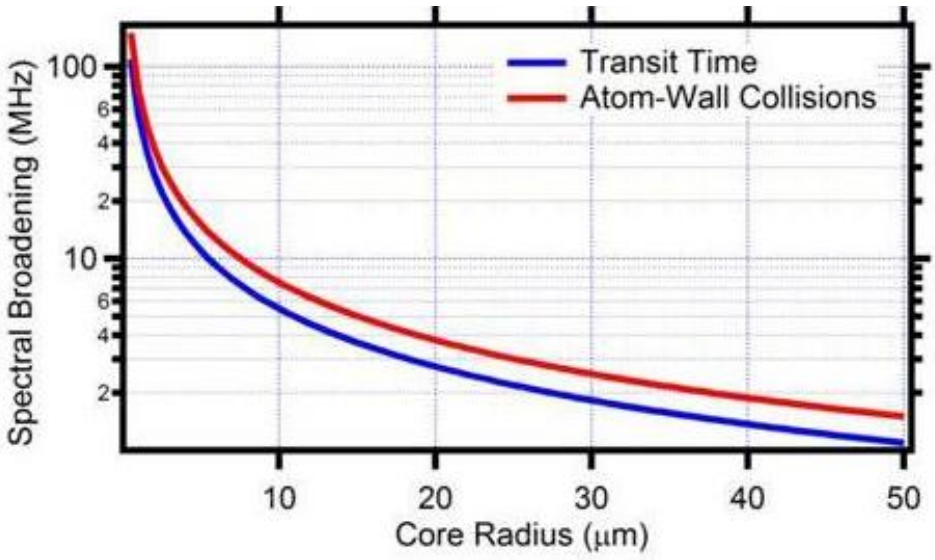

Figure 2.10: Spectral broadening from the transit time (dash line) and atom-wall collisions of core radius (solid line) dependency.

As we can see from equation 2.4 and 2.5 that transit time broadening and atom-wall collision depend on the radius of core. By increasing the core size we can reduce these two effects. The curve in the above figure clearly shows HC-PCF with large core has the advantage to reduce the transit time broadening and atom-wall collisions. Kagome fibres offer the advantage of exhibiting broadband transmission but also has reduced dephasing rate compared to PBG guiding HC-PCF because of its large core. As we can see from the figure 2.10 that spectral broadening for core radius ~ 35 μm is less than 2 MHz while increasing the core size the spectral broadening is dencreasing. The small difference between the two dephasing mechanisms makes it challenging to distinguish the transit time from the wall

collision rate in HC-PCF's sub-Doppler transparencies which is difficult to investigate the performance of antirelaxtion coating material for quantum sensor applications. In fact, antirelaxation material coating performance has been studied in macroscopic Alkali atom vapor cells by Balabas and Budker [44-52] with outstanding performance of ultra-long transverse relaxation times.

Here in next section we will see the contribution of physical structure of the fibre (on the basis of figure of merit and dephasing effects, as explained in previous section) and its effects on atomic or molecular gasses on the basis of few studies done in past, to study non-linear gas laser interactions, guidance of cold as well thermal atoms through the hollow-core of PCF.

2.3.3 Surface induced potential

The atom-surface interaction takes several forms, from an elastic collision such as the one described above and whereby an atom bounces back with no change to its quantum state to adsorption whereby the atom is trapped on the surface for a given laps of time. The physical mechanisms entailed in atom-surface are also of different nature, and can be split into two categories-depending on the surface bonds involved: physisorption and chemisorption. In the case of physisorption, the surface bond results from the Van-der-Waals (VdW) force between the atom and the surface, the energy range for such an atom-surface interaction is less than 0.1 eV (*i.e.* 152 THz). In chemisorption, the atoms and the surface substrate create a true chemical bond, thus changing the chemical structure of the surface. Here the required energy level range is between 1 and 10 eV (*i.e.* 1.52 - 15.2 PHz). For our experimental conditions, the atom-surface interaction is of physisorption nature. The effect of this surface-atom interaction on the atomic transitions has always been of interest in applications such as frequency metrology and in fundamental physics such as the quantum electrodynamics interaction of atom with the electromagnetic vacuum through Casimir force [53]. In recent years, and with the progress made in nano- and micro-photonics, the topic of atom-surface dynamics has regained a renewed and timely attention. For example, long-range atom-surface interaction,

such as Casimir-Polder effect [54] is becoming highly relevant for nano- and micro-photonic components like HC-PCF [55,56].

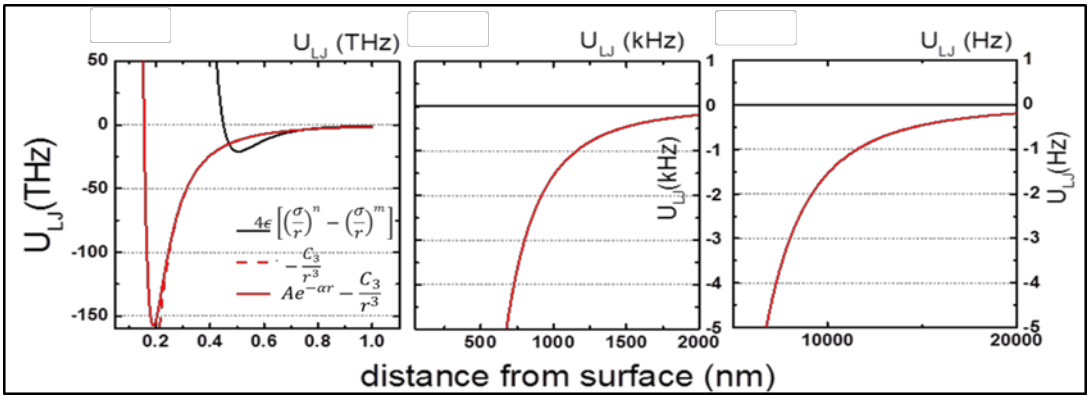

Figure 2.11: Surface-atom potential for the case of Rb ground state and for different ranges of the atom-surface distance. The black curve corresponds to 6-12 type potential with the parameters taken from reference [58]. The red curve corresponds to the potential of equation 2-7 with the parameters taken from reference [61].

Near a flat surface, the atom-surface interaction is often presented by Lennard-Jones (LJ) potential. This is often deduced empirically and combines the attractive and repulsive potential in the interaction [57]. One form of LJ potential is the so called 6-12 potential version of Mie potential (*i.e.* with n = 12 and m = 6) [57]:

$$U_{LJ}{}^{(1)}(r) = 4\epsilon\left[\left(\frac{\sigma}{r}\right)^{n} - \left(\frac{\sigma}{r}\right)^{m}\right] \qquad (2.6)$$

Here, the first term accounts for the repulsive potential and the second for the attractive potential. The quantity r is the distance between the atom and the surface. σ is the distance at which the potential is nil, and is also related to position where the potential is minimum and is given $r_{min} = \sigma e^{-\frac{\ln(m)+\ln(n)}{m-n}}$. The black curve in Figure 2.11 shows the shape for the Lennard Jones 6-12 potential. Here we have taken the values reported for rubidium-perfect metal interactions $\epsilon = 58.6\,THz$ and $\sigma = 0.45\,nm$ [58] and multiplied ϵ by $(n^2-1)(n^2+1)^{-1}$ to correct for the fact that the surface is made of silica with a refractive index n. Based on these values one observes that the potential minimum occurs at r_0 ~ 0.5 nm away from the surface and corresponds to a potential depth of 60 THz. The figure also illustrates the potential values for different distance ranges from the surface wall. For the 6-12 the

potential reaches close to zero values for r > 100 nm, and contrasts with other commonly used VdW potential. Among the most common expressions to represent the atom-surface potential is the one written below [59] :

$$U_{LJ}{}^{(2)}(r) = Ae^{-\alpha r} - \frac{C_3}{r^3} \tag{2.7}$$

Here, the short range (*i.e.* atom-surface distance < 1 nm from the surface wall) repulsion is approximated by a negative exponential function, where the parameters A and α determine the height and range, respectively, of the repulsion. The term $-\frac{C_3}{r^3}$ represents the long-range (> 1 nm) VdW attraction potential. Here, C_3 is the VdW coefficient. In this potential's expression we ignore the Casimir-Polder potential evolution from r^{-3} length scale law to r^{-4}, as it was recently shown that the experimental data fits well with the VdW scale of r^{-3} [60]. The red curve in the figure shows profile of this potential for the values of C_3, A and α being respectively equal to 1.53 THz nm^3, 1.6×10^6 THz and 53 nm^{-1}. These value correspond to Rb-silica interaction for the case of the atom ground state [61]. For comparison, the VdW asymptote term of $-\frac{C_3}{r^3}$ is plotted in the red dashed line, and which shows that both expressions are very close for r > 1 nm. On the other hand, this potential strongly differs from the 6-12 potential. For example, the depth $U_{LJ}{}^{(2)}(r)$ reaches over 150 THz whilst $U_{LJ}{}^{(1)}(r)$ is only 20 THz deep. Furthermore, the minimum of $U_{LJ}{}^{(2)}(r)$ is around $r_0 \sim 0.2$ nm and is closer that of $U_{LJ}{}^{(1)}(r)$ is ~ 0.5 nm. This example illustrates the difficulty in rigorously determining the exact profile of $U_{LJ}(r)$, especially at short range. Indeed, whilst the long range profile and the VdW coefficient C_3 are sufficiently well documented [60], the potential parameters for atom-surface distances below 1 nm remain very scarce, and a conclusive theoretical model is yet to be developed. This situation casts a large uncertainty on location of the potential minimum and depth as illustrated in the Figure 2.11. For the following of this chapter, we take $U_{LJ}{}^{(2)}(r)$ as a representative profile for atom-surface interactions because of its long range accuracy, and we consider the repulsive part of the potential as a qualitative conjecture. Moreover, in considering the case of atom-

surface interaction inside HC-PCF, we make the following assumptions. We approximate the core-contour to a flat semi-infinite dielectric surface. This means that we ignore the geometrical factor and the nano-metric thickness of the fibre silica web that affects the atom-surface potential [53]. Second, we ignore the surface roughness, height of which is typically less than 1 nm [54]. We also ignore local clustering of atoms or time evolution of the surface due to processes such as adsorption/desorption. Finally, we ignore the dispersive nature of C_3 and deduce its value from atom-perfect mirror ${C_3}^{(mirror)}$ using the following identity:

$$C_3 = \frac{n^2-1}{n^2+1} {C_3}^{(mirror)} \tag{2.8}$$

Using the above assumptions, the following section addresses the additional potentials that rubidium atoms confined in the core of a HC-PCF experience. In the case of a HC-PCF loaded with rubidium, the atoms are surrounded by the core inner-wall. In our case, the surface can be engineered by coating with a given material, and thus we can control the surface potential, but also this material is chosen for different purposes such as anti-relaxation, electrostatic charge draining or anti-sticking. In this thesis we are using two coating materials: PDMS and Aluminosilicate ceramic (see Chapter 3).

Furthermore, is an example we consider the case where the atoms are excited with a HE_{11} fibre mode. Consequently, and ignoring surface roughness or approximating the core contour to that of a cylinder, the total potential the atoms experience can be written in the following form:

$$U_{tot}(r) = U_{light}(r) + {U_{LJ}}^{(2)}(r) \tag{2.9}$$

The first term $U_{light}(r)$ in the right hand side of the equation corresponds to optical dipole potential, or Stark shift. Near a resonance with an angular frequency ω_0, the expression of the optical dipole potential can be written as $U_{light}(r) = \frac{\pi c^2 \Gamma}{2 {\omega_0}^3} \wp \frac{I(r)}{\Delta}$. Here, the quantity $\wp$ is a function dependent of the light polarization and the transition states, Δ is the frequency detuning of the laser frequency from that of the considered

transition. In the case of rubidium D2 line, it is more practical to deduce $U_{light}(r)$ from the values of the static scalar polarizability α_0 and tensor polarizability α_2 using the expressions $U_{ligh}(r) = \frac{1}{2}E^2(\alpha_0 - \alpha_2 \mathrm{F}(J))$, and where $\mathrm{F}(J)$ is a function of the electronic angular moment J. A quick calculation of $U_{light}(r)$ with our typical experimental parameters (fibre core diameters and laser powers) shows that the induced frequency shift is well below Hz-level. Consequently, we will ignore this effect in our consideration, and limiting thus the additional potential to the in-fibre atoms to that of the atom-surface one.

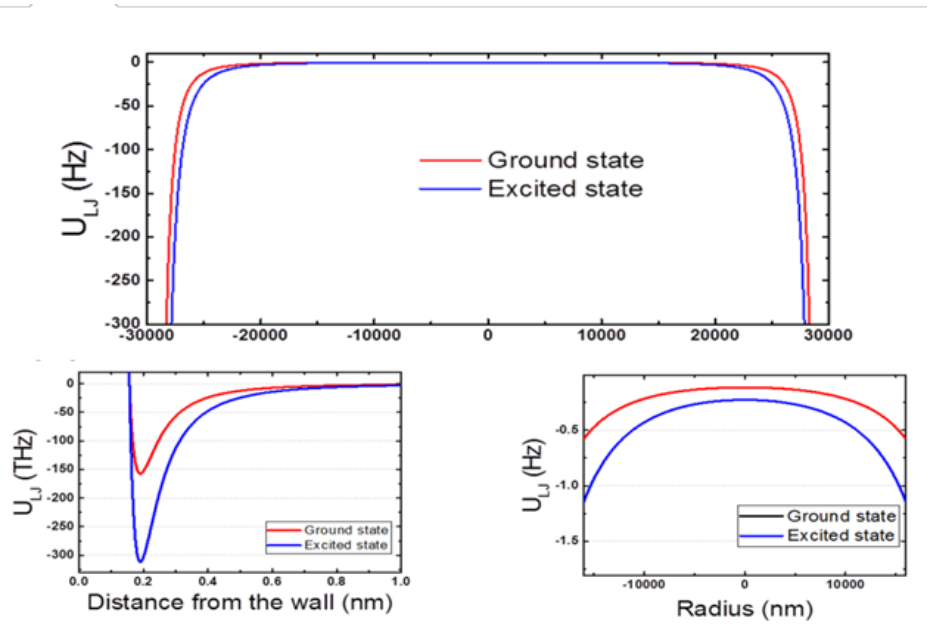

Figure 2.12: Surface-atom potential profile as experienced by a Rb atomic inside and a 60 µm diameter core of HC-PCF for the D2 transition ground (red curve) and excited state (blue curve).

In the case of an atom inside the fibre core, it will see a radial potential from both opposite surfaces of the fibre core, which is written below:

$$U_{tot}(r) \approx {U_{LJ}}^{(2)}(r) + {U_{LJ}}^{(2)}(D_f - r) \qquad (2.10)$$

Figure 2.12 shows this potential profile along a radial axis of a 60 µm diameter HC-PCF with a cylindrical core-contour and for ground and excited states of the D2 transition of ^{85}Rb. Examination of the potential at the center and near wall of the fibre core shows that frequency shift of both states is negligible for atoms which

distance from the wall is larger than 5 μm. For these atoms the potential depth and the transition shift remain less than 100 Hz.

2.3.4 The modal properties

Among the most important features of HC-PCF is that we can guide over well engineered spatial mode with extremely low loss. Figure 2.13 shows different guided mode in a Kagome hypocycloid-core contour HC-PCF along with their associated loss. The fibre dimensions are representative of the fabricated HC-PCF we are using in this work. The fibre core inner diameter was set to be 46 μm and has a negative curvature parameter b= 0.8.

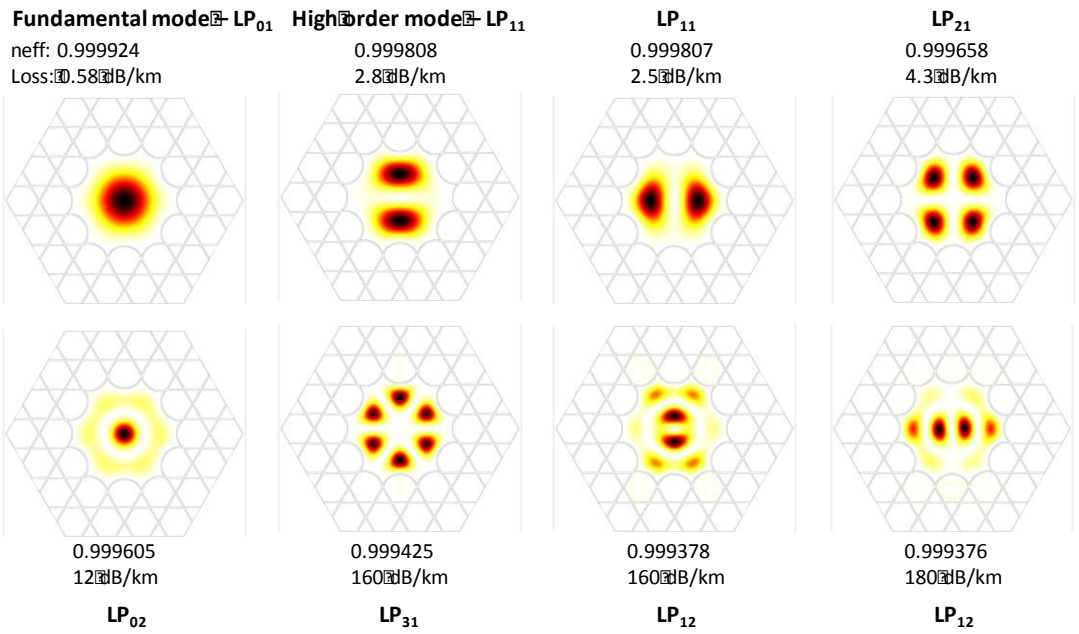

Figure 2.13: Examples of the first guided modes calculated in a 46 μm core diameter 7-cell hypocycloid core Kagome lattice HC-PCF.

For the fundamental core mode HE_{11} (which is the LP_{01} under the linear polarization approximation), the confinement loss at 780 nm is below 1 dB/km, which unprecendelty low and can be ignored for the length of fibres we will be using. This is also true with a large number of high order modes. Among these, there are several modes which have a donut-like profile such the mode LP_{31}, which loss is as low as 0.16 dB/m.

A selective modal excitation so the fibre guides a HE_{11} mode at a red detuned frequency from an atomic resonance and LP_{31} mode at a blue-detuned frequency is one example that could be explored for a longitudinal Doppler cooling and transverse trapping. Figure 2.14 (top) shows the radial profile of the intensity of the HE_{11} and the LP_{31} mode in the 7-cell hypocycloid core HC-PCF mentioned above. Indeed, recalling the induced potential by each mode, $U = \frac{\hbar\Gamma^2}{2\delta} I(r)/I_s$, one can use these modes to cool and trap in-fibre atoms.

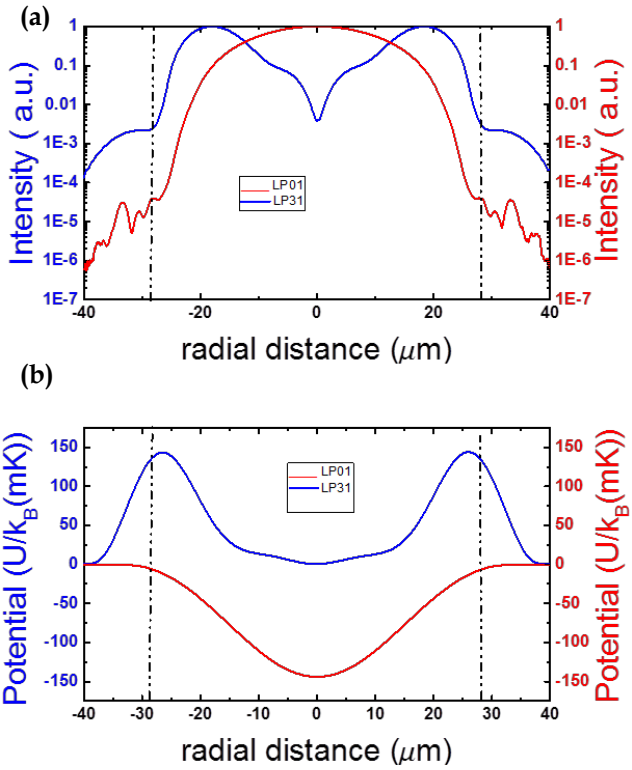

Figure 2.14: (a) Intensity radial profile for the HE_{11} or LP_{01} (red curve) and LP_{31} mode (blue curve) in a 46 µm core diameter 7 cell hypocycloid core contour Kagome HC-PCF. (b) the potential radial profile deduced from a red detuned HE_{11} mode (red curve) and blue detuned LP_{31} mode. Here the intensities and detuning values are the same as in figure 1. 13.

They also can be used for atom guidance as demonstrated with capillary fibre but without the deleterious high transmission loss. Figure 2.14 (bottom) shows the potential induced by HE_{11} (red curve) and by LP_{31} mode (blue curve) when we use

the same intensity and detuning values as the one in Figure 1.13, which were representative for the prior work done with capillaries. The results show that potential depths of >100 mK can be obtained with powers as low as μW. The figure also illustrates the capabilities of such fibres in supporting low loss modes with different transverse profile. The in-fibre laser cooling platform is designed so to accommodate such fibres and to selectively excite the desired mode for a given application using existing beam shaping technique such spatial light modulators or fibre gratings.

2.4 Fibre used for "in-fibre laser cooling" characterization

For the purpose of this thesis, we have used ten Kagome fibres with different geometries and with core inner-surface that are either coated with a particular material or kept uncoated. These fibres are then placed in UHV chamber of the in-fibre laser cooling experimental platform (see Chapter 3).

In this last section, the different HC-PCFs used in the thesis are detailed. Four designs have been selected to present high transmission around 780 nm and different core size and shape. In particular, we choose a kagome lattice cladding combined with one, seven and nineteen hollow core defect respectively named 1 cell, 7 cell and 19 cell kagome lattice HC-PCF. These last two fibres present a hypocycloid core shape to optimize the loss figure. Finally, the more recent tubular lattice has also been added due to its extremely low loss performances down to few tens of dB/km in the spectral range of interest.

The first fibre is a conventional hexagonal 1 cell kagome lattice HC-PCF (see Figure2.15). The outer diameter is 300 μm and the core size is 42 μm so a mode field diameter (MFD) of 32 μm. The silica thickness is quite thin to reach value of 200 nm resulting in a broad fundamental transmission band ranging from 400 nm to the end of our detecting system at 1600 nm. The loss obtained by the cut-back technique is found minimum around 800 nm with 150 dB/km as shown in the figure above.

The second fibre is a 7 cell kagome lattice HC-PCF with a hypocycloid core contour (see Figure2.16). The outer diameter is 350 µm and the core size is 58 µm so a MFD of 46 µm. The cups curvature is almost optimum to reach *b* equal to 0.9. The silica thickness is thicker with value of 830 nm. This allow guidance at 780 nm in the second high order transmission band. The measured loss reaches values of 200 dB/km. This figure is little bit higher than our recent developments due to stability of our process and extra bending loss which has been observed during this measurement. In a straight configuration and for a short piece of few meters, the loss level decreases by a factor of two and becomes close to the one presented in the Figure 2.7.

The third fibre is equivalent to the previous one but with a core defect larger obtained by 19 capillaries missing in the center (see Figure2.17). Consequently, the core size is much bigger to reach a diameter of 82 µm so a MFD of 64. The cups curvature is here also close to the optimum of 1. The silica thickness is slightly thinner (650 nm) resulting in near IR guidance in the first high order band. Around 800 nm, the loss figure is in the same range of 250 dB/km.

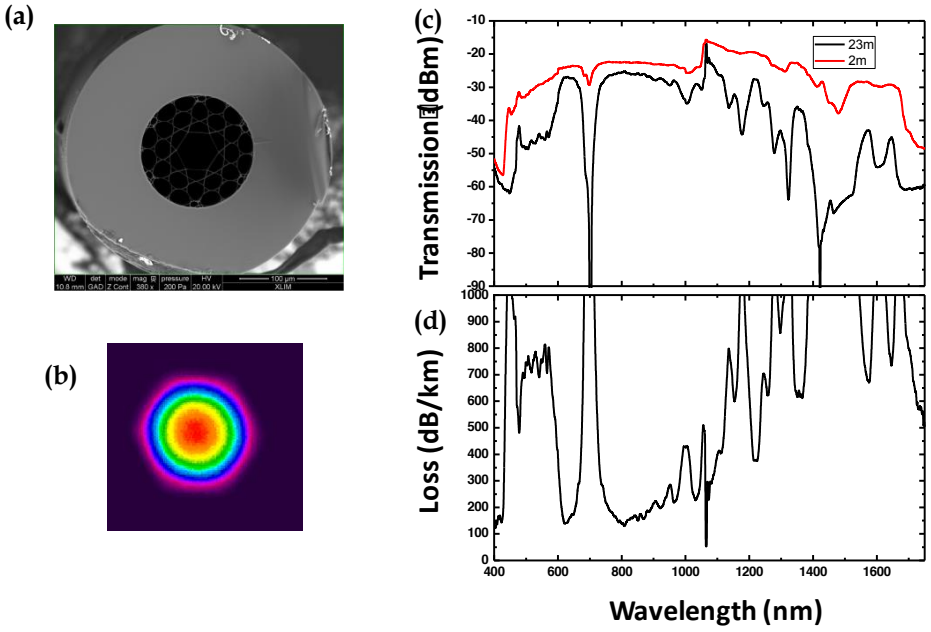

Figure 2.15: Optical characterizations of the 1 cell kagome lattice HC-PCF used for experiments (a) SEM image of kagome fiber (b) near field image at the output of fiber (c) transmission spectra (d) loss spectrum.

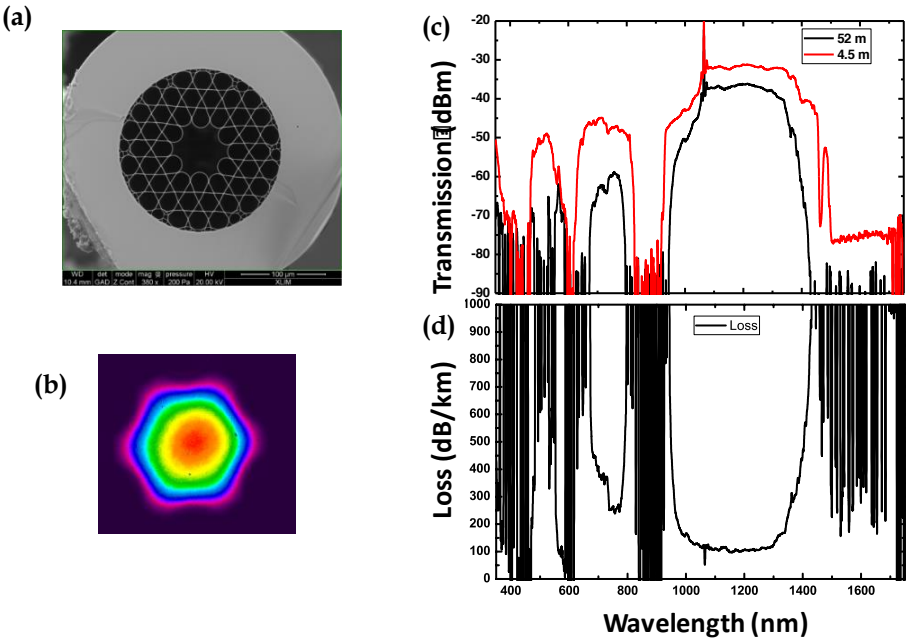

Figure 2.16: Optical characterizations of the 7 cell kagome lattice HC-PCF used for experiments (a) SEM image of kagome fiber (b) near field image at the output of fiber (c) transmission spectra (d) loss spectrum.

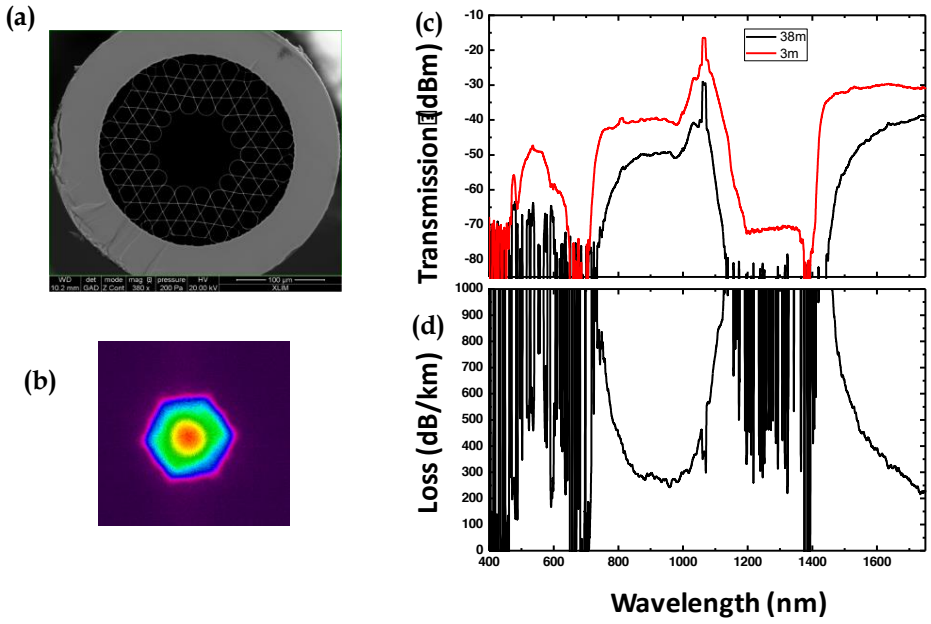

Figure 2.17: Optical characterizations of the 19 cell kagome lattice HC-PCF used for experiments (a) SEM image of kagome fiber (b) near field image at the output of fiber (c) transmission spectra (d) loss spectrum.

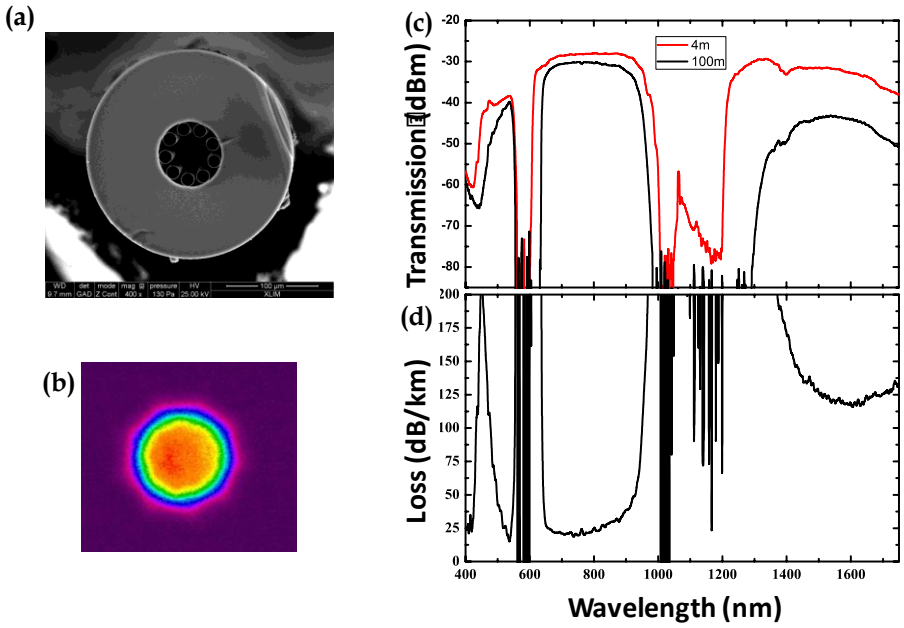

Figure 2.18: Optical characterizations of the 9 tubular lattice HC-PCF used for experiments (a) SEM image of kagome fiber (b) near field image at the output of fiber (c) transmission spectra (d) loss spectrum.

Finally, the last fibre design is based on the recent tubular cladding. Nine un-touching holes are used to form the single ring structure (see Figure2.18). The spacing between them is set to 1-3 µm to optimize the transmission according to scaling law determined in our recent publication in Optica [9]. The outer diameter is 230 µm and the core size is 38 µm so a MFD of 30 µm. The silica web presents a thickness of 550 nm which corresponds to a light transmission around 800 nm in the first high order band. As expected, with this design, the loss figure is significantly reduced to reach a record of 20 dB/km in this near IR spectral region, limited by the confinement loss. Quasi single mode guidance is also obtained as illustrated by the measured near field pattern.

In the next chapter, post-processing based aluminisilicate ceramic (sol-gel) and PDMS coating on these fibre core inner-wall are reported. These coating fibres along with uncoated ones have then been put in a high vacuum system for rubidium loading and for spectroscopy experiments.

2.5 Summary

In this chapter, we described the main two HC-PCF types: photonic bandgap HC-PCF and IC guiding HC-PCF. We reviewed in detail how the guidance takes place in both fibre types by describing the modal spectrum of their cladding photonic structure. We have shown how the optical and physical properties of both fibres led us to choose IC guiding HC-PCF over PBG guiding HC-PCF for our in-fibre laser cooling platform. In particular, we have highlighted the major requirements for most in-HC-PCF atom-optical application, which are larger fibre-core to minimize atom-wall collisions, versatile and controllable modal content and wall inner-surface that can be engineered for different purposes whilst avoiding physiochemical reactions of the loaded atoms with the inner surface. In the last section of the chapter we presented the designed and fabricated fibres for the purpose of this thesis and their transmission spectrum. This fibre will then be post-processed and placed in the UHV system of the in-fibre laser cooling platform.

References

[1] "*Ultra-low-loss (0.1484 dB/km) pure silica core fibre and extension of transmission distance*", **K. Nagayama, M. Kakui, M. Matsui, T. Saitoh, and Y. Chigusa,** Elect. Lett., vol. 38, 1168-1169, (2002).

[2] "*Analysis of OH absorption bands in synthetic silica*", **O. Humbach, H. Fabian, U. Grzesik, U. Haken, and W. Heitmann**, Journal of Non-Crystalline Solids, vol. 203, 19-26, (1996).

[3] "*Single-mode photonic band gap guidance of light in air*", **R. F. Cregan, B. J. Mangan, J. C. Knight, T. A. Birks, P. S. Russell, P. J. Roberts, and D. C. Allan**, Science vol. 285, pp. 1537-1539, (1999).

[4] "*Stimulated Raman scattering in hydrogen-filled hollow-core photonic crystal fibre*", **F. Benabid, J. C. Knight, G. Antonopoulos, and P. S. J. Russell**, Science, vol. 298, No 399, pp. 399–402, (2002).

[5] "*Ultimate low loss of hollow-core photonic crystal fibres*", **P. J. Roberts, F. Couny, H. Sabert, B. J. Mangan, D. P. Williams, L. Farr, M. W. Mason, A. Tomlinson, T. A. Birks, J. C. Knight, and P. St.J. Russell**, Optics Express, vol. 13, Issue 1, pp. 236-244, (2005).

[6] "*Generation and photonic guidance of multi-octave optical-frequency combs*", **F. Couny, F. Benabid, P. J. Roberts, P. S. Light, and M. G. Raymer**, Science, vol. 318, pp. 1118–1121, (2007).

[7] "*Large pitch kagome-structured hollow-core photonic crystal fibre*", **F. Couny, F. Benabid, and P. S. Light**, Optics Letters, vol. 31, Issue 24, pp. 3574–3576, (2006).

[8] "*Ultralow transmission loss in inhibited-coupling guiding hollow fibres*", **B. Debord, A. Amsanpally, M. Chafer, A. Baz, M. Maurel, J. M. Blondy, E. Hugonnot, F. Scol, L. Vincetti, F. Gérôme, and F. Benabid**, Optica, vol. 4, Issue 2, pp. 209–217 (2017).

[9] "*Linear properties of inhibited coupling hollow-core photonic crystal fibres*", **A. Amsanpally**, Thesis 2017.

[10] "*Photonic band-gap structures*", **E. Yablonovitch,** J. Opt. Soc. Am, Vol. 10, pp 283-295, (1993).

[11] "*Photonic band gap guidance in optical fibres*", **J. C. Knight, Jonathan C., Jes Broeng, Tim A. Birks, and P. St J. Russell**, Science vol. 282, no. 5393, pp. 1476-1478 (1998).

[12] "*Photonic crystal fibres*", **Philip Russell**, Science vol. 299, pp. 358-362, (2003).

[13] "*Hollow-core photonic bandgap fibre: new light guidance for new science and technology*", **F. Benabid**, Phil. Trans. R. Soc. A, vol. 364, pp. 3439–3462, (2006).

[14] "*Linear and nonlinear optical properties of hollow core photonic crystal fibres*", **F. Benabid and P. J. Roberts**, Journal of modern optics, vol. 58, No. 2, pp. 87-124, (2011).

[15] "*Identification of Bloch-modes in hollow-core photonic crystal fibre cladding*", **F. Couny, F. Benabid, P. J. Roberts, M. T. Burnett, and S. A Maier**, Opt. Express, vol. 15, No. 2, pp. 325–338, (2007).

[16] "*Endlessly single-mode photonic crystal fibre*", **T. A. Birks, J. C. Knight, and P. St. J. Russell,** Optics letters, vol. 22, No. 13, (1997).

[17] "*Hollow metallic and dielectric waveguides for long distance optical transmission and lasers*", **Marcatili, Enrique AJ, and R. A. Schmeltzer,** The Bellsystem technical journal, July 1964.

[18] "*Double photonic bandgap hollow-core photonic crystal fibre*", **P. S. Light, F. Couny, Y. Y. Wang, N. V. Wheeler, P. J. Roberts, and F. Benabid**, Opt. Express, vol. 15, No. 2, pp. 325–338, (2007).

[19] "*Low loss broadband transmission in optimized core-shape Kagome Hollow-Core PCF*", **Y. Y. Wang, F. Couny, P. J. Roberts, and F. Benabid**, Lasers Electro- Optics Quantum Electron. Laser Sci. Conf. (QELS), p. CPDB4 (2010).

[20] "*Low loss broadband transmission in hypocycloid-core Kagome hollow-core photonic crystal fibre*" **Y. Y. Wang, N. V. Wheeler, F. Couny, P. J. Roberts, and F. Benabid**, Opt. Lett. vol. 36, pp. 669-671 (2011).

[21] "*Hypocycloid-shaped hollow-core photonic crystal fibre Part I: Arc curvature effect on confinement loss*", **B. Debord, M. Alharbi, T. Bradley, C. Fourcade-Dutin, Y.Y. Wang, L. Vincetti, F. Gérôme, and F. Benabid,** Optics Express, vol. 21, Issue 23, pp. 28597-28608, (2013).

[22] "*Génération et micro-confinement de plasmas microondes dans des fibres optiques creuses microstructure* , **Benoît Debord,** thesis 2013.

[23] "*Ultra-low loss (8.5 dB/km @ Yb-laser region) inhibited-coupling Kagome HC-PCF for laser beam delivery applications*", **B. Debord, M. Maurel, A. Amsanpally, M. Adnan, B. Beaudou, J.-M. Blondy, L. Vincetti, F. Gérôme, and F. Benabid**, Photonic West, Paper 10094-58, (2017).

[24] "*Demonstration of a waveguide regime for a silica hollow - core microstructured optical fibre with a negative curvature of the core boundary in the spectral region > 3.5 μm*", **A. D. Pryamikov, A. S. Biriukov, A. F. Kosolapov, V. G. Plotnichenko, S. L. Semjonov, and E. M. Dianov**, Opt. Express, vol. 19, No. 2, pp. 1441–1448, (2011).

[25] "*Low loss silica hollow core fibres for 3–4 μm spectral region*", **F. Yu, W. J. Wadsworth, and J. C. Knight**, Opt. Express, vol. 20, No. 10, pp. 11153–11158, (2012).

[26] "*Hollow-core fibres for high power pulse delivery*", **M. Michieletto, J. K. Lyngsø, C. Jakobsen, J. Lægsgaard, O. Bang, and T. T. Alkeskjold**, Opt. Express, vol. 24, No. 7, pp. 7103–7119, (2016).

[27] "*Antiresonant Hollow Core Fibre with Octave Spanning Bandwidth for Short Haul Data Communications* ", **J. R. Hayes, S. R. Sandoghchi, T. D. Bradley, Z. Liu, R. Slavik, M. A. Gouveia, N. V. Wheeler, G. T. Jasion, Y. Chen, E. Numkam-Fokoua, M. N. Petrovich, D. J. Richardson, and F. Poletti**, Lasers Electro- Optics Quantum Electron. Laser Sci. Conf. (QELS), p. Th5A.3 (2016).

[28] "*Analysis of light scattering from surface roughness in hollow-core photonic bandgap fibres* ", **E. N. Fokoua, F. Poletti, and D. J. Richardson**, Opt. Express, vol. 20, No. 19, pp. 20980–20991, (2012).

[29] "*Nested antiresonant nodeless hollow core fibre*",**F. Poletti**, Opt. Express, vol. 22, No. 20, pp. 23807–23828, (2014).

[30] "*Low-light-level optical interactions with rubidium vapor in a photonic band-gap fibre.*", **Ghosh, Saikat, Amar R. Bhagwat, C. Kyle Renshaw, Shireen Goh, Alexander L. Gaeta, and Brian J. Kirby**., Phys. Rev. Lett. vol. 97, no. 2, 023603 (2006).

[31] "*Sensitive magnetometry based on nonlinear magneto-optical rotation.*" **Budker, D., D. F. Kimball, S. M. Rochester, V. V. Yashchuk, and M. Zolotorev.** Phys. Rev., vol. 62, no. 4, 043403, (2000).

[32] "*Electromagnetically induced transparency in Rb-filled coated hollow-core photonic crystal fibre.*", **Light, P. S., Fetah Benabid, F. Couny, M. Maric, and A. N. Luiten**. Opt. Lett. vol. 32, no. 10, pp. 1323-1325, (2007).

[33] *"Light and gas confinement in hollow-core photonic crystal fibre based photonic microcells,"*, **F. Benabid, P. J. Roberts, F. Couny, and P. S. Light,** J. Eur. Opt. Soc., vol. 4, no. c, pp. 1–9, (2009).

[34] "*Compact, stable and efficient all-fibre gas cells using hollow-core photonic crystal fibres*", **F. Benabid, F. Couny, J. C. Knight, T. A. Birks and P. St J. Russell,** Nature, vol. 434, (2005).

[35] *"Optical Guiding of Atoms through a Hollow-Core Photonic Band-Gap Fibre,"* **R. J. Knize and T. Takekoshi,** in Quantum Electronics and Laser Science Conference (QELS), vol. 1, (San Jose), p. 2 (2008).

[36] *"Efficient All-Optical Switching Using Slow Light within a Hollow Fibre,"* **M. Bajcsy, S. Hofferberth, V. Balic, T. Peyronel, M. Hafezi, A. S. Zibrov, V. Vuletic, and M. D. Lukin,** Phys. Rev. Lett. vol. 102, 203902, (2009).

[37] *"Electromagnetically induced transparency in Rb-filled coated hollow-core photonic crystal fibe"*, **P. S. Light, F. Benabid, F. Couny, M. Maric and A. N. Luiten**, Optics Letters, vol. 32, No. 10, (2007).

[38] "*Efficient guiding of cold atoms through a photonic band gap fibre"*, **S Vorrath, S A Moller, P Windpassinger, K Bongs and K Sengstock,** New Journal of Physics vol. 12, 123015, (2010).

[39] "*Van der Waals interaction between an atom and a solid surface*." , **Zaremba, Eugene, and Walter Kohn**. Phys. Rev. B, vol. 13, 2270, (1976).

[40] "*Atom-surface Van der Waals potential induced sub-Doppler transparencies in Rb vapor filled Kagome HC-PCF*", **Ekaterina Ilinova, Tom Bradley, Ximeng Zheng, Benoît Debord, Frédéric Gérôme, and Fetah Benabid,** CLEO US, paper SM2H.7 (2016).

[41] "*Saturation spectroscopy of iodine in hollow-core optical fibre"*, **Anna Lurie, Philip S. Light, James Anstie, Thomas M. Stace, Paul C. Abbott, Fetah Benabid, and Andre N. Luiten,** , Opt. Exp., vol. 20, No. 11, 11906, (2012).

[42] "*Bichromatic laser cooling in a three-level system"*, **R. Gupta, C. Xie, S. Padua, H. Batelaan, and H. Metcalf,** Phys. Rev. Lett. vol. 71, No. 19, (1993).

[43] "*Kinetics of Atoms in a Bichromatic Field"*, **O. N. Prudnikov, A. S. Baklanov, A. V. Taichenachev, A. M. Tumaikin, and V. I. Yudin**, Journal of Experimental and Theoretical Physics, vol. 117, No. 2, pp. 222–231, (2013).

[44] "*Sensitive magnetometry based on nonlinear magneto-optical rotation.*", **Budker, D., D. F. Kimball, S. M. Rochester, V. V. Yashchuk, and M. Zolotorev**, Physical Review A, vol. 62, no. 4, 043403, (2000).

[45] "*Method for characterizing self-assembled monolayers as antirelaxation wall coatings for alkali vapor cells.*", **Yi, Y. W., H. G. Robinson, S. Knappe, J. E. Maclennan, C. D. Jones, Chengjie Zhu, N. A. Clark, and J. Kitching**. J. App. Phys., vol. 104, no. 2, 023534, (2008).

[46] *"Magnetometry with millimeter-scale anti-relaxation-coated alkali-metal vapor cells,"*, **M. V. Balabas, D. Budker, J. Kitching, P. D. D. Schwindt, and J. E. Stalnaker**, J. Opt. Soc. Am. B, vol. 23, no. 6, p. 7, (2005).

[47] *"Investigation of antirelaxation coatings for alkali-metal vapor cells using surface science techniques,"*, **S. J. Seltzer, D. J. Michalak, M. H. Donaldson, M. V. Balabas, S. K. Barber, S. L. Bernasek, M. a. Bouchiat, a. Hexemer, a. M. Hibberd, D. F. J. Kimball, C. Jaye, T. Karaulanov, F. a. Narducci, S. a. Rangwala, H. G. Robinson, a. K. Shmakov, D. L. Voronov, V. V. Yashchuk, a. Pines, and D. Budker**, J. Chem. Phys., vol. 133, pp. 1–11, (2010).

[48] "*Microwave transitions and nonlinear magneto-optical rotation in anti-relaxation-coated cells.*"**, Budker, Dmitry, Leo Hollberg, Derek F. Kimball, J. Kitching, Szymon Pustelny, and Valeriy V. Yashchuk** Phys. Rev. A 71, no. 1, 012903, (2005).

[49] *"Relaxation of atomic polarization in paraffin-coated cesium vapor cells,"*, **M. T. Graf, D. F. Kimball, S. M. Rochester, K. Kerner, C. Wong, D. Budker, E. B. Alexandrov, M. V. Balabas, and V. V. Yashchuk**, Phys. Rev. A - At. Mol. Opt. Phys., vol. 72, no. 2, (2005).

[50] *"Testing the effect of surface coatings on alkali atom polarization lifetimes,"***, S. J. Seltzer, D. M. Rampulla, S. Rivillon-Amy, Y. J. Chabal, S. L. Bernasek, and M. V. Romalis**, J. Appl. Phys., vol. 104, no. 10, pp. 1–7, (2008).

[52] *"Hyperfine frequency shift and Zeeman relaxation in alkali-metal-vapor cells with antirelaxation alkene coating,"*, **E. P. Corsini, T. Karaulanov, M. Balabas, and D. Budker,** Phys. Rev. A, vol. 87, no. 2, p. 22901, (2013).

[53] *"Atom-wall interaction,"* **D. Bloch, and M. Ducloy**, Adv. At. Mol. Opt. Phys., vol.

50, pp. 91–154 (2005).

[54] *"Using atomic interference to probe atom-surface interactions,"* **R. Marani, L. Cognet, V. Savalli, N. Westbrook, C. I. Westbrook, and A. Aspect**, Phys. Rev. A, vol. 61, no. 5, p. 53402, (2000).

[55] *"Lamb-Dicke spectroscopy of atoms in a hollow-core photonic crystal fibre,"* **S. Okaba, T. Takano, F. Benabid, T. Bradley, L. Vincetti, Z. Maizelis, V. Yampol'skii, F. Nori, and H. Katori,** Nat. Commun., vol. 5, p. 4096, (2014).

[56] *"Quantum optics, what next?,"* **J. I. Cirac and H. J. Kimble,** Nat. Phot., vol. 11, no. 1, pp. 18–20, (2017).

[57] "*Intermolecular and surface forces*," **J. N. Israelachvili,** Academic press (2015).

[58] *"Molecular Dynamics Study of Liquid Rubidium and the Lennard--Jones Fluid.,"* **R. D. Mountain and . S. W. H.,** J. Res. Natl. Bur. Stand., vol. 48.6, pp. 439–446, (1979).

[59] *"Long-range atom-surface bound states,"* **E. G. Lima, M. Chevrollier, O. Di Lorenzo, P. C. Segundo, and M. Oriá,** Phys. Rev. A, vol. 62, no. 1, p. 13410, (2000).

[60] "*Casimir–Polder interactions in the presence of thermally excited surface modes,*" **A. Laliotis, T. P. de Silans, I. Maurin, M. Ducloy, and D. Bloch,** Nat. Commun., vol. 5, p. 4364 (2014).

[61] *"Spontaneous radiative decay of translational levels of an atom near a dielectric surface,"* **F. Le Kien and K. Hakuta,** Phys. Rev. A, vol. 75, no. 1, p. 13423 (2007).

Chapter 3

Ultra-high vacuum system of the in-fiber laser cooling platform

This chapter describes the ultra-high-vacuum platform for in-fiber laser cooling experimental platform. First, the chapter discusses the design and the rationale of the specification requirements for a large volume ultra-high vacuum (UHV) chamber that can accommodate the test of several HC-PCF and the generation of two magneto-optical traps (MOTs), along with all the required signal monitoring, Rb source, vacuum pumping, and the opening of the UHV chamber for part replacement. Then the chapter describes the installation and assembly of all the parts such as the vacuum pumps, feedthroughs, viewports, vacuum gauge, fibres holder, position of Rb sources, and position of MOTs. In a second section, we describe the components to generate the MOT anti-Helmholtz coils, and to accommodate the fibres. In a third section, we cover the process in achieving UHV and in HC-PCF inner-surface coating. We finish the chapter by measuring the different HC-PCF transmission spectrum as a means to characterize the functioning of the mounted UHV system.

3.1 Introduction

Towards the long term and challenging aim of demonstrating the feasibility of laser cooling atoms that are confined in a HC-PCF, the objective of this work is to build an experimental platform that is designed in a manner to address experimentally several interrogations such as the effect of atom-surface interaction on the cooling process, or exploring the best HC-PCF modal excitation for both transverse and longitudinal trapping and cooling. Furthermore, the experimental platform will be the test-bed in identifying and qualifying the best HC-PCF design for atom optical applications. Indeed, whilst in our group, designing and fabricating tailored HC-PCF along with coating them with specific materials is a well mastered expertise, the spectroscopy dynamics of atoms inside HC-PCF is not fully explored and recent results show that in-fibre atoms have dynamics and laser-atoms spectral signatures that significantly differ from the conventional macroscopic configurations [1].

Within this context, this chapter describes the design, assembly and characterization of an ultra-high vacuum system that is sufficiently versatile and efficient to be able to explore several studies using the spectroscopy of both thermal and cold atoms inside different HC-PCF and with different core inner-wall surfaces. This platform will be able to study the effect of atom-surface interaction for different type of fibres and to identify the best parameter space of the fibre's modal content, effective area and coating surface with regard to achieving stable in-fibre atom trapping and cooling schemes. For example, the platform will be able to explore how the hollow-core reduction in diameter affects the increase of the atom-surface interaction, or how the wall surface material impacts the physio-chemical adsorption of the atoms on the core inner-wall. In addition, to its relevance to the objective of achieving cold atom inside the fibre, because HC-PCFs exhibit a large surface-to-volume and a close vicinity of the atom to the core inner-wall surface, they represent a unique stage for atom-surface studies. Indeed, currently the effect of atom-surface interaction on the atomic transitions is not only of interest to our aim of in-fibre laser cool rubidium but is of interest in several applications such as frequency metrology

and in fundamental physics such as the quantum electrodynamics interaction of atom with the electromagnetic vacuum through Casimir force [2-4]. Another example where the UHV chamber design must fulfil is the investigation of different modal excitation. As seen in chapter 2, the IC HC-PCF can support a variety of low loss spatial modes, from a Gaussian like mode (*e.g.* HE_{11} core mode) to a donut like modes (*e.g.* LP_{31}) [5]. The design of the UHV chamber must allow to excite these modes selectively and easily so to investigate the best modal excitation for trapping and cooling. Moreover, the UHV chamber must allow spectroscopic studies of cold as well as thermal atoms inside the hollow-core of fibres. Finally, the UHV platform must be easy to operate so to replace the fibres or the optical layout when needed.

In the first section of this chapter, we will describe how our UHV system was designed and built. We list all the system components and the interconnections of the subsystems such as pumping system, electrical feedthroughs. After, we will present the installation of our ultra-high vacuum system and details the characteristics of the main elements of the UHV system, such as the alkali atomic rubidium source, anti-Helmholtz coils and the fibre holder. In the third section, we will describe the followed procedure of baking in order to achieve the desired pressure inside the chamber. In the last section, we will give a description of the preparation of Kagome HC-PCFs that will be tested. In particular, we describe the core inner-wall coating with several special coatings in some of the HC-PCFs.

3.2 Ultra-high vacuum system

3.2.1 Ultra-high vacuum chamber specification requirements

In designing the UHV chamber, we have endeavoured to respect the following specification requirements:

1. The UHV platform must sufficiently versatile and large so to be able to be arranged for different optical set-ups ranging from MOT generation to atom loading and guidance in different HC-PCFs.
2. The system must be able to simultaneously accommodate experiments with cool and thermal atoms.
3. UHV chamber having capabilities to cool and trap atoms at lowest possible temperature (*few* μK) and with maximum number of trapped atoms. Thus the vacuum must lower than 10^{-8} torr for a volume larger than 0.25 m^3.
4. The system must be able to have at least two simultaneously operating MOTs
5. The system must handle the test of several HC-PCFs with different geometries and different inner wall surface treatment to study the alkali-materials interaction with the surface of these fibres.
6. The system must be equipped with the required optical windows for the various lasers beams necessary in MOT generation, atom guidance, in-fibre transverse trapping, spectroscopy and imaging.
7. The system must accommodate the necessary monitoring tools of the atom guidance and MOT generation throughout the full experimental sequence.

The design and fabrication of this platform with these conditions is really challenging because in addition to gather all the components in the same platform is added the need to create a very low pressure not only in the large chamber but also inside the core of the HC-PCFs, which is time taking. In the next sub-section, we will discuss the design and the fabrication of our UHV chamber.

3.2.2 Designing and fabrication of ultra-high vacuum chamber

The vacuum system was designed with the goals to have a low pressure as soon as possible inside the chamber and having a maximum optical access, for cooling, trapping and guiding beams, and for imaging system to collect the results. The chamber is designed to be opened and replace some optical parts like HC-PCF. Figure 3.1 shows the industrial drawing of the design UHV chamber. The chamber

is cylindrically shaped and outstands from the common MOT UHV chambers with its large volume and its layout. The chamber has inner diameter of 60 cm and height of 22 cm. The inside of the chamber harbours a circular breadboard that can support several optical components along with the HC-PCF under test. Such a large chamber dimensions stem from the necessity to be able to use several meter long coiled HC-PCFs, translation stages, lenses and wave plates holders for pre-aligned optical set-up on an easy to place breadboard. Figure 3. 2 shows an example of a breadboard that can be harboured by the UHV chamber. In this example, the breadboard supports a holder for a set of HC-PCFs whose tips are aligned with MOTs. Figure 3.3 shows 3D schematic diagrams of how the chamber can be positioned on an optical table and how is connected to the rest of the parts of the platform such as the vacuum pumps and the laser beams. The chamber comprises a total of nineteen conflat flanges (CF) for optical access, monitoring and imaging. The chamber is equipped with additional ports for the vacuum pumps (ion and turbo pumps), vacuum gauge, inlet angle valve for flushing the inert gas to keep the set up free from contamination during opening and sealing process, electrical feedthroughs for Rb sources, anti-Helmholtz coils and other computer run UHV compatible devices such as motorized translation stages (see table 3.1 for details). The top viewport (200 CF) will be used to have eye view on the vacuum components like Rb sources, anti-Helmholtz coils, fibre base plate and fibres. The rest of viewports (200 CF and 160 CF) on top and bottom of the chamber will be used for laser beams propagation for atom cooling. Four 65 CF viewports are on the side of chamber: one for electrical feedthrough for anti-Helmholtz coils, second for jointly connected ion and turbo pumps, third is to view MOT and fourth is for vacuum gauge. The last ten 40 CFs are for cooling, guidance system and probing cold atoms.

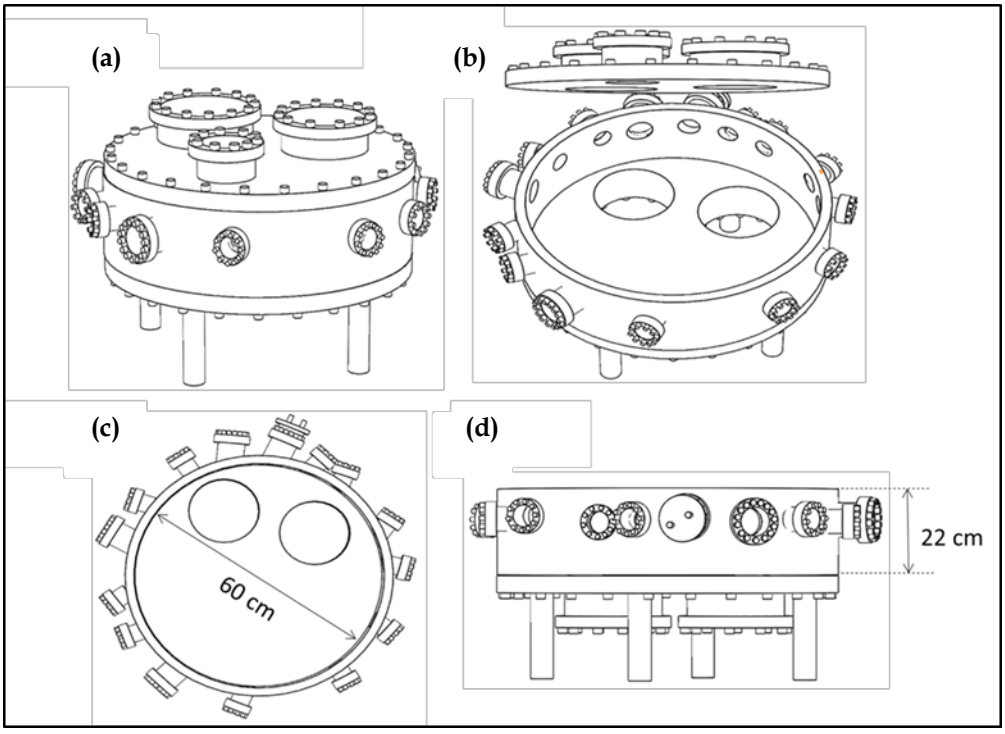

Figure 3.1: Drawing of chamber in different positions: (a) when the lid is closed (as on the laser table), (b) and when the lid is partially opened. (c) Open lid top-inside view. Diameter of chamber is 60 cm (d) and side view (in real position on the laser table). Height of the chamber is 22 cm.

The chamber top is a movable lid to replace the breadboard and/or any components inside the chamber. All the elements inside the chamber are mounted on a breadboard inside the chamber: anti-Helmholtz coils and Rb sources for magneto-optical-trapping, also a fibre set holder to accommodate the under test fibres.

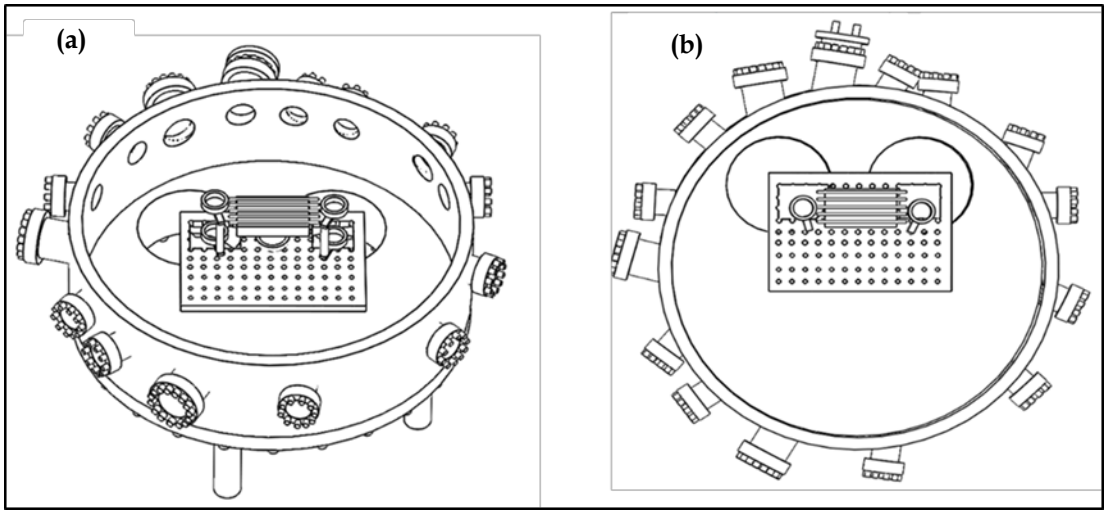

Figure 3.2: Position of breadboard, fibres and anti-Helmholtz coils inside the UHV chamber.

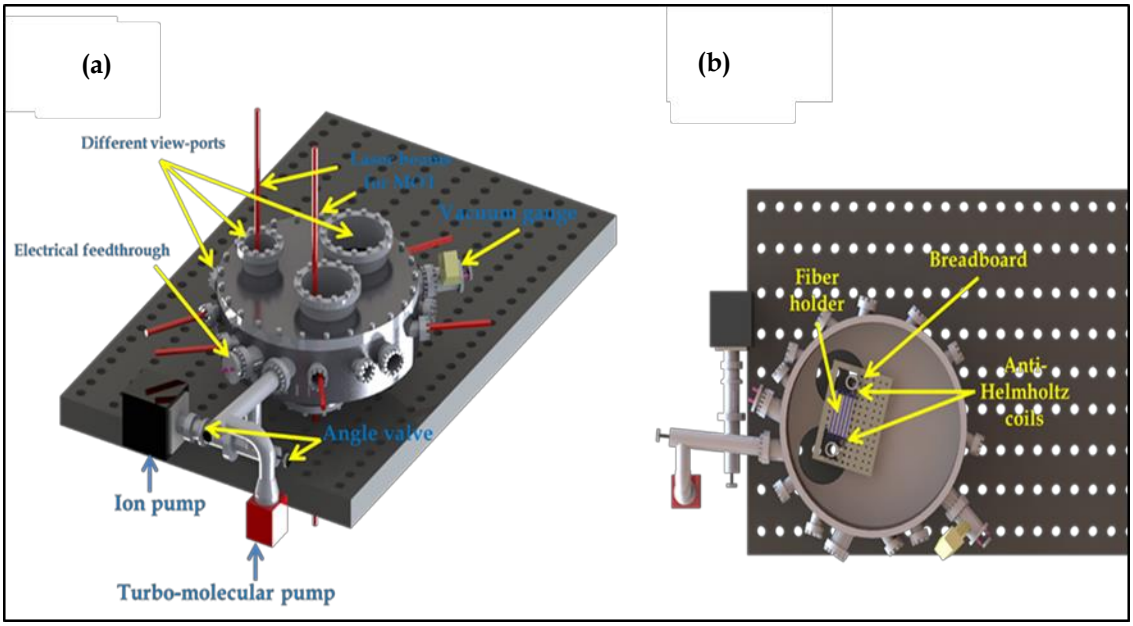

Figure 3.3: (a) and (b) are solid work drawings of UHV chamber showing the position of laser beams for MOT, ion and turbo-molecular pumps.

Item description	Fitting dimensions				
Conflat flanges (CFs) (with nominal diameter)	200 CF	160 CF (on the top)	100 CF (on the top)	65 CF (on the side)	40 CF (on the side)
Number of CFs installed on chamber	03	01	01	05	09

Table 3.1: Viewport details.

3.3 Installation and assembly of the ultra-high vacuum system components

The chamber is made of 316L stainless steel and the fabrication of the UHV chamber after design has taken four months. The assembly and the installation of UHV chamber have gone through several procedures so to ensure in a systematic fashion optimal working conditions. Indeed, we first baked all in-vacuum components like viewports, electrical feedthroughs, and spools of anti-Helmholtz coils, fibres holder and kapton coated wires in an oven before to install in the main assembly. After the UHV chamber was positioned on the laser table, we tightened

the viewports one by one. The viewports are made from fused silica (MDC vacuum). The viewports for cooling and trapping laser beams have (on our demand) broadband anti-reflected coating (BBAR) centred around 780 nm on both side to avoid the multi reflection inside the chamber which can cause several effects on trapped atoms. There are two viewports for blue and red-detuned lasers propagation for guidance of cold as well as thermal atoms. The inner edge of flanges on the UHV chamber and viewports, electrical feedthroughs, tees are knife edged. For tightening viewports, electrical feedthroughs and other components to their proper flanges on the UHV chamber or to make seal between these components and CF flanges, we used annealed OFHC (Oxygen-free high conductivity) copper gaskets because these are softer than normal copper gaskets. This help, during tightening the viewport and other components, to lessen the stress from an uneven torque which can damage the viewport. The alignment of copper gasket with both the component to be installed and flange is very important, if there is no proper alignment between them can cause leakage. A copper gasket should be used once and be checked properly. If the surface of gasket is uneven, it cannot be used. Before to put it on the flange, inner edges of both the components to be installed and flanges on chamber, should be cleaned properly to remove any dust or debris by using commercially available tissues for cleaning optical components. All viewports, tees, electrical feedthroughs were screwed in proper way (star pattern). This method reduces the stress by distributing it uniformly across the viewport in order to avoid the risk for cracking of viewport. Figure 3.4 shows the sequence of screw's tightening for every viewport.

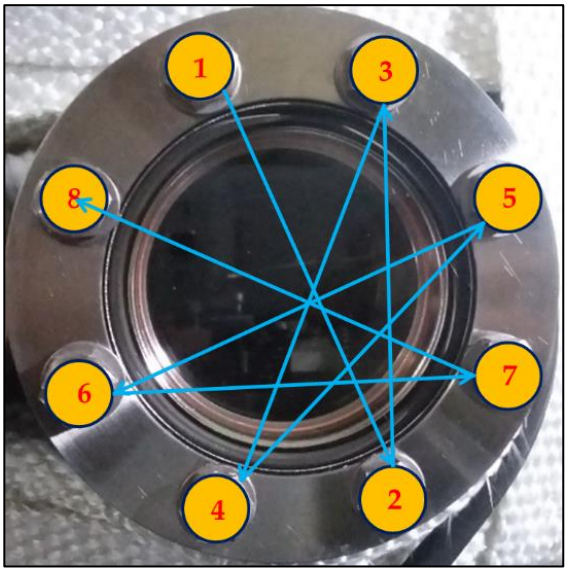

Figure 3.4: The star-cross method that is used for tightening viewports to a vacuum system.

Notice that all the UHV components are reusable. We need only to change the copper gaskets in case of viewports and top lid of the chamber but with much care not to damage any of the knife edge on the CF flanges. Once we finished with viewports, electrical feedthroughs and tees we then moved to the installation of vacuum pumps. This part has been done at the end to avoid any mishap or damage to them while installing other components. During all this process, we used powder free hand gloves, clean room coat and masks to avoid any contaminate of the components and chamber. When the chamber is mounted, we operated a preliminary vacuum pumping (the full vacuum process us details in section 3.5.1) to minimize leakage, and then we tested the top-lid opening and closing to assess the timing of the procedure and make sure that the chamber can be properly evacuated post lid-opening. Figure 3.5 shows pictures of the top-lid opening, aligning and closing. The latter is open and closed with a crane. The opening of the lid follows the following process: we first close the vacuum pump valves, and then we fill the chamber with nitrogen to atmospheric pressure before opening the lid. A nitrogen gas flow is kept on during the whole duration when the chamber is open. This allows avoiding too strong inner-surface contamination from the ambient air, and to redo the baking process (see section 3.5.1). The results show that one can open the chamber for necessary replacements in a lid time of 6 to 8 hours.

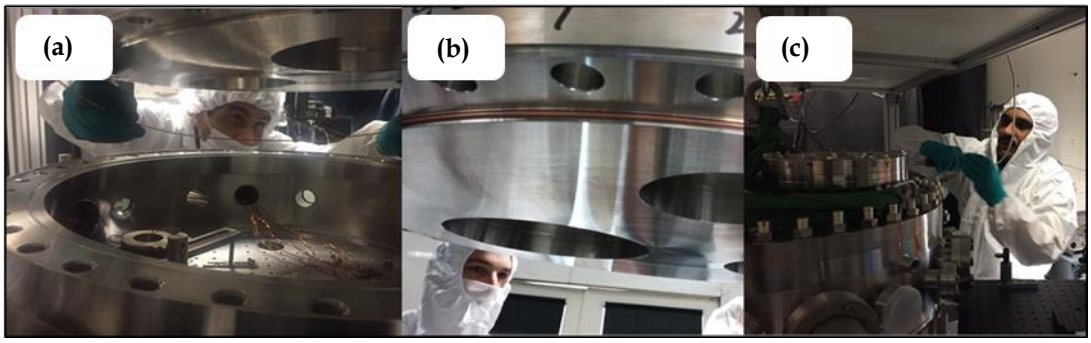

Figure 3.5: Pictures of the top-lid opening, aligning and closing: (a) when the lid open (alignment of wire seal copper gasket with the proper grove on lower portion of lid). (b) Lid is held by crane (while working on in-vacuum components). (c) Tightening the screws after sealing the platform.

Figure 3.6 shows photographs of the fabricated UHV chamber when fully assembled and set on the optical table that will harbour the full experimental platform for in-fibre cold atom optics. After, the above preliminary tests on evacuation and the lid opening and closing, and a full baking to outgas the inner-surface of the chamber (see section 3.5), we proceeded the assembly of Rb dispenser, the Helmholtz coil for the MOT generation and the HC-PCFs. Figure 3.7 shows photos during this procedure, and the section below describes in more detail each of the three part.

Figure 3.6: Different viewing angles of Ultra-High-Vacuum system (on laser table).

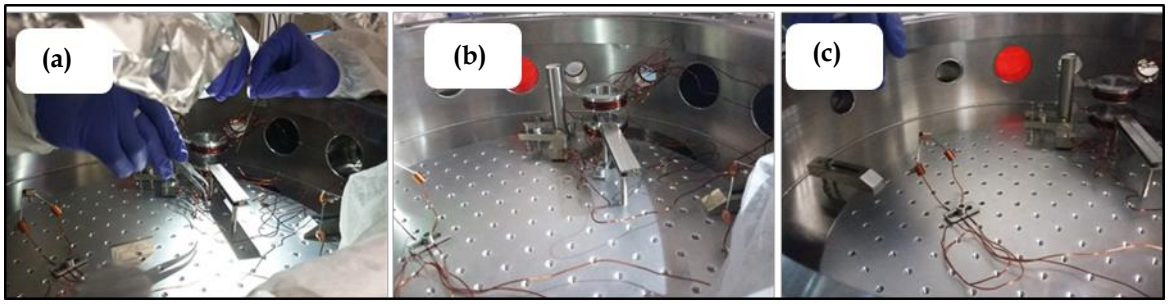

Figure 3.7: (a) Setting HC-PCFs under test on the holder. (b) The fibres holder, kapton coated copper wire (used for internal wiring for dispensers) and anti-Helmholtz coils. (c) The Rb dispenser and the breadboard with M6 threads on it.

3.3.1 Atomic rubidium vapour

The in-fibre laser cooling platform was set to operate with rubidium atoms. These are dispensed using a specific type of alkali sources and the atomic density can be controlled, if the environment is properly evacuated, with chamber temperature. The choice of Rb was motivated because of its widespread use in coherent and atom optics. Rb is a readily available with alkali metal and contains a well-documented closed-cycle transition for cooling. Also, we can excite the rubidium atoms with several commercially available tunable lasers which there wavelength is in the near infra-red region.

3.3.1.1 Rb sources

In our experiment, the atomic rubidium vapour was produced by an alkali rubidium dispenser (getter)[6], which has several advantages. It is easy to implement them inside the vacuum chamber and also we can control the flow of rubidium vapour by adjusting the electric current. To produce the rubidium vapour we are using a commercial "rubidium dispenser", Rb/NF/14/50FT10, with long active length of 50 mm (see figure 3.8 (a)). The dispenser is several milligrams of a rubidium compound that is contained in a small (50 x1.12 x1.35 mm) stainless steel oven and blocked over its length by a fine diameter wire. The current feeding the dispenser is controlled by a power supply. When the dispenser is heated by the applied current, the wire cracks and opens the reservoir to release rubidium atoms in the chamber. When the applied current is switched off, the wire cools down and

the reservoir is sealed again preventing out-gassing of atoms/molecules to the vacuum. Figure 3.8 shows its vapour density as a function of temperature for rubidium [7]. To obtain the vapour pressure of only 1 µbar, a temperature of 117 °C is required. As the volume of our vacuum chamber is quite large, we are using four dispensers. These are connected to the feedthrough wires with Kapton coated UHV compatible copper wires (figure 3.8 (c)). The dispensers are placed near the MOT location to increase the density of atomic vapours in their vicinity.

3.3.1.2 Rb loading

To produce the Rb vapour inside our chamber, the Rb dispenser is heated resistively to a suitable temperature under vacuum condition to release Rb vapour (Rb alkali metal dispensers evaporate between 550 to 850 °C). Furthermore, for a new Rb getter, the chamber is first heated to a temperature in the range of 100-200 °C for 4 to 8 hours so to outgas the getter from any contamination on its surface. Second, we increase the current slowly [8, 9] at an increment of 0.1 A/min. to slowly remove the protection layer. For every increment in current applied, we keep an eye on the pressure, inside the UHV chamber, and to keep it as low as possible. Also, at each increase, the current is kept constant until the chamber pressure reaches a stable value. We repeat this process until we reach a threshold specified by the getter supplier, and which correspond to a Rb release with no contaminants. After the decontamination of the Rb source, the current is set to a value, which is defined by the desired atomic density deduced from the contrast of the Rb D2 optical absorption lines. The observation of this fluorescence is also a checkpoint to see whether the Rb source is working and the laser is on resonance as can be seen in Figure 3.9.

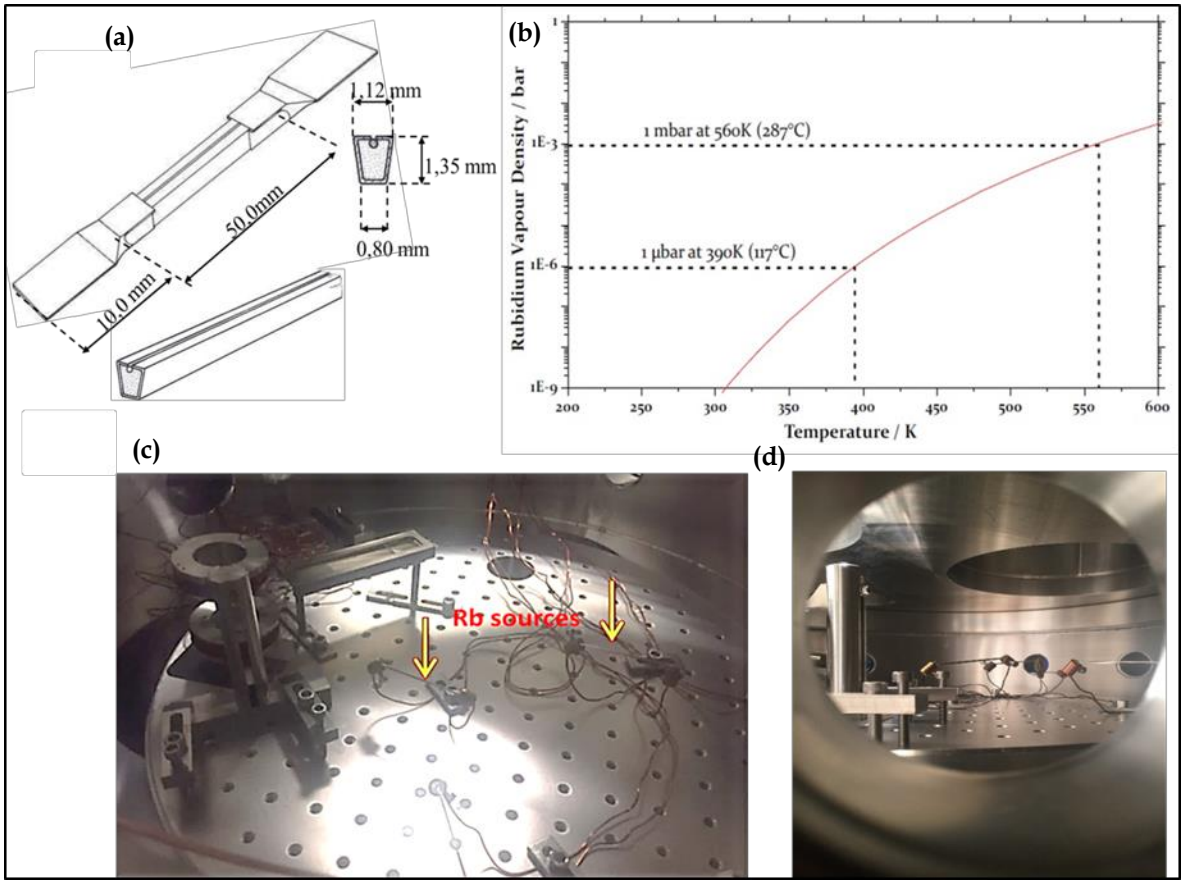

Figure 3.8: (a) Rubidium dispenser (Rb/NF/14/50FT10). (b) Rb vapor density VS temperature. The density of Rb at room temperature is negligible. The pressure of 1 µbar and 1 mbar are obtained at temperature of 117 °C and 287 °C respectively [11]. (c) & (d) Top view and side view of the connection and position of Rb dispensers. It is connected with homemade copper connector at the center of chamber, few centimetres away from the MOT region by using UH vacuum compatible kapton coated wires.

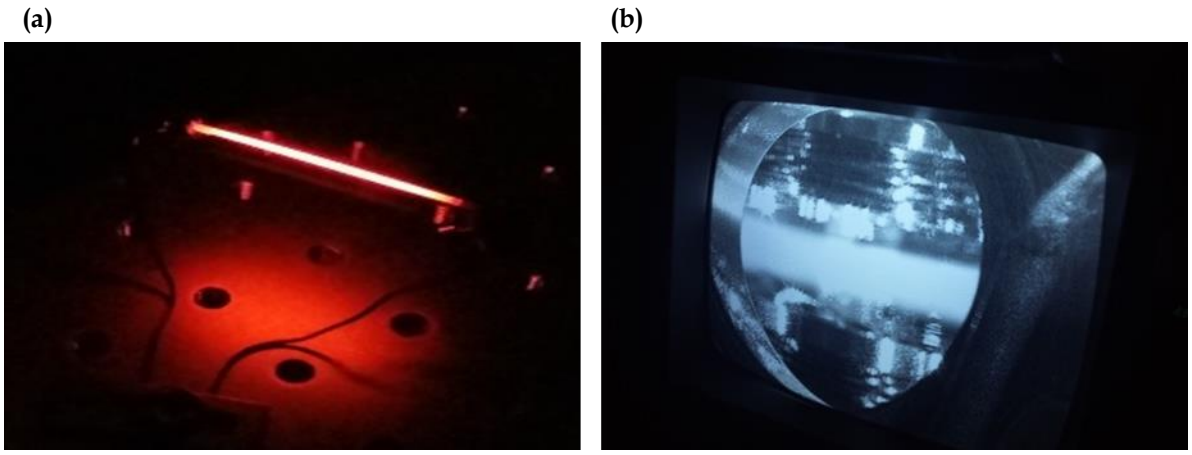

Figure 3.9: (a) Rb dispenser is glowing when current above threshold passes through it. (b) Fluorescence can be seen, when denser vapors of Rb interact with on-resonance laser beam coupled via one of the view port.

Finally, to ensure that vacuum is sufficiently "clean" when the Rb is at thermal equilibrium, we compare the measured UHV pressure with the rubidium vapour density presented in Figure 3.8 (b). For example, at room temperature the Rb vapour density corresponds to pressure of approximately 5 x 10^{-5} Pa which is higher than the 10^{-6} at 10^{-7} Pa (~ 10^{-8} at 10^{-9} Torr) pressure of rubidium vapor which is optimal for trapping. However, it is important to maintain the Rb at well below its room temperature pressure by continuously pumping the system.

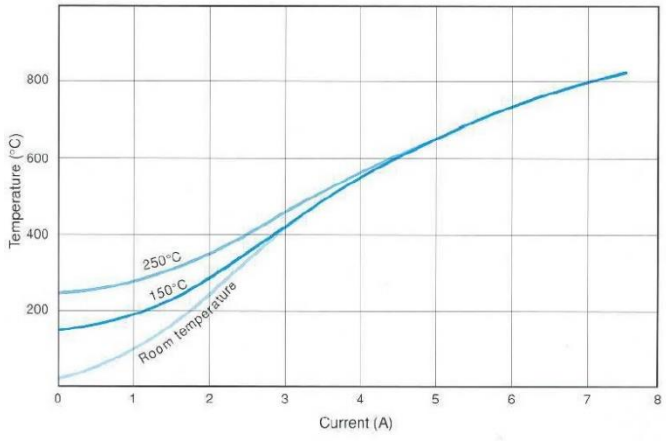

Figure 3.10: The temperature of dispenser as a function of applied current to the dispenser for different environmental temperature [7].

3.3.2 Magnetic trap design and characterization

The magnetic field coils is a key ingredient for atoms trapping. In addition to cooling the atoms, the MOT is also designed to spatially trap the atoms and this requires the generation of a force by exploiting the Zeeman effect, resulting in drawing atoms into the centre of the trap. Figure 3.11 illustrates the basics of trapping with a Rb atoms with a magnetic field. Under a magnetic field, the degenerate atom energy levels split by virtue of Zeeman effect. Furthermore, as mentioned in chapter 1, the presence of a magnetic field gradient along a given direction, *e.g. z,* produces a restoring force $\overrightarrow{F_{mag}} = -\kappa\vec{z}$, with $\kappa \propto z\delta_m(\partial B/\partial z)$ being the effective spring constant, which is proportional to the field gradient and the laser frequency detuning from the resonance. As a result, in the presence of a magnetic field gradient as shown in Figure 3.11 (a), an atom away from the position z = 0 experiences a Zeeman splitting that is set by the magnitude of the field, and a push

towards z = 0 whose strength is proportional to the field gradient. This effect is used to increase the capture rate in cooling the atoms. In order to find out the required magnetic field for our Rb MOT, we recall the Zeeman splitting for both Rb isotopes. Figure 3.11 (c) shows the Zeeman splitting of the two $|5^2S_{1/2}, F = 1,2\rangle$ hyperfine ground states for ^{85}Rb and ^{87}Rb respectively. The results show that we have a splitting rate of up to 2 MHz/Gauss for both isotopes.

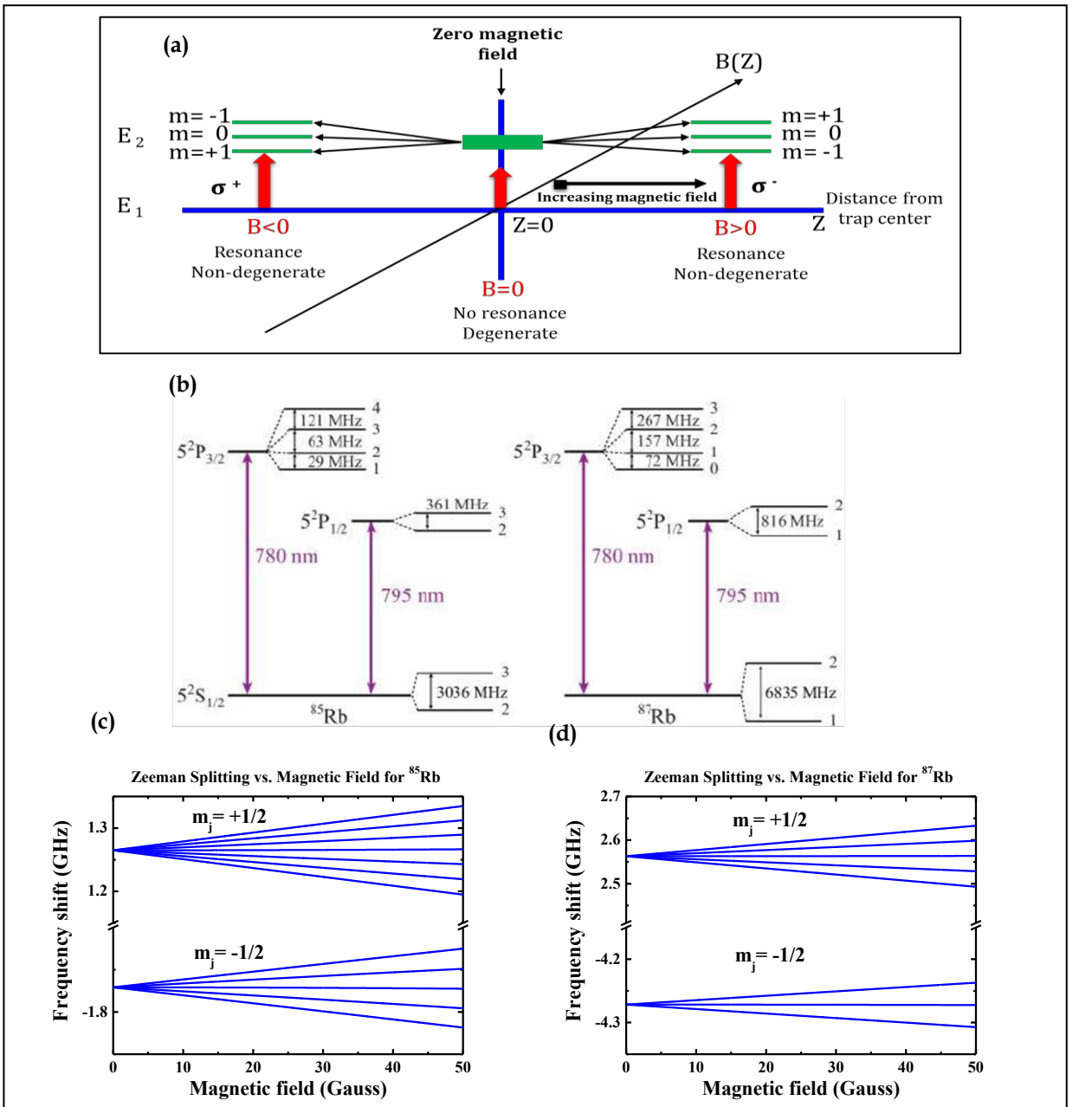

Figure 3.11: (a) Schematic of Zeeman splitting and magnetic gradient trapping. (b) The ^{85}Rb and ^{87}Rb $5^2S_{1/2}$ ground state energy (and the resulting hyperfine structure) is shown as a function of an external magnetic field. The levels are grouped according to F in the anomalous Zeeman Effect regime. The hyperfine levels in the (c) ^{85}Rb and (d) ^{87} Rb involved in the D1 and D2 transitions,

In practice, the most common way to produce the desired magnetic field amplitude and gradient whilst having a zero field position is made by running a current through two spools of wire in the anti-Helmholtz configuration [10], and

whereby the current in one ring runs in opposite direction to the current in the second ring. Figure 3.12 shows schematically such anti-Helmholtz coils.

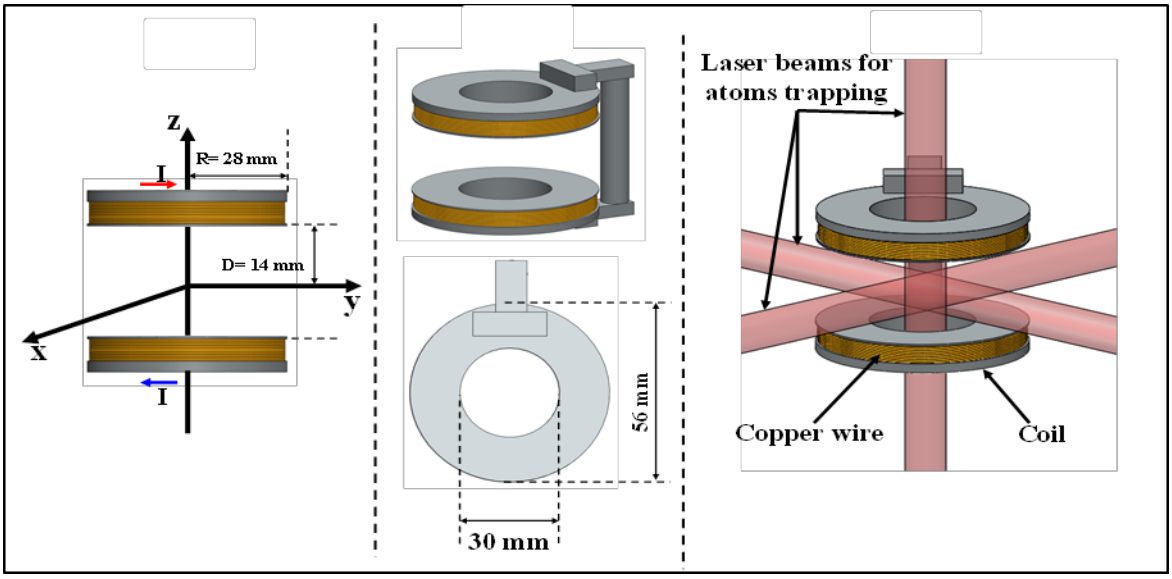

Figure 3.12: The Anti-Helmholtz coils design.

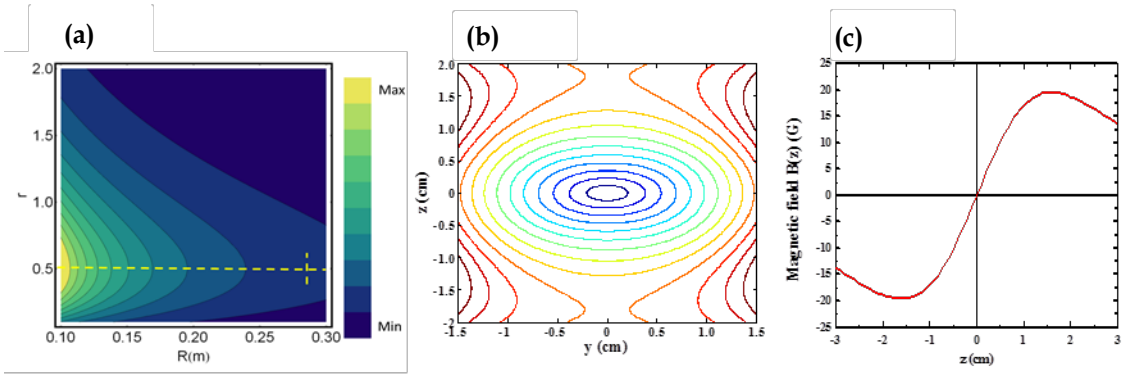

Figure 3.13: (a) Image of a contour plot of ratio r between the coil radius and the distance of the two coils. (b) Field magnitude of the quadrupole trap in the y–z–plane in Anti-Helmholtz configuration. Each contour line corresponds to a field increase of 1.5 G. (c) The magnetic field value between the coils for a current of 3 Am.

These have a zero point in the middle of the trap, and can exhibit a large magnetic field gradient, and whose expression is given by:

$$\partial_z B = \frac{3\mu_0 I}{2} \frac{r}{R^2(1+r^2)^{5/2}}. \quad (3.1)$$

Here, I is the electric current in each coil, $2D$ is distance between the two coils, and r is the ratio D/R between the coil radius and the distance of the two coils. Figure 3.13 (a) presents a contour plot of $\frac{r}{R_C^2(1+r^2)^{5/2}}$, and clearly shows the field gradient is maximum for r=0.5, *i.e.* R=2D regardless of the coil radius. Furthermore, the plot shows, as expected, the gradient increases with the radius decrease. However, for practical reasons, such as having a radius larger than the laser beam waist, there is a lower limit in the coil radius. In our case we have taken a radius of 28 mm. The Figures 3.13 (b) and (c) show the calculated magnetic field along z for R=2D= 28mm (2.8 cm) and a contour plot of the magnetic field strength. With this size, the anti-Helmholtz coils can be placed inside the vacuum chamber with no need of water cooling as cooling is compulsory for set of coils having large dimension to avoid any damage. The conduction between the body of chamber and set of coils is sufficient to dissipate the generated heat. The inconvenience by using this small size of coils concerns the alignment of the zero point magnetic fields of coils with the MOT laser beams common intersecting point. However this can be avoided by optimizing the parameters and the alignment of the coils with the centre point of overlapping laser beams before sealing the chamber. In figure 3.14 the fabricated anti-Helmholtz coils is shown. To have insulation between the wires in the spools a vacuum compatible Kapton coated copper wires with 1 mm of diameter is used. These coils are wound around spools made from 316L stainless steel. Each spool has outer and inner diameter 30 and 56 mm respectively. The distance between the centers of the coils is 2.8 cm. The coils are designed to operate with variable current from 0 to 4.5 A. Forty loops of wire are wound tight around the each spool. The coils are mounted such that the current travels through the loops in opposite directions and the coil axes are collinear with one of the laser beam axes. The fabricated coils parameters are listed in table 3.2. For a current of 3 A the gradient is about 0.15 T/m corresponding to 15 G/cm which is needed for trap operation (normal trap operation is between 10 and 20 G/cm).

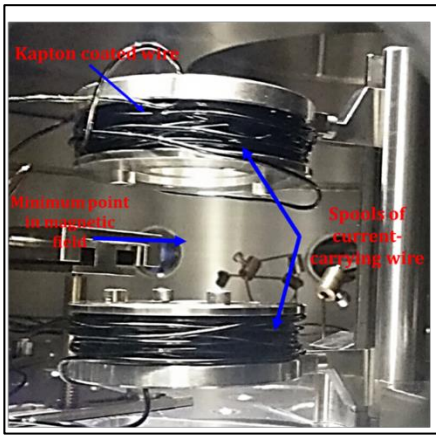

Coil parameters	Value	Units
Shape	Circular	
Length of wire	5	m
Loops	40	/coil
Radial thickness	1.2	cm
Axial thickness	1.7	cm
Radial wall thickness	0.4	cm
ce to face separation	2.8	cm
Inner diameter	3	cm
Average diameter	5.6	cm

Figure 3.14: Home-made UH vacuum compatible pair of anti-Helmholtz coils made from 316L stainless steel. Table 3.2: Anti-Helmholtz coils parameters.

These coils are connected with DC power supply, which run through the wires on the spools, allowing to the anti-Helmholtz coils to provide the necessary magnetic field gradient to produce enough Zeeman-splitting of the energy levels of the atoms in the trap. Before the installation of the coils inside the chamber, the coils were baked. First both coils without the wires were washed and baked for long period of times. Then the Kapton coated copper wire is wound on the spools by doing much care not to remove the Kapton coating. After fixing this inside the vacuum system, a current of 5 Am is passed through the coils for short periods of time to remove the contamination from the spools. In this process, the coils are heated to get rid of contamination which was stuck during winding the coils on the spools.

3.3.3 Fibre preparation and insertion

To place our fibres inside the chamber we are using home-built fibre holder. This is also made from the 316L stainless steel as shown in Figure 3.15 below. It can accommodate ten HC-PCFs. First we roughly couple the laser beam with the fibre after placing them on the fibre holder to avoid any problem of alignment after sealing the chamber. This fibre holder is fixed on the breadboard with vacuum compatible screws (see Figure 3.16). Just to hold the fibres firmly on the holder's groove, glass placed on the top of the fibres is clamped by stainless frame plate. The

advantage of this glass plate is one to hold the fibres firmly and other to have view of coupling of light in to the fibres.

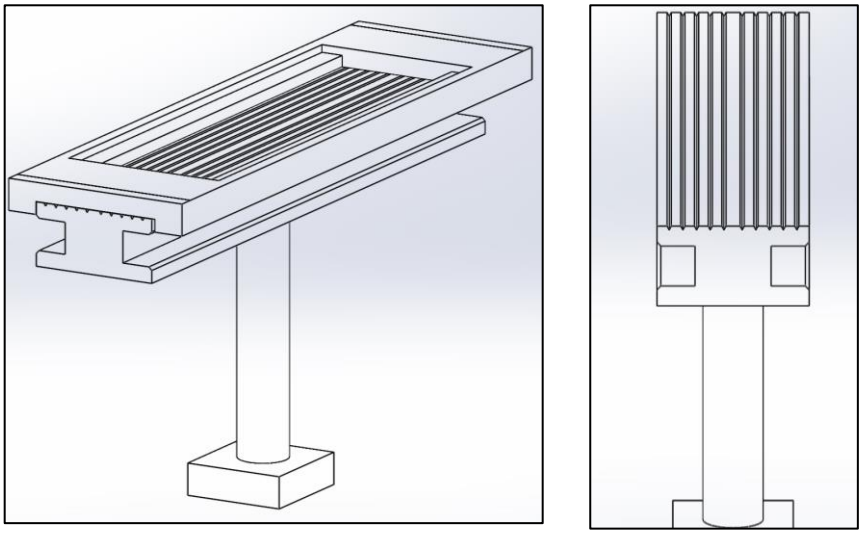

Figure 3.15: Design of fibre holder.

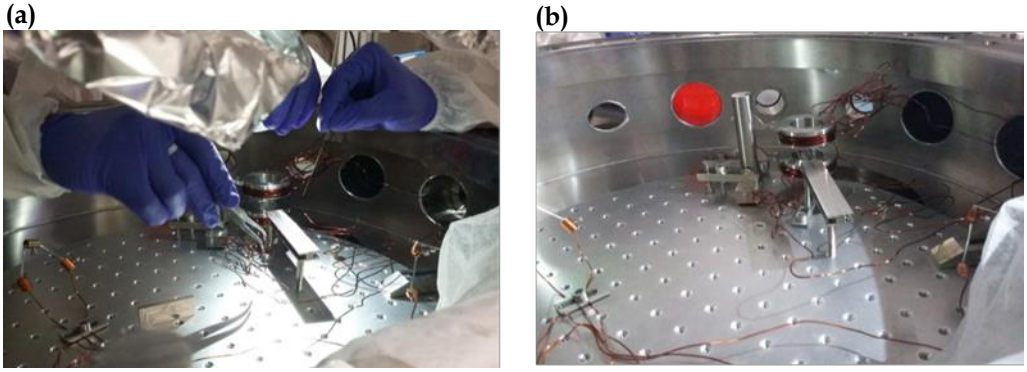

Figure 3.16: (a) Fibre installation inside the chamber (b) Fibre holder position on the breadboard near the anti-Helmholtz coils.

3.4 Post-processing of HC-PCF under test

As mentioned in the introduction to this chapter, one of the aims of the thesis is to study the effect of atom-surface interaction between Alkali atoms and IC Kagome HC-PCF. Using a small size core HC-PCFs have advantages and disadvantages. Among the advantages of using fibres, the long interaction length (kilometre ranges), the use of less amount of gasses (to be filled in hollow-core) which is far less than those are being used in microcells, the low transmission losses and the controlled modal contents. The disadvantages of using tight geometries will result

in an increases of the atom-atom collision and atom-wall collision effects [11]. For these issues there are three solutions: one is engineering the excitation of blue-detuned donut mode in Kagome lattice fibres which will keep the atoms away from the surface due to its repulsive behaviour. The second solution is to use HC-PCF with large core size because it reduces the effect of dephasing due to atom-wall interaction. The third one is coating the inner wall of the hollow-core with coating material through a chemical deposition. Moreover, the coating materials used on the inner core wall can be transparency at desired spectral range operation and the coating deposition thickness can be less than 100 nm in order to not affect the optical guidance properties. For that, we choose to coat our fibre with coating materials which have a low dielectric constants, low surface absorption energy, low out gassing rates and low reaction ratios. The PDMS and Aluminosilicate (Sol-Gel) were identified as suitable materials for atomic vapor applications. In this section we will report on the fibre baking process, coating material synthesis and on the process of the fibre inner-wall coating. Several HC-PCFs with Aluminosilicate (Sol-Gel) and PDMS coated and uncoated core have been put in a high vacuum system for rubidium loading and for spectroscopy experiments.

3.4.1 Fibre baking

Before filling the fibre with a coating, the first and very important stage is to remove the contamination, impurities, water and other bulk gasses from the core of fibres, deposited during the fabrication process, which can create problem of degassing for ultra-high vacuum environment [11]. To do this, one end of the fibre is attached to gas chamber filled with high purity argon or nitrogen, typically at ~5 bar. The fibre is heated to 120 °C, which is the limit for coating of fibre, to ensure the vaporization of water, and other impurities removed by the gas flow through the fibre.

3.4.2 Fibre coating

3.4.2.1 Coating materials

We used two surface coating materials for the set of fibres, made in collaboration with laboratory SPCTS of European ceramic centre at Limoges. The first one is Polydimethylsiloxane (PDMS) [12] and the second is Aluminosilicated Sol-Gel.

To make the PDMS solution synthesis, 0.5% volume of silicon oil is diluted into diethyl ether. All of this must be done under controlled temperature to avoid the boiling point of solution at 35 °C. To ensure that the PDMS is uniformly dissolved in diethyl ether solvent, continuous stirring for 24 hours is done. Now the solution is ready. The process to fill HC-PCF is applied by the method as explained in the next section. The samples are dried at 80 °C for 24 hours. For the second solution, the Aluminosilicate (Sol-Gel) is synthesized by dissolute Aluminium nitrate hexahydrate [Al $(NO_3)_3$, ^9H_2O] in ethanol at room temperature. To get a uniform dissolution, stirring is done for half a day. Then slowly, 1.4 ml of tetraethoxysilane (TEOS) is added in transparent solution [13,14], storage solution contain Al/Si ratio = 2 and the metal concentration 0.8 mol. L^{-1}. In order to reduce the viscosity, the final solution is diluted in a 2% molar concentration of ethanol to metal concentration of 0.1 mol.L^{-1}. Similarly, pumping this solution into the hollow-core fibre is followed. The motivation of using this material is, its high corrosion resistance and low out-gassing rate. Table 3.3 shows the properties of surface coating materials.

Coating Materials	Activation Energy E_a (eV)	Dwell Time(ns) (T=20˚C)	Outgassing Rate (Torr $cm^{-3}cm^2/s$)	Refractive Index	ε_r
PDMS	***0.18 ± 0.01 [15]***	***1.3***	***10^{-4}***	***1.4***	***2.8 [20]***
Aluminosilicate	***0.28±0.04 [16]***	***4.4***	***10^{-13}[17]***	***1.54 [18,19]***	***4.5 [21]***

Table 3.3: Properties of surface coating materials

3.4.2.2 Coating procedure

For inner wall coating of our fibres, firstly HC-PCF's cladding structure is collapsed by using hot filament of fusion splicer (Model: Vytran GPX3000) so to leave the hollow core open. In this way, the hollow-core region of fibre is only filled with solution. Then,

the fibre is baked at 135 ˚C in oven containing vacuum for 4 hours to outgas the in-fibre potential contaminations. At the meantime, synthesized coating solution is prepared according to the procedures described in the section 3.4.2.1. The second step consists of chemical deposition of the coating material on the inner core wall surface (interface between core/clad). This process is very important and sensitive and takes long time. Thickness of coating and other parameters involve in this process have effect on the guidance of light through the fibres coated. Inner core wall surface of HC-PCF can be coated by uniformly depositing layers of required solution by following the procedure in Figure 3.17.

The end of the fibre with collapsed cladding prepared in first step is inserted in a vacuum chamber which is connected with a roughing pump and pressure gauge. The second end of fibre is placed in the coating solution. Now the fibre is evacuated by using vacuum pump. First it removes all the air and contamination from the core of fibre and other it creates vacuum inside the fibre core. After 2-5 minutes process, the hollow-core is completely filled depending on the length. The liquid droplets can be seen at the end of fibre by window fixed on the vacuum chamber. This coating deposition method is vast applicable to multi-types of coating materials which could be of interest for other HC-PCF applications. Coating properties depend slightly on the baking temperature and time taken by fibre to be dried. The fibre filled with PDMS solution is then placed in an air ambient oven heating at 80 °C for 24 hours. During this process, diethyl ether is evaporated from the diluted solution with chemical reaction in order to get a uniform layers of PDMS on inner core wall surface.

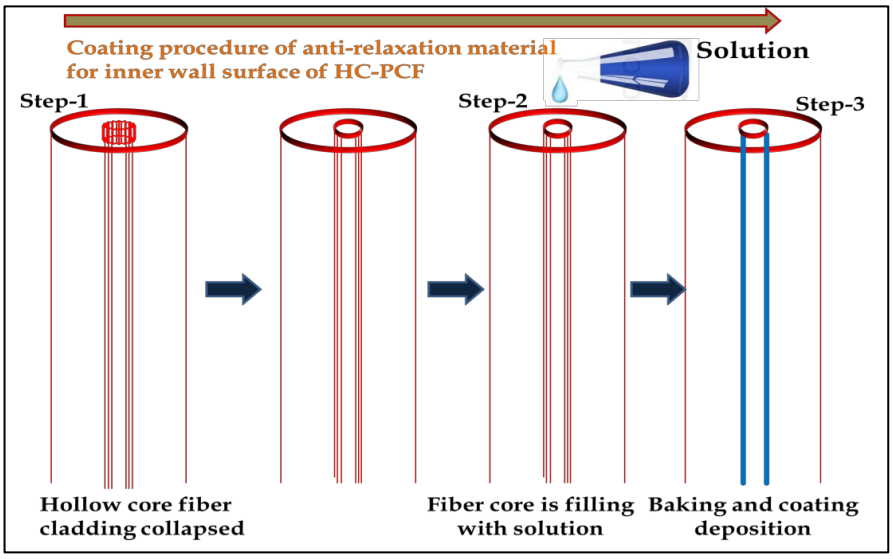

Figure 3.17: Illustration of coating procedure of the inner core wall surface of HC-PCF. In first step, cladding is collapsed, second step is about filling of solution and third step is for baking and coating deposition.

During the baking process, a more delicate process is used for deposition of Aluminosilicate (Sol-Gel). To remove the ethanol and to dry Aluminosilicate (Sol-Gel) solution, first the coated HC-PCF is placed under 80 °C in an air ambient oven for 24 hours as before. But after, fibre sample is baked at 600 °C for 5 hours with heating ramp 1 °C/min and finally stop to wait for a natural cooling. By this process, a thin Aluminosilicate (Sol-Gel) layer of 30 nm can be deposited on the inner core wall surface of fibre as shown in Figure 3.18.

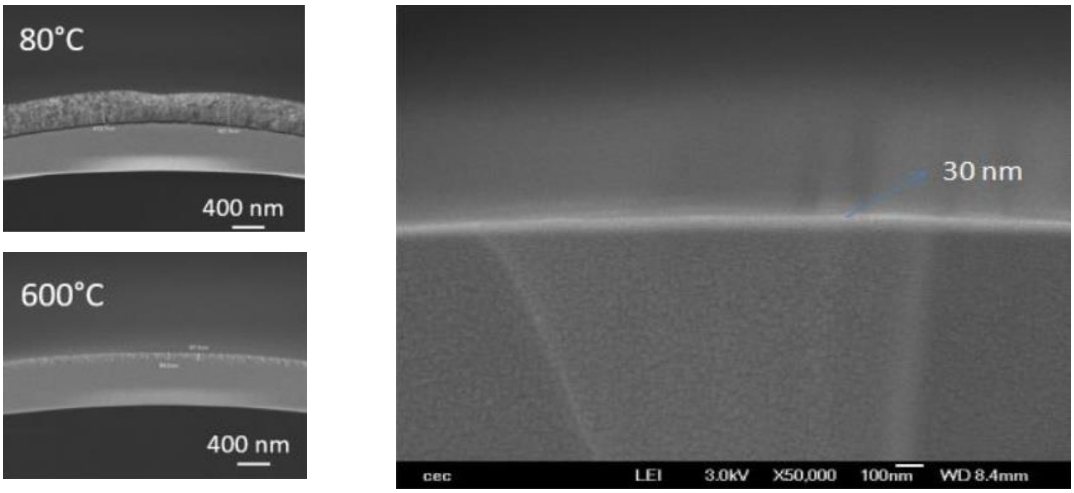

Figure 3.18: SEM images of deposition layer thickness obtained inside the HC-PCFs versus the drying temperature.

3.4.3 Characterization of coated HC-PCF

After coating the inner core wall surface of HC-PCFs with coating material, we characterized them to see the optical characteristics of the fibres after coating. Figure 3.19 shows the SEM images of uncoated HC-PCFs with different geometries. The table 3.4 summarizes the characteristics of uncoated HC-PCFs used for coating. We characterize the fibres optically by using a super continuum source coupled into the different kind of coated Kagome HC-PCF. For comparison, we added the transmission spectrum of coated Kagome HC-PCF to the uncoated Kagome HC-PCF with the same physical properties as reference (presented in Chapter 2).

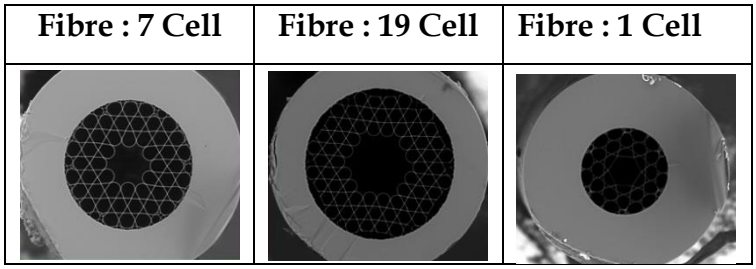

Figure 3.19: SEM images of uncoated HC-PCFs with different geometries.

Fiber	Curvature parameter (b)	D_{in} (µm)	MFD (µm)	Loss (dB/Km)
7 cell	0.90	58	45	200
19 cell	0.98	82	64	250
1 cell	-	42	32	150

Table 3.4: Characteristics of fibres shown in figure 3.16.

Figure 3.20 presents a typical transmission spectra for Aluminosilicate (Sol-Gel) coated and uncoated (a) and PDMS coated and uncoated (b) of 19 cell Kagome HC-PCFs (red curve is with coating and black is uncoated fibre) along with their near field images of uncoated and coated fibers. The light red, blue and gray bars show the wavelengths for red detuned, blue detuned and two photon ionization. The small difference of intensity level is attributed to the condition of light injection and length of fibres. The result shows a frequency shift by coating the inner wall surface

of fibre by a surface material. Red shifts in wavelengths for PDMS and Aluminosilicate (Sol-Gel) coating clearly appeared (red arrows). As example, for two 20 cm-long pieces (one PDMS coated and one uncoated – see Figure 3.20 (b)) a shift of 52 nm is measured which corresponds to an extra-increase of the silica thickness of 53 nm which is in good agreement with the measured PDMS thickness. To deduce this value, the following expression showing the spectral position where the fiber does not guide is implemented:

$$\lambda_m = \frac{2t}{m}\sqrt{n^2 - 1} \tag{3.2}$$

where n is the refractive index of the material, m the order of transmission band and t the silica thickness. Indeed, the spectra curve of fiber shows several transmission bands. Then if we consider the thickness of fiber before coating t_0, and t_c after coating, the difference between the thickness of two fibers will be simply the thickness of coating layer, given by the expression:

$$\Delta t = t_c - t_0 = \frac{m}{2}\frac{\Delta\lambda_m}{\sqrt{n^2-1}} \tag{3.3}$$

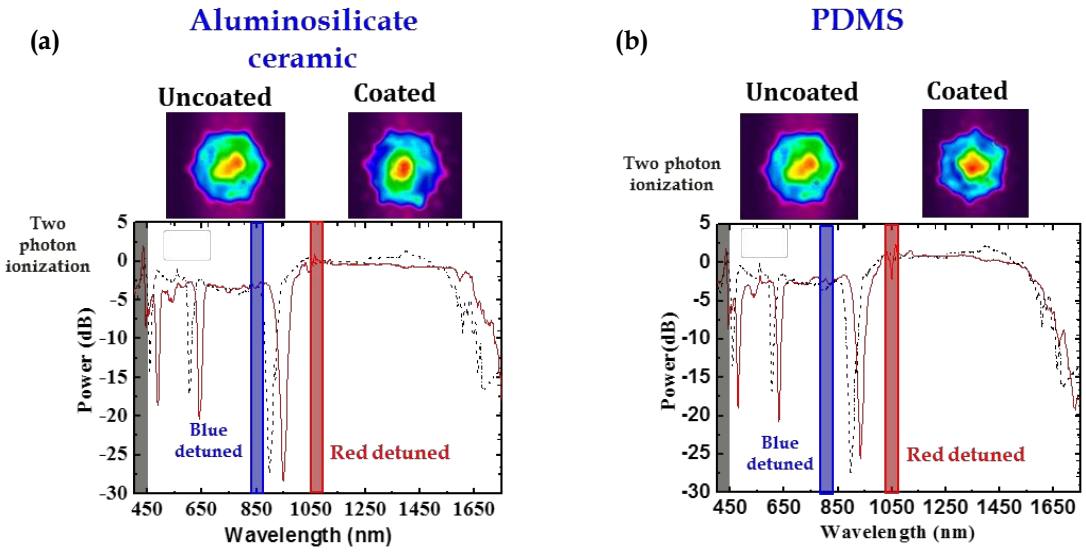

Figure 3.20: Transmission spectra of 19 cell Kagome HC-PCF. Red (solid) curve shows the spectrum with coating and black (dotted) without coating (a) Aluminosilicate ceramic (b) PDMS with their near field images. Light red, blue and gray bars show the wavelength for red detuned, blue detuned and two photon ionization.

Due to the coating thickness, the thickness of contour changes and as such transmission changes which means that the λ_m is shifted. We measured the shift from optical transmission spectra (Figure 3.20 (b)) and we found out for the second band (m=2) $\Delta\lambda \backsimeq$ 52 nm. As $n_{PDMS} \backsimeq n_g \backsimeq 1.40$, we can deduce the thickness of coating which is $\Delta t =$ 53 nm.

3.5 Ultra-high vacuum processing

3.5.1 Vacuum pumping and baking process

In order to produce a MOT with a suitable number of atoms and with a sufficient life time, the setup needs to be run at pressure of 10^{-9} Torr. This is achieved in three steps. First we pump the chamber with a roughing pump (Pfeiffer MVP 040-2 diaphragm pump). These both pumps are connected by relay switch which turn on automatically the turbo-molecular pump (Pfeiffer HiPace 80) when the pressure is down to 16.5 Torr. When the turbo-pump brings the pressure down to 10^{-7} Torr, we turn on the ion pump (Agilent VacIon 55 plus) by keeping the turbo-molecular pump switch on. The UHV pressure is monitored by a single vacuum gauge ATMION (VACOM). The advantage of this gauge is to measure pressure from atmospheric pressure to $7.6X10^{-11}$ Torr (in combination of Pirani and Bayard-Alpert systems). The most important part in achieving vacuum as low as possible (in our case 10^{-9} Torr) is to bake the UHV platform to accelerate the pump of foreign gases, particles and water vapors. Usually there are two procedures for baking the UHV chamber to avoid the contaminations which were embarked during fabrication, installation and putting vacuum compatible components (in our case we put in-vacuum components). First is wrap the whole system with heating tape or heating jackets and second is to put vacuum chamber inside a big oven, heat it up and pump the water vapors, dust and other gasses. As previously mentioned, the volume of chamber is too large to be baked in an oven. Consequently, we used heating tape (isopad T-7000) which is wrapped around the chamber and can provide temperature up to 450 °C. Notice that the whole system is covered with aluminium foil to reduce the conductance between the body of chamber and the outer atmosphere. The heating tape is provided with thermocouple and

attached with the body of chamber to control the temperature evolution. We used heat gun to bake other parts, like valves, tees, vacuum pumps. As the copper gaskets and wire seal copper gasket (top lid) annealed (softer). When we bake the chamber, the heat softens further the copper gasket and expands it. So all the screws are tightened during baking of chamber to seal more effectively the gap which is created due to an effect of heat on gaskets. Using this method, we achieved vacuum pressure around 2 X 10^{-9} Torr. This whole process of pumping and baking takes about three months.

In more detailed, initially we bake the chamber at low temperatures of 150-200 °C maximum for two-three days and then slowly increase the temperatures to 300 °C the next four-five days. Finally we redo a baking with lowest temperature like 7 °C and increase the temperature by a constant ramp of 75 °C/hour until to reach 450 °C. Figure 3.21 summarizes the measured baking temperature and pressure for the first five days. If we set 300 °C temperature as a reference, we can see that the pressure is decreasing from 1 4.67x10^{-7} Torr (day 1) down to to 9.24x10^{-8} Torr (day 5).

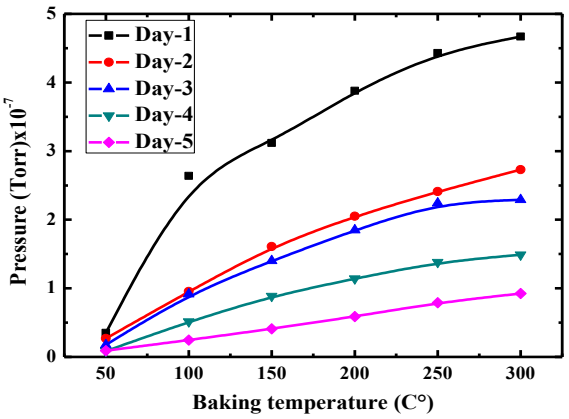

Figure 3.21: Evolution of the baking temperature and pressure for five days. This reflects the procedure used to bake our chamber until to get the minimum vacuum pressure.

This process is repeated until to get the lowest possible pressure which is achieved approximately in three months as illustrated in Figure 3.22.

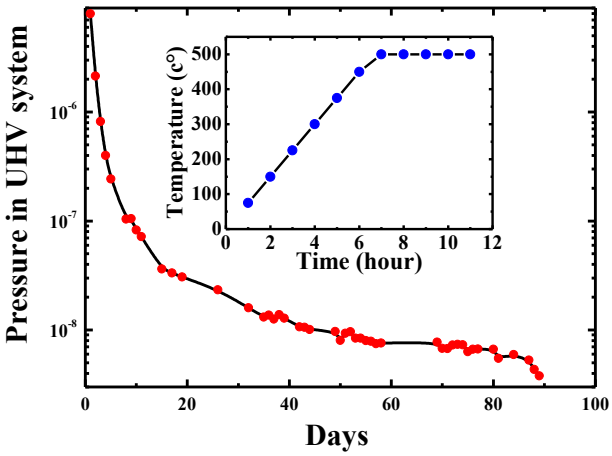

Figure 3.22: The comparison between the pressure and days took to be evacuated. Inset shows the baking procedure followed every day.

Notice that the reason to increase the temperature slowly to avoid thermal shocks, especially at the connectors and viewports. We stopped baking after 3 months because 10^{-9} Torr is enough to proceed with the experiments.

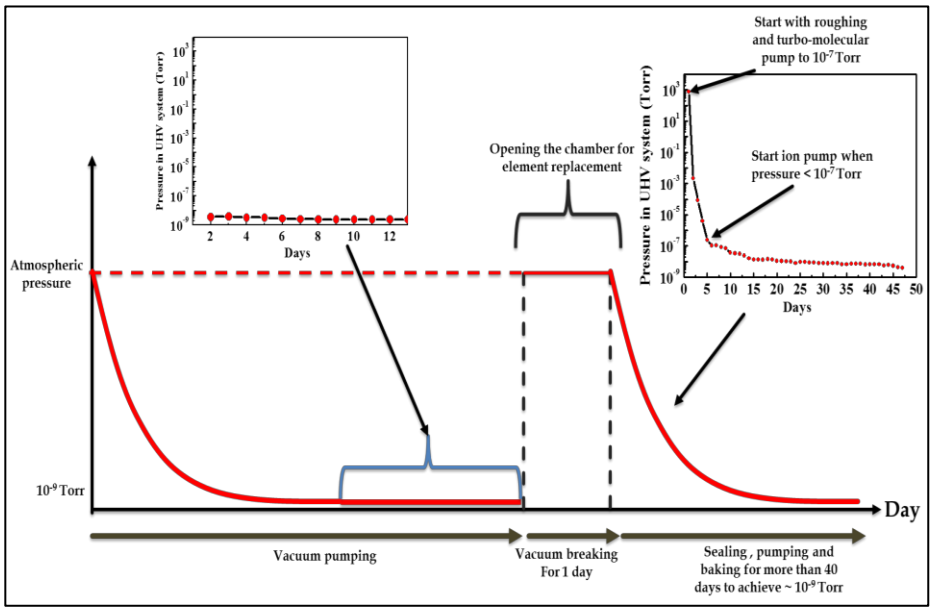

Figure 3.23: Sequence of sealing and unsealing the UHV chamber.

Figure 3.23 shows sequence of opening and closing the chamber. We open the chamber and break the vacuum whenever we have to do modifications inside the chamber like to change the getters or fibres. We finish this process of modifications with in one day. After sealing the chamber, we start to create the vacuum initially with roughing and turbo pump until we reach 10^{-7}. Then we start ion pump and bake the

chamber. We achieve the pressure as low as 10^{-9} in more than 40 days. We have broken the vacuum 4 times during my thesis.

3.6 Rubidium vapor loading in coated and uncoated Kagome HC-PCF

In this sub-section we will discuss about loading atoms into a micro-geometric hollow-core waveguide such as HC-PCF which is quite challenging. Indeed, in addition to the vacuum chamber volume, the geometry of the core size combined with ultra-high operation pressure does not lid an easy loading process into the HC-PCF. Moreover the highly reactive Alkali atoms with the surface will limit the lifetime of Rb atom inside the HC-PCF. For that reason, the Rb atom is released in the UHV chamber few days before to achieve a stable pressure below 2×10^{-8} Torr. Ten Kagome HC-PCFs with ~ 10 cm length are inserted inside the chamber (1 cell, 7 cell and 19 cell, uncoated and coated (Aluminosilicate (Sol-Gel) and PDMS), nine Kagome HC-PCFs plus one new tubular uncoated HC-PCF). The stable pressure without the Rb inside the chamber is 2.45 10^{-9} Torr. The current used for the Rb dispenser is 6.8 A. The used setup for the measurement of absorption line in different fibres is shown in Figure 3.24.

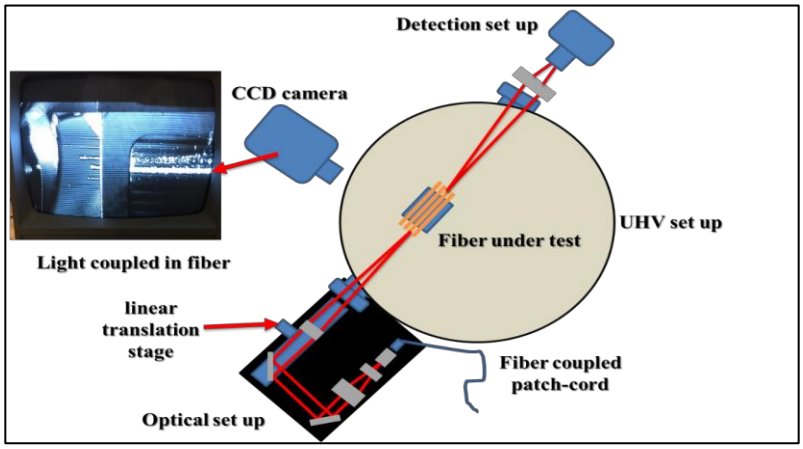

Figure 3.24: Optical setup for the measurement of the absorption spectrum of under test fibres inside the chamber.

The Rb absorption lines for both ^{87}Rb and ^{85}Rb D_2 contrast in vacuum, uncoated, Aluminosilicate (Sol-Gel) and PDMS coated for different Kagome HC-PCF are illustrated in Figure 3.25. The results show that the best contrast of the Rb absorption

line is obtained for the coated Kagome HC-PCF (Aluminosilicate (Sol-Gel) and PDMS) compared to the uncoated one, which indicate that the coating plays its role to better maintain Rb atoms inside the hollow-core by reducing the physio-chemical interaction between Rb atoms and the wall of fibres.

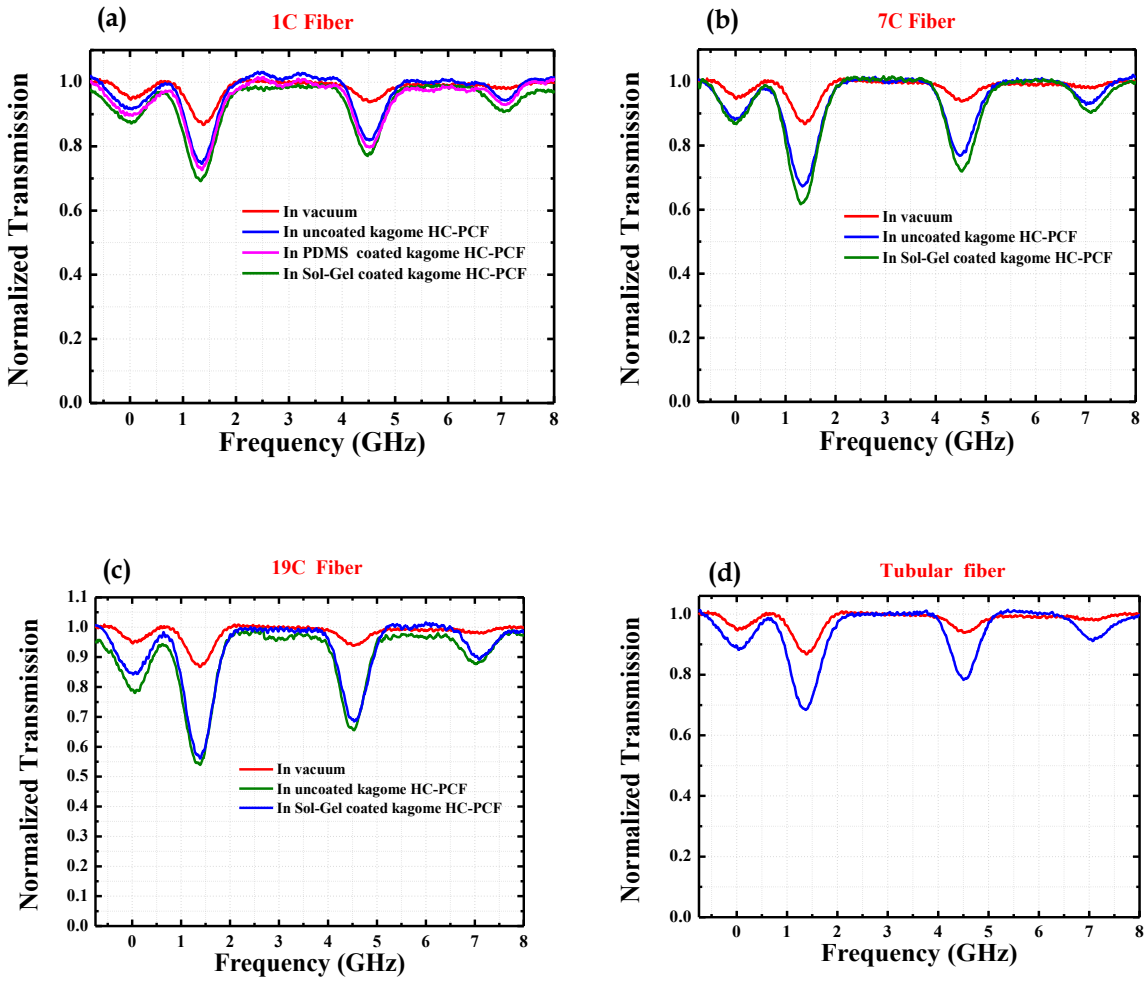

Figure 3.25: Measured Rb D_2 absorption lines of Rb vapor contained in under test Kagome HC-PCFs (a) 1 cell (b) 7 Cell (c) 19 Cell (d) tubular fibres and vacuum chamber. In vacuum (red solid line) for reference, in PDMS coated Kagome HC-PCF (magenta solid line), in sol-gel coated Kagome HC-PCF (olive solid line) and in uncoated Kagome HC-PCF (blue solid line).

To confirm this result we switched off the Rb dispenser to investigate the Rb lifetime inside the different fibres. In the Figure 3.26, the absorption contrasts decay in HC-PCFs is plotted. The results indicate that the absorption contrast dropped exponentially down to few percent during the first 15 s.

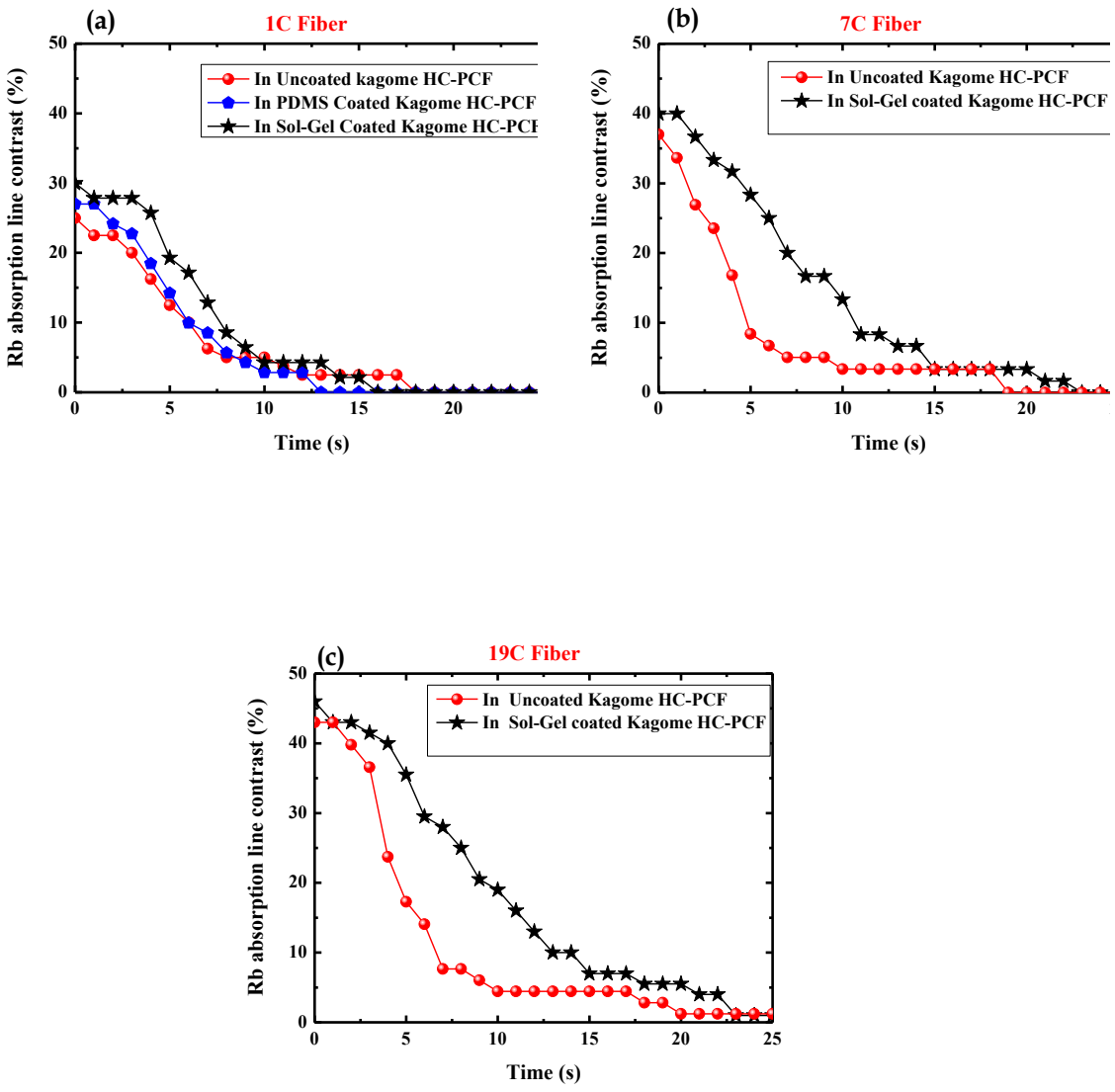

Figure 3.26: Evolution of Rb absorption contrast in under test Kagome HC-PCFs (a) 1 cell (b) 7 Cell (c) 19 Cell uncoated Kagome HC-PCF fibre (red dots), sol-gel coated Kagome HC-PCF (black dots) and PDMS coated Kagome HC-PCF (blue dots).

Then, the absorption contrast drops slowly over 10 s. In comparison, the contrast for the case of Aluminisilictae (Sol-Gel) coated HC-PCF decay slowly than the other cases. This indicates that the Aluminosilicate (Sol-Gel) coating reduced more the reaction rate as expected. In conclusion, the experimental measurements demonstrate that Rb atoms can be loaded inside different under test fibres despite the large volume of the vacuum chamber and more maintained in the coated HC-PCFs due to the reduction of atom-surface reaction.

3.7 Summary

In this chapter we described in detail the design, assembly and installation of UHV chamber and its components (in- and outside of chamber). Also the design of anti-Helmholtz coils, its role in cooling and trapping of neutral atoms and fibres holder are presented. On the basis of spectroscopic studies inside the HC-PCFs will straighten the route towards in-fibre laser cooling and Rb filled photonic micro cell (PMC). This study will help in the selection of suitable HC-PCF for two main goals, as mentioned above. We also reported about the procedure from preparation of coating solution to resulted coated fibres. Vacuum pumping and baking of chamber is important to have vacuum as low as possible, it is also explained in details. Finally we presented the absorption spectra of thermal Rb atoms loaded in different coated, uncoated fibres, their comparison with absorption spectra via background Rb atoms inside the chamber and the life time of Rb atoms inside the fibres.

References:

1- *"Atomic polarization relaxation time measurement of Rb filled hypocycloidal core shape Kagome HC-PCF"* **T. D. Bradley, J.J. McFerran, J. Jouin, P. Thomas, E. Illinova & F. Benabid**, CLEO 2013, CM3I.8

2- "*Lamb-Dicke spectroscopy of atoms in a hollow-core photonic crystal fiber.*" **S. Okaba, T. Takano, F. Benabid, T. Bradley, L. Vincetti, Z. Maizelis, V. Yampol'skii, F. Nori and H. Katori,** Nat. Comm., vol. 5, p. 4096, (2014).

3- *"Quantum vacuum experiments using high intensity lasers",* **M. Marklund and J. Lundin,** The Eur. Phys. Jour. D, vol.55, pp. 319, (2009)**.**

4- *"Trapping atoms using nanoscale quantum vacuum forces",* **D. E. Chang, K. Sinha, J. M. Taylor & H. J. Kimble,** Nat. Commun., vol. 5: pp. 4343, (2014).

5- *"Linear and nonlinear optical properties of hollow-core photonic crystal fiber",* Invited Topical Review, **F. Benabid and P.J. Roberts,** Journal of Modern Optics, vol. 58, No. 2, pp.87–124, (2011)

6- *"Laser-cooled atoms inside a hollow-core photonic-crystal fiber"*, **M. Bajcsy, S. Hofferberth, T. Peyronel, V. Balic, Q. Liang, A. S. Zibrov, V. Vuletic, and M. D. Lukin,** Phys. Rev. A vol. 83, 063830, (2011)

7- *"Alkali metal dispensers"* **SAES getters**

8- *"Fast loading of a magneto-optical trap from a pulsed thermal source"*, **J. Fortagh, A. Grossmann, T. W. Hansch, and C. Zimmermann**, J. Appl. Phys. vol. 84, pp. 6499, (1988).

9- *"Loading of a Rb magneto-optic trap from a getter source",* **U. D. Rapol, A. Wasan, and V. Natarajan**, Phys. Rev. A, vol. 64, 023402, (2001).

10- *"Trapping of neutral sodium atoms with radiation pressure".* **E.L.Raab, M. Prentiss, A.Cable, S.Chu and D.Pritchard**, Phys. Rev. Lett. Vol. 59, 2631, (1987)

11- "*Electromagnetically induced transparency in Rb-filled coated hollow-core photonic crystal fiber*" **P. S. Light, F. Benabid, and F. Couny,** Opt. Lett., vol. 32, No. 10, p. 1323-1325, (2007).

12- "*Characterization of polydimethylsiloxane (PDMS) properties for biomedical micro/nanosystems*"**, A. Mata, A. J. Fleischman, and S. Roy,** Biomed. Microdevices, vol. 7, no. 4, pp. 281–293, (2005).

13- "*Physical properties of sol-gel coatings*"**, J. D. Mackenzie and E. P. Bescher,** J. Sol-Gel Sci. Technol., vol. 19, pp. 23-29, (2000).

14- "*Corrosion resistance of stainless steel coated with sol–gel silica*", **D. C. Vasconcelos, J. A. . Carvalho, M. Mantel, and W. Vasconcelos,** J. Non. Cryst. Solids, vol. 273, no. 1–3, pp. 135–139, (2000).

15- "*Kinetics of the fusion of drops of polydimethylsiloxane on solid surfaces*", **Arslanov V V, Ogarev VA, Izvestiya** ,Akademi Nauk SSSR. Vol. 8, pp. 1795–9, (1974).

16- "*Aluminosilicate surface energy and its evolution upon adsorption using dielectric relaxation spectroscopy*", **Giuntini J. C, Douillard J. M, Maurin G., Devautour-Vinot S, Nicolas A., Henn F**. Chemical Phys. Lett. vol. 423, pp. 71–5, (2006).

17- "*The ultimate vacuum.*" , **Redhead**, **P. A**. Vacuum, vol. 53, pp. 137-149, (1999).

18- "*Refractive Index of Several Glasses as a Function of Wavelength and Temperature*", **Farrell R.A., Neu J.T**., J. Opt. Soc. America., vol. 59 pp; 774–6, (1969).

19- "*Structural and Optical Properties of Sol-Gel Derived Aluminosilicate Planar Waveguides Doped with Er3+ Ions*" ,**Benatsou M, Capoen B, Bouazaoui. M**., **W. Tchana, Vilcot. J. P**., J. Sol-Gel Sci. and Tech., vol. 13, pp. 529–33, (1998).

20- "*Poly (dimethylsiloxane).*" , **Kuo, Alex C.M.**, Polymer data handbook, pp. 411-435, (1999).

21- "*Investigation of alumina–silica films deposited by pulsed injection metal–organic chemical vapour deposition.*", **T. Arunas, *et al.*** Thin solid films, vol. 515, pp. 1830-1834, (2006).

22- "*Inhibited coupling guiding hollow fibers for label-free DNA detection*", **F. Giovanardi, A. Cucinanotta, and L. Vincetti,** Opt. Express, vol. 25, No. 21, pp. 26215-26220, (2017).

Chapter 4

Laser platform for MOT and in fibre laser cooling

This chapter reports on the laser system part of the "in-fibre laser cooling" platform. The laser system comprises several lasers dedicated to cooling, repumping for magneto-optical trap generation, to cold and thermal rubidium atom guidance and spectroscopy inside hollow-core photonic crystal fibres. At this stage of our work, we have implemented laser architecture for cooling and repumping. This dual frequency laser is frequency stabilized using frequency modulation (FM) spectroscopy technique. A further required work in implementing the lasers for the atom guidance and for spectroscopy is outlined.

4.1 Introduction

Towards the realization of our platform for in-fibre laser cooling, the second objective after setting up the UVH system is to build the laser system dedicated to cool, trap, and guide to undertake spectroscopy measurements of both isotopes of rubidium atoms in cold and thermal phase. The system comprises three main lasers that cover the above functionalities. At this stage of our work, we have implemented a laser architecture for cooling and repumping [1]. In this dual frequency laser, the frequency is stabilized using frequency modulation spectroscopy (FMS), which is adaptation of Pound-Drever-Hall (PDH) [2] method to absorption lines. A further required work in implementing the lasers for the atom guidance and for spectroscopy is outlined. This chapter is structured as follow. We start with giving an overview of the laser system for in-fibre laser cooling platform. In the following section, we give a reminder of the energy structure of both isotopes rubidium atom with an emphasis to identify the working wavelengths. After, we will describe the characteristics of our laser system for Magneto-Optical Trap (MOT) [1] such as its optical power, spectral content, linewidth, and frequency stability. Finally, we will give details about the guiding and cooling lasers to carry out the in-fibre laser cooling.

4.2 Description of "in-fibre laser cooling" lasers system requirements

At this step of my thesis, the aim is to create a self-contained and as versatile as possible lasers system for cooling, trapping and guidance of thermal and cold rubidium atoms. The laser system designed for our platform "in-fibre laser cooling" depends on the atom resonances and hence on its electronic structure. For that, the laser system is tailored for both isotopes of rubidium atoms. Figure 4.1 gives an

overview of the laser system chosen for the platform. Four different laser frequencies are used for cooling, repumping and guiding the Rb atoms. Laser 1 is set for MOT generation; laser 2 has a frequency blue-detuned from Rb cooling resonance for transverse trapping and guidance. Laser 3 has a far red-detuned frequency from resonance, and is set for longitudinal guidance and to create a trapping optical lattice for atoms inside the HC-PCF.

Commonly two independent lasers are used for cooling and repumping, but in our platform one single laser was used to generate both frequencies (laser 1: more details will be given after in section 4.3.2). The cooling process of Rb through the Doppler scheme uses the resonance F → F′ of the D2 line ($5^2S_{1/2}$ (F) → $5^2P_{3/2}$(F′)). For the case of both Rb isotopes, one requires a laser operating near 780 nm and detuned on red side in frequency in the range of 2Γ, where Γ is natural linewidth of transition [3]. The red arrow 1 (Figure 4.1) represents the cooling line which excites the population from $5^2S_{1/2}$ (F =3) → $5^2P_{3/2}$(F′ = 4) for ^{85}Rb and $5^2S_{1/2}$ (F =2) → $5^2P_{3/2}$(F′ = 3) for ^{87}Rb (see Figure 4.1: energy levels of ^{85}Rb and ^{87} Rb). The repumping process has the function of exciting the atoms which are relaxed to a different state from the ground state of the cooling transition back to the cooling transition cycle. This process is fulfilled by a laser illustrated by the orange arrow 1 of (Figure. 4.1). The repumping laser excites the population from $5^2S_{1/2}$ (F =2) → $5^2P_{3/2}$(F′ = 3) for ^{85}Rb and $5^2S_{1/2}$ (F =1) → $5^2P_{3/2}$(F′ = 2) for ^{87}Rb. In our case, both cooling and repumping wavelengths are generated from laser 1 by generating sidebands using an electro-optic phase modulator (EOM) at specific frequencies shift of both isotopes (here the frequency modulation is ν_{m_1}= 3.036 GHz for ^{85}Rb and ν_{m_2}=6.835 GHz for ^{87}Rb). For the MOT we need narrow linewidth and also an ultra-stable laser. In order to achieve the required stability, the laser 1 was stabilized using saturated absorption spectroscopy of Rb and Pound-Drever Hall (PDH) laser locking method [2]. This laser configuration has the advantage that cooling and repumping beams

are stabilized simultaneously, along with the fact that they are intrinsically collinear, which reduces the alignment difficulty. Details about the cooling and repumping laser frequencies stabilization are provided in sections 4.4.

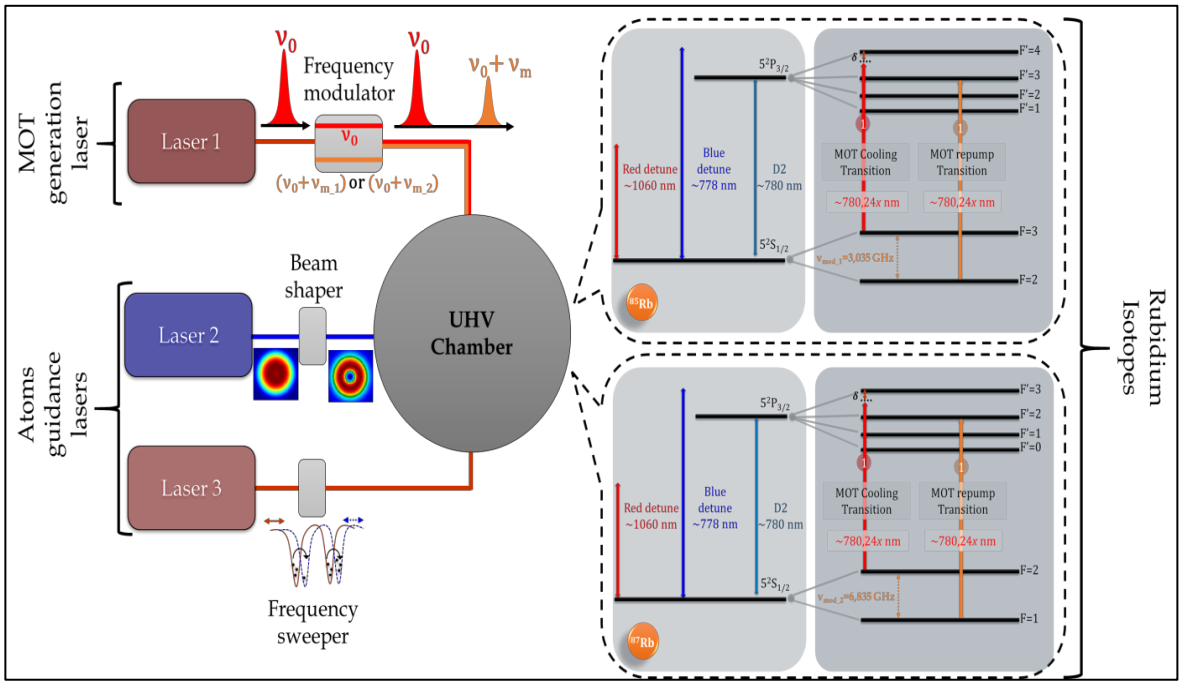

Figure 4.1: Overview of the laser system setup for in fibre laser cooling experiment.

For guidance and cooling atoms inside the HC-PCF, we will use two lasers (laser 2 and laser 3 in Figure 4.1). The first laser for guidance is a blue-detuned laser labeled 2 (Toptica-DL Pro grating stabilized tunable single mode diode laser) slightly detuned from the resonance and has been tested to couple into the HC-PCFs which are inside the vacuum and got absorption signal of thermal Rb atoms (see Chapter 3). This laser, in future, will be used to guide the atoms in transverse direction also for transverse trapping. For blue-detuned atomic guidance in HC-PCF, a hollow beam (or a donut shaped) is needed to keep the atoms trapped in transverse direction. The hollow shape of beam can be obtained by using a beam shaper like S-wave plate or spatial light modulator (SLM) or with fiber Bragg gratings so to

selectively excite appropriate guidance mode in the fibre (see Chapter 2). The second laser for guidance is far red-detuned laser labeled 3 (Yb laser amplifier seeded with a Toptica- DL 100 Pro grating stabilized tunable single mode diode laser) and would be used to create optical lattices and to cool atoms in longitudinal direction. Table 4.1 gives some important specifications about lasers for cooling/trapping for MOT, guidance/cooling inside the fibre. All lasers are continuous wave (CW) with different wavelengths. Laser 1 for MOT is fibre laser and has wavelength tuning range between 780.23 ~ 780.25 nm. Blue-detuned laser 2, illustrated with navy blue arrow in Figure 4.1. The laser is tunable over a range of about 30 nm from 765nm to 795 nm, and has a maximum power about 80 mW. The laser is set to be slightly blue-detuned from the resonance line of Rb. The far red-detuned laser 3 also operates over a large wavelength range, and its power can be as large as 50 W. The laser is a Yb amplifier with seed laser operating in the wavelength range of 1045 - 1085 nm. The laser, schematically shown in dark red arrow in Figure 4.1, will be used for different purposes. The laser will be used for atom guiding and optical lattice generating. The lattice will be used for cold atom loading into a HC-PCF but also as an optical lattice trap for in-fibre atoms.

Laser (C.W)	Function	Central wavelength (nm)	Tuning range(nm)	Beam profile
Fibre	**Cooling**	**780.24**	**780.23 ~ 780.25**	**Gaussian**
Fibre	**Repumping**	**780.24**	**780.23 ~ 780.25**	**Gaussian**
Tunable diode	**Red-detuned guidance/cooling**	**1065**	**1045 ~ 1085**	**Gaussian**
Tunable diode	**Blue-detuned guidance/cooling**	**780.24**	**765 ~ 795**	**Gaussian**

Table 4.1 Specifications of lasers for in fibre laser cooling platform.

4.3 Cooling and repumping laser system

4.3.1 Rubidium energy structure

Because the experimental platform is designed for rubidium atom, we recall here its electronic energy structure and the working wavelengths of the platform laser system. The Rubidium exists as two natural isotopes, ^{85}Rb and ^{87}Rb. The two isotopes differ in their nuclear spin, which is manifest in their difference in hyper fine splitting. The natural abundance of the two isotopes are 72.2% for ^{85}Rb, where the nuclear spin quantum number is I=5/2, and 27.8% for ^{87}Rb where I=3/2. The energy levels of both ^{85}Rb and ^{87}Rb are illustrated by the Figures 4.2 and 4.3 respectively. The rubidium has a single electron $5s^1$ in its outermost shell, which becomes $5p^1$ for the first excited state. The orbital-spin interaction states with different "J" values to have different energies and creates a fine structure splitting of the p-orbital doublet 5P. For ^{85}Rb and ^{87}Rb the D-lines are: D1 line is ($5^2S_{1/2}$ ➔ $5^2P_{1/2}$) transition at ~795 nm and D2 line is ($5^2S_{1/2}$ ➔ $5^2P_{3/2}$) transition at ~780 nm. The energy structure difference between the two atoms appear at the hyper fine level caused by the nuclear spin coupling with the electron's magnetic and electric momenta. In our experiments for the MOT we will use the $5P_{3/2}$ excited state while the lower $5P_{1/2}$ level at 795 nm is beyond the tuning range of our laser system.

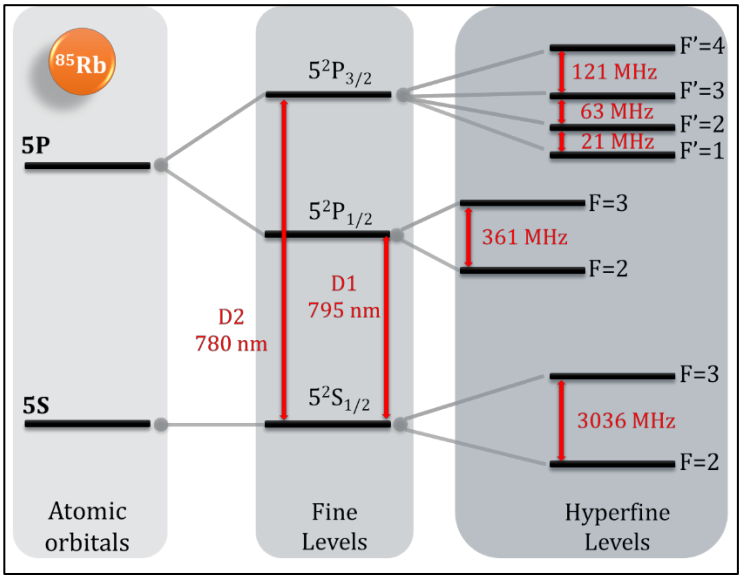

Figure 4.2: Energy levels of ^{85}Rb split from the 'two level atom' with fine and hyperfine levels. The picture involved the D1 and D2 transitions, labeled with their F values. The figure is not drawn to scale but each hyperfine splitting frequency is identified, as well as the fine structure transition at 795 nm (377 THz) and 780 nm (384 THz). The hyperfine level separations are also illustrated.

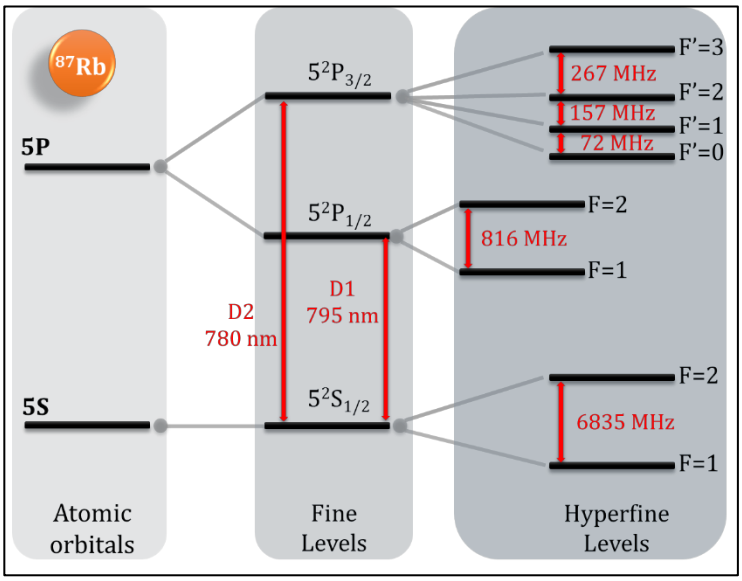

Figure 4.3: Energy levels of ^{87}Rb split from the 'two level atom' with fine and hyperfine levels. The picture involved the D1 and D2 transitions, labeled with their F values. The figure is not drawn to scale but each hyperfine splitting frequency is identified, as well as the fine structure transition at 795 nm (377 THz) and 780 nm (384 THz). The hyperfine level separations are also illustrated.

The difference in nuclear spin of 5/2 in ^{85}Rb and 3/2 in ^{87}Rb causes the hyper fine level splitting for the two isotopes and so leading to different total angular momentum values, where F is given by F = I + J, as shown in the right of Figures 4.2 and 4.3. For example, for ^{87}Rb I = 3/2, in the ground state J = 1/2 we have F = 1 or F = 2. For the $5^2P_{3/2}$ excited state J = 3/2, F′ can take the following values: 0, 1, 2, or 3. Table 4.2 gives the energy shift of the hyperfine levels of the ground and excited state of the D2 transitions in ^{85}Rb and table 4.3 for ^{87}Rb. The hyperfine splitting and differences are shown in Figure 4.2 for ^{85}Rb and Figure 4.3 for ^{87}Rb. ^{87}Rb shows a wider spread of excited state hyper fine levels of ~ 500 MHz between the top and bottom F′ levels, on the scale of the Doppler broadening at room temperature, compared with a difference of only ~ 200 MHz for ^{85}Rb. The ground state hyper fine splitting is around 3.036 GHz for ^{85}Rb and 6.835 GHz for ^{87}Rb. The permitted transitions between hyperfine ground states and excited states have a momentum change ΔJ = 0, ±1 as dictated by quantum selection rule [4].

Fine level	Hyperfine level	Energy shift / MHz
$5^2S_{1/2}$	F=2 F=3	-1771 +1265
$5^2P_{3/2}$	F′=1 F′=2 F′=3 F′=4	-113.81 -83.867 -20.486 100.254

Table 4.2: Energy shift for ^{85}Rb.

Fine level	Hyperfine level	Energy shift / MHz
$5^2S_{1/2}$	F=1 F=2	-4271.676632 2563.005979
$5^2P_{3/2}$	F′=0 F′=1 F′=2 F′=3	-302.07375 -229.85175 -072.91125 193.74075

Table 4.3: Energy shift for ^{87}Rb.

Figure 4.4 shows the relevant possible transitions for ^{85}Rb and ^{87}Rb MOTs and approximate wavelengths. Cooling Rb using the Doppler scheme, can be done using the resonance F=3→ F′=2, 3, 4 states for ^{85}Rb or F=2→ F′=1, 2, 3 states for ^{87}Rb of the D2

line (see red arrow 1, 2 and 3 in Figure 4.4). Ideally, the atoms recover their initial fundamental state after spontaneous emission in order to be excited again and so on and this is called the cycling transition. But unfortunately, about one excitation out of one thousand will cause the atom to decay to the F=1 state instead of the F=2 state for ^{87}Rb and to F=2 instead of the F=3 state for ^{85}Rb. This takes the atom out of the cooling resonance. In this case, another laser (called the "repumping laser") is needed to excite the atom from the F=2→ F'=1, 2, 3 state for ^{85}Rb or F=1→ F'=0, 1, 2 state for ^{87}Rb, from which it can decay back to the F=3 state for ^{85}Rb or to the F=2 state for ^{87}Rb, where it will again be excited by the cooling laser (see orange arrow 1, 2 and 3 in Figure 4.4).

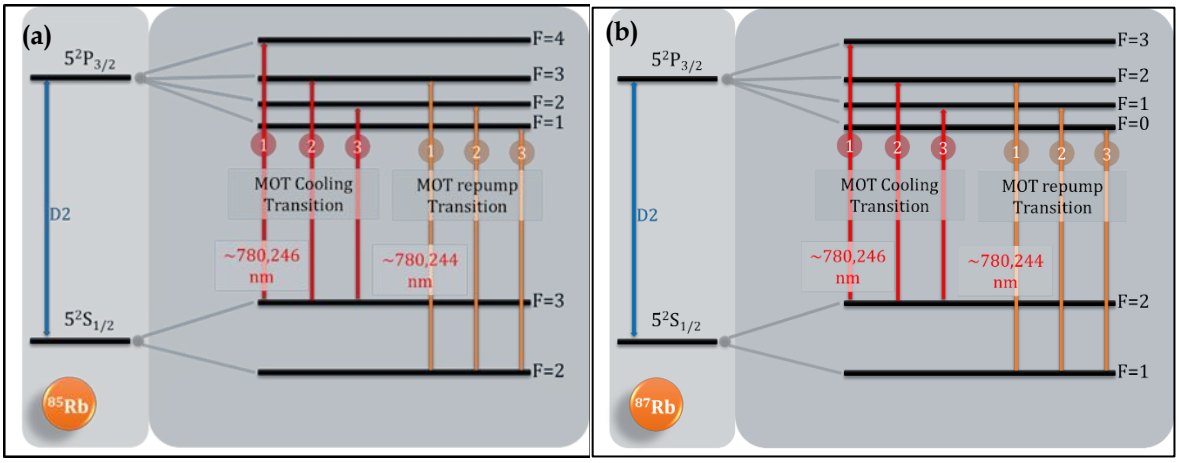

Figure 4.4: The possible cooling and re-pumping transitions for (a) ^{85}Rb and (b) ^{87}Rb for MOTs and approximate wavelengths.

4.3.2 Cooling and repumping laser

For cooling and repumping in our experiment, we used EYLSA-L-780.24-1.0-P-SN-M-FC from Quantel laser which has center wavelength at 780.240 nm. It is a high power single-mode fibre laser system operating at 780 nm. It provides up to 1 W of linearly polarized output power at 780 nm, with a diffraction limited Gaussian beam and <200 kHz linewidth with typical coarse tuning of 10 GHz with temperature and fine tuning of 1 GHz with current. The power provided is enough to demonstrate cooling and trapping for two MOTs because the saturation intensities for Rb^{85} and

Rb^{87} are 1.669 32(35) mW/cm² and 1.669(2) mW/cm² respectively. An external optical isolator is used (to avoid the reflected beam to go back in cavity), which let out around 70% of total power.

The general architecture of frequency doubled Er fiber laser (EYLSA) is depicted in Figure 4.5. We explore this architecture to generate the required two optical frequencies for cooling and repumping from this laser. The dual spectral component laser is achieved as follows. The field from the seed laser to be amplified is written as:

$$E_1 = E_0 e^{i\omega_0 t} \tag{4.1}$$

Where ω_0 is the frequency of the carrier signal at 1560 nm and E_0 is the amplitude [5]. This signal is sent to an Electro-Optic Modulator (from Photline (MPZ-LN-10)) to generate sideband frequencies for repumping laser for both isotopes of rubidium.

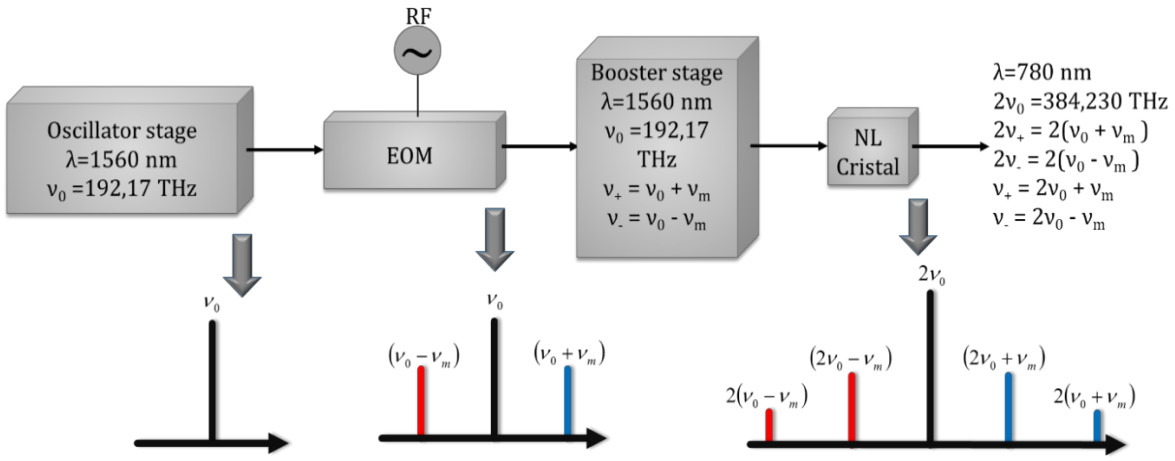

Figure 4.5: EYLSA laser architecture.

The EOM has a maximum optical input power about 20 dBm and modulation voltage range from -20 to +20 V. The operating wavelength of EOM is 1530 ~1625 nm. The bandwidth of EOM is 12 GHz which covers the both isotopes hyperfine transition, and thus the generated sidebands can be used a repumping laser. EOM is driven by a high quality factor frequency synthesizer having bandwidth 2 ~ 8

GHz. The synthesizer signal can be attenuated by a resonant attenuator. We use two attenuators; the first is resonant at ~3.04 GHz for ^{85}Rb, and the second is resonant at ~6.83 GHz for ^{87}Rb. The attenuator is used to adjust the power of the repumping laser. After passing through the EOM, the field spectrum shows the carrier frequency (frequency $\nu_0=\omega_0/2\pi$ and amplitude E_0) with two sidebands at a shifted frequency $\nu_{m=}{}^{\pm\Omega}/_{2\pi}$. Here the higher order sidebands are too small to be considered. The resulting signal becomes:

$$E_2 = E_0\, e^{i\omega_0 t} \sum_{n=-\infty}^{+\infty} J_n(\beta) e^{in\Omega t} \tag{4.2}$$

$$E_2 = \left[J_0(\beta)E_0 e^{i\omega_0 t} + J_1(\beta)E_0 e^{i(\omega_0+\Omega)t} - J_1(\beta)E_0 e^{i(\omega_0-\Omega)t}\right] \tag{4.3}$$

Where $J_n(\beta)$ is the Bessel function of order n and β the modulation depth [2]. This signal is then composed by a carrier frequency with sidebands equally spaced (by the modulation frequency) whose amplitude depends on J_n, and is controlled with the resonant attenuators.

The modulated optical field is then amplified with an Er fibre amplifier, and sent to a frequency doubling crystal to generate the required wavelength corresponding to the transition lines of both Rb isotopes at ~780 nm. The crystal exhibits a second order susceptibility and thus the resulting nonlinear polarization is of the form:

$$P^2 = \varepsilon_0 \chi^2 E_2^2 \tag{4.4}$$

where χ^2 is the second order nonlinear optical susceptibility and ε_0 is the permittivity of free space[2]. Substituting equation (4.3) in equation (4.4) we obtain:

$$P^2 = \chi^2\left[\left(J_0^2(\beta) - 2\,J_1(\beta)\right)E_0^2 e^{2i\omega_0 t} + J_1^2(\beta)E_0^2 e^{2i(\omega_0+\Omega)t} + J_1^2(\beta)E_0^2 e^{2i(\omega_0-\Omega)t} + 2J_0(\beta)\,J_1(\beta)E_0^2 e^{i(2\omega_0+\Omega)t} - 2J_0(\beta)\,J_1(\beta)E_0^2 e^{i(2\omega_0-\Omega)t}\right] \tag{4.5}$$

Here, we can see that the nonlinear crystal modulates the field at several frequencies. In addition to the doubling the carrier frequency, $2\omega_0$, we have two

sidebands at $2\omega_0 \pm 2\Omega$ corresponding to the frequency doubling of E_2 sidebands, two sidebands at $2\omega_0 \pm \Omega$ corresponding to the frequency sum and difference between central frequency and the first order sideband. For a small modulation depth, the intensity of the field at $2\omega_0 \pm 2\Omega$ is negligible. Indeed, the relative intensities of sidebands at $2\omega_0 \pm 2\Omega$ and at $2\omega_0 \pm \Omega$ are respectively equal to $J_1^2(\beta)$ and $2J_0(\beta)\,J_1(\beta)$. The spectrum of the 780 nm laser is thus mainly composed of one central peak and two sidebands at $2\omega_0 \pm \Omega$ as shown in Figure 4.6. The main peak at $2\omega_0$ is tuned to the target cooling transition and the blue-shifted sideband, $2\omega_0+\Omega$, is used for repumping. The other higher-order sidebands are too small and well out of resonance to affect the laser cooling and the trapping. We should also point out that the intensity of the repumping laser can be controlled easily with the amplitude of the microwave modulation.

Figure 4.7 shows the measured RF spectra of the both sidebands at the output of laser for repumping of ^{85}Rb and ^{87}Rb. In these spectra, the resonant attenuator and the EOM modulation depth was adjusted so to have extinction ratio of ~45 between the cooling laser power and the repumping laser power. Furthermore, the spectra show that the two spectral line frequency spacing is well set to the desired frequency. Finally, the dual frequency laser power stability was measured to over several hours. Figure 4.8 shows the detected power when the laser is set at 1 W. The results measured after isolator (75% of total output power of 1W) show that the power fluctuation was less than 1%.

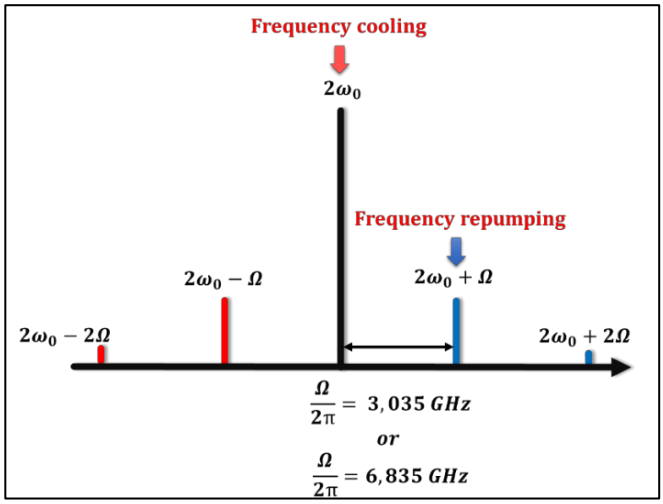

Figure 4.6: Carrier and sidebands generated after passing through the non-linear crystal.

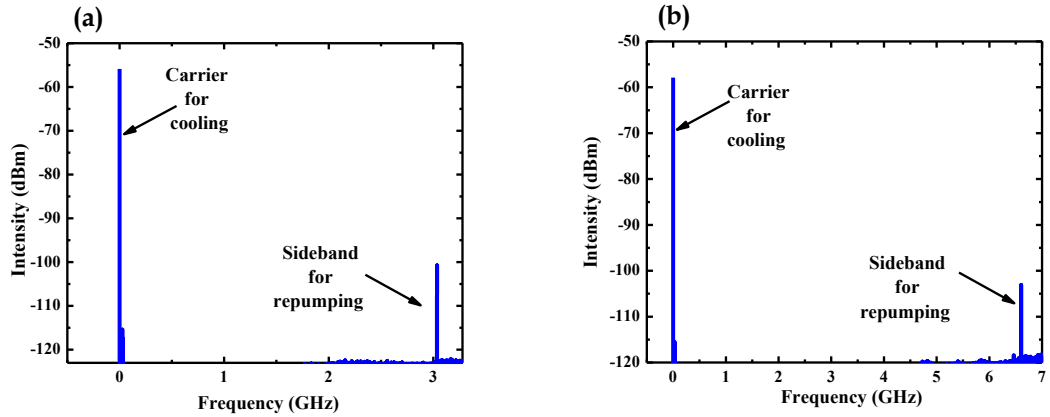

Figure 4.7:Spectra of generated sidebands (a) 3.036 GHz (b) 6.835 GHz for repumping laser for ^{85}Rb and ^{87}Rb respectively.

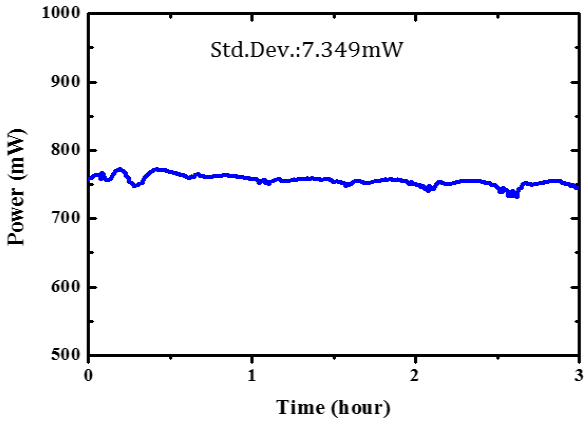

Figure 4.8: Frequency laser power stability measured for 3 hours.

4.4 Cooling and repumping laser frequency stabilization and control

Cooling and trapping of atoms need robust frequency-stabilized lasers [5]. In order to avoid drifting or fluctuation in laser frequency, the laser is locked on a frequency reference. This can be either a high finesse optical cavity or a stable narrow absorption or transparency line of an atom or a molecule.

In our setup we use a sub-Doppler transparency line of Rb. The spectral feature to which laser is locked, is a sub-Doppler transparency generated via saturated absorption technique.

The frequency locking technique is based on Frequency Modulation spectroscopy (FMS) technique [6], which is derived from Pound-Drever-Hall (PDH) technique [2]. Figure 4.9 schematically illustrates experimental setup for frequency stabilization, where yellow and black lines are for optical and electrical signal.

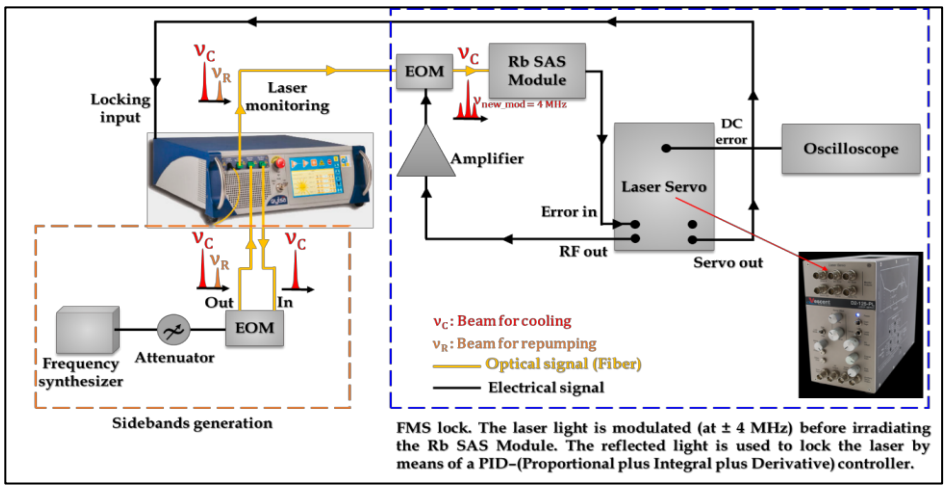

Figure 4.9: Schematic drawing of the laser set-up with FMS locking setup (in the blue dashed box). The generation of the sideband signal for repumping (in the orange dashed box). Yellow lines are optical paths and black lines are electrical signal paths.

4.4.1 Saturated absorption spectroscopy

SAS is a powerful technique to lock a laser frequency to that of specific transition lines. Figure 4.10 shows schematically the principle of SAS. The SAS provides sub-Doppler transitions by using the phenomenon of population saturation [4], and thus allowing hyperfine transitions to be resolved. It works by splitting a single laser into two counter-propagating beams: a powerful "pump" beam and a weak "probe" beam. The pump beam is passed through the rubidium cell and saturates the atoms while the weaker (probe) beam is steered to overlap in counter-propagating direction with the pump beam through the reference gas cell. The transmitted probe beam through the cell exhibit sub-Doppler transparency peaks which can be recorded with a photodetector.

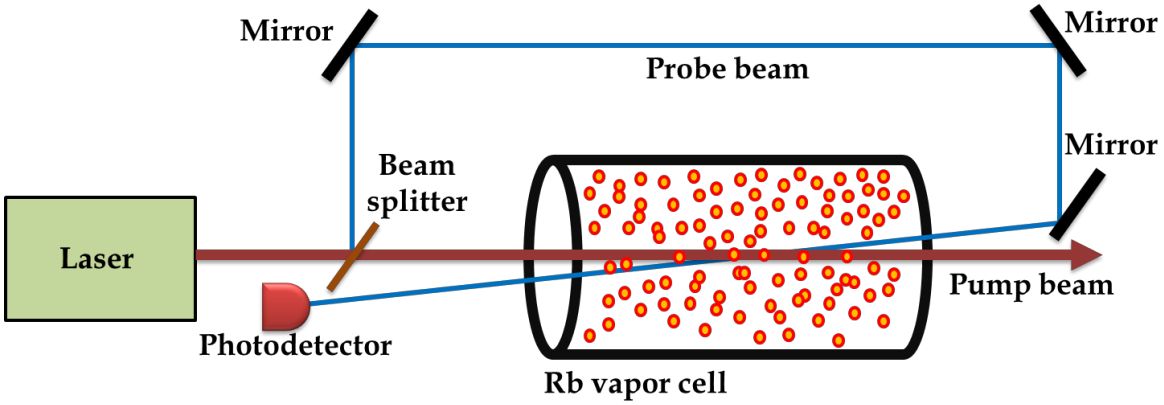

Figure 4.10: The optical layout for saturated absorption spectroscopy.

The sub-Doppler features are generated as follows. Doppler effect ensures that only atoms with no velocity component along the laser beam propagation axis see the frequencies of both pump and probe beams. These atoms begin to absorb photons from both (pump & probe) on resonance laser beams. However the much stronger pump beam quickly saturates the excited states of atoms and the probe beam is unable to be absorbed [4]. At this point the photodetector measures a sharp increase

in the probe power transmitted (*i.e.* a sharp decrease in absorption). When the probe absorption is at a minimum, the laser wavelength is on an atomic transition frequency of one of the hyperfine levels. Experimentally, if the photodiode measures the optical power of the probe beam as the laser is scanned across the entire Doppler width-covering all the hyperfine levels- the spectrum would show the Doppler broadened profile but at each hyperfine transition there would be a sharp peak in transmitted probe power.

The rubidium hyperfine structure can thus be resolved using the aforementioned SAS. In practice, and in order to avoid to be sensitive to the laser power fluctuation, the probe signal is normalized with another weak control beam by passing it through the rubidium cell (with no overlap of the pump and probe beams), which sent to another photo-detector. The two photodetectors form a balanced photodetector, i.e. the photodetector have equal gain and their respective signal is sent to differential amplifier which output is the difference between the two signals.

Figure 4.11 shows the SAS traces we obtain with our laser. The hyperfine structure for ^{85}Rb and ^{87}Rb has three principle hyperfine and three cross overs, (four levels each, but up to six peaks can be seen for each spectrum). The extra peaks are called cross-over resonances but do not imply further atomic structure. Cross over resonances occur at the mid-point between two principle hyperfine transitions. In our setup, to generate the saturated absorption signal and then subsequently to convert them into error signals, we are using commercially available spectroscopy module D2-210-FC-Rb with fibre coupling from Vescent photonics. The spectroscopy module provides Doppler free absorption signals derived from SAS of rubidium atoms. The module contains a vapor cell, internal temperature controller, balanced photodetector, and aligning optics (see Figure 4.12-a). The temperature controller stabilizes the density number of atoms in the cell. The

balanced photodetector has the advantage to not be sensitive to the laser intensity fluctuations or drifts. The temperature of the Rb vapor cell is set at 45 C° (factory setting) and the atomic density at this temperature is ~ $8X10^{10}/cm^3$. The absorption signals from spectroscopy module are fed to laser servo controller.

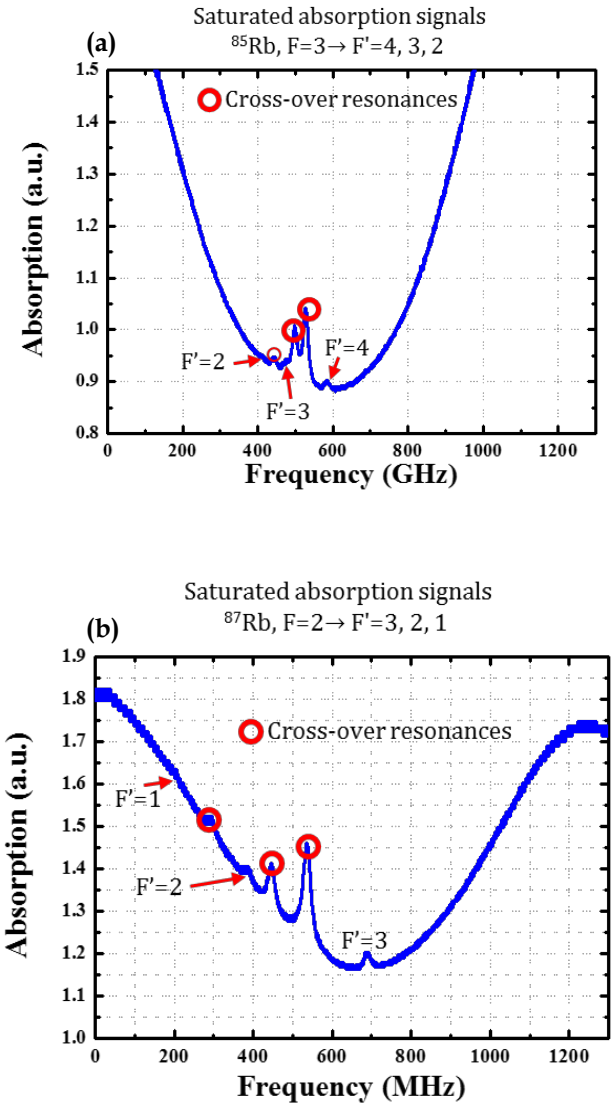

Figure 4.11: Saturated absorption spectroscopy for both (a) ^{85}Rb (b) ^{87}Rb showing the upper ground state to hyperfine (F') levels.

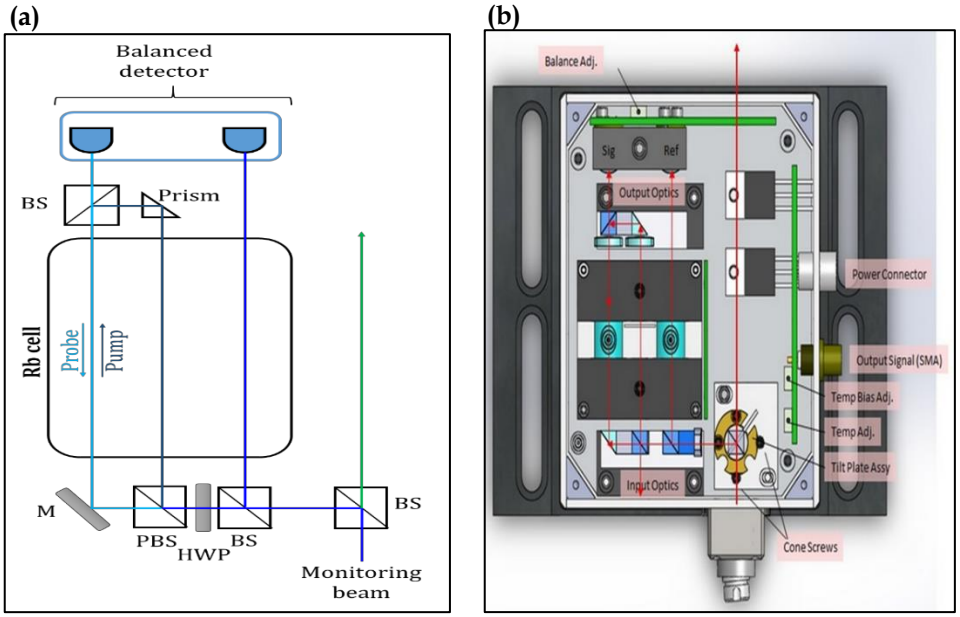

Figure 4.12: (a) Optical scheme for Doppler free saturated absorption spectroscopy. (b) Beam paths with components map of spectroscopy module (right).

4.4.2 Servo locking set-up

In FM locking technique, the laser is frequency modulated with an EOM at ± 4 MHz before being sent to Rb SAS module and detected by a photodetector. The photodetector signal is then fed to the servo locking electronics to take the derivative of the SAS (Figure 4.13) and to produce the error signals. The locking point corresponds to the zero-crossing of the error signal and also at the peak of the different sub-Doppler spectral features of a desired Rb transition. A schematic of the feedback electronics is shown in figure 4.9 in blue dashed box. In this setup the EOM modulates te laser frequency at (adds an RF modulation about) 4 MHz. (and this adds side-bands to the laser signal). The resultant is a beam with a central carrier and sidebands (higher and lower side-bands). For ideal FMS, only two side-bands are required (as opposed to additional, higher orders). After the beam passes through the SAS module, the signal from the balanced photodetector is demodulated to obtain the error signal. The demodulation occurs by mixing the

photodetector signal with the laser servo controller frequency. The figure 4.13 shows the servo locking electronics. The error signal from the frequency mixer is amplified by 26 dB. This produces an AC signal at twice the modulation frequency with an added DC offset. The AC term can be removed using a low-pass filter (<200 KHz) and the DC term remains. This DC signal is proportional to the change in absorption of the probe beam. As frequency modulation technique is being used, there is also an extra information in the form of phase information between the side-bands. The phase difference between the two side-bands is π when there is no absorption in either side-band. When one of the side-bands encounters an absorption line, this phase difference and the difference in magnitude between the side-bands is seen in the error signal.

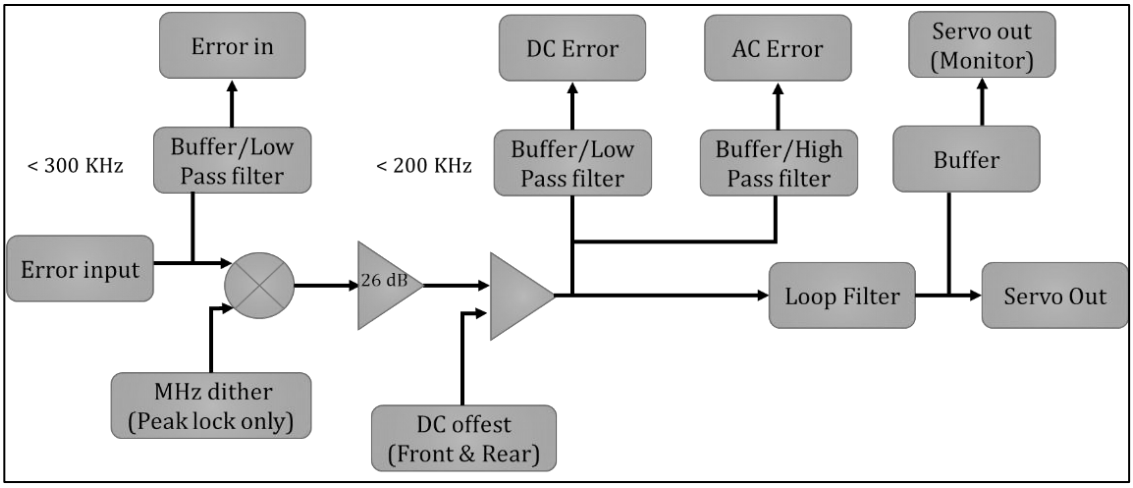

Figure 4.13: Electronic diagram of the servo locking system.

Figure 4.14 (blue line) shows the obtained error signals for ^{85}Rb and ^{87}Rb respectively. Once we have error signal, now we lock the laser by looking the error signal on oscilloscope and bring the cycling transition to zero crossing by decreasing the scan amplitude. The laser servo has both options: side and peak lock. We are locking the frequency of our laser by using peak lock as can be seen in Figure 4.14. For the ^{85}Rb locking scheme, the laser is locked to the F= 3→ F′= 4 transition and for

^{87}Rb to the F= 2→ F′ = 3 transition. If there is frequency drift in locked signals from their zero set point due to any external noise or vibration. The controller measure that drift and send feedback to laser cavity through laser servo controller and compensate that frequency to stabilize the laser.

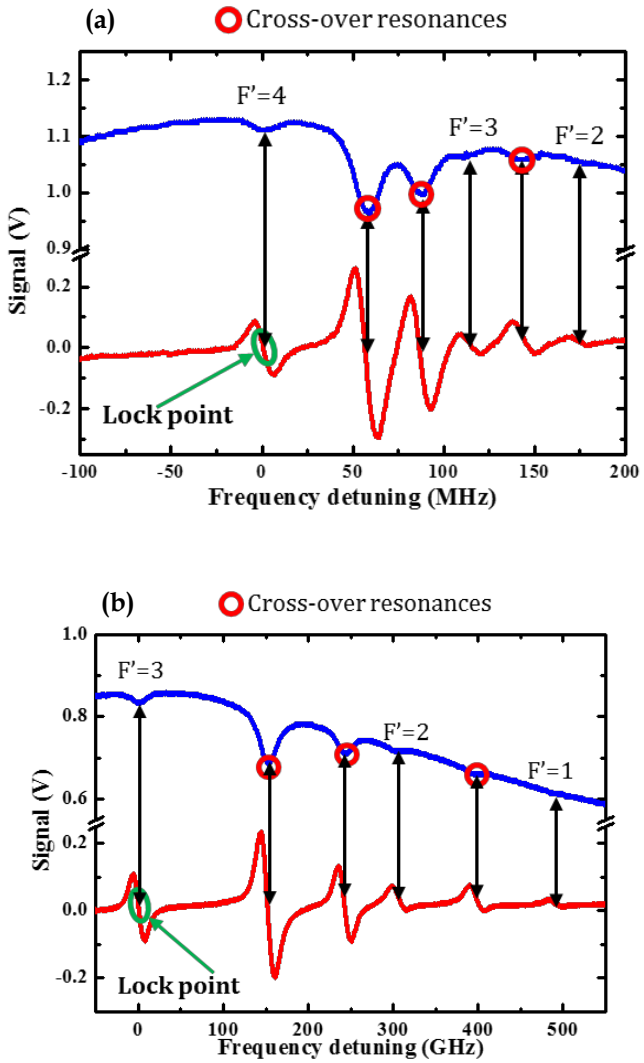

Figure 4.14: Comparative frequency spectrum of the saturated absorption DC signal (blue trace) and its error signal obtained at 4 MHz (red trace) for (a) ^{85}Rb and (b) ^{87}Rb.

A quantitative measurement of frequency stability is obtained by measuring the Allan variance. The Allan variance is a two-sample variance formed by the average

of the squared differences between successive values of regularly measured quantities taken over sampling periods from the measuring interval up to half the maximum measurement time. In comparison with the commonly used standard variance, the Allan variance is based on measurement to measurement variation rather than on individual measurement to mean measurement variation [7]. For example, for N measurement the Allan variance is:

$$\sigma_y^2(\tau_0) = \frac{1}{2(N-2m+1)} \sum_{i=1}^{N-m+1} [Y(i+m) - Y(i)]^2 \qquad (4.6)$$

σ_y^2 is Allan variance, τ_0 is the sampling time. We measured Allan variance of frequency stability at different integration times of 1, 5 and 1300 seconds and free running laser (as shown in the figure below). Here we mean by "free running" a beat frequency of laser with itself.

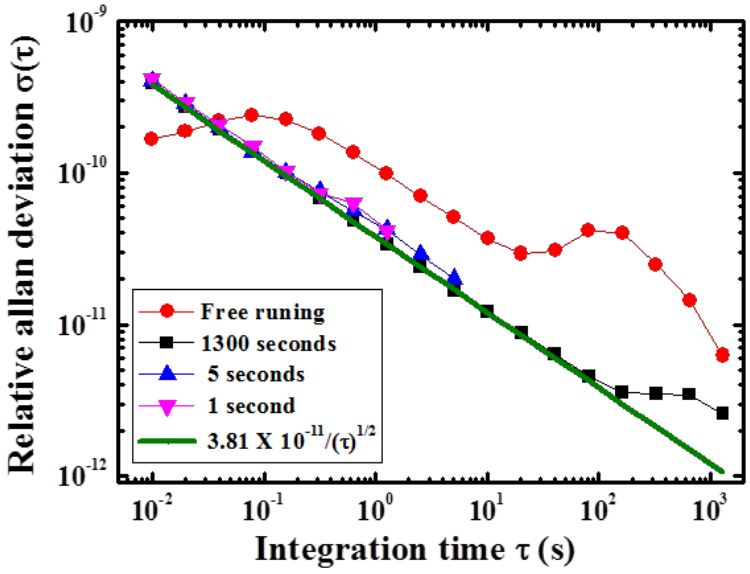

Figure 4.15: Measured Allan variance (σ) of cooling and repumping lasers locked for different time intervals (black, blue and pink), free running (red) and the fit (olive). Cooling / repumping lasers were frequency stabilized at an Allan variance of 2x10^{-12} for 1300 s.

The sampling time was 2ms, 10ms and 2.6 s respectively for an integration time of 1s, 5s and 1300s. Figure 4.15 shows the measured Allan variance traces for free running laser (red curve) and locked laser with the aforementioned integration and sampling times. The results show that compared to the free running laser, the locked laser exhibits a better long term stability and fits with $\sigma(\tau) = 3.8 \times 10^{-11}/\sqrt{\tau}$, indicating the white nature of the noise.

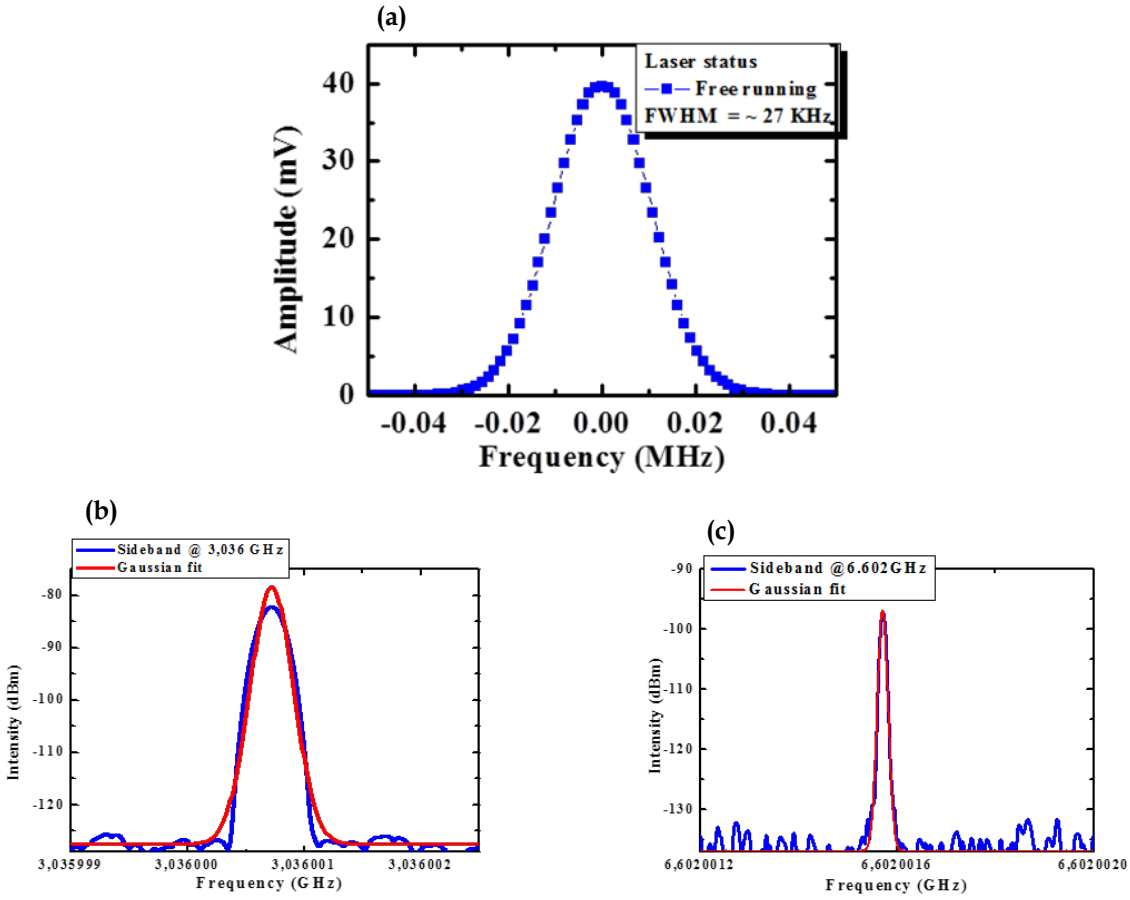

Figure 4.16: Measured linewidth of the dual frequency laser (a) cooling laser. Repumping laser (b) ^{85}Rb and (c) ^{87}Rb.

Furthermore, we also measured the linewidth of the two spectral components of the laser under free running regime using self-heterodyne interferometer. Figure 4.16 shows the linewidth of both the cooling and the repumping line. The results show a linewidth of (a) 27 kHz for the cooling laser, and (b) 441 Hz and (c) 26 Hz (for ^{87}Rb and ^{85}Rb respectively) of repumping laser. These results are consistent with the Allan deviance result of the free running laser.

4.5 Guidance and in-fibre cooling laser systems

4.5.1 Red shifted laser

The laser system of the platform comprises a far red detuned laser. The latter consists of seed laser and an amplifier. The seed laser is a grating stabilized tunable single-mode diode laser with wavelength centered around 1070 nm with a tuning range from 1045 ~ 1085 and emitting up to 100 mW optical power. The amplifier is a polarization maintaining Yb fibre amplifier, which can emit up to 50 W with linearly polarized output power, operating wavelength 1064 ~ 1083 nm. It is noteworthy that such a large amount of optical power can be handled with our HC-PCF (chapter 2). This laser is aligned in such a way that is coupled to one of the HC-PCF set from both fibre ends. The coupling into the fibre is achieved by using a fibre link with several meter long IC guiding HC-PCF. The HC-PCF output beam is then collimated and coupled into one of the HC-PCF inside the UHV chamber. The frequency of this laser is set to be far-off resonant from the atomic resonance so to undertake atom guidance from both MOTs into one of the HC-PCF, but also to generate optical lattice for adiabatic cold atom guidance and in-fibre atom trapping.

4.5.2 Blue shifted laser

The last laser of the "in-fibre laser cooling platform" consists of grating stabilized tunable single-mode diode laser which has wavelength range from 765 ~ 795 with maximum peak power of 80 mW. This laser can be finely detuned to the blue side of Rb cooling resonance.

The laser is coupled to the fibres in the same manner as for the far red detuned laser. For this purpose, we superpose the two beams using a dichroic mirror. Furthermore, the blue-detuned laser passes through an S-wave plate in order to shape its beam into a donut transverse profile. Our preliminary results show that we can produce a hollow beam. However, work is underway to investigate the use of a spatial light modulator (SLM) and Fibre Brag Grating (FBG) so to compare which is the best solution in generating the best beam profile. Finally, the SLM and FBG will allow us to selectively excite a given higher order mode of the HC-PCF under test (see chapter 2) for transverse trapping.

4.6 Summary

In this chapter we described the laser system that has been constructed for the in-fibre laser cooling platform. In our setup, we constructed three lasers. The first laser was constructed in such way to emit at two frequencies. The first one is tuned on the cooling transition and the second on the repumping transition. This dual frequency laser can emit up to 1 W and was frequency stabilized using FSM/PHD technique by locking it to another Rb spectroscopy cell. We achieved frequency stability, expressed in Allan deviation of $\sigma(\tau) = 3.8 \times 10^{-11}/\sqrt{\tau}$. The frequency stabilization system was tested for both Rb isotopes with comparable performances. This dual frequency laser fulfills thus the requirements for the generation of the two MOTs of the platform.

Furthermore, we have set-up two additional lasers for different configuration of atom guidance and trapping.

These lasers are integrated into the overall platform scheme and are ready for operation. Future work is still necessary to properly shape the beam for the blue-detuned laser and to generate the optical lattice with the red detuned laser.

References

[1]-"*Three-dimensional viscous confinement and cooling of atoms by resonance radiation pressure*", **Steven chu, L. Hollberg, J.E. Bjorkholm,, Alex cable, and A. Ashkin**, Phys. Rev. Lett., vol. 55, 48, (1985).

[2]-"*An introduction to Pound-Drever-Hall laser frequency stabilization*" **Eric. D. Black**, Am. J. Phys. vol. 69 (2001).

[3] "*Rubidium D line data*", **Daniel. A. Steck**, available online at http://steck.us/alkalidata

[4] "*Laser spectroscopy*", **W. Demtroder,** Springer, Heidelberg, 1991.

[5] "*Compact and robust laser system for rubidium laser cooling based on the frequency doubling of a fiber bench at 1560 nm*", **F. Lienhart, S. Boussen, O. Carraz, N. Zahzam, Y. Bidel, A. Bresson,** Appl. Phys. B, vol. 89, pp. 177–180, (2007).

[6] "*Frequency modulation (FM) spectroscopy*" **G. C. Bjorklund, M. D. Levenson, W. Lenth and C. Ortiz** , App. Phys. B Photophysics and Laser Chemistry, vol. 32, p. 145-152, (1983).

[7] "*The use of Allan deviation for the measurement of the noise and drift performance of microwave radiometers*", **D. V. Land, A. P. Levick and J. W. Hand,** Measurement Sci. and Tech., vol. 18, (2007).

Chapter 5

Generation and characterization of ultra-cold rubidium

This chapter presents the experimental protocol for the generation of ultra-cold rubidium using magneto-optical trap. Different techniques were used to measure the atomic density and temperature of the generated molasses. Optimization of the trap to obtain the coldest temperature was undertaken to adjusting the laser power and frequency detuning, magnetic field and Rb background density. The result of such optimisation process led to temperature values as low as 7 μK for ^{87}Rb. Finally, the chapter presents the work left to carry out with regard to red-detuned and blue-detuned laser beam coupling into the HC-PCF before considering the platform operational for the different necessary experiments in-fibre cold atom guidance and spectroscopy and sub-consequently to demonstrate the feasibility of in-fibre laser cooling.

5.1 Introduction

In chapters 3 and 4 we described the different parts of the "in-fibre laser cooling" experimental platform and the performances of the main components such as the achievable vacuum pressure, the HC-PCF optical properties and the cooling-repumping lasers and their frequency stabilisation. In this chapter, we detail the experimental procedures and properties of the magneto-optical trap (MOT) to generate ultra-cold atomic molasses with both Rb isotopes, and present the preliminary results to undertake the atom guidance in HC-PCF. The chapter is structured as follows: we first recall the basic principal of a MOT; we then present the operation principles and the specifications of our MOT. In the following sections, we describe the trap loading process and its characterization by measuring the atomic density and the temperature of the cold atom molasses. Here, in order to ensure a consistency in the trapped atom number and temperature, we have measured them using two different techniques; the time of flight (TOF) [1] and the release and recapture methods [2]. We then undertake a systematic measurement campaign to study the evolution of the cloud temperature and density with the intensities of laser beams, the current of Rb source and the magnetic field gradient. This is motivated so to find the set points of the different control parameters for optimum cooling but also to build procedures to operate the "in-fibre laser cooling". The last section covers the primary results with regard to the future plans of exploring the different known approaches of guiding the cold atoms through the hollow core of photonic crystal fibres.

5.2 Basic principle of MOT

We have seen in chapter 1 that trapping and cooling atom by magneto-optical trap relies on an induced force that is viscous in the velocity-space to slow down the atoms and is restoring in the z-coordinate space to trap the fast atoms, which can be written as:

$$\overrightarrow{F} = -\alpha\overrightarrow{v} - k\overrightarrow{z} \tag{5.1}$$

The viscous force is provided by the cooling laser using the Doppler cooling effect (chapter 4). This effect is generated on ^{85}Rb and ^{87}Rb by slightly red detuned the frequency of the laser from the transitions $|5^2S_{1/2}F = 3\rangle \rightarrow |5^2P_{3/2}F' = 4\rangle$ and $|5^2S_{1/2}F = 2\rangle \rightarrow |5^2P_{3/2}F' = 3\rangle$ respectively. Fig 5.1 recalls the laser wavelengths involved for both Rb isotopes. The cooling power of the system is determined by the strength of the friction coefficient α given below:

$$\alpha = \frac{\delta\, \eta k^2 \Gamma \Omega^2}{\left[\delta^2 + \frac{\Gamma^2}{4} + \frac{\Omega^2}{2}\right]^2} \tag{5.2}$$

This expression shows that in order to maximize α one needs to operate at laser intensities well below the saturation intensity (i.e. $\Omega = \Gamma\sqrt{I/2I_s} \ll 1$), and frequency detuning set at $\delta = \sqrt{(\Gamma/2)^2 + (\Omega^2/2)}$. Furthermore, α also determines the strength of the spring constant of the MOT, κ, as they are related by $\kappa = \mu_B(\hbar k)^{-1}\partial_z \mathrm{B}\,\alpha$ (see chapter 1 and 3). Consequently, properly setting the cooling laser intensity and frequency is paramount for a successful MOT generation and optimal operations.

In addition, because of the specific hyperfine energy structure of Rb, a supplementary laser, repumping laser, is required to compensate for the lost atoms via optical pumping from the cooling resonance cycle [4]. This requirement is

illustrated in Fig. 5.1(a), and is explained as follows. In Rb atoms, the excited state of the cooling transition $|5S_{1/2}F\rangle \rightarrow|, 5^2P_{3/2}F' = F + 1\rangle$ has small frequency spacing with the other F' states. This leads via optical pumping to populate the ground state F=1 from the atoms in the state $|5^2P_{3/2}F' = 2\rangle$ for ^{87}Rb and F=2 ground state from $|5^2P_{3/2}, F' = 3\rangle$ for ^{85}Rb. A remedy to this loss can be achieved with a laser resonant with $|5^2S_{1/2}F = 1\rangle \rightarrow|5^2P_{3/2}, F' = 2\rangle$, which excites the ground state atoms from F=1 to the excited manifold state in case of ^{87}Rb. The details of the configuration of our cooling-trapping and repumping laser system which was described in chapter 4.

Furthermore, as seen in chapter 1, the atom trapping in a MOT relies also on magnetic field gradient created by anti-Helmholtz coils. In chapter 3 we described the design and specifications of the anti-Helmholtz coils that will be used in the MOT generation. Below we will detail the experimental parameters and configuration of our MOT.

To further complete the aforementioned physical principles in trapping and cooling atoms using a MOT, we recall that the resulting forces in a MOT configuration exhibit fluctuations that are inherent to the stochastic nature of the spontaneous scattering of the photons. In turn, such fluctuations induce a continuous heating of the trapped atoms. Consequently, at equilibrium the atoms dynamics in a MOT will be a balance between the cooling rate of the viscous force mentioned above and the heating effects such as the fluctuations of the atomic-photon interaction. This balance, in turn, determines the characteristics of the MOT such as its temperature ,T, velocity distribution and density profile, which can be written for 1D case as follows [5]:

$$\begin{cases} T = k_B^{-1}\frac{D}{\alpha} \\ n(v,z) = \frac{N}{\pi\, v_0 z_0} e^{-\left(\frac{v}{v_0}\right)^2} e^{-\left(\frac{z}{z_0}\right)^2}, \end{cases} \tag{5.3}$$

with $D = \hbar^2 k^2 \Gamma \rho_{ee}$; $v_0 = \sqrt{\frac{2D}{m\alpha}}$; $z_0 = \sqrt{\frac{2D}{\alpha\kappa}}$.

Here, D is the momentum diffusion coefficient of the MOT atoms, ρ_{ee} is the excited state population and N is the total number of atoms in the MOT. The expression of the temperature clearly shows that is the results of the balance between the heating effects, represented by the diffusion coefficient, and the cooling, represented by α. The expression of the atom distribution shows a Gaussian distribution of the trapped atoms in both the momentum-space and coordinate-space, and is deduced from the Fokker-Planck equation [5]. The equations clearly show that the temperature, the velocity distribution and the spatial profile of the MOT are strongly influenced by α andκ. As a result, the steady-state MOT can be controlled by four parameters: the laser intensity or Rabi frequency Ω, the cooling laser detuning δ, the magnetic field gradient ∂_zB and the number of trapped atoms N. Conversely, and depending on these four parameters, the final equilibrium state of the MOT atomic cloud can exhibit different set points in its temperature, density and size, and slightly deviate from those in equation 5.3.

Four phase density regimes are commonly identified in a MOT [6]. They differ in their stationary phase-space density, which means in the established relationship between the size, number of atoms, temperature and density.

The first regime which is called "temperature limited", corresponds to a cloud atom number that is typically less than 10^4. In this trap, the density is low and interaction affect within the trap is neglected. In this regime, the atomic spatial and momentum distribution are close to Gaussian and can be characterized by radii r_x, r_y, r_z and temperature T. These radii are given by equipartition theorem

$$\frac{1}{2} k_{x,y,z} r_{x,y,z,t}^2 = \frac{1}{2} k_B T \qquad (5.4)$$

This indicates that in the first regime the size of the trap depends only on the temperature and not on the number of atoms in the trap. In the case of the anti-

Helmholtz configuration, the spring constant κ along the z-axis is twice that the value along the transverse plane. Thus, the MOT cloud has an elliptical shape and we have the following identity between the radii along the three axes:

$$r_T \approx r_Z = \frac{r_{x,y}}{\sqrt{2}} \tag{5.5}$$

Consequently, the density of cold atoms can be calculated by dividing the number of atoms per unit volume. So we can write the density as

$$n_{TL} = \frac{3N}{\pi(2r_T)^3} \tag{5.6}$$

In the second regime, called "multiple scattering", the cloud has become dense enough (typically N>10^4), and the re-absorption of scattered photons with in the trap cloud is an important effect. The re-absorption and scattering results in a repulsive force between atoms, limiting the atomic density in this regime.

$$n_{MS} = \frac{3kc}{I_{Total}\sigma_L^2\left(\frac{\sigma_R}{\sigma_L}-1\right)} \tag{5.7}$$

Where $I_{Total} = \frac{2I_s\Omega_{Total}^2}{\Gamma^2}$ is the total light intensity of six trapping beams, σ_L is the optical cross-section for absorbing photons from the laser field, σ_R is the optical cross-section for absorbing photons from atom in the trapped cloud, κ is the MOT spring constant. The density in this regime is independent of number of atoms and dependent of spring constant and trapping intensity. The third is two-component regime, where the number of atoms is too high to be packed into the harmonic potential of the trap and the atoms spill out into the weaker potential well around the trap. The approximation of the trap as a damped harmonic oscillator no longer holds. The cloud will appear to have two different density components with the denser part residing inside the harmonic potential. The fourth regime is optically dense (or optically thick) regime, where the shallow part of the trap is also filled. It has the highest number of atoms of the four regimes. Experimentally, the trapped

atom's temperature, density and size are also sensitive to other phenomena such as collisions with the vacuum background or between trapped atoms. Consequently, the number of trapped atoms in the steady-state results from a balance between the capture rate and the losses due the aforementioned collisions.

The capture rate is related to a convenient quantity called capture velocity v_c . The capture velocity is defined as the maximum speed of the atoms that can be trapped within a sphere of a given volume V and radius r at a given rate R. For a gas with Maxwellian distribution with a thermal velocity v_{th} and density n, we can deduce the following approximate expression for the number of atoms entering this sphere per second:

$$R \approx \frac{A}{4\sqrt{\pi}} n \frac{v_c^4}{v_{th}^3} \tag{5.8}$$

Here, A is the trap surface which is related to the laser beam diameter. Determining the expression of the capture velocity is challenging because of the MOT trap potential is a complex combination of trapping from the magnetic gradient and from the laser beams. However, and to a reasonable approximation the velocity capture can take the following expression [7]:

$$v_c = \left(\frac{\hbar k \Gamma d}{m}\right)^{1/2} \tag{5.9}$$

Here, d is beam diameter of the cooling laser, and according the equation it is advantageous to have a large laser beam.

In parallel with the above trap loading process, the atoms are lost from the MOT by either collision with the background gases in the UHV chamber or via two body intra-trap collisions. Consequently, the number of trapped atoms can be described by the following rate equation of the number of cold atoms in a cloud [8]:

$$\frac{dN}{dt} = R - \gamma N - \beta \int n^2(r,t) dV \tag{5.10}$$

The expression shows three terms in its right hand member. The first is the loading rate, which was described above. The second term, γ, is the first order loss rate constant due to collisions with hot atoms and or background gas and usually dominates the losses in a typical MOT. The third term $\beta\int n^2(r,t)dV$ represents the number of atoms lost due to collision between cold atoms in the trap. The term $n(r,t)$ is the density of the trapped atoms at position $\vec{r}$ and time t, and β is the loss rate constant of two-body intra-trap collisions. The above equation (5.10) can be easily and conveniently solved if we separate the different regimes of the phase-space density of trapped atoms. Here, the initial time (i.e. t=0) is set when both the magnetic field and the laser beam are one.

If we consider the intra-trap collisions between the cold atoms to be negligible, we can ignore the third term in equation 5.10, and have a number of cold atoms in function of time to be given by the following expression:

$$N = N_{eq}[1 - exp(-\gamma t)], \tag{5.13}$$

Where $N_{eq} = R/\gamma$ is the steady-state trapped atom number (i.e. $N_{eq} = N(t = \infty)$). Also, we recall the expression R and γ:

$$R = \frac{nv_c^4}{2V^{3/2}}\sqrt[3]{\left(\frac{m}{2K_BT}\right)} \tag{5.14}$$

$$\gamma = n\sigma\sqrt{\frac{3K_BT}{m}} \tag{5.15}$$

On the other hand, if n is larger than 10^{10} atoms/cm^3, $\beta\int n^2(r,t)dV$ is no longer negligible. However, if we assume a Gaussian profile of the atom density like in equation. 5.3, the rate equation 5.10 takes the following form:

$$\frac{dN}{dt} = R - \gamma N - \alpha N^2 \tag{5.16}$$

Where

$$\alpha = \gamma + 2\beta n_{eq} \tag{5.17}$$

Finally, in the regime of multiple scattering, the atom density is large (higher than 10^{10} atoms/cm^3) and can be considered as constant. In this regime, the cloud density rate equation takes the following form:

$$\frac{dN}{dt} = R - \gamma N - \beta n N \tag{5.18}$$

Consequently, the solution to Equation. 5.18 can be written as

$$N = N_{eq}\left[1 - exp\left(-\gamma_{eff} t\right)\right], \tag{5.18}$$
$$\text{with } \gamma_{eff} = \gamma + n\beta.$$

By exploring the above equation and recording experimentally how the MOT size and fluorescence signal evolve with time we can deduce the density of the MOT and its temperature.

5.3 Operation and specifications of the platform MOT

As mentioned in the previous chapters, the experimental platform for the in-fibre laser cooling is equipped with two MOTs located in the vicinity of the two tips of each of the HC-PCF. Each MOT is comprised with a pair of anti-Helmholtz coils set up vertically and spaced by 2.8 cm. The cancellation of the earth's magnetic field and other stray fields in the centre of the coils is achieved by a slight unbalance in the current in the coils.

The cooling and repumping beam setup is composed by three pairs of counter propagating laser beams. The polarization of each beam is independently controlled by a combination of quarter-wave plates and PBS just before viewports specified for laser beams propagation for MOT. This choice made the setup and alignment more complex but also provided the experimenters with freedom to fine-tune the MOT

shape, position and launch parameters. In our case, our laser is described in chapter 4.

The diameter of laser beams we are using for MOT generation is ~1cm so to have a sufficiently large capture rate. The laser beam size control was carried out by using telescope. All the beams come from a single laser. The beam of this laser is first passed through an optical isolator to prevent any un-wanted optical feedback, and has maximum output optical power about ~1 W. Also this beam is first expanded in diameter up to 3cm by using telescope and then is reduced up to 1cm by using iris. This 1 cm beam is split into two beams by using a beam splitter. One beam is going for vertical direction propagation. The second beam is again passing through beam splitter to be divided in to two beams. These two beams are aligned along the horizontal directions. The optical power in each beam is adjusted by a set of waveplates, polarizing beam splitters and density filters. The 1W initial power is sufficient to operate the two MOT of the UHV system and also have several additional beams for monitoring and frequency stabilisation.

The polarizations of all the beams are set to circular polarization to set the cooling configuration to $\sigma^{+} and\ \sigma^{-}$. The polarization of each beam was measured using a polarimeter (Meadowlark) and controlled using a quarter waveplate. The wave plates are placed in front of each of the incident three beams and mounted just before the reflecting mirrors for the three retro-reflected beams. The laser beams pass through the quarter wave plates two times (double pass) and it brings 180° phase change in polarization of each beam. If the polarization of incident beam is σ^{+} then the polarization of retro-reflected beam will be σ^{-}. These beams are intersecting each other at the centre of anti-Helmholtz coils where magnetic field gradient is zero. The intensities of laser beam can be either increased or decreased depending on the demand of experiment. For our MOT generation, the intensity of each of the six beams ranges from 4 mW/cm^2 to 10mW/cm^2 (see table 5.1).

Moreover, the laser can emit both at the cooling transition with a red-detuning range of 5 to 10 MHz from the $|5^2S_{1/2}F=3\rangle \rightarrow |5^2SP_{3/2}F'=4\rangle$ for ^{85}Rb and $|5^2S_{1/2}F=2\rangle \rightarrow |5^2P_{3/2}F'=3\rangle$ for ^{87}Rb. The repumping laser was generated from the same laser by sum frequency (see chapter 4). This configuration has the advantage of the fact that the frequencies of cooling and repumping lasers are better locked to each other than independent lasers. Furthermore, these frequencies are frequency stabilized by locking the resonant repumping laser to $|5^2S_{1/2}F=2\rangle \rightarrow |5^2P_{3/2}F'=3\rangle$ for ^{85}Rb and $|5^2S_{1/2}F=1\rangle \rightarrow |5^2P_{3/2}F'=2\rangle$ for ^{87}Rb using FM-PDH technique (see chapter 4). The net result is a laser emitting at both cooling and repumping frequencies with a measured Allan variance when stabilized on ^{85}Rb and $|5^2S_{1/2}F=3\rangle \rightarrow |5^2P_{3/2}F'=4\rangle$ transition of $\sim 3\times 10^{-11}/\sqrt{\tau}$, which represent a frequency stability that is good enough to undertake stable MOT generation.

Furthermore, a second advantage of our laser system is that both cooling and repumping beams are collinear, which makes it very convenient for alignment. The system is set such both MOT could be activated independently by using one laser. We used these parameters as shown in table 5.1 to measure the number of trapped atoms and their temperature.

Laser	**Beam size (cm)**	**Total intensity in six beams (I_0) mW/cm²**	**Detuning (red-side) MHz**	**Magnetic field gradient (G/cm)**	**Rb source (A)**
Cooling/repumping	**1**	**27 to 60**	**10 to 15**	**9 to 17**	**4.0 to 7**

Table 5. 1 Parameters for MOT to measure the number of trapped atoms and temperature

Regarding the magnetic field gradient we can generate up to 17G/cm which is limited due to heat dissipation in the coils. In other words, we can safely say that we can have maximum magnetic field gradient up to the above said value. The detuning of laser beam depends on the acousto-optical modulator (AOM) and its arrangement in experimental set up.

Based on the above, we measured the values of α and κ for ^{87}Rb using equation (5.2). For this measurement we used total intensity of laser beams of 21mW/cm^2. The measured value of α is 1.19x10^{-19} N/m and $\kappa = \partial_z B$ 1.3x10^{-19} N/m. These values agree with [3].

Two cameras were used for observation and imaging of the MOT. One overhead TV camera provided real-time imaging of the MOT (at 15 fps) for alignment. For imaging, a triggered CCD photo-camera with a zoom tele-objective was implemented to capture the trapped atoms for TOF temperature measurements.

Figure 5.1 shows a typical view of unsaturated image of ^{85}Rb cloud in a MOT taken with the CCD camera. The cloud shows closed to spherical spatial distribution. The image also shows the cooling/repumping beam via the fluorescence from thermal atoms.

In the sections below we detail the measurements of the trapped atoms and the temperature of the cloud for both isotopes of Rb.

Figure 5.1: Photograph of ^{85}Rb atoms trapped in the MOT.

5.4 Trap loading

Once the preliminary work in a setting up the MOT set-up and demonstrating its generation, we carry out measurement protocol to characterize it by measuring its atom number and temperature.

To measure the number of trapped atoms, we used the fluorescence detection method [11]. On the other hand, to measure the temperature of atoms we used two different methods: one is time of flight of method (TOF) which was developed at NIST to measure the temperatures of 3D optical molasses [9]. The other method is release and recapture (R&R) developed by P. Lett et al [12]. Both of these methods like the other alternatives [13-15] take advantage of the thermal expansion of the atomic cloud after its release from the trap. The optimization of the MOT (i.e. maximum of atom number and the lowest temperature) is undertaken by varying the laser power, magnetic field of anti-Helmholtz coils and the Rubidium density. This study provided relationship relating to the variation of the number of trapped atoms/density with the current of Rb sources, intensity of laser beams, gradient of magnetic fields produced by anti-Helmholtz coils. Similarly, we studied the

dependence of temperature on the same parameters as for trapped atoms. These results are motivated not only to optimize the MOT operating parameters but also to provide setting points and references to conduct guidance and cooling of Rb inside the hollow core PCF.

5.4.1 Loading the trap (experimental technique)

Now we will discuss about the experimental method to measure the number of trapped atoms which is carried out by fluorescence detection method (Figure 5.2). In this method the fluorescence light from trapped atoms is detected on photodetector. Figure 5.2 shows the fluorescence detection of trapped atoms in the form of voltage signal on the oscilloscope.

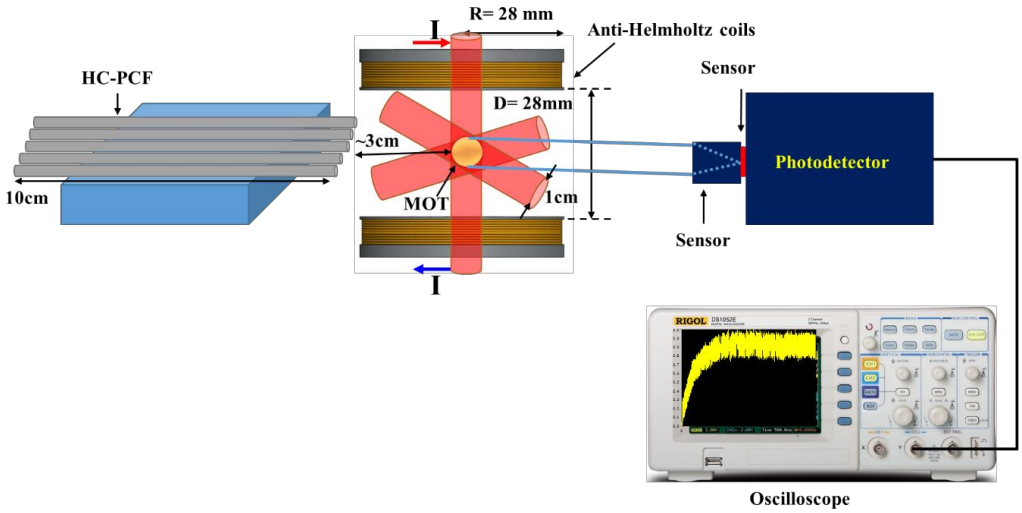

Figure 5.2: Optical scheme for fluorescence detection. Fluorescence of MOT at equilibrium state is detected on oscilloscope.

The fluorescence signal is detected by the femtoWatt sensitive photodetetor, which is aligned through one of the view port (CF40), and is recorded with an oscilloscope. The amplitude of the detected signal is directly proportional to the fluorescence emitted from trapped atoms. If the trap is turned on at t=0, the number N of atoms in the trap will increase with the same functional form as that of capacitor charging, as given in equation below

$$N(t) = N_0 (I - e^{-t/\tau}) \quad (5.19)$$

Where τ is the time constant for the trap to fill its steady state value N_0 ($N_0 = R\tau$: R is the trap loading rate).

When the trap is on, the photons are emitted in random directions giving the fluorescence, which is the power emitted from trapped atoms.

We can write this power in the expression below

$$P_{MOT} = N.E.\Upsilon \quad (5.20)$$

Where N is the number of atoms trapped in MOT, $E = h\nu$ is the energy of single photon and Υ =750Hz is bandwidth of photodiode.

The same power as measured by the photodetector is

$$P_{PD} = V_{signal}/k.G.\alpha \quad (5.21)$$

Where V_{signal} is related to the power impinging on the photodetector surface and $K = r^2/f^2$ is detection solid angle for lens of radius r and MOT distance f. The radius of lens is 1cm and distance of MOT is 22cm from the photodetector. The gain of photodiode is $G = 2X10^{10}$ V/A and the responsivity of photodiode is α = 0.5 A/W.

By comparing equation (5.21) and (5.22) and re-arranging, we get the expression

$$N = V_{signal}/k.G.\alpha.E.\Upsilon \quad (5.22)$$

The above equation gives the number of trapped atoms in MOT.

In this method, first we measure the loading curve by using the photodetector and oscilloscope as shown in Figure 5.2. Then we fit the measured loading trace to the theoretical curve given by equation 5.19. This fit provides the number of trapped atoms and their loading times.

5.4.2 Measurement of number of trapped atoms of ^{87}Rb

Below are experimental results for the measurement of number of trapped atoms. We studied the dependence of number of trapped atoms on different current for

anti-Helmholtz coils, laser intensities (here intensities are mentioned for single beam) , Rb density. The optical set up used is shown in Figure 5.2.

5.4.2.1 Laser intensities dependent

Recalling that the phase density of the trapped atoms in MOT is strongly dependent on the cooling laser intensity, we have recorded the atom loading temporal traces for different laser intensities. Figure 5.3 shows representative loading curve when the laser intensity is increased from 4.5 to 10 mW/cm^2.

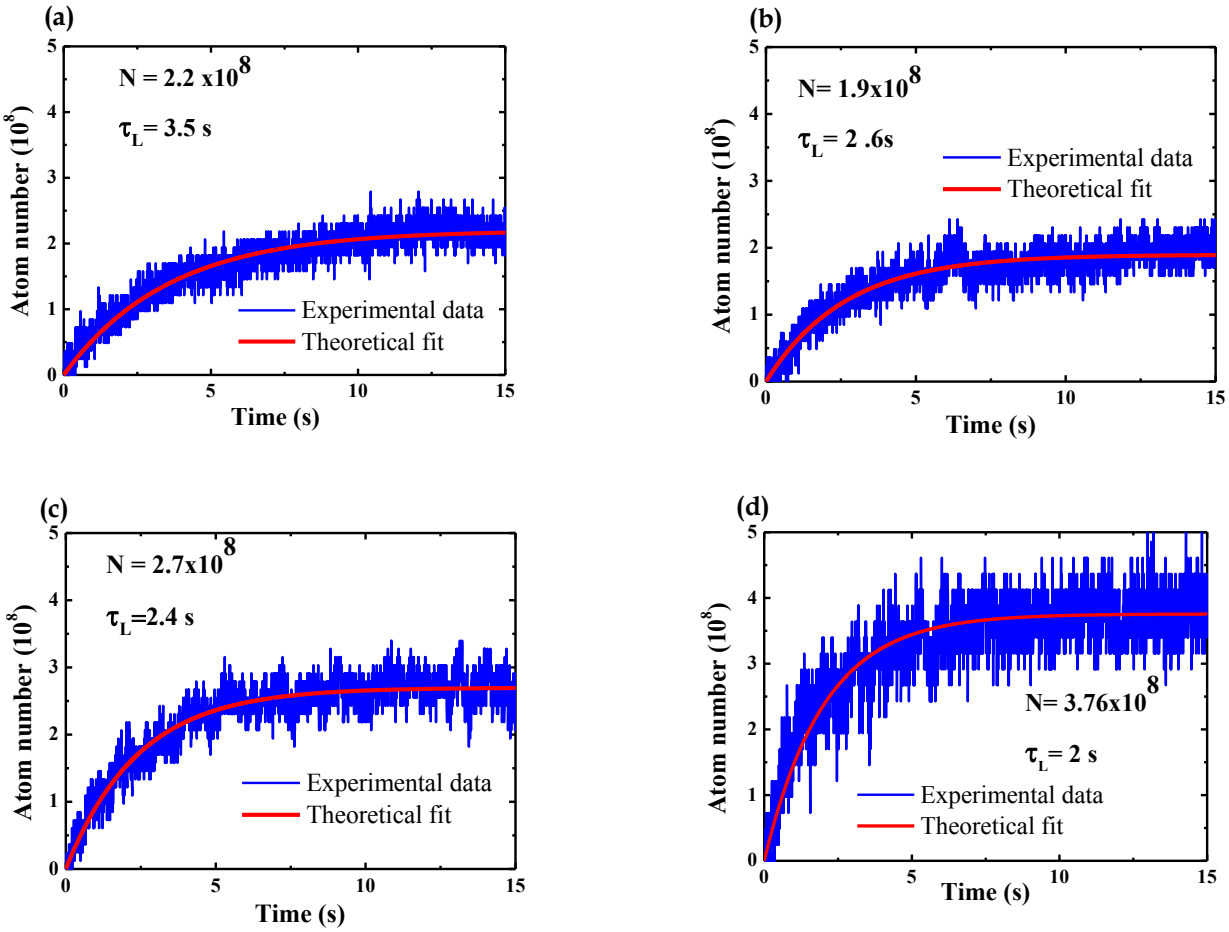

Figure 5.3: Loading curves for measurement of number of atoms of Rb^{87} at different laser intensities (a) 4.5 mW/cm^2 (b) 6.5 mW/cm^2 (c) 8 mW/cm^2(d) 10 mW/cm2. While keeping magnetic field gradient (9.6 G/cm) and current for Rb source (4.5 A) constant. The curve was fitted a function of the form equation (5.19) (red curve).

Figure 5.4 shows the deduced trapped atom number and loading time in function of the cooling laser beam intensity. The results show a trapped atom number in the range of $1.5x10^8$-$4x10^8$, and it increases with intensity for values higher than 6 $mWcm^{-2}$. The loading time ranges between 2 and 3.5 s and decreases with laser intensity.

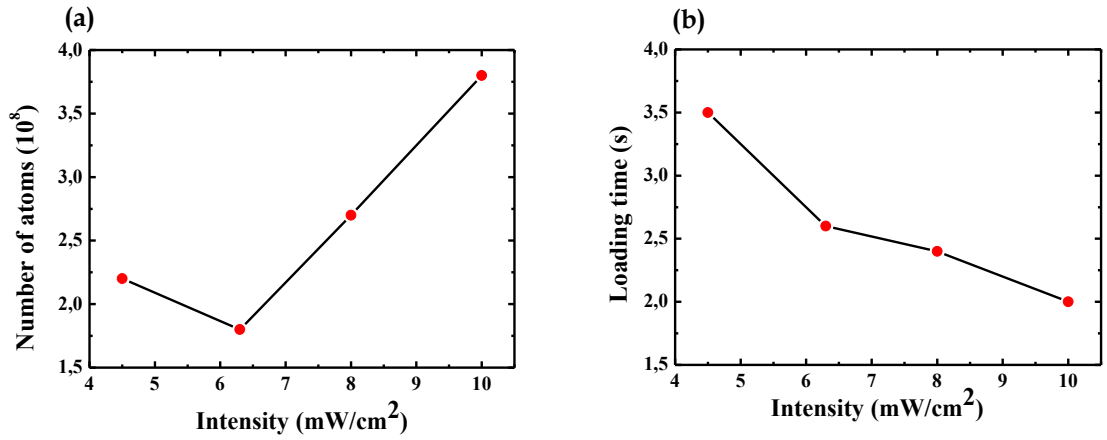

Figure 5.4: Relationship between (a) Laser power and number of trapped atoms (b) Laser intensities and loading time.

5.4.2.2 Magnetic field dependent

The loading curves of ^{87}Rb were also taken for different magnetic field gradients by keeping the values of current for Rb source and for two laser powers 8 mW/cm^2 and 10 mW/cm^2.

Figure 5.5 show the different loading curves and the number of trapped atoms at different values of magnetic field gradients, for Rb getter current of 4.5 A and laser intensity for this data was chosen $8mW/cm^2$. Figure 5.6 shows the number of trapped atoms and the loading time for different magnetic field gradient. The number of atoms initially increases but suddenly decreases for last two values. We think that the reason behind this is at higher current the magnetic field started to compress the trap zone but at the same time number of atoms is increasing. At

higher densities atoms are kicked out of the trap due to inter-atomic collision inside the cold cloud and number of atoms started to decrease.

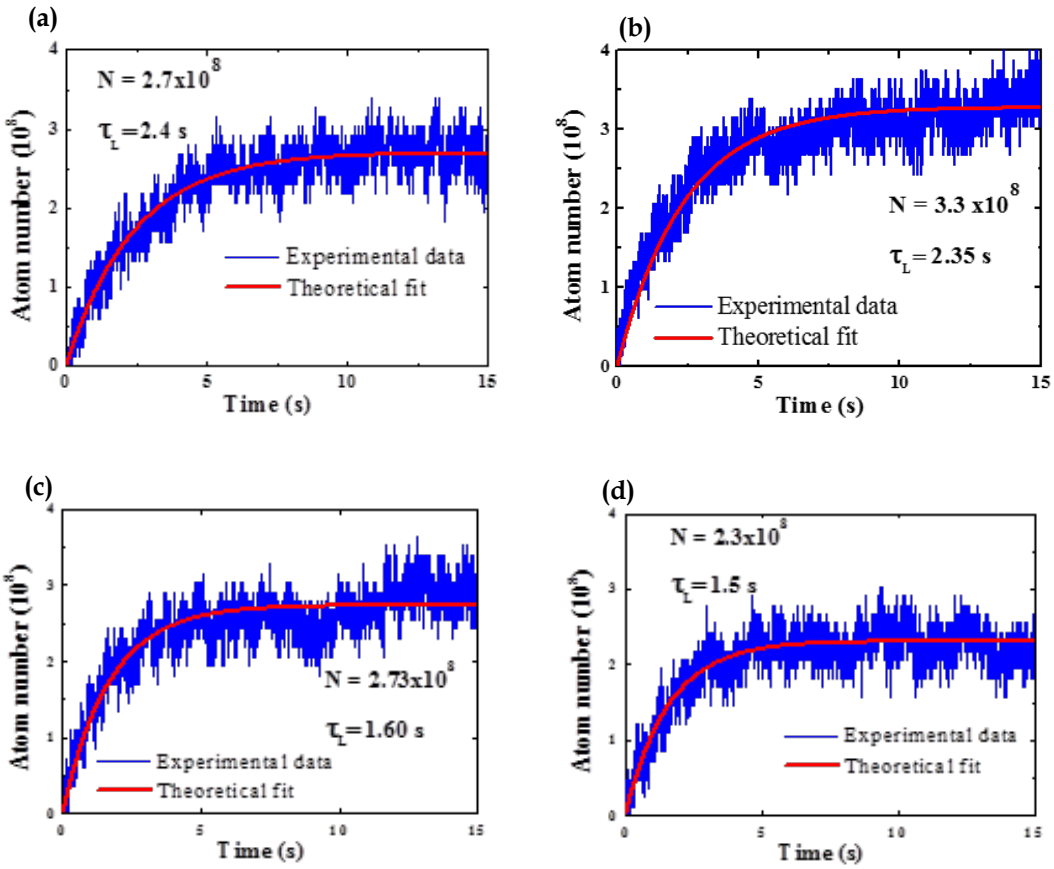

Figure 5.5: Loading curves for measurement of number of atoms of Rb^{87} at different magnetic field gradients (a) 8.8 G/cm (b) 11.8 G/cm (c)14.4 G/cm (d) 16.4 G/cm. While laser intensity (8 mW/cm²) and current for Rb source (4.5 A) are constant. The curve was fitted a function of the form equation (5.19) (red curve).

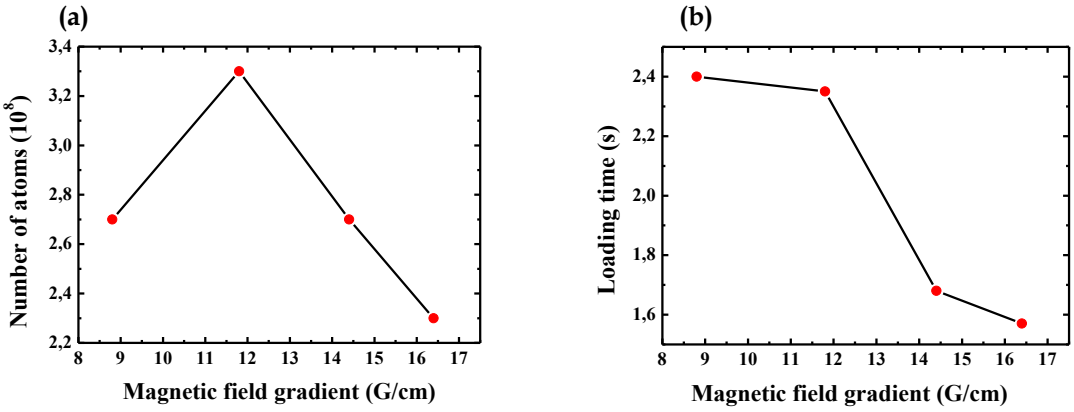

Figure 5.6: Comparison between (a) magnetic field gradient and number of trapped atoms (b) magnetic field gradient and loading time.

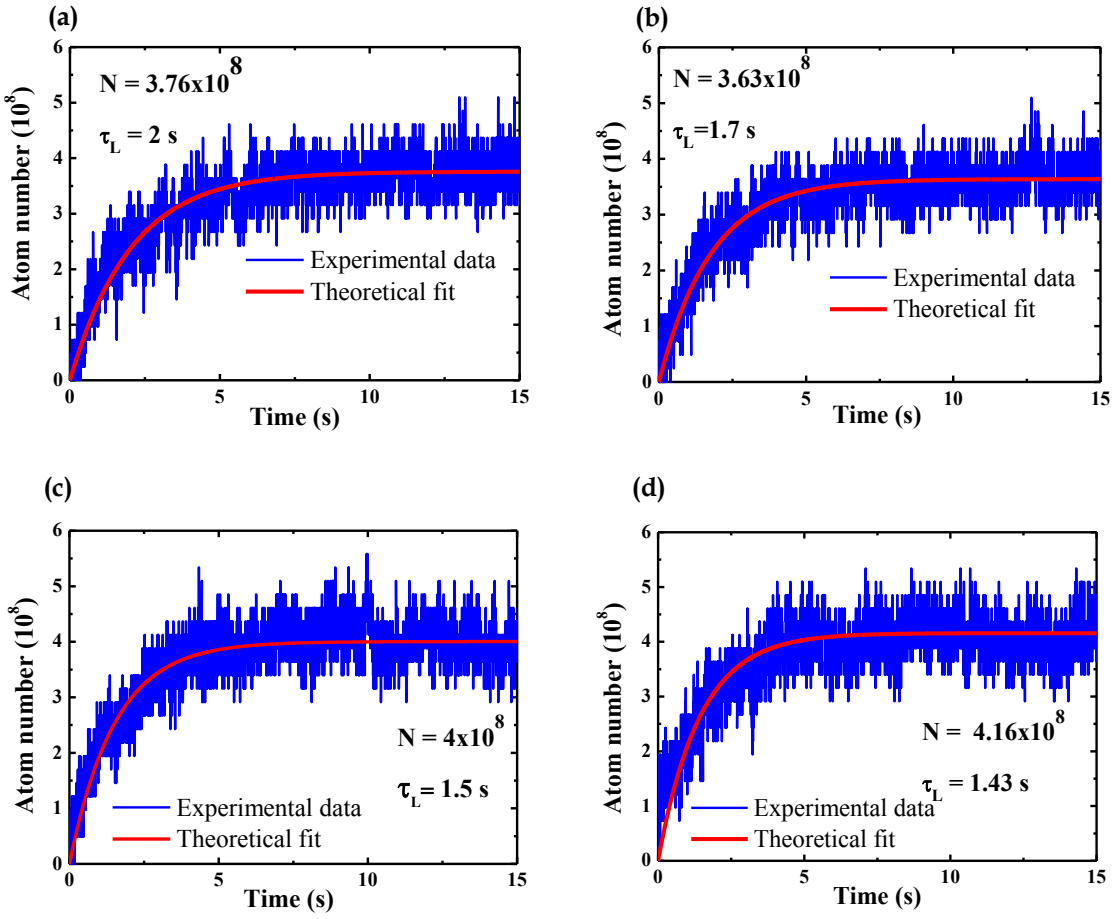

Figure 5.7: Loading curves for measurement of number of atoms of Rb^{87} at different magnetic field gradients (a) 9.6 G/cm (b) 11.8 G/cm (c) 14.4 G/cm (d) 16.4 G/cm. While intensity (10 mW/cm²) and current for Rb source (4.5 A) are constant. The curve was fitted a function of the form equation (5.19) (red curve).

Figure 5.7 shows the different loading curves and the number of trapped atoms at different values of magnetic field gradients, for Rb getter current of 4.5 A and a laser intensity for this data was chosen 10 mW/cm².

Figure 5.8 shows the deduced trapped atom number and loading time in function of the magnetic field gradient. The results show the increase of the atom number form $3.76x10^8$ to $4.16x10^8$ for magnetic field gradient from 9.6 G/cm to 16.4 G/cm. The loading time ranges between 1.4 and 2 s and decreases with increase in magnetic field gradient.

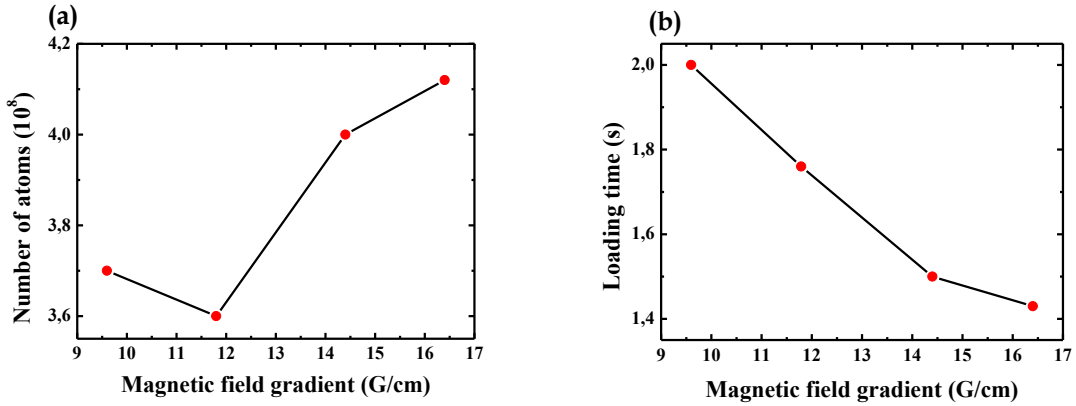

Figure 5.8: Comparison between (a) magnetic field gradient and number of atoms (b) magnetic field gradient and loading time.

5.4.2.3 Rb density dependent

Loading curves in Figure 5.9 are taken for different current of Rb source by keeping the values of magnetic field gradient and laser intensity constant. Releasing Rb vapor changes the background pressure inside the UHV chamber. During this measurement the current for Rb source was varied from 3.5 to 5 A while the laser power and magnetic field gradient were 10 mW/cm² and 9.6 G/cm, respectively.

The atom number in the MOT is dependent on the background pressure of rubidium, supplied by the dispensers. In Figure 5.10 the achievable atom number was measured as a function of dispenser current. The generation of the MOT can be observed only if the dispenser current is above 3.5 A, which agrees with the specifications of the dispensers used (SAES Getter). By increasing the dispenser current, the number of atom increase which is shown in Figure 5.10. Higher dispenser current of 5 A gives a large number of trapped atoms of 5.1 x 10^8 atoms.

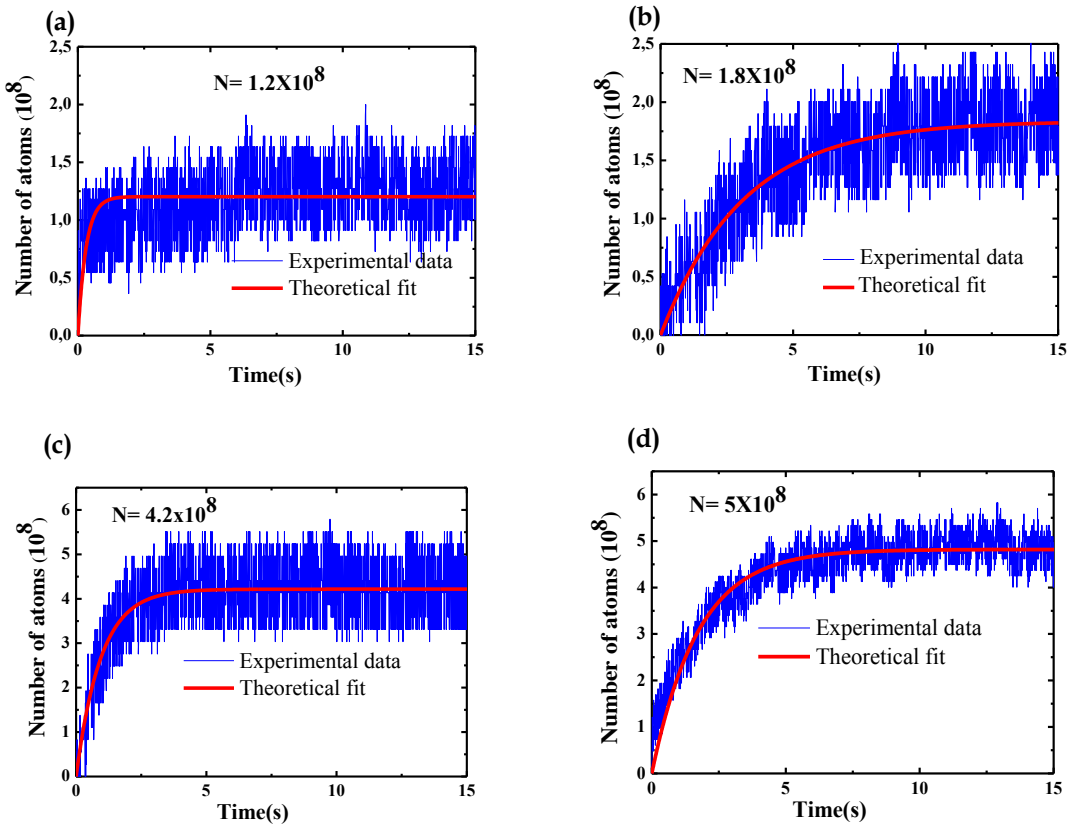

Figure 5.9 Loading curves for measurement of number of atoms of Rb^{87} at different current of Rb source (a) 3.5 A (b) 4 A (c) 4.5 A (d) 5 A while laser intensity (10 mW/cm²) and magnetic field gradient (9.6 G/cm) are constant.

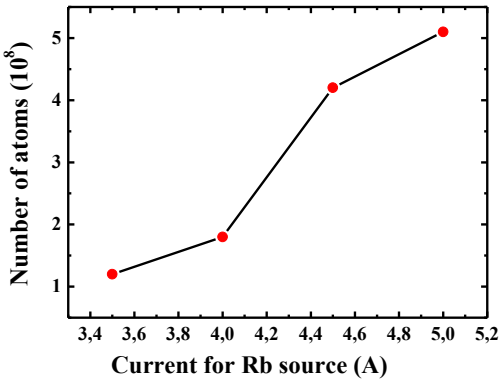

Figure 5.10: Comparison between (a) Rb dispenser current and number of atoms.

5.5 Temperature measurement and MOT optimization

Two invaluable quantities which can be extracted from the cold cloud are atom number and temperature. The former is presented in previous section. Here we will present the temperature measurement by using two methods. First is time of flight (TOF) and second is release and recapture (R&R) method. TOF method requires the sequences of images in time. In this method, temperature is measured by free expansion of atoms.

5.5.1 Time of flight method (TOF)

In this technique, the spatial distribution of atoms released from MOT is monitored by camera. When atoms are released from trap, its initial position x_i and final position x_f can be related by

$$x_f = x_i + v_x t \tag{5.23}$$

Where v_x is the velocity of the atom and t is the expansion time. The final position $P(x_f,t)$ of cloud of atoms can be written as a convolution of the initial position

distribution $P(x_i)$ and the velocity distribution $f(v_{xi})$. Assuming that the cloud has uniform temperature then the initial position distribution has the Gaussian shape

$$P(x_i) = \frac{1}{\sqrt{2\pi\sigma_x}} e^{-x_i/2\sigma_x^2} \quad (5.24)$$

Velocity distribution of cloud is Maxwellian

$$f(v_x) = \left(\frac{m}{2\pi k_B T_x}\right)^{1/2} exp\left(\frac{-mv_x^2}{2k_B T_x}\right) \quad (5.25)$$

Where m is the mass of single atom, T_x is the temperature of the cloud. The final position of cloud after release can be written as

$$P(x_f, t) = \int_{-\infty}^{+\infty} P(x_i) f(v_x) dx_i = \int_{-\infty}^{+\infty} P(x_i) f \frac{x_f - x_i}{t} = P(x_i) \times f(v_x) \quad (5.6)$$

By putting the values of $P(x_i)$ and $f(v_x)$ in equation 5.26, we can have the expansion of cloud over time

$$\sigma_x(t) = \sqrt{\sigma_x^2(0) + \frac{2k_B T_x}{m} t^2} \quad (5.27)$$

In the above equation, it is seen that the final position distribution is the root of the quadrature sum of the standard deviation of the velocity distribution and the standard deviation of the initial position distribution.

5.5.1.1 Experimental procedure

First, we used TOF technique to measure the temperature of cold Rb atoms. Our results include about how this technique depends on the magnetic field gradient, laser intensities and current of Rb source.

The experimental setup is depicted in Figure. 5.11. In the setup we used high speed and sensitive CCD camera, ProcImage500-eagle having 1280X1024 pixels and frame rate of 1000 fps. The size of each pixel is 14X14µm. We are using MVL 7000 zoom lens. The focal length range of this lens is 18 ~ 108 mm. The camera was mounted above the chamber such that the MOT was viewed through one of the viewports

(CF40). After setting all the parameters for MOT, we take two videos for measurement. One is with MOT and other is without MOT on same parameters to remove the background. The MOT is loaded from background Rb atoms and by switching-off the laser beams and the magnetic field at the same time, the atoms expand ballistically and images are taken within the time set by camera exposure time.

The size of the MOT is extracted by calibrating it against a known size of screw located at the same transverse plane as that of the MOT relative to camera direction (see Figure 5.11).

Figure 5.13 shows four frames from a represented sequence when the MOT lasers and anti-Helmholtz coils are switched off. Here the sequence duration was set to ~6 ms, and each frame represents a close-up of the MOT cloud. The MOT size and its expansion during the sequence were deduced by fitting the recorded fluorescence spot to a 2D Gaussian profile extracted from the images. The data fit was undertaken using Matlab. From the fit of the different frames, we deduced the MOT temperature by its initial size $\sigma_{(0)}$ using equation 5.27 and by plotting the evolution of the full width at half maximum of the Gaussian profile (FWHM) with time.

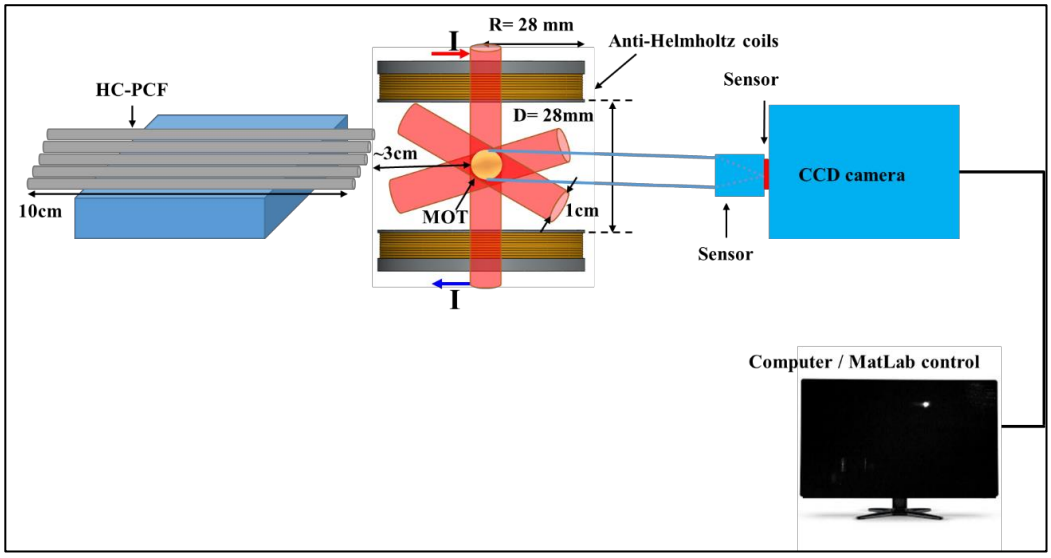

Figure 5.11 The optical scheme for time of flight measurement technique.

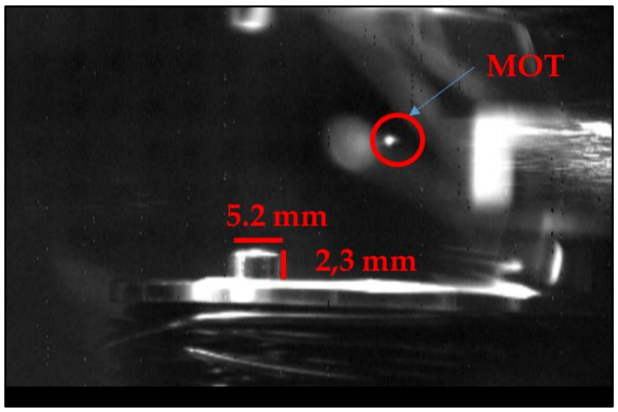

Figure 5.12 Cloud of ^{87}Rb in a MOT taken from side view with CCD camera and the size of screw used for the pixel size calibration.

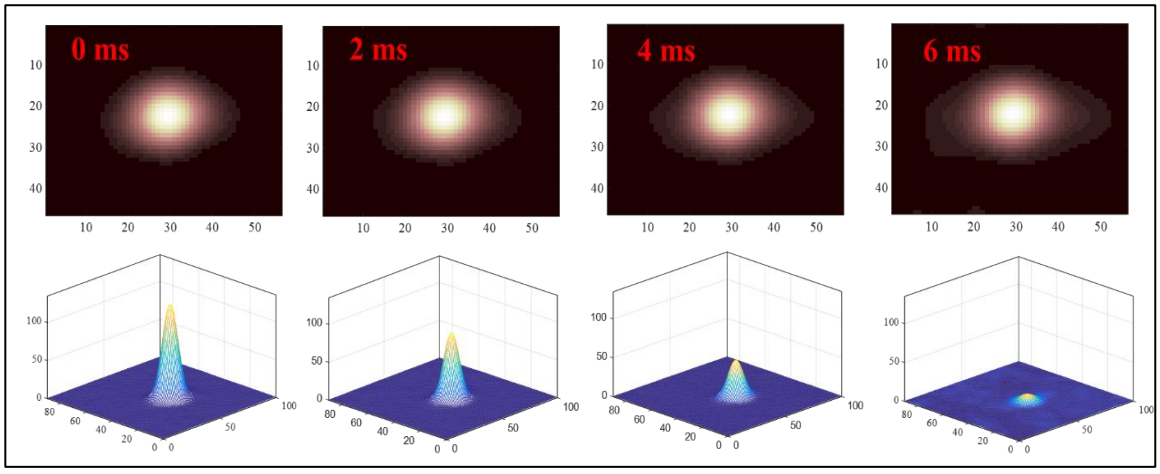

Figure 5.13 Cloud expansion of MOT obtained from the recorded decay. The image of the cloud is taken every 2 ms from an expansion time of 1 ms to 15 ms. The cloud radius is measured using the Gaussian fit.

The temperature measurements were undertaken in different experimental conditions so to assess the convenience of our platform relative to the MOT generation but also to find the optimum parameters for MOT generation.

5.5.1.2 Rb density dependent

Figure 5.14 shows the results for temperature measurement by using the aforementioned TOF method for different Rb source current whilst keeping constant the magnetic field gradient and the intensity of laser beam. Here the extracted atomic cloud FWHM is plotted against time and fitted against equation 5.27. From a best fit of Equation 5.27, the temperature was found to depend on the atom number (see Figure 5.15 (a)). At high number of atom, 5.1×10^8, the temperature is 78 µK. This is significantly above the low temperatures of 10 µK which is achieved with atom numbers of 1.2×10^8 see Figure 5.15 (b)).

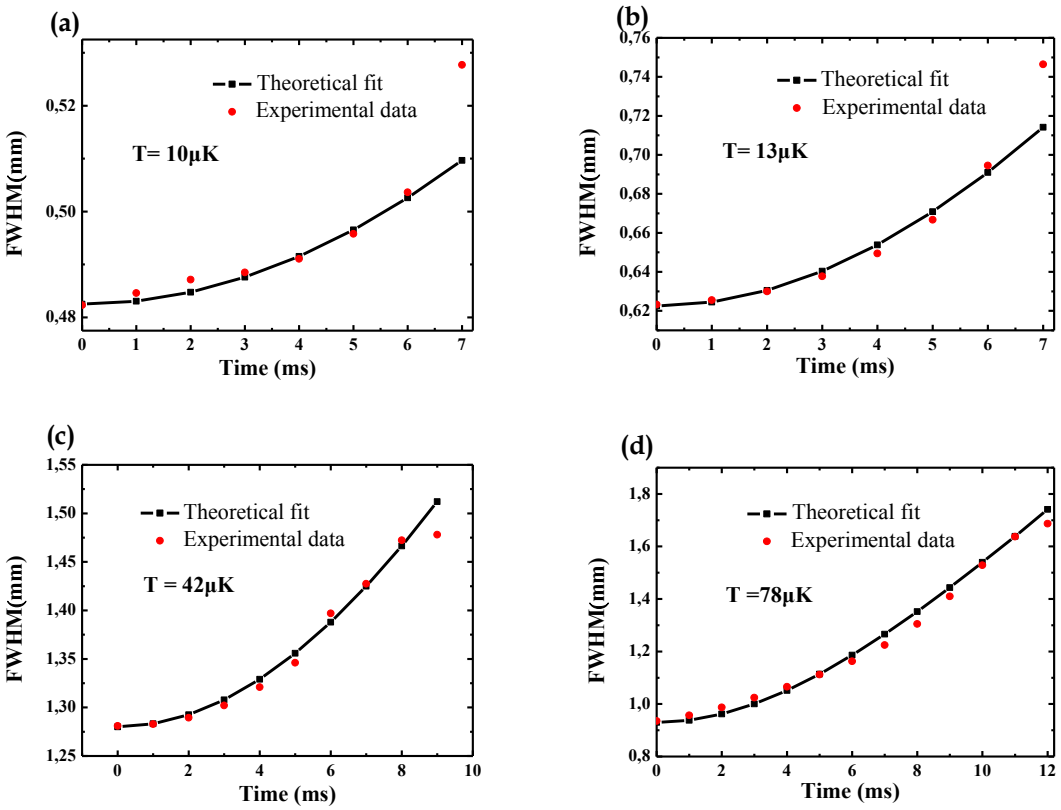

Figure 5. 14 Measured temperature of Rb^{87} at different current for Rb source (a) 3.5 A (b) 4 A (c) 4.5A (d) 5 A. While intensity (10 mW/cm²) and magnetic field gradient (9.6 G/cm) are constant

Figure 5.15 synthesises the above results by plotting both the MOT number of atoms and the extracted temperature for the different Rb source current. The results show that for our Rb-source current range, the number of atoms is in the range of 10^8 and 5 10^8 atoms and the temperature is between 10 μK and 80 μK.

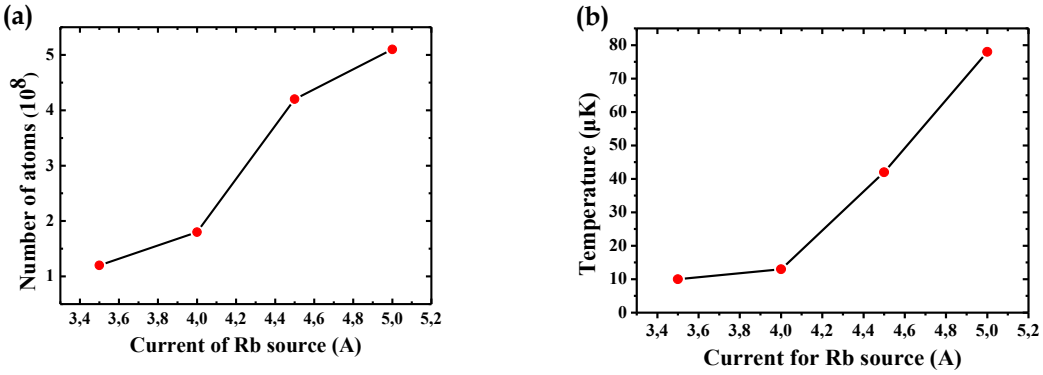

Figure 5.15 (a) Gives the comparison between the number of trapped atoms and current for Rb source (Rb density) given in Figure 5.10 (b) The comparison between temperature measured by using TOF method and different values of current for Rb source given in Figure 5.15. Both the measurements (number of atoms and temperature) were taken at same time by using same parameters. The trend in both the graphs is same.

Moreover, by setting the laser intensity to a lower value of 4.5m W/cm^2 and increasing the magnetic field gradient to 14.4 G/cm, we measured a minimum temperature of our cold cloud to be about 7μK (Figure.5.16).

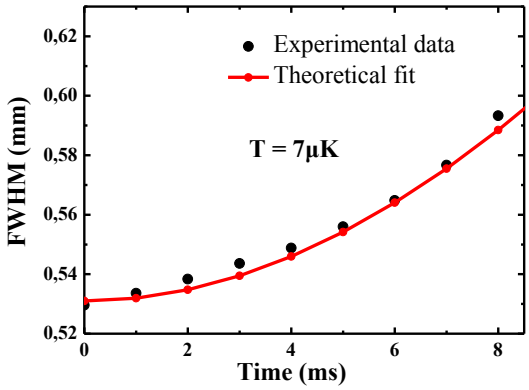

Figure 5. 16 Minimum measured temperature of ^{87}Rb by using time of flight method. The laser intensity 4.5 mW/cm^2 and magnetic field gradient of 14.4 G/cm.

5.5.2 Release and recapture (R&R) method:

The temperature values measured by TOF method are highly sensitive to the cloud size and the dominant uncertainties in the measurements are the error of the Gaussian fit and the calibration of the pixel size. To confirm the temperature values obtained in our experiment we used another method to measure the temperature called release-and-recapture (R&R), developed by P. D. Lett et al. [12]. This method was introduced as the most accessible means of measuring a cloud temperature.

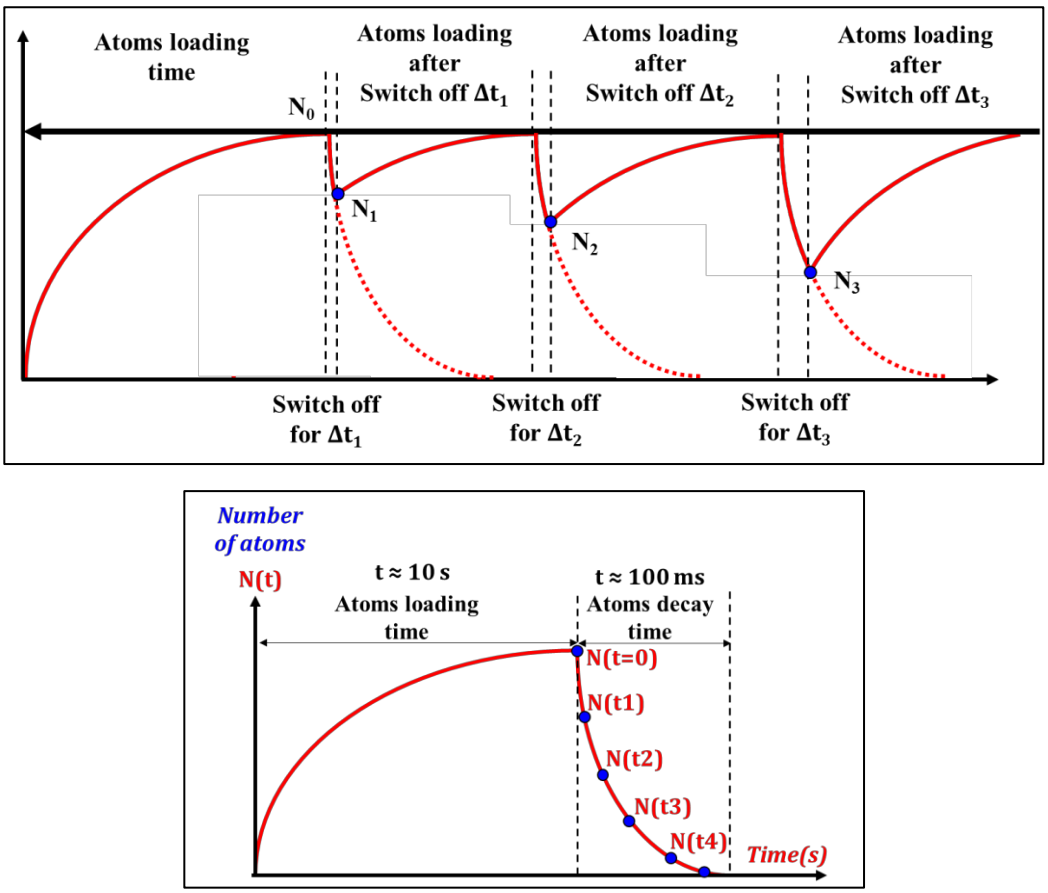

Figure 5.17: Scheme of temperature measurement by using release and recapture technique (top). When the delay between switch-off and switch-on, the MOT is increased, the amount of atoms recaptured in the MOT becomes smaller and smaller. The reconstructed curve after collecting the number of atoms for several interval time Δt (down).

During this measurement the MOT is released by switching off the laser beams (see Figure 5.17). After time "Δt" the beam is turned on again and we observe the number of atoms that have not escaped from the trap region during the time interval "Δt". This process is repeated for different time intervals. The method is repeated by increasing the time interval Δt inducing a decrease in the number of atoms of the MOT after few release and recapture shots. The measured number of atoms for different Δt allows to have the atom decay curve (see Figure 5.17 above) and the temperature can be deduced form the following equation

$$\frac{N(t)}{N(0)} = erf(\chi) - \frac{2}{\sqrt{\pi}}\chi e^{-\chi^2}$$

$$\chi = \frac{R}{t}\sqrt{\frac{m_{Rb}}{k_B T}} \qquad (5.28)$$

The detection scheme is shown in Figure (5.18) has been used for release and recaptures measurement. By using equation 5.28, we can measure the temperature.

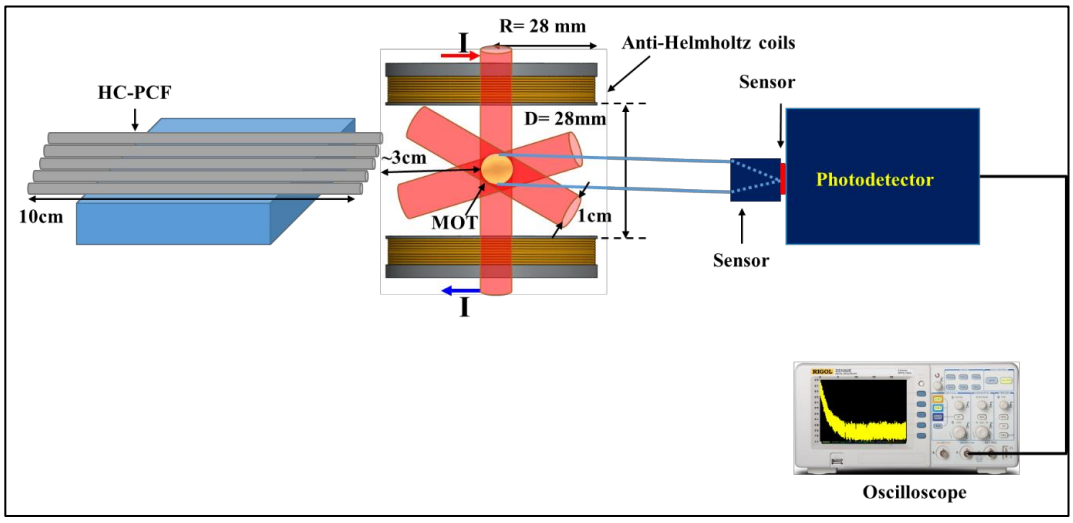

Figure 5.18: The optical setup for release and recapture method.

We measured the temperature of cold cloud by keeping laser intensity (6.3m W/cm²) and current for Rb source (4.5 A) constant. The graph below shows the

values of temperature on two magnetic field gradients i-e 8.8 G/cm and 16.4 G/cm respectively.

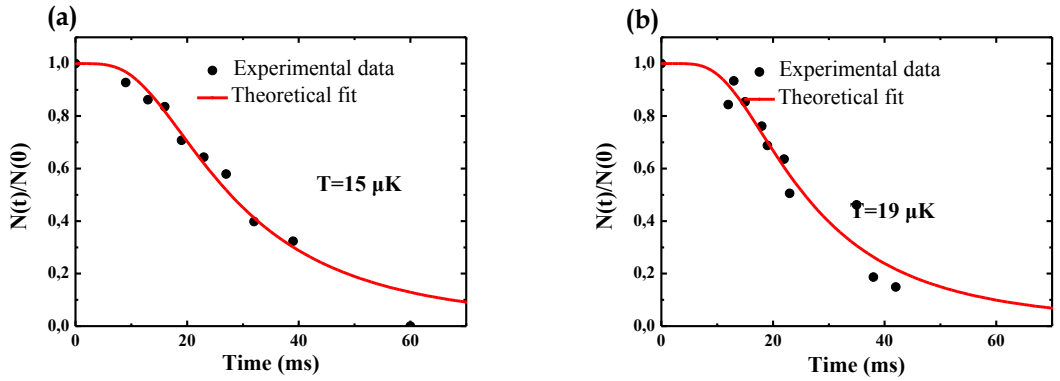

Figure 5.19: (R&R)- Measured temperature of Rb^{87} at different magnetic field gradients (a) 8.8 G/cm and (b) 16.4 G/cm while intensity (6.3 mW/cm²) and current for Rb source (4.5 A) are constant

In Figure 5.19 temperature is increases by increasing the magnetic field gradient. As the measured temperature at 8.8 G/cm is 15µK lower than the temperature at 16.4 G/cm which is 19µk. The increase in magnetic field compresses the atoms by pushing them towards the centre of trap. Collision between atoms causes increase in temperature. The results of temperature measurement using TOF for the same parameters of Figure 5.19 are given in Figure 5.20.

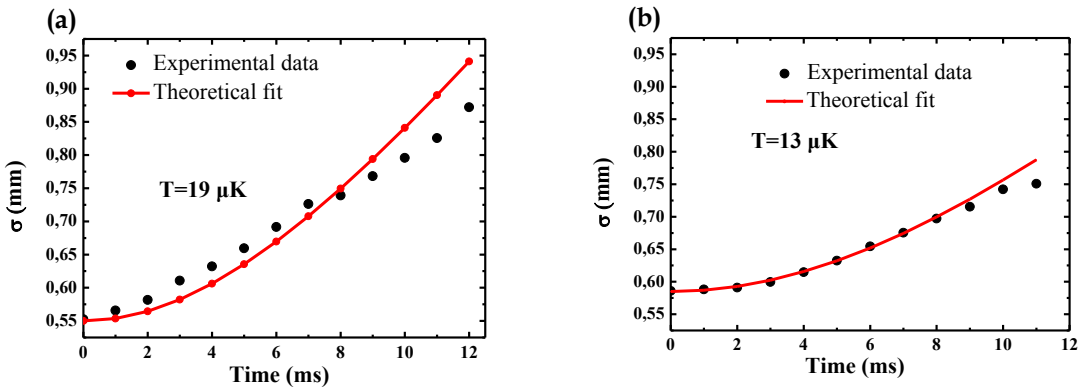

Figure 5.20: (TOF)- Measured temperature of Rb^{87} at different magnetic field gradients (a) 8.8G/cm (b) 16.4 G/cm while intensity (6.3 mW/cm²) and current for Rb source (4.5 A) are constant

Below results are measurements of temperature using both TOF and release and recapture method. The intensity is 4.5 mW/cm^2, magnetic field gradient is 14.4 G/cm and current for Rb source is 4.5 A.

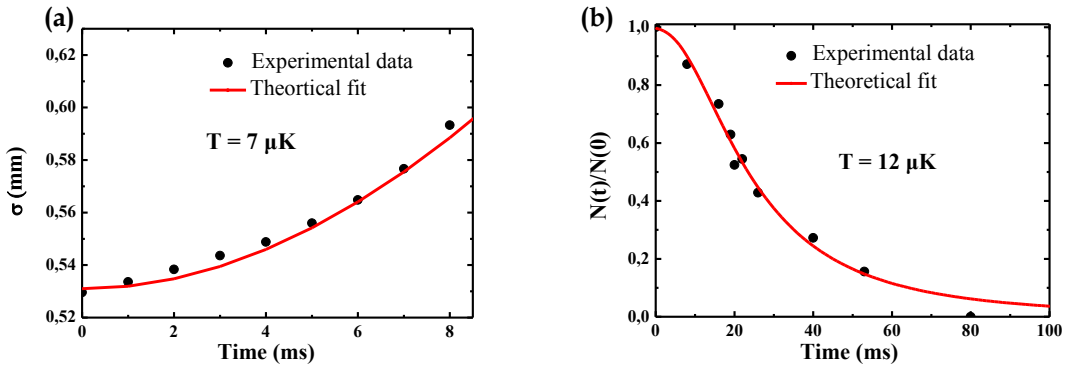

Figure 5.21: Temperature measurement by using (a) Time of flight (TOF) method (b) release and recapture method.

We measured the temperature of Rb^{87} by using both, TOF and R&R methods and the results are below 20 µK. From above results, we can see that there is no big difference between the temperature measurements by two methods.

Furthermore, such temperature and atom number range is sufficient to undertake future in-fibre cold atom spectroscopy.

5.6 Summary

In this chapter we revisited the basic principle of MOT specifically evolution of the regimes of trapped atoms, role of viscous confinement force due to optical field and restoring force due to magnetic field gradient. We mention about transition involve in the cooling and trapping of atoms by showing the energy level diagram. There are two main parameters of trapped in which we are interested: the number of trapped atoms and their temperature in molasses. We measured the number of

trapped atoms by using fluorescence detection methods. We used two methods for measurement of temperature: one is time of flight method and second is release and recapture method. We measured the maximum number of trapped atoms about $5.1x10^8$ (fig. 5.9) and minimum measured temperature is 7μK (fig. 5.13).

These results indicate that the experimental platform for in-fibre cold and thermal atom optics is close to be fully operational. The work left to be done is to demonstrate atom guiding with the blue- and far red-detuned lasers. Once this demonstration is achieved, the "in-fibre laser cooling" can be considered to be operational for undertaking the different experiments required in assessing the feasibility of in-fibre laser cooling of thermal Rb atoms.

References:

1- *"Three-dimensional viscous confinement and cooling of atoms by resonance radiation pressure",* **Chu, S., Hollberg L, Bjorkholm J. E., Cable. A., & Ashkin. A**., Phys. Rev. Lett, vol. 55, 48, (1985).

2- *"Observation of atoms laser cooled below the Doppler limit*", **P. Lett, R. Watts, C. Westbrook, W. Phillips, P. Gould and H. Metcalf,** Phys. Rev. Lett., vol. 61, , p. 169-172, (1988).

3- *"Measurement of temperature of and spring constant in a magneto-optical trap***", G. D. Wallace, T. P. Dinneen, K. Y. N. TanA. Kumarakrishnan, P. I. Gould, and J. Javanainen**, J. Opt. Soc. Am B, vol. 11, No. 5, (1994)

4- *"Trapping of neutral sodium atoms with radiation pressure"*. **E.L.Raab, M. Prentiss, A.Cable, S.Chu and D.Pritchard,** Phys. Rev. Lett. vol. 59, 2631 (1987).

5- *"Three-dimensional spatial diffusion in optical molasses",* **T. W. Hodapp, C. Gerz, C. Furtlehner, C.I. Westbrook, W.D. PhilIips, and J. Dalibard**, Appl. Phys. B, vol. 60, pp. 135-143, (1995).

6- *"Phase space density in magneyo optical trap",***C. G. Townsedn, N. H. Edwards, C. J. Kooper, K. P. Zetie, C. J. Foot, A. M. Steane, P. Szriftfiser, H. Perrin, and J. Dalibard,** Phys. Rev. A, vol. 52, No. 2, (1995).

7- *The escape velocity in a magneto optical trap and its important to trap loss investigation"* , **K. M. F. Magalhaes, S. R. Muniz, G. D. Telles,P.W. Courteille, V. S. Bagnato, and L. G. Marcasa**, Laser Physics, vol. 12, pp.145–151, (2002).

8- *"Very cold trapped atoms in a vapor cell***", C. Monroe, W. Swann, H. Robinson and C. E. Wieman,** Phys. Rev. Lett., vol. 65, p. 1571-1574, (1990).

9- *"Three-dimensional viscoud confinement and cooling of atoms by resonance radiation pressure***", Steven Chu, L. Hollberg, J. E. Bjorkholm, A.Cable, and A. Ashkin,** Phys. Rev. Lett. vol. 55, No. 1, (1985).

10- *"Trapping of neutral sodium atoms with radiation pressure"* **E. L. Raab, M. Prentiss, A. Cable, S. Chu, and D. E. Prtichard**, Phys. Rev. Lett, vol. 59, No. 23, (1987).

11- *"Development of cesium fountain frequency standard at the National Physical Laboratory, India"* **A. S. Gupta, A. Agarwal, P. Arora and K. Pant**, Current Science, vol. 100, (2011)

12- *"Observation of Atoms Laser Cooled below the Doppler Limit*",**P. Lett, R. Watts, C. Westbrook, W. Phillips, P. Gould and H. Metcalf,** Phys. Rev. Lett., vol. 61, p. 169-172, (1988).

13- *"Localization of atoms in a three-dimensional standing wave"*, **Westbrook. C. I., Watts. R. N., Tanner. C. E., Rolston. S. L., Phillips. W. D., Lett. P. D. and Gould. P. L**., Phys. Rev. Lett., vol. 65, 33, (1990).

14- *"Recoil-induced resonances in cesium: An atomic analog to the free-electron laser"*, **Coutois. J. Y., Grynberg. G., Lounis. B., and Verkerk. P**., Phys. Rev. Lett., vol. 72, 3017, (1994).

15- *"Temperature diagnostics for cold sodium atoms by transient four-wave mixing"*, **Mitsunaga. M., Yamashita. M. and Lomoto. N**., Opt. Lett, vol. 23, 840, (1998).

16- *"Experimental and theoretical study of the vapor-cell Zeeman optical trap"*, **K. Lindquist, M. Stephensn and C. Wieman**, Phys. Rev. A, Vol. 46, No. 7, (1992).

Chapter 6

Summary and future work

During the course of this thesis, an experimental platform for Rb laser cooling and atom guidance in hollow-core photonic crystal fibres (HC-PCF) has been built from scratch.

The system has been designed to provide a versatile platform to carry out spectroscopy studies of thermal and cold Rb inside the HC-PCF. Such in-fibre thermal and cold atom spectroscopy is justified by the potential of HC-PCF and their stand-alone gas filled form photonic microcells (PMC) in atom and quantum optics. Rb filled HC-PCF and PMC are interesting candidates for compact and efficient photonic components to explore fundamental phenomena such as cold matter in dielectric microstructures or atom-surface interactions. Furthermore, alkali vapours filled HC-PCF or PMC are ideal to develop compact quantum sensors such as magnetometers, accelerometers or gravimeters. Finally, if in-fibre thermal vapour could be laser cooled, one could envision a radically new breed of atom-photonic devices such as cold-atom core PCF, which could bring, for example, the laboratory performance in atomic clocks into a tiny and portable apparatus.

The present thesis is part of a work which aims to explore in-fibre laser cooling by using an experimental and systematic approach. This methodology entailed the use of purposely designed and fabricated HC-PCFS with different physical and optical properties, thus providing comparative tools, and the development of an experimental set-up that enables filling the fibres with both cold and thermal atoms, and explore several experiments related to the dynamic and spectroscopy of

thermal and cold atom confined in HC-PCF, and with the prospect to study the feasibility of laser cooling thermal atom inside the fibre and then to undertake it with PMC.

The present work presents one of the founding milestones towards in-fibre laser cooling and cold-atom PMC, which is the construction and operation of an experimental platform that permits to undertake the required experiments and investigate the feasibility of different laser cooling schemes.

6.1 Summary

In chapter 1, we have reviewed the historical context of cold atoms and the current trends in the field. Particularly, we listed the seminal works on HC-PCF based atom optics.

We described, in chapter 2, in more details the guidance mechanisms in these HC-PCFs, by reviewing the differences between photonic bandgap (PBG) guiding HC-PCF and Inhibited Coupling (IC) guiding HC-PCF. We then highlighted the most relevant fibre properties to atom and coherent optics. We particularly emphasised the challenge on how to mitigate and/reduce the atom-wall collision and atom-surface physicochemical reactions, on how to engineer surface potential and its effect on atom internal energy structure. In this chapter, we also provided the modal properties of IC guiding HC-PCF, which will be used during the thesis. These fibres have been designed to have large and different core diameters, ranging from ~40 μm and to 85 μm. The fibres exhibits very low loss (all less than 0.2 dB/m and with low figures in 0.02-0.05 dB/m) and guide over a large optical bandwidth so to accommodate the wavelength ranges of ~ 780 nm for Rb cooling and spectroscopy, of >1000 nm for far-red detuned guidance and trapping, and of ~400-500nm for two

photon spectroscopy. For each of these fibres we have coated their samples so to provide a set of HC-PCF having different surface material.

Chapter 3 describes the design and assembly of a UHV chamber which harbours the in-fibre Rb spectroscopy. The UHV chamber has been designed to have a sufficiently large volume to accommodate an optical broadband which supports the optics such as the HC-PCF set. The set comprised ten fibres each 10 cm long from four different HC-PCFs. For each HC-PCF type, we have different core inner-surface. One sample remained uncoated (i.e. SiO_2), one sample has its core inner surface coated with aluminasilicate ceramic and the last with PDMS. The chapter described the coating material and the deposition process, and the optical characterisation of the fibres upon coating. The optical transmission results show a good guidance of the coated fibres, and a spectral shift in their transmission windows due to the thickness change of the core contour. The fibre set is then baked for hours at 100 °C before being placed in the UHV chamber. The chamber has a mountable lid for easy part replacement and thus complying with the need of carrying out different experiments with different fibres if needed. The chamber was assembled, baked and evacuated to obtain a stable pressure in the range of 2-4 10^{-9}torr. Given the large volume and surface of chamber this pressure figure is satisfactory and is sufficient in generating cold atoms. The chamber was then tested upon Rb releasing by monitoring the absorption spectra of Rb outside and inside the fibres. The results show that the fibres are loaded with a rate that can be controlled with the Rb current getter. In order to test the UHV chamber handling during opening and closing, we proceed to open the lid four times during the tenure of thesis. The results show that a pressure of $2X10^{-9}$torr can be retrieve within 50 days from lid closing. This is an important figure in the operation of the platform.

Chapter 4 was dedicated to describe the laser system for cooling and guiding. The laser system was designed and assembled to simultaneously generate two magneto-optical traps (MOTs), to guide and trap thermal and cold atoms inside a chosen fibre from the HC-PCF set. Based on a commercial 1W power and tunable CW laser emitting around 780 nm, we have developed a laser beam comprising two spectral components to address both cooling and repumping. The laser was frequency stabilized using saturated absorption spectroscopy and FM/PDH technique. The results show an Allan deviation of $3X10^{-11}/\sqrt{\tau}$ and an instantaneous frequency linewidth of 27 KHz. This frequency stability fulfils well-above the requirements for MOT generation in laser narrow linewidth and frequency stability. The laser system of the platform that was constructed also includes two additional lasers. The first one is a tunable laser emitting around 780 nm and is set to be coupled to any HC-PCF from the set. The laser will be used for blue detuning guiding by shaping the beam transverse profile to a donut profile. Moreover, we used this laser to carry out preliminary spectroscopy tests for all the fibres. The results showed the characteristic absorption spectra from the hyperfine transitions of both rubidium isotopes, and thus indicating the good operation of the Rb releasing and the fibre filling with the alkali vapour. The second laser is a tunable amplified laser operating around 1060 nm. The laser has been set so to be coupled into one of the HC-PCF from both ends so to enable to generate optical lattices but also to undertake adiabatic transport of cold atoms from the MOTs into the fibre.

The last experiment of the present thesis was dedicated to generate MOT and demonstrate laser cooling in the constructed UHV chamber. The set-up and the results of this work were reported in chapter 5. In this chapter we described the MOT layout and the generated MOT. The results showed that we successfully cooled atoms of ^{87}Rb and ^{85}Rb and that setting the lasers from cooling one isotope to cooling the second one was quick and stable. Moreover, we have undertaken

several measurements to assess how the trapped atom number and temperature behave with the laser intensity, magnetic field gradient and Rb background density. By considering different values for the aforementioned control parameters, we obtained for ^{87}Rb atom number in the range of $1X10^8$ to $5X10^8$, cloud temperature in the range of 20 μK with a minimum of 7μK achieved with laser intensity of 4.5 mW/cm^2, B-field of 14.4 G/cm and background pressure ~ $5X10^{-9}$ Torr, and a cloud size of ~1 mm diameter. For ^{85}Rb, the obtained ranges for atom number and temperature were 10^7-10^8 and 30-50μK respectively. These results show that the phase density of the cooled Rb fulfils the set requirements for in-fibre cold-atom spectroscopy.

6.2 Future work

The above results are the necessary milestones towards achieving a fully operational platform for in-fibre spectroscopy of cold and thermal Rb. To fully complete this *in-fibre laser cooling platform*, the atom guidance have to be demonstrated, and its associated laser layout to be completed. The latter is the first requirement before the start of in-fibre spectroscopy and exploring atom trapping and cooling inside HC-PCF. Also, the accomplishment of operational guiding lasers will complete the platform.

Among the immediate future work to be undertaken once the guiding lasers are set, we count: (1) Red-detuned guidance; (2) Blue detuned guidance; (3) Guidance in different HC-PCF; (4) Guidance with different modal excitation; (5) Lifetime measurement of cold atom for different HC-PCF. For the red-detuned guidance, it is planned to use first a simple forward propagating high power beam from the 1060 nm laser. The comparison of the achieved atom flux from this guiding mechanisms in the same HC-PCF but with different surface coatings will provide us with the key

information on the most adequate surface material for anti-sticking. In a second stage, far-red detuned guidance with a spatially shifting optical lattice will be explored for adiabatic cold atom loading inside HC-PCF. This experiment will be used to investigate the lifetime of cold atom inside the different HC-PCF under test. Furthermore, this lifetime measurement will be also carried out in the presence of a blue-detuned donut-shaped mode so to assess the effect of surface heating effect but also to explore the transverse trapping of different donut-shaped modes. Undertaking these experiments with different HC-PCF will provide a lower to clarify the impact of modal area and/or the surface material on the atom dynamics inside the fibre core.

The above future work will be next necessary step toward undertaking the challenging aim of in-fibre laser cooling. In parallel to this work, there is another work in our group to develop Rb-PMC. This work will be other necessary step before considering stand alone in-fibre laser cooling.

Plateforme expérimentale pour l'optique atomique et le refroidissement d'atomes intra-fibre creuse

[Résumé de la thèse]

Cette these décrit la conception et la réalisation d'une plateforme expérimentale pour le refroidissement par laser et le guidage d'atomes de Rb dans les fibres à cristal photonique à cœur creux (HC-PCF). Cette plateforme a pour but de fournir un système polyvalent pour explorer le refroidissement par laser à l'intérieur des fibres avec l'objectif à plus long terme de réaliser une fibre optique constituée d'un cœur rempli d'atomes froids (micro-cellule photonique). La plateforme a été conçue pour héberger plusieurs expériences sur le guidage d'atomes froids et thermiques ainsi que la spectroscopie dans les HC-PCFs pour répondre à plusieurs questions ouvertes liées par exemple à l'effet de la surface interne des HC-PCFs sur la structure énergétique des atomes ainsi que le piégeage et le refroidissement des atomes. La plateforme comprend une chambre spécifique à vide ultra-élevée (UHV) et un ensemble de lasers pour le refroidissement et le guidage des atomes à l'intérieur du HC-PCF hautement adapté. La chambre UHV a été conçue pour accueillir plusieurs HC-PCFs et deux pièges magnéto-optiques (MOT). Les HC-PCFs ont été conçus et fabriqués avec différents diamètres de cœur, contenu modal et post-traités avec des matériaux différents pour la surface interne du cœur. Par exemple, les diamètres du cœur varient de ~ 30 µm à ~ 80 µm traités avec une couche d'aluminosilicate ou une couche de PDMS afin de fournir un grand espace de paramètres pour évaluer l'effet de la surface sur les atomes confinés dans les fibres. Ainsi, le système a été construit et caractérisé. Le laser de refroidissement/repompage a été stabilisé en fréquence, avec une variance d'Allan de $\sigma(\tau) = 3.8 \times 10^{-11}/\sqrt{\tau}$. Avec ce système nous avons généré un MOT avec les deux isotopes du Rb, avec une température de refroidissement faible de l'ordre de 7 µk. La plateforme est maintenant opérationnelle pour entreprendre le premier guidage atomique et explorer la faisabilité du refroidissement des atomes à l'intérieur des HC-PCFs.

Mots-clés: Fibre creuse à cristal photonique (HC-PCF), Micro-Cellule Photonique.

Experimental platform towards in-fibre atom optics and laser cooling

[Summary of the thesis]

This thesis reports on the design and fabrication of an experimental platform for in-fiber laser cooling of Rb and atom optics. By in-fiber laser cooling, we mean the long term aim of laser cooling thermal Rb atoms of a Photonic MicroCell (PMC), and subsequently developing what would be cold-atom photonic crystal fibre (PCF). The platform was designed to harbor several experiments on cold and thermal atom guidance and in-fiber spectroscopy so to address several open questions related for example to the effect of the core inner-wall surface on the atom energy structure and on selective fiber mode excitation for atom trapping and cooling. The completed platform comprises a specific and large ultra-high vacuum (UHV) chamber and a set of lasers for both atom cooling and atom guiding inside highly tailored hollow-core photonic crystal fiber (HC-PCF). The UHV chamber was designed to accommodate several HC-PCFs and two magneto-optical traps (MOTs). The HC-PCF were designed, fabricated and post-processed to exhibit different core diameter, modal content and core inner surface material. For example, the mode field diameters range from ~30 µm to ~80 µm for the fundamental Gaussian-like core mode, and the surface materials include pure silica, a layer of Aluminosilicate or a layer of PDMS so to provide a large parameter space in assessing the effect of surface on the fiber-confined atoms. The system has been constructed and characterized. The cooling/repumping laser was frequency-stabilized, with measured Allan variance deviation of $\sigma(\tau) = 3.8 \times 10^{-11}/\sqrt{\tau}$. With the system we generated MOT with both isotopes of the Rb atom, with a cooling temperature as low as 7 µK. The platform is now operational to undertake the first atom guidance and explore the feasibility of atom cooling inside a HC-PCF.

Keywords: Hollow-Core Photonic Crystal Fiber (HC-PCF), Photonic MicroCell (PMC).